UNIVERSIDAD COMPLUTENSE DE MADRID

FACULTAD DE CIENCIAS QUÍMICAS

TESIS DOCTORAL

Covalent Organic Frameworks: tailored design and synthesis towards sustainable applications

Redes Orgánicas Covalentes: diseño y síntesis de nuevos materiales para aplicaciones sostenibles

MEMORIA PARA OPTAR AL GRADO DE DOCTOR

PRESENTADA POR

Paloma García Arroyo

DIRECTORES

José Luis Segura Castedo
María José Mancheño Real

UNIVERSIDAD COMPLUTENSE DE MADRID
FACULTAD DE CIENCIAS QUÍMICAS
Departamento de Química Orgánica

TESIS DOCTORAL

Covalent Organic Frameworks: tailored design and synthesis towards sustainable applications.

Redes Orgánicas Covalentes: diseño y síntesis de nuevos materiales para aplicaciones sostenibles.

MEMORIA PARA OPTAR AL GRADO DE DOCTOR
PRESENTADA POR:

Paloma García Arroyo

Directores: José Luis Segura Castedo
y María José Mancheño Real

Madrid, 2021

UNIVERSIDAD COMPLUTENSE DE MADRID
FACULTAD DE CIENCIAS QUÍMICAS
DEPARTAMENTO DE QUÍMICA ORGÁNICA

TESIS DOCTORAL

Covalent Organic Frameworks: tailored design and synthesis towards sustainable applications.

Redes Orgánicas Covalentes: diseño y síntesis de nuevos materiales para aplicaciones sostenibles.

MEMORIA PARA OPTAR AL GRADO DE DOCTOR
PRESENTADA POR:

Paloma García Arroyo

Directores: José Luis Segura Castedo y María José Mancheño Real

Madrid, 2021

COVALENT ORGANIC FRAMEWORKS: TAILORED DESIGN AND SYNTHESIS TOWARDS SUSTAINABLE APPLICATIONS

REDES ORGÁNICAS COVALENTES: DISEÑO Y SÍNTESIS DE NUEVOS MATERIALES PARA APLICACIONES SOSTENIBLES.

Directores:

José Luis Segura Castedo y María José Mancheño Real

Memoria que para optar al grado de

DOCTOR EN CIENCIAS QUÍMICAS

presenta

Paloma García Arroyo

Madrid

Abril, 2021

D. **José Luis Segura Castedo**, Catedrático de Universidad y Dña. **María José Mancheño Rea**l, Catedrática de Universidad, adscritos al Departamento de Química Orgánica de la Universidad Complutense de Madrid,

CERTIFICAN:

Que la presente memoria, titulada: "**COVALENT ORGANIC FRAMEWORKS: DESIGN AND SYNTHESIS TOWARDS SUSTAINABLE APPLICATIONS**" se ha realizado bajo su dirección en el departamento de Química Orgánica de la Universidad Complutense de Madrid, por la Graduada en Química Dña. Paloma García Arroyo, y autorizan su presentación para ser calificada como **Memoria de Tesis Doctoral**.

Y para que conste, firman el presente certificado en Madrid, a 6 de mayo de 2021.

Fdo. José Luis Segura Castedo María José Mancheño Real

Los estudios recogidos en esta memoria relacionados con el uso de COFs para el almacenamiento de energía y su uso en el desarrollo de envases activos se han financiado gracias al proyecto MAT2016-77608-C3-2-P del Ministerio de Economía y Competitividad (MINECO).

Los estudios relacionados con el uso de COFs para electrocatálisis y la detección fluorescente de iones metálicos se han financiado gracias al proyecto PID2019-106268GB-C33 del Ministerio de Ciencia e Innovación (MICINN) así como gracias a una Ayuda para la contratación de investigadores predoctorales de la Comunidad de Madrid tutorizada por José Luis Segura Castedo.

Los resultados de investigación descritos en esta Memoria se encuadran dentro del marco del Plan de Investigación presentado para la consecución del título de Doctor en el Programa de Doctorado en Química Orgánica de la Universidad Complutense de Madrid. Estos resultados han dado lugar, hasta el momento de la edición de esta memoria, a las siguientes publicaciones:

-P. García-Arroyo, E. Martínez-Periñán, J. J. Cabrera-Trujillo, E. Lorenzo, J. L. Segura; "Pyrenetetraone-based Covalent Organic Framework as an effective electrocatalyst for oxygen reduction reaction"; *submitted.*

-S. Medina Rivero, P. García-Arroyo, L. Li, S. Gunasekaran, T. Stuyver, M. J. Mancheño, M. Alonso, L. Venkataraman, J. L. Segura, J. Casado; "Single-molecule conductance in a unique cross-conjugated tetra(aminoaryl)ethene"; *Chem. Commun.*, **2021**, 57, 591-594.

-P. García-Arroyo, P. Navalpotro, M. J. Mancheño, E. Salagre, J. J. Cabrera-Trujillo, E. G. Michel, J. L. Segura, J. Carretero-González; "Acidic triggering of reversible electrochemical activity in a pyrenetetraone-based 2D polymer"; *Polymer*, **2021**, 212, 123273 (1-5).

-P. García-Arroyo, M. P. Arrieta, D. Garcia-Garcia, R. Cuervo-Rodríguez, V. Fombuena, M. J. Mancheño, J. L. Segura; "Plasticized poly(lactic acid) reinforced with antioxidant covalent organic frameworks (COFs) as novel nanofillers designed for non-migrating active packaging applications"; *Polymer*, **2020**, 196, 122466 (1-11).

A mis padres y mi hermana

ACKNOWLEDGMENTS

Esta Tesis Doctoral se ha llevado a cabo en el Departamento de Química Orgánica de la Universidad Complutense de Madrid bajo la dirección de los profesores José Luis Segura Castedo y María José Mancheño Real, a los cuáles me gustaría agradecer en primer lugar. A José Luis, muchísimas gracias por brindarme la oportunidad de unirme a tu grupo de investigación para poder llevar a cabo la presente tesis, así como por toda la orientación y ayuda que me has proporcionado durante estos años. A María José, gracias por tu enorme ayuda en el laboratorio durante todo este tiempo, por tus consejos y sobre todo por animarme a lo largo de este (no siempre fácil) camino.

Asimismo, me gustaría agradecer la participación de otros profesores e investigadores con los que he tenido el placer de colaborar en distintos proyectos durante el desarrollo de este trabajo. Al Dr. Emiliano Martínez y a la Dra. Encarnación Lorenzo de la UAM por los estudios de electrocatálisis del COF de quinonas, y al Dr. Javier Carretero y a la Dra. Paula Navalpotro por los estudios electroquímicos del polímero análogo. Al Prof. Enrique García Michel de la UAM por las medidas e interpretación de resultados de XPS, y al Dr. José Ignacio Martínez del ICMM-CSIC y Jorge J. Cabrera de la UCM por los cálculos teóricos y modelizaciones estructurales de los distintos COFs. Al Prof. David Ávila y Elena García Chamocho por las medidas de capacitancia de los CTFs así como por las interesantes discusiones científicas y la gran ayuda aportada en la interpretación de los resultados. A la Dra. Marina P. Arrieta, al Dr. Daniel García García y al Dr. Vicent Fombuena por su ayuda en el desarrollo y caracterización de los films biodegradables así como los estudios de capacidad antioxidante de los mismos.

Igualmente me gustaría extender mi agradecimiento a todas aquellas personas cuya ayuda ha permitido la realización de muchos de los experimentos y ensayos incluidos en esta tesis. A los técnicos de laboratorio (Francisco Javier García y Laura García) por la realización de los espectros de FTIR, así como a Javier Cornejo por su ayuda y disposición. Al CAI de RMN de la Facultad de Ciencias Químicas de la UCM, especialmente a Ángel Sánchez por los espectros de RMN de carbono en sólido. Al CAI de Difracción de Rayos X, en especial a Julián Vázquez por los difractogramas recogidos en esta memoria. Al Centro de Microscopía Electrónica, especialmente al Dr. Javier García García por la realización de las imágenes de SEM y TEM. También querría expresar mi gratitud

a Emilio y al resto del personal del taller de vidrio, por su gran eficacia y ayuda y por su buen humor en todas las visitas que nos hemos hecho.

Muchas gracias también al Prof. Carlos Seoane por su gran amabilidad y a la Prof. Rocío Cuervo por su cercanía e interés en todo momento (desde que le entregaba los cuadernos de prácticas hace ya muchos años).

Me gustaría mencionar también a la Prof. Raquel Cortés Gil del Departamento de Inorgánica de la UCM. Gracias por todo tu ánimo y apoyo desinteresado.

También querría agradecer a todas las personas con las que he coincidido en el laboratorio y que han conseguido hacer mucho más ameno y agradable todo el trabajo diario. A Matías, por mantener siempre tu buen humor, hasta enfadado. Gracias por tus conversaciones y sobre todo porque has hecho que trabajar contigo sea no sólo fácil sino de lo más divertido. A Sergio, gracias por tus consejos y tu infinita paciencia en diversos momentos, y sobre todo por escuchar sin queja todos mis lamentos y lloros. Marquitos, muchas gracias también por mantener tu buen rollo siempre, sé que te irá muy bien en todo. Muchas gracias a Elena, Esther y Álex, por compartir vuestro conocimiento y por vuestro compañerismo y amabilidad. Querría hacer especial mención a Marina. Muchas gracias por toda tu ayuda, tu experiencia y sobre todo por transmitir esa pasión por la investigación como nadie. También me gustaría agradecer a todas esas personas a las que he podido guiar y las cuáles me han permitido disfrutar de una de mis grandes pasiones, la docencia (Sergio, Alia, Manu, Lagoma y Siham).

A toda la gente del Departamento con la que he compartido risas tanto dentro como fuera, y que habéis hecho de esta experiencia algo inolvidable repleto de buenos momentos. A Andrea, porque siempre tienes una sonrisa, da igual lo pronto o tarde que sea. Al Canario, gracias por todas las risas y por mantenernos siempre al día de las últimas noticias con el Depar Today. A Cris, los Manus, Eider, Jon, Silvia y Ana, ojalá y podamos repetir un viaje tan genial como el que hicimos. A esas personitas que, aunque casi no compartimos tiempo en el Departamento, lo hemos suplido con incontables cenas y fiestas fuera: Elena, Sara, Yago.

No puedo olvidarme de mi Jose Q. Porque empezaste siendo un compañero (que casi ni me caía bien) y te has convertido en uno de mis grandes apoyos, tanto estos

años de tesis como todos los de antes. Sé que siempre estarás ahí, en la puerta de enfrente (aunque deje de ser literal).

También querría agradecer a todos los compañeros y amigos que he tenido la suerte de conocer durante mis años de investigación en Helsinki y en Copenhague. Marta, Rebecca, David, Francesco, Ádel, Dorleta… porque con vosotros he aprendido que la amistad no se mide en kilómetros sino en ataques de risa y buenos momentos. Y como no, dar las gracias a las de siempre, a mis sexy ladies, a las que siempre han estado acompañándome a lo largo y ancho de mi camino, fuera cual fuese la dirección…

Muchas gracias a ti, Jorge, porque has estado a mi lado desde el principio, apoyándome en los momentos buenos y en los no tan buenos. Gracias por animarme siempre, y por ser capaz de "apartarme los árboles" que no me han dejado ver el bosque en alguna ocasión. Eres lo más bonito que me llevo de esta etapa, gracias por ser el mejor amigo y compañero de viaje. Te quiero muchísimo.

Y por último, gracias a mi familia, por todo vuestro cariño, por estar siempre cerca a pesar de la distancia. A Alicia, porque no podría tener una hermana mejor. Gracias por apoyarme y ayudarme a ver la objetividad y el lado bueno de casi todo. Y por último, gracias a mis padres, por estar siempre ahí, por animarme a conseguir todos mis objetivos y proyectos. Sois el pilar fundamental en mi vida, gracias por todo vuestro amor incondicional. Os quiero muchísimo.

ABBREVIATIONS AND ACRONYMS

The common abbreviations and acronyms employed in organic chemistry have been used in the present thesis by following the "Guidelines for authors" of *Journal of Organic Chemistry* (2021). These words can be found in the following journal webpage:

https://pubs.acs.org/paragonplus/submission/joceah/joceahauthguide.pdf

Furthermore, the next abbreviations have been also included:

2D	Two-dimensional
3D	Three-dimensional
ATBC	Acetyl tributyl citrate
BET	Brunauer-Emmett-Teller
BEX	Binodal net assembled from 3-c and 4-c secondary building blocks
BODIPY	Boron dipyrromethene
BOR	Boracite net topology
COF	Covalent organic framework
CON	Covalent organic nanosheet
CP/MAS	Cross-polarization/magic angle spinning
CTF	Covalent triazine framework
CTN	Carbon nitride net topology
CuAAC	Copper-catalyzed azide-alkyne cycloaddition
CV	Cyclic voltammetry
DCC	Dynamic covalent chemistry
DIA	Diamond
DIPEA	*N*,*N*-diisopropylethylamine
DLS	Dynamic light scattering
DOPA	Dopamine

DPPH	2,2-diphenyl-1-picrylhydrazyl
EDLS	Double-layer supercapacitors
EDX	Energy-dispersive X-ray spectroscopy
FAAS	Flame atomic absorption spectroscopy
FESEM	Field emission scanning electron microscopy
FS	Faradaic supercapacitors
GC	Glassy carbon
GFAAS	Graphite furnace atomic absorption spectrometry
HCB	Honeycomb
HR-SEM	High resolution scanning electron microscopy
HR-TEM	High resolution transmission electron microscopy
HTB	Hexagonal tungsten bronze
HXL	Hexagonal
ICP-AES	Inductively coupled plasma atomic emission spectroscopy
KGD	Kagome-dual
KGM	Kagome
MOF	Metal-organic framework
NLDFT	Non-local density functional theory
PLA	Polylactic acid
PTS	Platinum sulfide
PXRD	Powder X-ray diffraction
RSA	Radical scavenging activity
SCs	Supercapacitors
$scCO_2$	Supercritical carbon dioxide
SCE	Saturated calomel electrode

SEM	Scanning electron microscopy
SQL	Square lattice
SRS	$SrSi_2$ net
TEM	Transmission electron microscopy
TGA	Thermogravimetric analysis
XRF	X-ray fluorescence

TABLE OF CONTENTS

Chapter 1:

Introduction and Background

1.1 The atom, the molecule, and the covalent organic framework

Since Gilbert N. Lewis´ publication in 1916 on the covalent bond and its effect on molecular reactivity and specific features,[1] great efforts have been made by organic chemists to develop synthetic methodologies for covalent molecular chemistry, and further extension of these organic reactions beyond the molecule to afford the synthesis of two- and three- dimensional (2D and 3D) extended frameworks. The expansion of supramolecular chemistry in the late 90´s helped organic chemists to understand the interaction between molecules, addressing the dynamic processes which constitute the basis of the reversible noncovalent interactions.[2,3] This progress allows the assembling of small molecules intro well-defined extended architectures. However, the design and synthesis of extended and ordered frameworks by the link of organic molecules through covalent bonds remained a challenge until the heyday of reticular chemistry.

Reticular chemistry is the chemistry of linking molecular units by strong bonds into extended crystalline frameworks.[4] This breakthrough enabled the development of the chemistry "beyond the molecule". The first examples were porous networks constituted by the linkage of inorganic clusters, followed by the emergence of metal-organic frameworks (MOFs), constructed by the union of organic molecules and metal ions. Afterwards, the reticular synthesis of covalent organic frameworks (COFs) by linking organic molecules through robust covalent bonds finally settled down the concept of "covalent chemistry beyond molecules", or in other words, the development of the covalent chemistry of the network, which assumes that the framework is just the progression of the molecule.[5–8] Hence, linking organic molecules into crystalline frameworks has been a major field of reticular chemistry, which in combination with dynamic covalent chemistry (DCC) permitted the rapid development of COFs.

The concept of DCC, firstly developed in the supramolecular and polymer chemistry field and mainly inspired by nature, explains how the reversibility of the chemical reactions under thermodynamic control allows "error checking" and "proof-reading" to afford the thermodynamically most stable product under certain reaction conditions.[9–11] Thus, as shown in Fig. 1, the reaction outcome relies on the relative stability of the products (thermodynamic parameters) and not in the energy barriers of each pathway (kinetic parameters).

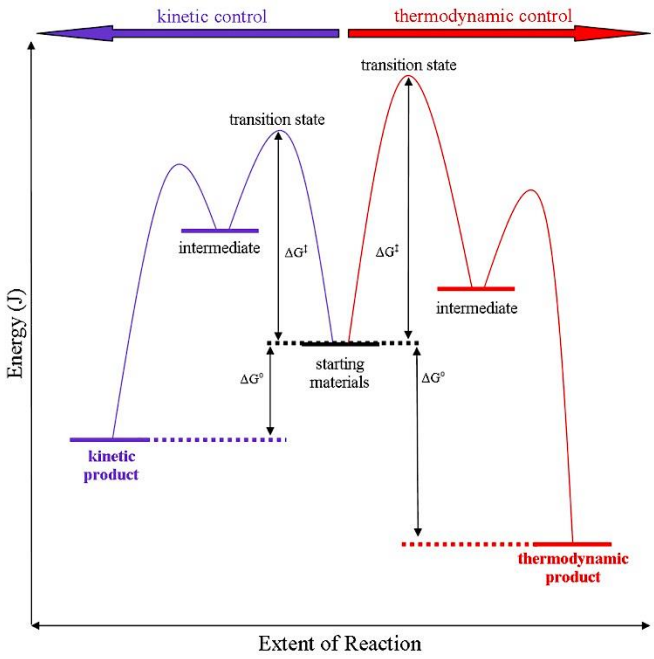

Figure 1. Free energy profile diagram illustrating thermodynamically and kinetically controlled reactions.

As stated before, the combination of reticular chemistry and DCC concepts enabled the design of 2D and 3D frameworks with different topologies starting from relatively rigid molecular building blocks, leading to the big expansion of COFs.[8,12]

Covalent organic frameworks (COFs), firstly described by Yaghi and co-workers in 2005,[13] constitute an emerging class of organic polymers which display high crystallinity and porosity. They are fully designable, meaning that predefined 2D and 3D extended networks can be readily obtained *via* strong covalent bond formation, allowing the atomically precise assembly of organic building blocks. Thus, by tuning the size, symmetry and connectivity of the monomers, the geometry and topology of the resulting network can be successfully tailored.

COFs are constructed purely from light elements (C, H, B, N, and O), while their counterpart MOFs include heavier metal atoms within their structure. This grants COF materials with lower densities and makes them potential candidates for energy and molecular storage. In addition, they present other enhanced features

compared to other well-stablished materials (e.g. zeolites, MOFs, etc.) including large surface area, tunable pore size or readily functionalization. Because of that, COFs have gained increased attention and great advances have been achieved over the past decade. An example of the fast and vast growing field of COFs is reflected in the increasing number of publications in the subject year by year (Fig. 2).

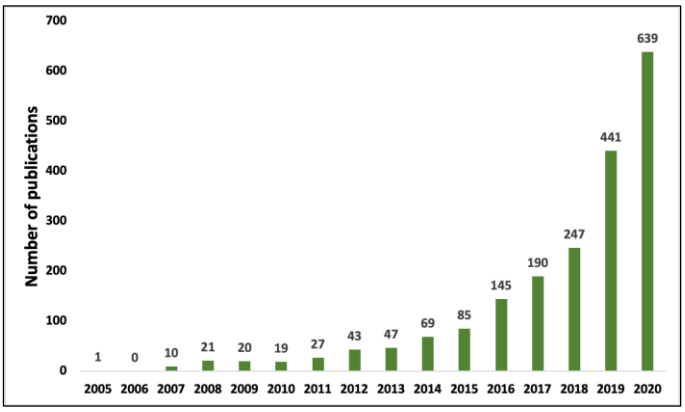

Figure 2. Publications on COFs as of December 2020 (Data taken from Web of Science).

1.2 Design principle: structural diversity

There are several aspects to be considered when designing a new COF, including the linkage between monomers, topology of the network, pore size or the possible functional moieties within the framework. Probably, one of the most important features is the connectivity and geometry of the building blocks. The geometry matching of monomers is essential to enable the formation of the desired topology, since each formation of a covalent bond guides the spatial orientation of the following one. Thus, the polymerization reaction should strictly follow this predesigned topology diagram to avoid defects and assure a high ordered structure. Depending on the dimensionality of the building blocks, the resulting COFs will grow in two or three dimensions (2D or 3D COFs, Fig. 3), and they are characterized based on their connectivity.

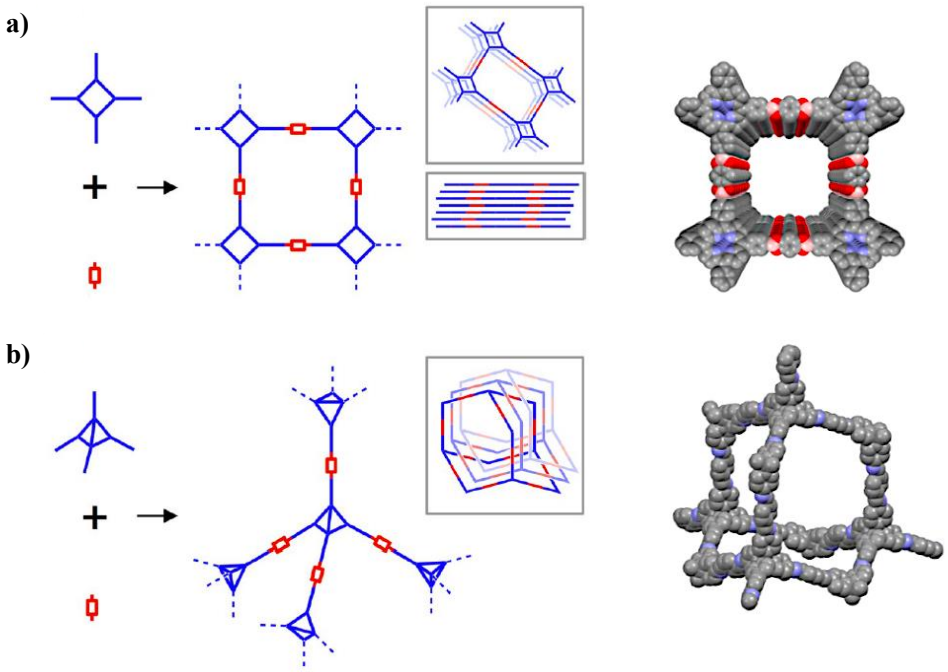

Figure 3. Schematic representation of (a) 2D COF network derived from square planar and linear monomers and (b) 3D diamondoid COF network derived from tetrahedral and linear monomers, and their space-filling models. The insets show a top and side view of the 2D framework and the interpenetration of congruent 3D network, respectively.

In 2D COFs, monomers are usually required to be planar and rigid, and their reactive sites should be distributed in a concern geometry in order to assure the correct orientation of each covalent bond in the framework. Consequently, the combination of planar monomers restricts covalent bond formation to be in a plane, leading to the formation of layers with specific topologies.[14–16] Moreover, in 2D COFs the relative position of adjacent layers are directed and controlled by interlayer interactions, frequently π-π stacking.[17] In this sense, 2D COFs form layered materials in which each monomer unit is overlapped, maximizing the attractive energy. Combination of monomers with different connectivities have led to a huge diversity of COF structures. To date, nine different topologies have been accessed for 2D COFs: the **hcb**,[13] **sql**,[18] **kgm**,[19] **hxl**,[20] **kgd**,[21] **bex**,[22] **fxt**,[23] **tth**[24] and **htb**[25] topologies (Fig. 4). According to the reticular chemistry theory, the most regular nets are more likely to be formed. Thus, the vast majority of the reported COFs have **hcb**, **sql** and **kgm** topologies.

Besides the geometry of the building blocks, by varying the length of the linkers multiple different frameworks can be obtained with the same topology but different pore diameter (isoreticular COFs).[26,27] Indeed, a wide library of monomers with different sizes, docking sites, chiral centers, reactive groups or even redox-active or photoactive groups have been developed, generating COFs not only with different structures but also with various functionalities, skeletons and pores.

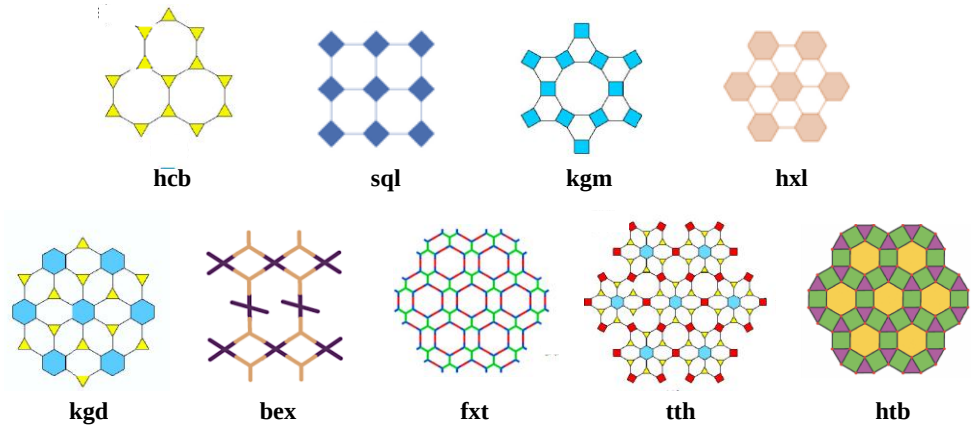

Figure 4. Reported topologies for 2D COFs.

3D COFs permit the formation of the polymer backbone in all directions, generating structures supported only by covalent interactions. In contrast with 2D COFs, the design of these 3D structures requires that at least one of the monomers present a T_d or orthogonal geometry in order to allow the formation of all covalent bonds. Different topologies for 3D COFs have already been reported, including **ctn**, **bor**, **dia**, **srs**, **rra**, and **pts** examples. However, the synthesis of organic molecules with 3D symmetries is rather difficult, which hampers the development of novel 3D networks. In addition, controlling multifold interpenetration and folding in these structures during the synthesis remains a challenge, what makes 3D COFs barely predesignable. Thus, the structural diversity of 3D COFs is more limited.

Not only the skeleton and the pore size can be modulated, but also the pore-surface can be engineered using different approaches.[28] On one hand, the proper functionalization of the edges has enabled the synthesis of COFs with different groups on the pore walls, ranging from hydrogen to propyl substituents.[29] On the other hand, ionic exchange can be used as an effective tool to modulate the pore

size by replacing the counterions that are present in the pores.[30] However, the most general approach is pore-surface engineering, in which one of the building blocks is decorated with hydroxyl, alkyl or azide groups prior to the COF synthesis.[31] Hence, the as-obtained framework can readily undergo quantitative post-synthetic reactions to incorporate specific functional groups to the pore surfaces including redox-active sites, photofunctional units, catalytic groups, etc.

1.3 General features of COFs

One of the most remarkable characteristics of COFs, as previously stated, is the possibility of molecularly designing a material to achieve 2D and 3D polymer frameworks with highly-ordered structure. This feature affords COFs with unique morphologies in comparison to other similar materials such as linear polymers, hyperbranched polymers, conjugated microporous polymers, and cross-linked polymers. This molecular design principle makes possible an outstanding and unprecedent control over design and functional development, creating novel molecular platforms for tailored applications. Besides this structural designing, some other remarkable properties of COFs are their crystallinity, porosity and stability.

1.3.1 Crystallinity

Crystallinity is the key feature that makes COFs different from other organic polymers, whose monomers are randomly placed within an amorphous structure. Furthermore, many of the unique properties of COFs arise from their structural order. However, understanding and rationalizing the factors that control the long-range order in these materials remains a challenge, specially due to the huge variety of linkages and building blocks described in the literature.

Several reported studies pinpoint the evident and basic principle that crystallinity requires the reversible formation of covalent bonds,[32] since this allows the correction of wrongly formed linkages during the polymerization process. The possibility of removing these defects in the framework successfully leads to a crystalline structure.

Other important parameters affecting the crystallinity of the framework are related with the selected building blocks: their solubility, their geometry and their functionalization. A great example is the functionalization of aldehydes with -OH groups in imine COFs.[33–35] The hydroxy group can readily establish hydrogen bond with the vicinal imine linkage, granting not only superior stability to the resulting COF but also higher crystallinity in comparison to the -OMe functionalized structures. These hydrogen bond interactions favor the planarization of the COF skeleton, minimizing the interlayer repulsion of the stacked COF layers and stabilizing interlayer adhesion. However, it is important for them to have the proper orientation between layers.

Dong et al. also investigated another parameter regarding to the building blocks: the influence of the monomer planarity on the crystalline order of several nitrogen-rich COFs.[27] Dong suggested that the planarity of the core linker facilitated the formation of a crystalline COF structure.

The nature of non-covalent interactions also plays an important role in COF crystallinity, since they control the adhesion of 2D layers and have an impact in the polymerization mechanism.[17,36] In general, the COF structure benefits from favorable π-interactions between the COF linkers. Thus, the stacking ability of COFs to constitute layered structures also favor the formation of crystalline domains.

A well-known parameter that influence the crystallinity of a COF material is the solvent o solvent mixture used during the synthetic protocol. It should be highlighted that the most favorable solvent mixture varies from one system to another, not being universal. Up to date, besides the great efforts devoted to these studies, the correlation between the linkers and the solvents of the COF synthetic reaction has not been reported.

Despite all these strategies to improve the crystallinity of the framework, COFs are usually obtained as polycrystalline materials and feature small crystalline domains sizes, typically under 100 nm. This hinder their structural resolution since, in contrast to MOFs and other inorganic materials, only a few single-crystalline COFs have been reported in the literature.[37–40] These COFs obtained as single crystals have been resolved using single-crystal X-ray diffraction (SXRD), while the polycrystalline COFs are analyzed using powder X-ray diffraction (PXRD)

experiment.[41] Clear PXRD patterns displaying strong diffraction peaks suggest the high homogeneity of the periodic network.

In combination with PXRD analysis, structural simulations (*vide infra*) are used to predict the COF structure.[42] Using sophisticated software suits like Materials Studio, the structure can be modelled and a simulated PXRD pattern can be obtained. Since the geometry and dimensions of the building block determine the structure of the COF, multiple structures can be plausible generated when combining monomers with multiple active sites. In addition, different stacking modes of the individual layers can be generated in a 2D COF: the eclipsed AA stacking mode and the staggered AB stacking mode. In the AA stacking mode atoms of parallel layers have identical lateral coordinates, while in the AB stacking mode layers are shifted to each other, with the vertices of one layer overlapping with the center of the pores of the following layer. Between both stacking modes there are intermediate structures, in which the slipped AA stacking present small offsets along the a and/or b direction between layers. The slip distance relies on the topology, volume and planarity of vertices, edges and linkages.[43] These are usually the most common and stable stacking modes. In contrast, in AB staggered stackings there is a considerable loss of π-π interactions, and therefore the stabilization energy is reduced. In 3D COFs these multiple structures can be generated when the network is interpenetrated (entanglement). By comparing the simulated Bragg positions with the experimental PXRD pattern, the correct structure can be elucidated, and the crystal facet of each peak can be assigned.

Besides PXRD technique, transmission electron microscopy (TEM) or high resolution (HR) TEM are used to corroborate the crystal structure of COFs by evaluating the electron diffraction pattern obtained. However, this method is less common since in the traditional HR-TEM the electron beam can easily damage the COF sample, resulting in limited resolution. The early developed low-dose TEM technique is less harmful and clear structures of COFs have been successfully observed (Fig. 6),[44] but the high economical cost of this characterization technique limits its implementation.

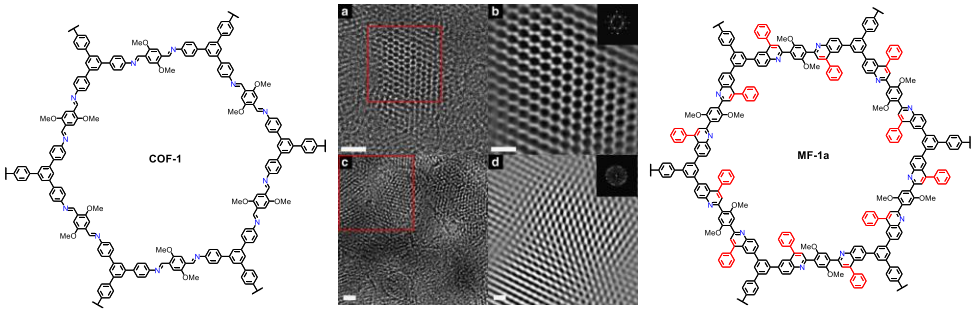

Figure 6. Example of HRTEM characterization of **COF-1** and **MF-1a**. Adapted from reference 44.

1.3.2 Porosity

Porosity is another intrinsic property of COFs. The assembly of building blocks in 2D or 3D frameworks constitutes periodic and uniform voids that can be designed to meet certain requirements of shape, size and functionality (Fig. 7). Thus, the discrete pore size can be tuned ranging from micropore to mesopore (from diameters of 0.64 nm up to 5.3 nm)[45,46] and they can be endowed with different functional groups to successfully interact with different guests.

COF pores display distinctive properties in comparison with zeolites, porous silicas, porous carbons or MOFs. Firstly, COF pores are 1-dimensional and accessible only from the top or the bottom of the 2D layered structure. In addition, the interlayer distance of 2D COFs, which is commonly around 3.5 Å, makes the COF channels independent from each other. Therefore, the pores are completely individual spaces and free of interpenetration. However, the most remarkable feature of the porous networks of COFs is the structural designability. Their unique and diverse pore designability can be achieved by pore-surface engineering,[28] and it is not possible to other porous materials.

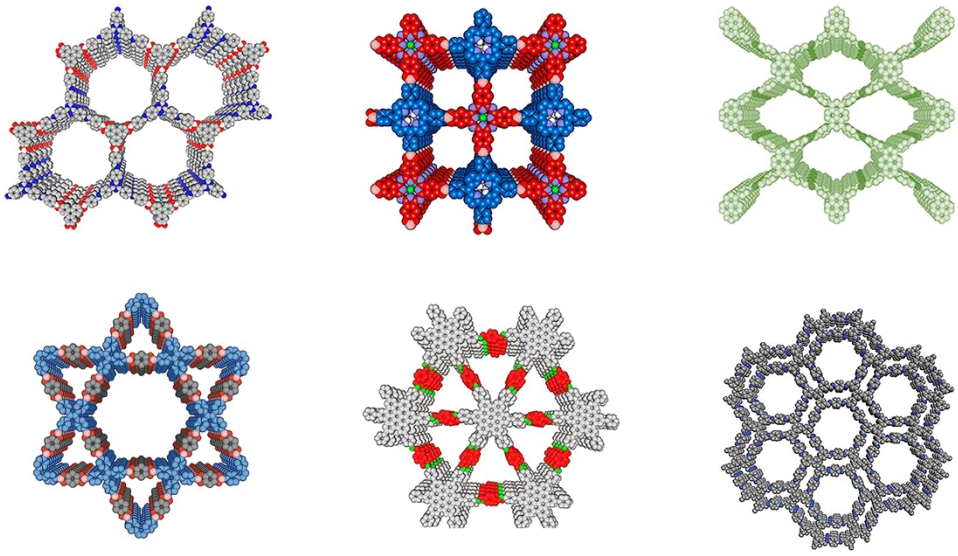

Figure 7. Examples of different pore structures.

The porosity of COFs strongly relies on the size and molecular weight of the building units, but also on the crystallinity of the network. It is of big interest to explore the full potential of porosity in COFs, since enhanced surface area and large pore volume can be thus achieved. Even though some COFs display an exceptional porosity, with outstanding theoretical surface areas of 5070 $m^2\ g^{-1}$, in some cases the dense π clouds from monomers forming the COF skeleton in 2D COFs hinder the development of high porosity. Something similar happens to 3D COFs, whose porosity can be partially inhibited by the folded structures. For these reasons, activation of COFs, commonly referred to the elimination of trapped volatile molecules from the pores, is a crucial step that can strongly influence the final porosity and surface area of the material, and therefore its performance. The most widely spread strategies for COF activation include solvent exchange and evacuation at high temperatures under reduced pressure and drying with supercritical carbon dioxide.

As it has been mentioned before, the pore surface can be readily tuned by pore-surface engineering. This general approach, valid for different topologies, linkages and pore sizes, enables the introduction of different functional groups within the pores of the framework, developing the interface and changing the porosity. Using this tool, pore surface can be systematically tailored, generating more complex and diverse porous structures.

To analyze the porosity of COFs in a quantitative way, gas sorption isotherms are measured at the liquid temperature of the adsorptive gas (77 K for nitrogen or 87 K for argon).[47] Depending on their sorption isotherms, COFs can be microporous (when presenting pore diameters below 2 nm, type I isotherms) or mesoporous (pore diameters between 2 and 50 nm, type IV and V isotherms) materials.

From these sorption isotherms, the pore size distributions and the surface area can be calculated using nonlocal density functional theory (NLDFT) and Brunauer–Emmett–Teller (BET) model, respectively, which provide meaningful data for the structural characterization of these materials.

1.3.3 Stability

Due to the strong covalently bonded skeleton, COFs are thermally and chemically very stable compared to conventional polymers or their counterparts MOFs. Under inert atmosphere, most COFs are thermally stable between 300 and 450 ºC. This makes them interesting materials for carbonization processes, which render new properties to the COFs while their skeleton is preserved.

Robust chemical bonds enhance the chemical stability of COFs. However, they also affect the reversibility of the COF polymerization reaction, which can result in a lower crystallinity. For instance, boroxine linkage has a higher degree of reversibility compared to the imine bond. Therefore, boroxine-based COFs are generally more crystalline than imine-linked COFs, while they display a much lower chemical stability and are easily hydrolyzed under humid or protic conditions.[48] Among nitrogen-based linkages, covalent triazine frameworks (CTFs) have shown outstanding chemical stability towards hydrolysis, extreme pHs and oxidative conditions due to the formation of the triazine units.[49] Knoevenagel condensation or benzoxazole formation can be also considered when designing highly stable COFs.

The chemical stability of COFs can be further improved by strengthening the interlayer non covalent interactions, like intralayer hydrogen-bonding or interlayer complementary π-interactions (Fig. 8a and 8b).[33,50] In addition, inducing the

tautomerization of some linkages to a more stable bond, like the enol- keto tautomerization in some imine COFs, can also increase the stability of the resulting network (Fig. 8c).[51]

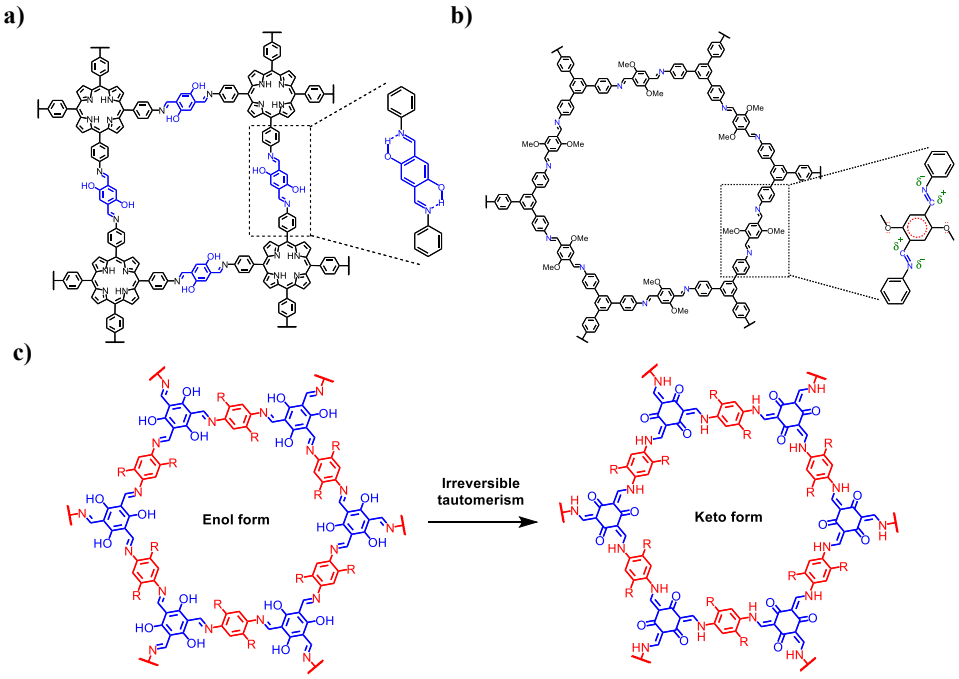

Figure 8. Inducing stability control of COFs by (a) hydrogen bonding, (b) interlayer interactions, and (c) tautomerization of imine linkages. Adapted from references 33, 55 and 51.

1.4 Synthesis of COFs

According to the dynamic covalent chemistry (DCC) theory, the synthesis of COFs requires reversible reactions in which covalent bonds can reversibly form and break up for correction during the reaction, yielding products that are obtained under thermodynamic control.[52] This reversibility is the key factor for the self-healing mechanism involved in the error-checking and proofreading of COF regular structures.[53] Remarkably, a few irreversible reactions, such as phenazine linkage,[54] dioxin linkage[55] or olefin linkage[56] have been reported for the

synthesis of new COFs. The main synthetic methods will be described in the following section.

1.4.1 Linkage diversities

Up to date, several linkages have been developed for the design and synthesis of novel COF structures, as illustrated in Fig. 9.

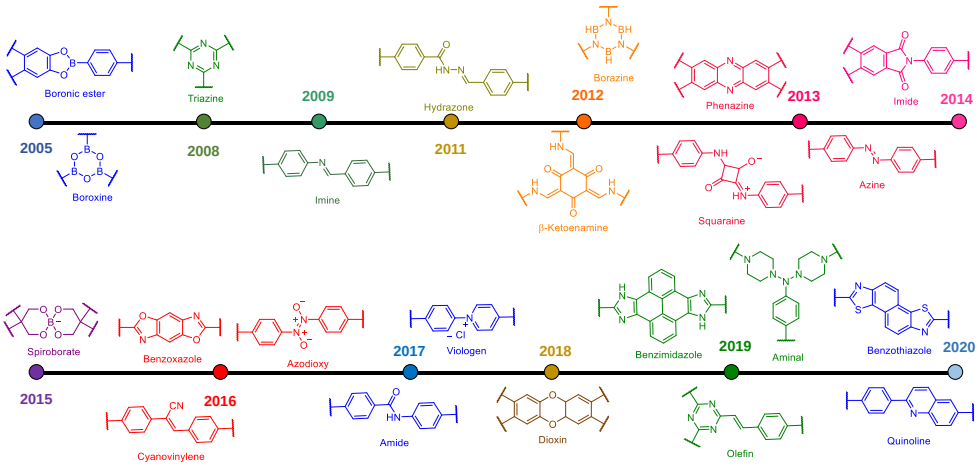

Figure 9. Timeline of various linkages for COF formation.

The first COFs were developed in 2005 by Yaghi and co-workers, who described for the first time the self-condensation of boronic acids affording a boroxine-based 2D **COF-1** (Fig. 10a) with a planar structure.[13] By the condensation of boronic acids and catechol derivatives, they also yielded boronate-ester-linked **COF-5** (Fig. 10b).[13] This linkage has been widely explored for the synthesis of several 3D and 2D COFs incorporating different π-systems (e.g. benzene, thiophene, triphenylene, tetraphenylethene, etc.). Due to the high reversibility of the reaction, boronate-ester-based COFs are also highly crystalline.

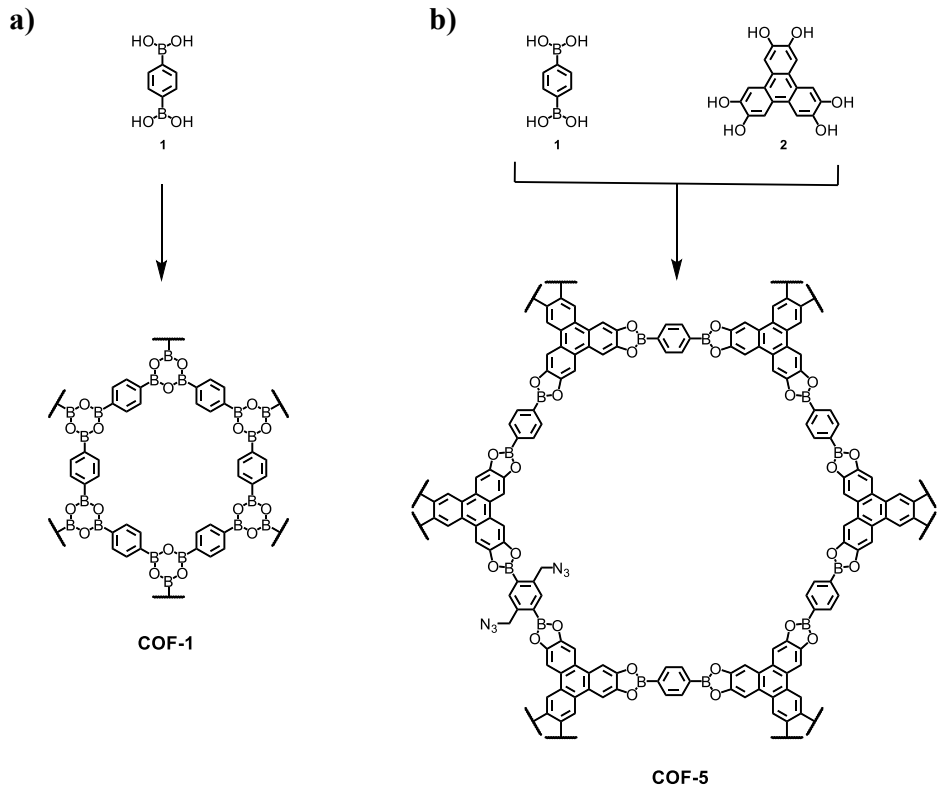

Figure 10. Synthesis of (a) **COF-1** and (b) **COF-5** reported by Yaghi.[13]

After that, C-N bonds were successfully achieved and incorporated into triazine-based COFs in 2008. Through the cyclotrimerization reaction of nitrile groups at 400 ºC in molten $ZnCl_2$, Thomas and co-workers successfully synthesized the first CTF.[49] However, the reported harsh conditions usually hamper the development of high crystalline and porous frameworks. Thus, it has been of big interest the development of milder conditions to afford the synthesis of more ordered networks. In this regard, several recently reported procedures have overcome this drawbacks, what will probably make CTFs even more popular in the near future.[57,58]

In 2009 the first imine-based COF was described by Yaghi and co-workers.[59] The imine bond can be formed by the condensation reaction of aromatic amines and aldehydes in the presence of an acid catalyst. Due to the high thermal and chemical stability of this linkage, imine-COFs have become the most widely used type of COFs. The most common synthetic procedure to afford the formation of

imine-based COFs is the solvothermal method, but several examples have been described using the mechanochemical approach.[26,60]

After the exploitation of the full potential of imine-based COFs, different linkages based on the formation of C-N bonds were developed. Hydrazone linkage (formed by the reaction of aldehydes with hydrazides in the presence of a catalytic amount of AcOH) and azine linkages (formed *via* condensation of hydrazine with ketones and aldehydes) enabled the formation of highly stable COFs.[61,62] A reported example of a squarine-linked COF enable the formation of a zwitteronic structure within the pores of a COF;[63] and phenazine linkage, because of its fused planar structure, permitted the obtaining of π-conjugated and stable COFs.[64]

The imide linkage, reported in 2014, can be obtained by the reaction between amine moieties and acetic anhydride.[65] Since this linkage is less reversible, high reaction temperatures are needed for the formation of the structure.

In order to enhance the π-conjugation and chemical stability of the COFs framework, increasing attention has been focused on the development of C=C linked fully π-conjugated COFs. The first example was achieved *via* the Knoevenagel condensation of aldehydes and cyanides catalyzed by a certain base, affording a cyanovinylene-based COF.[56] Furthermore, in 2019 a series of olefin-linked COFs were successfully synthesized by the reversible aldol condensation of aldehydes and *s*-triazine derivatives.[66] Due to their robust skeleton and π-extended conjugation, olefin-linked COFs present outstanding thermal and chemical stabilities, even in the presence of strong acids or bases.[67]

Besides the above explained linkages, a different strategy has been recently explored: the double-stage linkage. In this approach, a bifunctional building block is designed to allow the formation of two different linkages for the synthesis of one COF. Thus, COFs with boroxine and imine bonds or boronate-ester and hydrazine linkages have been obtained.[68,69]

Another approach consists in the transformation of conventional linkages into other that are difficult to synthesize directly. For example, imine-linked COFs can be oxidized and converted to amide-linked COFs, or reduced to amine-linked-COFs.[70,71]

Besides the huge expansion of COFs linkages, unveiling the reaction mechanisms to understand the polycondensation and crystallization processes remains quite a challenge. It is known that nucleation is the first stage that initiate the formation of oligomers of different sizes and structures during the induction period, ant they further react via reversible bond formation. Finally, an irreversible crystallization step affords the formation of crystalline structures (Fig. 11).[72] Different experimental and theoretical studies have been developed and combined to gain insight into the nucleation and growth of COFs. It has been revealed that the crystallization rate highly depends on the pore size and the interlayer interactions. Thus, extended π-monomers will boost the π-stacking interactions, and therefore will promote the reaction rate of polymer growth.

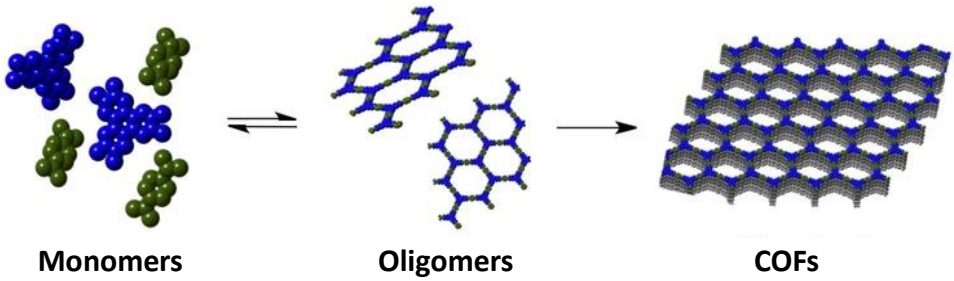

Figure 11. Proposed growth mechanism of COFs.

The growth of imine 2D COFs depends on the dynamic linkage exchange.[73] In addition, polymerization and crystallization do not occur at the same time for imine-based COFs, since it has been demonstrated that COF particles are formed prior to the crystallization process.[74,75] However, in a recent work, Dichtel and co-workers demonstrated that 2D imine-based COFs polymerize as crystalline sheets within the first seconds of the polymerization reaction.[76] Then, these periodic sheets reorganize to form more ordered stacked structures over several hours. These results can pave the way for the successful isolation of COFs sheets as few or single layer, which can significantly impact their application in different fields. In addition, this could eventually lead to the synthesis of single-crystalline 2D imine-linked COFs.

1.4.2 Synthetic methods

a) Solvothermal synthesis

As aforementioned, the synthesis of the first two COFs was firstly reported in 2005 by Yaghi and co-workers, who described the self-condensation of a boronic acid into boroxine-based **COF-1** and the condensation reaction of a boronic acid with a catechol moiety, affording the synthesis of **COF-5** using a solvothermal synthetic procedure (Fig. 10).[13]

Since then, most 2D and 3D COFs have been synthesized using this method, becoming the most popular approach in this field. The key factors are the reversibility of the selected reactions and the solubility and reactivity of the monomers. In addition, other reaction conditions such as the temperature, the reaction time, the solvent or solvent mixture used and the catalyst concentration should be also considered. These factors will determine the crystallinity and porosity of the final COF. Notably, when water is used as the solvent of the reaction, it is commonly referred to as hydrothermal synthesis. However, hydrothermal synthesis of COFs have been seldom described.[77,78]

In a general solvothermal synthetic procedure, the building blocks are placed in a Pyrex tube (or a thick-wall pressure tube) together with the proper volume of solvent or solvent mixture and the catalyst. The reaction mixture is briefly sonicated to get a homogeneous suspension, degassed via freeze−pump−thaw cycles and flamed sealed. Afterwards, the reaction vessel is kept at a suitable temperature for a certain period (from 3 to 7 days). After the reaction time, the tube is cooled to room temperature and the precipitated is filtered and thoroughly washed with different solvents to remove possible oligomers. Finally, as the activation step is concluded, the obtained solid is dried under vacuum.

Since COFs formation is basically a thermodynamic controlled reaction, several strategies can be applied to avoid the rapid reaction between monomers that inevitably lead to amorphous structures. Thus, the reactive sites of the building blocks can be protected prior to the COF formation reaction, reducing the reaction rate.[79,80] Multicomponent reaction have also proved to be an effective approach to optimize solvothermal thermodynamics by combining a reversible linkage and an irreversible one, achieving high complexity in covalent assembly.[81,82]

b) Ionothermal synthesis

This method has been widely applied for the synthesis of CTFs, and it consists in placing the selected monomer and $ZnCl_2$ in a Pyrex tube, which is further evacuated, flamed sealed and heated usually at 400 ºC for a given time. In analogy to the previous method, after the reaction time the mixture is cooled down and the resulting crude precipitate is thoroughly washed first with water, to remove unreacted catalyst, and then with THF. Finally, the product is dried under vacuum to afford the CTF.

The most remarkable characteristic of this method is that the molten salt acts as the solvent and successfully catalyze the cyclotrimerization reaction of aromatic nitriles or amides into triazine rings. Remarkably, this reaction becomes reversible at these temperatures.

Most of the reported CTFs present amorphous structures, lacking a long-range molecular order. However, several examples of crystalline or semi-crystalline CTFs have lately emerged, motivating a broaden implementation of this synthetic approach.[49,83]

A different ionothermal synthesis is referred to the use of ionic liquids (IL) as the reaction solvent. They offer a milder and more environmentally friendly alternative, and they have been quite used for the preparation of 3D COFs.[84]

c) Microwave synthesis

Since the previously described methods require long reaction times, microwave heating has become very popular for the rapid preparation of COFs. In a general protocol, the monomers and the suitable solvent mixture are sealed in a microwave tube under nitrogen or vacuum, and heated, while stirring, for a short period of time. The resulted precipitate is filtered, washed and dried. Different COFs have been successfully synthesized using this method, including boronate-ester linked COFs, imine-based COFs and even CTFs.[57,85,86] Thus, microwave heating can clearly enhance the reaction rate and reduce the reaction time.

d) Mechanochemical synthesis

This method represents a simpler economic and environmentally green approach, since it just consists in grinding the monomers in a mortar at room temperature (Fig. 12). To increase the reaction rate, a small amount of catalyst solution can be added, which has been proved to increase the crystallinity of the resulting structures.[60] Besides these advantages, there is still a lack of understanding of its mechanistic features which consequently leads to a trial-and-error basis, hindering its applicability.

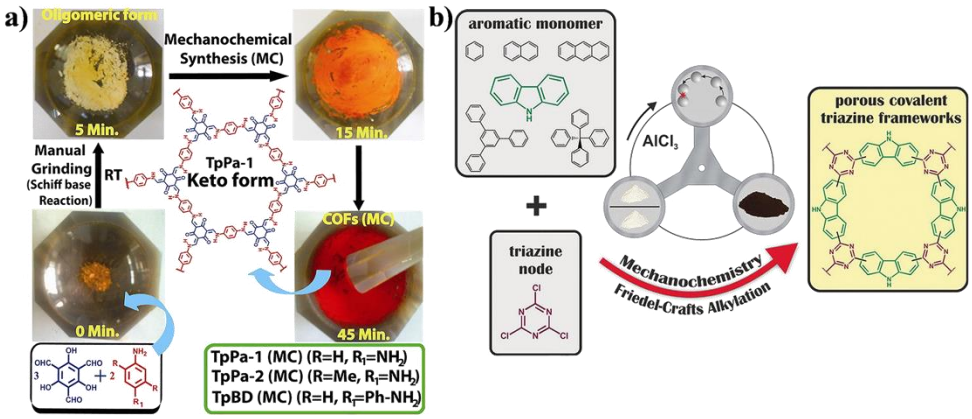

Figure 12. Schematic representation of mechanochemical synthesis of (a) enamine-linked COFs and (b) triazine-based COFs.[26,87]

e) Other methods

Besides the aforementioned strategies, different procedures have been developed for the synthesis of COFs for tailored applications. For instance, the interfacial synthesis enable the preparation of COF thin films with a thickness that can vary from 4 to 150 nm.[88]

Another alternative that has become very attractive is the synthesis of COFs under ambient conditions. This approach allows the incorporation of fragile monomers or sensitive functional groups. Interestingly, room-temperature vapor-assisted synthesis enable the preparation of boroxine-based COF films,[89] and a polydimethylsiloxane (PDMS) microfluidic device has been effectively used for

the preparation of COF fibres under ambient conditions. The resulting COF fibres can be readily printed onto surfaces while their crystallinity and porosity remain unchanged.[90]

Other novel and less conventional methods include photochemical synthesis or electron beam irradiation synthesis.[91,92]

1.4.3 Synthesis on substrates

Taking advantage of the above extended principle for the synthetic control over COFs formation, in recent years there has been considerable interest in the preparation of thin-films due to the insoluble and un-processable properties of bulk COF powders. Up to date, different substrates have been explored for the preparation of COF thin films with controllable arrangements, including single layer graphene (SLG),[93] graphene oxide (GO),[94] porous metal oxides,[95] three-dimensional graphene (3DG),[96] amino-functionalized carbon nanotubes (CNTs)[97] or polydopamine-coated capillary substrates[98].

Dichtel and co-workers paved the way in this field, reporting the preparation of the first 2D COF thin films by the deposition of the material on a quartz crystal microbalance (QCM) substrate.[93] The as-obtained films displayed higher crystallinity than the COF powders and could be readily incorporated into organic electronic devices. Since then, different methods have been investigated for the preparation of COF films, including vapor-phase deposition or spin-coating.[99]

1.5 Functionalization of COFs

As it has been previously discussed, COFs main properties can be modulated by selecting different network topologies and linkages. Furthermore, additional functionalities can be incorporated into the frameworks, enabling the design of COFs for tailored applications. The approaches to functionalize COFs can be generally divided into two main categories: pre-synthetic (pre-SM) and post-synthetic modifications (post-SM).

In the pre-SM, the desired functionality is incorporated into the building blocks prior to the synthesis of the framework (Fig. 13). This facilitates a homogeneous distribution of the active sites within the COF framework.

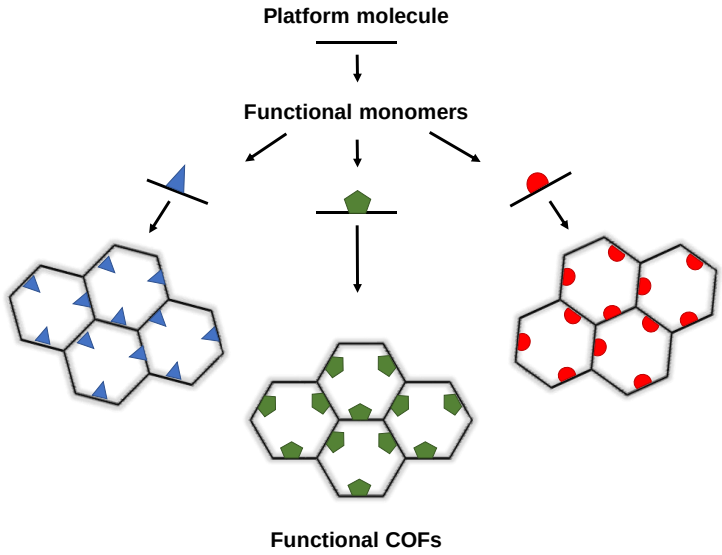

Figure 13. Schematic representation of pre-SM of functional COFs.

Even though this approach permits the preparation of COFs endowed with multiple functionalities, it is not suitable for all kind of networks, since the additional functional group must be compatible with the COF synthetic conditions and stable enough to allow the growth of the framework. Furthermore, the incorporated functional groups must preserve the geometry of the monomers, which have to keep their rigidity. These limitations can hamper the functionalization of a vast library of reported monomers.

Using pre-SMs, different functional groups have been successfully integrated into COFs including alkyl chains,[100,101] thioether,[102] imidazolium,[103] free radical,[104] crown ether[105] and quinoline derivatives.[106] More interestingly, several building blocks have been modified with chiral groups and their further polymerization has allowed the formation of chiral COFs, which are specially interesting for chiral separation and catalysis.[107,108]

On the contrary, in post-SM alternative reactions are carried out on pre-synthesized COFs.[109] Even though this implies less crystallization problems, this

approach is more prone to generate defects in the framework, due to the impossibility of completing the post-synthetic reaction in every reactive site of the network. Therefore, unreacted sites may remain randomly distributed in the modified COF.[6]

Up to date, several strategies have been explored for the post-synthetic modification of COFs, which have been extensively investigated by Segura and co-workers.[109] They can be generally classified into three main types: metalation, backbone modification and functional group interconversion.

A vast number of building blocks containing coordination sites have been described (porphyrin,[110] bipyridine,[111] catechol,[112] and annulene derivatives[113]). However, metal coordination sites for further post-SM of COF through metalation can be located either on the monomer or in the COF linkages.[114] Generally, metal coordination reactions are carried out by mixing COFs with the corresponding metal salts or metal complexes. Thus, several inorganic ions (e.g. Fe,[115] Cu,[116] Zn,[117] Pd,[118,119] etc.) have been successfully incorporated into COFs. In this regard, Wang and co-workers firstly reported on a seminal work the successful loading of Pd(II) ions within an imine-based **COF-LZU1** (scheme 1). Catalytic activity of **Pd/COF-LZU1** was further investigated in the Suzuki-Miyaura coupling reaction, showing outstanding catalytic activity and recyclability.[118]

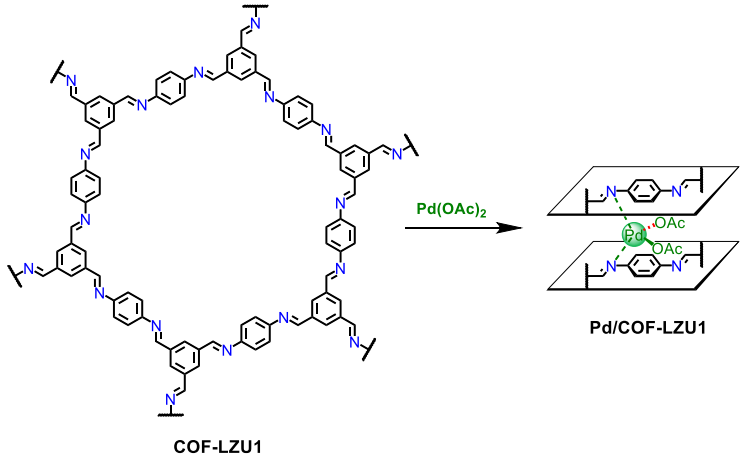

Scheme 1. Schematic representation of post-SM of **COF-LZU1** through metal coordination.

Another alternative is the framework´s backbone modification. This can be achieved by the conversion of reversible linkages in COFs to irreversible bonds. This allow the incorporation of new linkages that cannot be synthesized *de novo*. In this regard, imine-based COFs have become popular platforms for the transformation of C=N linkages. As aforementioned, the oxidation of imine bonds to amides was firstly reported in 2016.[70] Since then, the reduction reaction of imine linkages to amine-based COFs or the reaction with sulfur at high temperatures to convert imine linkages into thiazole-linked COFs have also been reported.[120,121] More recently, an aza-Diels-Alder reaction has allowed the conversion of dynamic imine linkages to robust quinoline rings (scheme 2).[44] The resultant COFs exhibit enhanced chemical and thermal stability and enhanced π-conjugation.

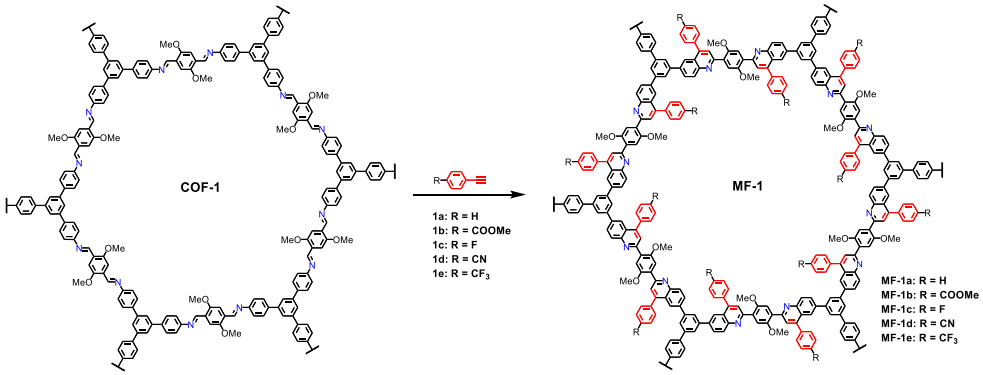

Scheme 2. Post-synthetic modification of imine-linked COF through backbone modification. The imine linkages are converted into quinoline linkages.[44]

By applying the main principles of DCC, COF-to-COF transformation has been successfully explored by the exchange of the building blocks. Due to the extended reversibility of COF linkages, monomers can be linked and disconnected under thermodynamic conditions. Even monomers with different functional groups can be exchanged.[122]

A different example of post-SM by backbone modification is based on cycloaddition reactions. A [4+4], [4+2] (scheme 3) and [2+2] cycloadditions have been described in the literature.[123–125]

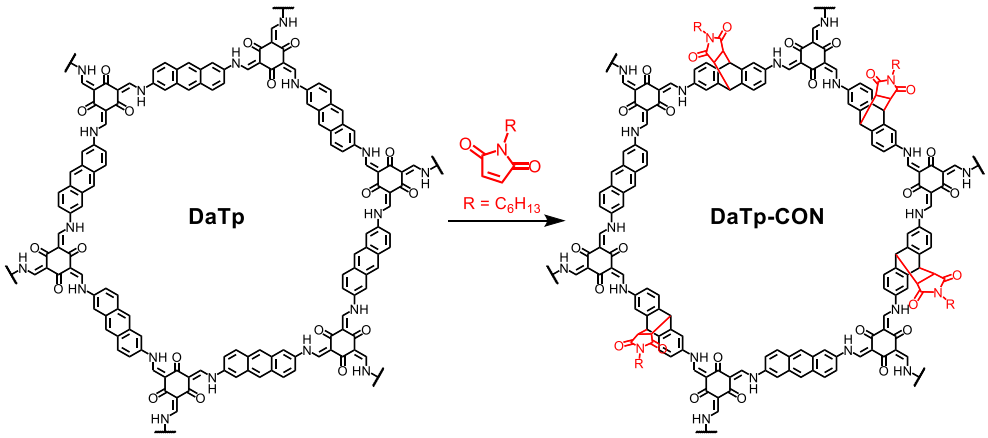

Scheme 3. Post-synthetic modification of **DaTp** through [4+2] cycloaddition reaction.

Besides the above-mentioned post-SM, selected functionalities can be integrated within pre-formed COFs *via* covalent bonds. The first and most extended covalent post-SM based on functional group interconversion was reported in 2011 by Jiang and co-workers by applying the copper catalyzed azide-alkyne cycloaddition (CuAAC) click reaction (Fig 14).[126] Therefore, click reactions between ethynyl and azide moieties were successfully performed in a quantitative way. Moreover, typical click reaction between vinyl and thiol units (thiol-ene reaction) was also explored. [127,128]

Electrophilic addition reactions of vinyl functional groups;[129] Williamson reaction and esterification of hydroxyl units;[130,131] amidation and imidization of amino groups;[132,133] or amidation, esterification and thioesterification of carboxyl moieties (described by Yaghi and co-workers in 2020) have been also reported for the post-synthetic covalent modification of COFs.[134]

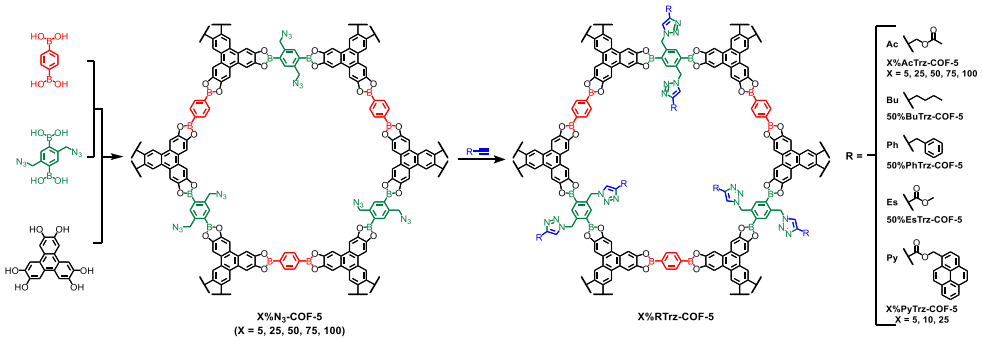

Figure 14. Schematic representation of the post-SM of COFs through click chemistry reaction between azide pendant groups and different alkyne derivatives. Adapted from reference 127.

1.6 Processing of COFs

Besides the great efforts devoted to the design and optimization of the building blocks in order to control the physical and/or chemical properties of COFs, a great number of strategies have been developed to successfully process COF materials into thin-films, membranes or nanoparticles with tunable shape and size.[135] Overall, it should be highlighted the importance of COF processability towards potential application of these materials in multiple fields.

In this regard, different approaches to growth a single or few-layer COF film on different surfaces have been developed. A simple procedure consists on the evaporation of the monomers over a metal surface on which they can further polymerize.[95] To confirm the correct formation of the layered structure, scanning tunneling microscopy (STM) can be used. Another approach consists in the incorporation of the selected substrate in the reaction vessel together with the building blocks, affording the formation of crystalline films with homogeneous tunable thickness.[93,136]

Furthermore, free-standing films have been also explored, leading to the formation of membranes that can be used in multiple applications. A conventional method for the synthesis of free-standing COF films is the interfacial synthesis,

which can be developed at the air-liquid interface or at the liquid-liquid interface.[137–139]

In contrast to the bottom-up approaches described above, exfoliation of COFs layered structures is an efficient and convenient top-down alternative method.[140] Since the covalent bonds present in the COF backbone are much stronger than the interlayer π-π stacking interactions, upon application of external energy the layered structure can de delaminated without the layers breaking apart. Several methods for COF exfoliation have been explored and are briefly summarized in this section.

Liquid-phase exfoliation (LPE) is the most common and universally spread exfoliation method, and theoretically can be applied to all type of COFs. Generally, bulk COFs are suspended in a specific solvent or solvent mixture and then sonicated. Due to their great surface tension, the bubbles formed during the sonication process burst into each other, inducing shock waves along the COF sample that destroy the interlayer interactions, affording the preparation of COFs nanosheets. Therefore, COFs displaying weaker interactions between their layers are more readily exfoliated. For example, reported **TPA-COF** (synthesized from tris(4-aminophenyl)amine and tris(4-formylphenyl)amine monomers) was sonicated for 3 h in ethanol to successfully afford high-quality nanosheets. However, **TPA-COF-2** (synthesized from tris(4-aminophenyl)amine and 1,3,5tris(4-formylphenyl)benzene monomers), which included a minor structural modification, could not be exfoliated under similar conditions (Fig. 15).[141] This can be explained by the stronger π-π interlayer interactions in **TPA-COF-2** due to its more planar framework together with its increased π-delocalized structure when compared to **TPA-COF**.

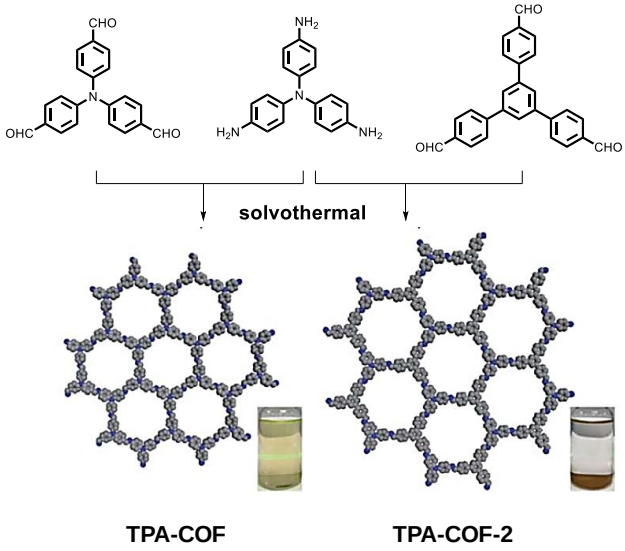

Figure 15. Syntheses of **TPA-COF** and **TPA-COF-2** and the illustration of the Tyndall effects in **TPA-COF** and **TPA-COF-2** suspensions obtained under identical processing conditions. **TPA-COF-2** colorless colloidal suspension presents a weak Tyndall effect, indicating the low concentration of **TPA-COF-2** NS. Adapted from reference 141.

As it has been pointed out, solvents have a major role in this method. Commonly, polar solvents are known to promote exfoliation while inhibiting structure aggregation.[142] Furthermore, centrifugation or filtration is usually performed after ultrasound sonication to remove the larger COF particles that remain unexfoliated.

An alternative approach is simply based on the grinding of the COF bulk powder in the presence (or not) of a small amount of solvent. The impact and friction generated by the grinding process can promote layer slips, leading to a suspension of COF nanosheets. Mechanically exfoliated COF nanosheets (CONs) were reported for the first time by Banerjee and co-workers.[143] They described the synthesis and further exfoliation of several imine-based COFs (Fig. 16). The reported CONs did retain some crystallinity, and their thickness ranged from 3 to 10 nm.

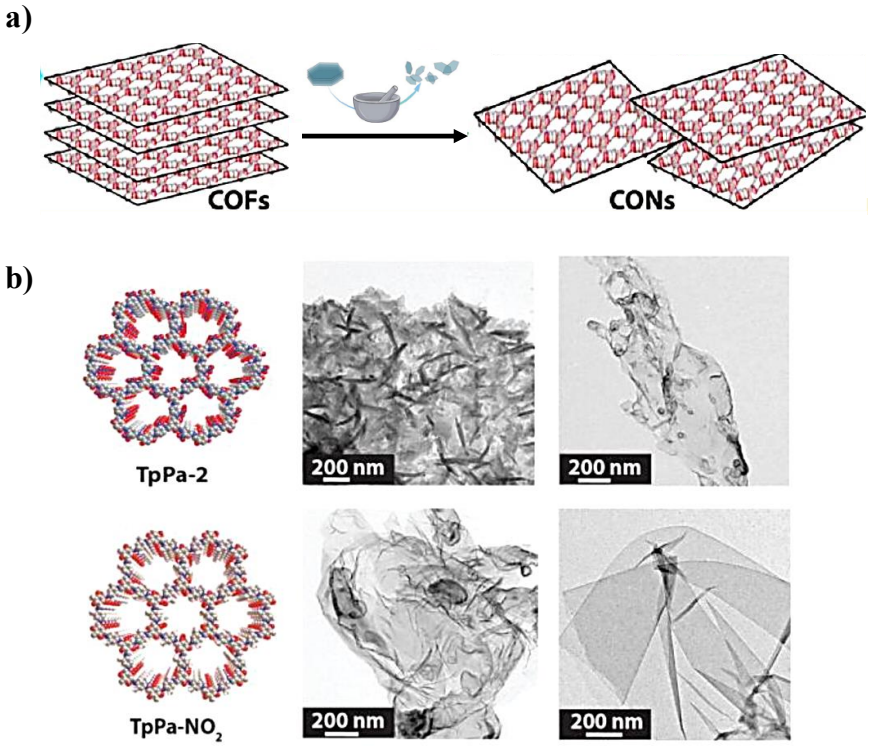

Figure 16. (a) Schematic representation of the preparation of CONs; (b) Packing diagrams, HR-TEM images before grinding and HR-TEM images of CONs (after grinding). Adapted from reference 143.

In addition, chemical exfoliation has been used to increase the interlayer spacing between COF layers and therefore weaken van der Waals interlayer forces. By introducing bulky groups within the COF layers, exfoliation can be induced. The first chemical exfoliated COF example was reported by Banerjee and co-workers in 2016.[124] By promoting the Diels–Alder cycloaddition reaction between N-hexylmaleimide and anthracene-based **DaTp COF**, π-π stacking interaction was diminished due to the induced corrugation and the COF could further be exfoliated (Fig. 17).

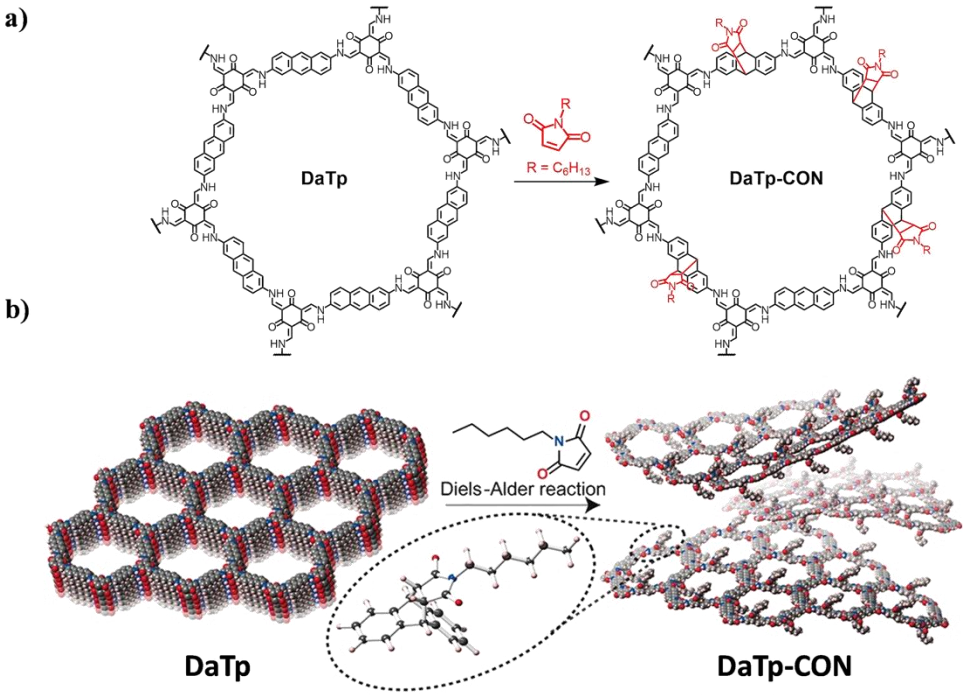

Figure 17. (a) Synthesis of **DaTp-COF** and **DaTp-CONs**. (b) Schematic representation of the preparation of CONs. Adapted from reference 124.

More recently, other processes as photochemical reactions (like the isomerization of *cis*-azobenzene into *trans*-azobenzene guest molecules in **TpAD COF**) or hydrolysis reactions (like hydrolysis of embeded *n*-buthyllithium in **TpPa-1 COF**) have been also used to induced chemically exfoliated CONs (Fig. 18).[144,145]

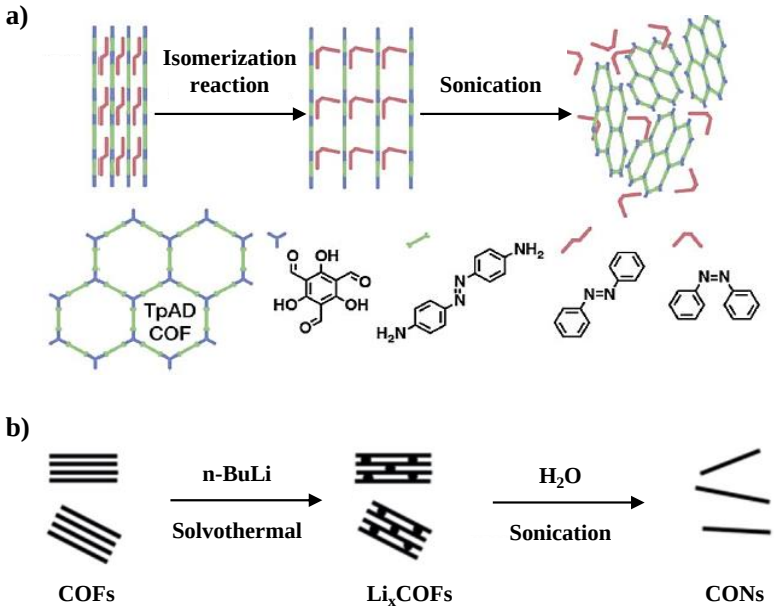

Figure 18. Schematic representation of chemical exfoliation of (a) **TpAD COF** and (b) **TpPa-1 COF**. [144,145]

Another method to induce exfoliation of COFs is the gas-driven exfoliation, based on the expansion of 2D materials at high temperatures and further vaporization of liquid nitrogen (Fig. 19). Even though three COFs have been successfully exfoliated into CONs by using this method,[146] its application to different COF frameworks needs to be further addressed.

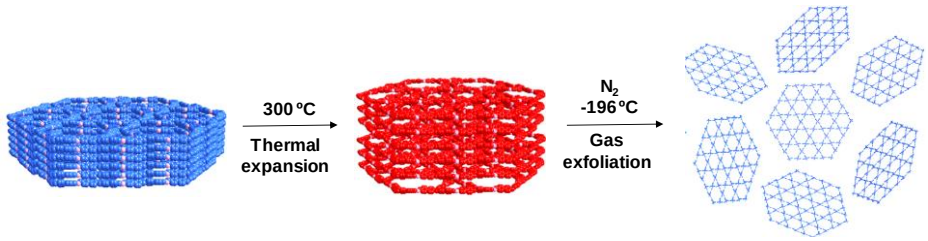

Figure 19. Schematic representation of gas-driven exfoliation of COFs. Adapted from reference 146.

A powerful alternative is the charge-mediated self-exfoliation, which consists in the spontaneous exfoliation of positively charged frameworks. In general, the charge is located in the building blocks and several examples based on benzimidazolium,[147] guanidinium,[148,149] pyridinium,[150] phenanthridinium[151]

and viologen[152] have been reported. However, self-exfoliation of COFs promoted by charged linkages was not described until 2020, when Dichtel and co-workers reported a general acid-mediated method to exfoliate imine-based COFs by the protonation of the imine bonds (Fig. 20).[153] Thus, the charged repulsion between positively charged COF layers promoted the self-exfoliation of the framework into nanosheets which thickness ranged from 5 to 50 nm. In a different work, Wang and co-workers demonstrated that acidulation of the media promoted the polarization of C=N bonds in imine-based COFs, inducing a significant slippage of the layered structure and finally forming uniform CONs.[154]

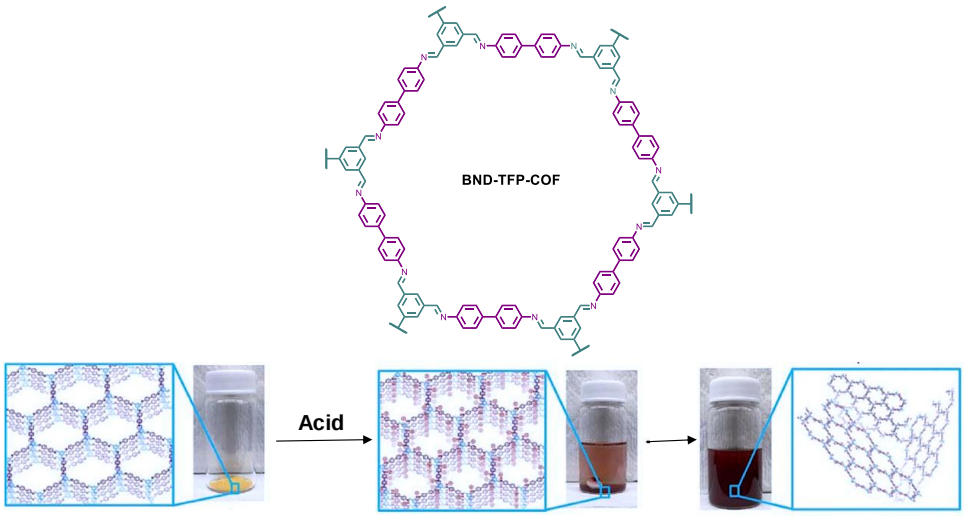

Figure 20. Acid-exfoliation into thin sheets by protonation of imine-based COF. Adapted from reference 153.

1.7 Potential applications of COFs

COFs can display excellent features and properties, and several functional COFs have already been applied in several fields. All these applications have been recently thoroughly reviewed.[155,156] In this section, only some of the most remarkable applications of COFs related with the work developed in this memory are enlisted and detailed.

1.7.1 Energy storage and conversion

Due to their porous and well-defined periodic extended structure, COFs display multiple high-rate charge carrier transport (electron, hole and ion). Their conjugated skeletons together with their π electron density overlapped among the layered framework has made COFs potential and promising materials for electrochemical energy storage and conversion (Fig. 21).[157]

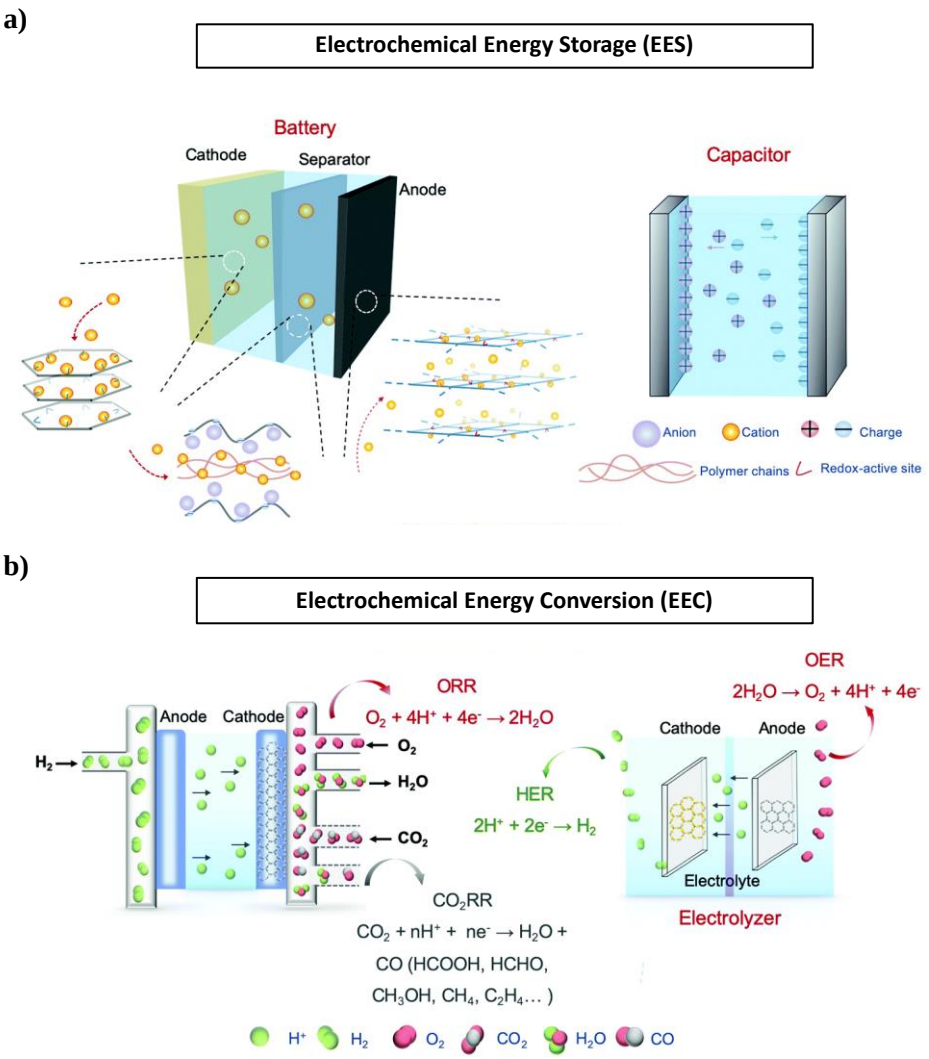

Figure 21. Schematic representation of the direct application of COFs in (a) EES and (b) EES.

The development of effective methods to functionalize COFs enabled the integration of redox/catalytic active sites within the COFs framework, offering a great opportunity to tune their electronic structures.[158,159] Furthermore, the vertical stacking of layers in 2D COFs through π-π interactions of aromatic monomers offer effective channels and pathways for the hole and electron diffusion. The successful incorporation of ions inside these channels can successfully enhance ion transport along ionic COFs framework.

a) Batteries

Because of their crystalline structure and the possibility of designing networks endowing redox-active sites, COFs have been regarded as potential electrode materials for energy storage devices like batteries, developing more environmentally benignity materials in comparison to conventional inorganic-based batteries.

Redox-active sites can be readily incorporated in the building blocks prior to the COF synthesis or in a post-SM, and they can fruitfully participate in multi-electron redox processes. The exploration of novel electroactive organic molecules as building units have enabled the development of electroactive COF materials with enhanced capacity and redox potential. In addition, COF polymerization prevent the dissolution of small molecular organic compounds in organic electrolytes which is responsible for the capacity fading, self-discharge and poor cycling performance.[160,161]

Besides the theoretical high conductivity of COFs in plane and along the layered structure, the defects present in the network inhibit an efficient electron transport.[162,163] To boost electron conductivity, COFs can be hybridized with conductive additives such as carbon nanotubes (CNTs) or graphene.[164,165]

Ion diffusion along the orientated pathways can be usually difficult.[158,166] Thus, several active sites within the frameworks cannot be reached. To overcame this issue, exfoliation of bulk COFs into few-layered materials (Covalent Organic Nanosheets or CONs) has become a promising alternative.[142,167,168]

COFs have been widely explored for electrochemical energy storage (EES) applications. In one hand, several examples have been reported for COF-based

cathodes, which generally exhibit high capacity (~200 mA h g^{-1}) and excellent cycling performance.[169,170] On the other hand, COF-based anode electrodes have also been investigated but are still a bit far from real application because of their high voltage, elevated cost and prolonged activation process.[171,172]

COFs have also been used as solid electrolytes, since their well-defined porous structures present several advantages: the stacked layered structure provide directional ion conduction channels and convenient structural design and functionalization make COFs potential platforms for enhancing ions hopping or migration along the framework. By designing ionic backbones or by introducing flexible polymer chains in the structure ionic migration and hopping centers can be increased.[173–175] In this regard, an imine-based COF was decorated with oligo(ethylene oxide) chains in the pore walls to allow the preparation of a polyelectrolyte COF upon complexation with Li^+.[173] The Li ion conductivity of the resulting COF was 731 times superior than the corresponding of the bare pore walls COF.

Besides Li ion conductivity, COFs can also act as proton conductors by the proper encapsulation of proton carriers within the COF channels.[176,177] The design of an ionic framework, COF functionalization with pendant acid groups or hybridization with a conducting polymer can also enhance proton conductivity.[30,178,179] Jing and co-workers designed COFs which incorporated proton carriers (triazole or imidazole units) in the pores (Fig. 23).[176] This functionalization resulted in COF platforms which achieve proton conductivities 2-4 orders of magnitude higher than those reported for microporous and non-porous conventional polymers.

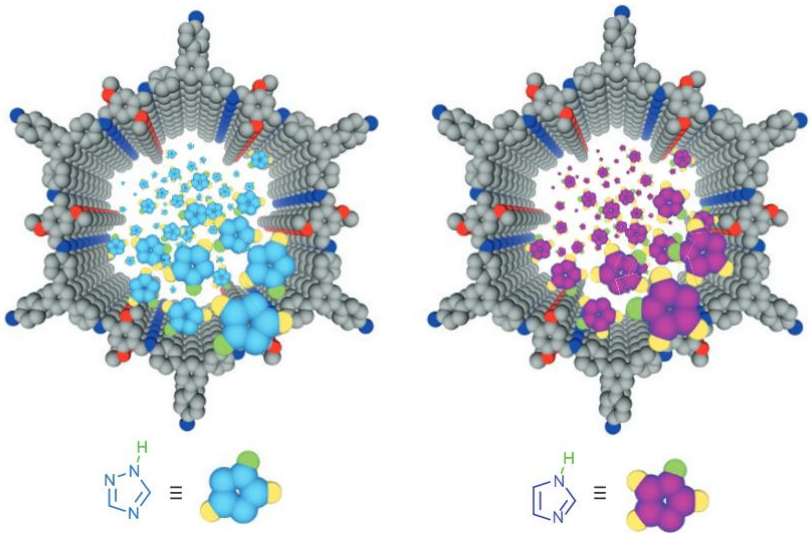

Figure 23. Graphic representation of proton-conducting COFs.

b) Supercapacitor

Supercapacitors (SCs) have emerged as very promising candidates for electrical energy storage devices, since they exhibit high power density, high coulombic efficiency, long cycling life and fast charge-discharge rate.[180] Depending on the mechanism they use to storage the charge, SCs can be widely classified into double-layer supercapacitors (EDLS) and Faradaic supercapacitors (FS) or pseudocapacitors.[181] It should be pointed out that the electrode material is not chemically active in EDLS. In contrast, efficient redox reactions take place in the electrodes in FS.[182] However, to achieve large capacitance, they both require electrode materials displaying large surface area, high porosity and conductivity.[183,184]

Up to date, different electrode materials have been applied in SCs, including metal oxides and hydroxides,[185] porous carbons[186] and conducting polymers.[187] Due to their large surface area, well-defined structure and long-range crystallinity COFs have greatly receive the interest among the researchers in this field. Three different approaches have been considered to apply COFs as electrode materials in SCs: pre- or post-synthetic functionalization of COFs with redox active units;

hybridizing COFs with conductive materials (to enhance electrical conductivity); or pyrolyzing COFs into porous carbon materials (to enhance electrical conductivity and capacitance).

Dichtel and co-workers pioneered the design and application of COFs in SCs. They successfully described the synthesis of **DAAQ-TFP-COF** by the condensation reaction of 1,3,5-triformylphloroglucinol (TFP) and the redox-active building block 2,6-diaminoanthraquinone (DAAQ) (Fig. 24a).[188] Due to the well-defined porous structure and its high surface area, efficient charge transfer from redox-active moieties to the surface of electrode could be acquired. Besides the great stability of the COF (up to 5000 charge-discharge cycles) only 40 F g^{-1} capacitance was achieved, and only 2.5% of the redox-active DAAQ units were electrochemically accessible. To overcame this issue, orientated 2D **DAAQ-TFP-COF** thin films were grown into Au substrates (Fig. 24b).[189] This modification led to a significant enhanced accessibility of the quinone units (up to 80-99%) and the capacitance was improved in a 400% in comparison to the randomly orientated polycrystalline COF powders. However, the use of Au electrodes showed considerable slow charge-discharge rates and very low power activities. Therefore, poly(3,4-ethylenedioxythiophene) (PEDOT) conducting polymers were absorbed within the COF nanoporous structure and further electropolymerized (Fig. 24c).[190] The PEDOT-modified **DAAQ-TFP-COF** thin films exhibited enhanced conductivity, an increased rate of electron transfer and a highly enhanced charge storage capacity, reaching a maximum capacitance of 350 F cm^{-3} and displaying excellent cycling stability (up to 1000 charge-discharge cycles).

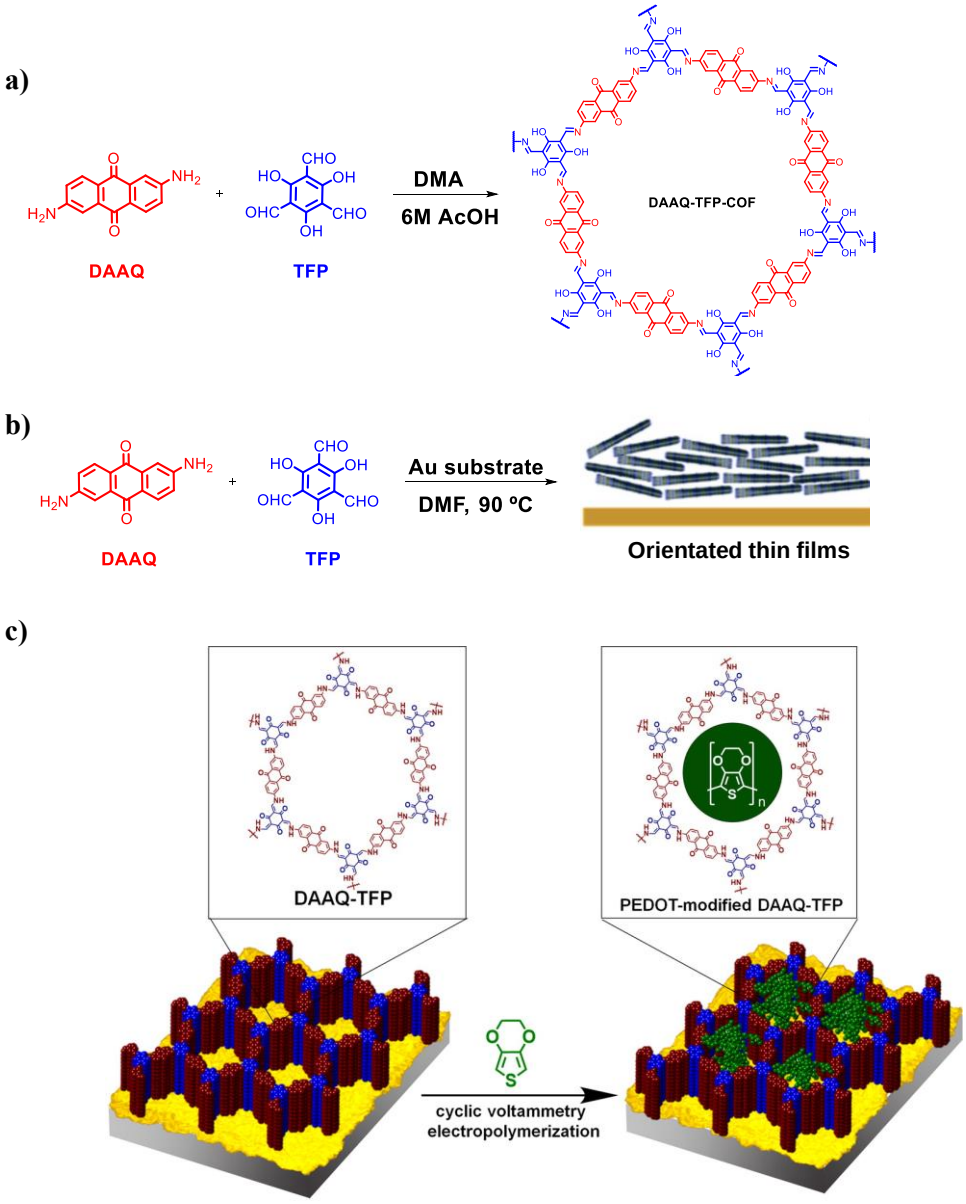

Figure 24. (a) Schematic representation of the synthesis of **DAAQ-TFP-COF**; (b) Representation of the preparation of orientated **DAAQ-TFP-COF** thin film on Au electrode susbtrates; (c) Graphical representation of electropolymerization of EDOT into **DAAQ-TFP-COF** films.

A similar strategy was described by Wu and co-workers to increase the electron transfer in COF electrode materials. They carried out a solid-state polymerization of 2,5-dibromo-3,4-ethylenedioxythiophene (DBrEDOT) within the **DAAQ-TFP-COF** channels, affording the formation of **PEDOT@AQ-COF** nanocomposite (Fig. 25).[191] The resulting material exhibited outstanding performance with excellent cycling stability and considerable enhanced rate of charge-transfer. Moreover, it reached the highest specific capacitance among COF-based electrode materials for supercapacitors reported in the literature (1663 F g^{-1} at 1 A g^{-1}).

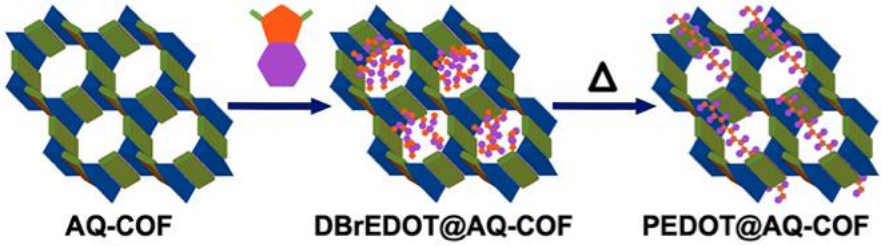

Figure 25. Graphical representation of the synthesis of **PEDOT@AQ-COF**.[191]

In 2018, Banerjee and co-workers developed a series of redox-active COFs which were successfully applied in pseudocapacitor electrodes.[192] These results unravel that the proper design and functionalization of the COF backbone with redox-active units grant COFs with competitive electrochemical performance.

Li and co-workers described an *in situ* oxidative polymerization growth onto copper foil substrate, affording the preparation of a 2D polyphorphyrin-based COF thin film with enhanced electrochemical.[193] However, Khayum and co-workers went one step further by synthesizing COF free-standing flexible thin films based on anthraquinone and anthracene moieties, which were successfully applied in flexible supercapacitor.[194]

Besides the integration of redox-active units within the COF framework, the preparation of COFs composites is also an effective method for their application as electrode materials in supercapacitors. In 2015 Wang and co-workers used amine modified reduced graphene oxide (NH_2-RGO) for the preparation of **COFs/NH_2-RGO** composite, which displayed both electrical double layer supercapacitor and pseudocapacitance behaviors.[94] This proves that the synergistic effect of COFs microporous structure and excellent electroconductivity of graphene can be further applied for the development of advanced electrode materials for SCs.[96] In this

regard, COFs have also been hybridized with MWCNTs and SWCNTs,[97,195] conductive polymers[196] and metal nanowires,[197] paving the way for the design of more COF-based electrodes for EES devices.

Nitrogen-rich COFs have also shown promising features as the electrode material in pseudocapacitors.[198,199] Xue and co-workers reported the outstanding electrochemical behavior and significance pseudocapacitance of a 2D COF linked with -NH- bonds.[200] Furthermore, Zhi and co-workers developed a series of CTFs which displayed microporous structures.[201] In this work, they showed that dopping the frameworks with nitrogen atoms efficiently enhanced the supercapacitor performance of these materials and their further potential application in ionic liquid-based supercapacitors.

As it has been previously explained, COFs can be predesigned and different heteroatoms (e.g. B, N, O, S) can be readily incorporated in their polymer backbone. The further pyrolysis of these frameworks has been widely applied for the development of novel electrodes. In this regard, Hao and co-workers synthesized three different benzotrithiophene-based COFs, which were further annealed with $ZnCl_2$ at 700º C for 20 h.[202] The resulting porous carbon materials displayed double-layer capacitor properties.

Besides direct carbonization of the COF pristine framework, many authors have investigated the pyrolysis of hybrid COF materials. Thus, Sun and co-workers reported the synthesis of **COF-1** (Fig. 10a) nanosheets perpendicularly grafted onto graphene oxide (GO) surfaces.[203] This hybrid structure was then carbonized into boron doped carbon material that featured high-performance electrode behavior.

Carbonized COFs have shown enhanced conductivity, great porosity and, very often, a great amount of heteroatoms within the framework. These features, together with the optimization of the working electrolyte as well as the loaded amount of active material, make COFs promising electrode materials for the fabrication of novel energy-storage devices.[168,204]

c) Electrocatalysts

When designing efficient catalysts for EEC devices several aspects must be considered, including the presence of abundant catalytic sites, inherent high electrical conductivity and orientated pathways for effective mass transport.

COFs high surface area and great porosity enhance their potential as electrocatalysts, since they facilitate charge and mass transport and assure an efficient contact between substrate and active sites.[205] The highly predesign ability of COFs enable the incorporation of multiple active sites in the building blocks prior to the COF formation or in the pore walls in a post-SM reaction. This allows the fine-tuning of the electrocatalytic properties of the material. In addition, COFs usually display high chemical and thermal stability.

To enhance electron conductivity within the 2D conjugated COFs, different approaches have been explored. In one hand, hybridizing COFs with conductive materials (e.g. graphene or CNTs) allows the preparation of COF-based composites with enhanced conductivity. On the other hand, by pyrolyzing COFs into porous carbon materials high conductivity and robust stability is achieved.

COFs have been successfully applied as electrocatalysts in different reactions, including oxygen reduction reaction (ORR), oxygen evolution reaction (OER), hydrogen evolution reaction (HER) and carbon dioxide reduction reaction (CO_2RR).

The oxygen reduction reaction (ORR, $O_2 + 4H^+ + 4e^- \rightarrow 2H_2O$) has a great influence in energy storage and conversion devices, since it is the rate determining step. Traditionally, Pt has stand out as the best catalyst for the ORR in fuel cells since they allow the direct 4-electron reduction pathway from O_2 to H_2O, preventing the formation of hydrogen peroxide (H_2O_2).[206] However, the scarcity and high cost seriously limit the commercial application of this noble-metal catalyst.[207] Thus, it is of big interest the development of cheaper alternatives that can provide similar catalytic features.

In this regard, 2D COFs have proved to be efficient electrocatalyst for ORR. Moreover, by combining proper COF design with a template carbonization process the preparation of well-defined porous carbons with high conductivity and heteroatom dopped catalytic edges can be achieved, what has shown great potential

for the development of new catalyst for the ORR. For instance, Mao and co-workers reported a cobalt-porphyrin-based COF and its subsequent pyrolization.[208] The resulting material (**Co-COF-900**) exhibited an electrochemical performance comparable to commercial 20%Pt/C catalyst in ORR, proving the effective design of transition metal-containing COFs to replace Pt-catalysts.

In a different example, Thomas´s group reported the synthesis of a bipyridine-COF (**TpBpy**) and the further coordination of iron species.[209] The material was subsequently pyrolyzed, and the electrochemical studies showed that the resultant **mC-TpBpy-Fe** also displayed comparable properties to those of commercial Pt/C electrocatalyst. Moreover, it exhibited excellent stability and no methanol crossover/CO-poisoning effects.

Besides this metal-containing COFs, a few examples of COF-based metal-free electrocatalysts have been reported. Wu and co-workers pioneered the synthesis of a 2D covalent organic radical framework (**PTM-CORF**),which was prone to receive electrons from oxygen and therefore displayed good electrocatalytic features towards ORR.[210]

Jiang and co-workers also reported the synthesis and further template carbonization of a COF into carbon sheets (**PA@TAPTDHTA-COF$_{1000}$**) which displayed not only great conductivity but also a well-defined porous structure with abundant catalytic edges, what enhanced the overall electrocatalytic properties of the material.[211]

Moreover Segura and co-workers recently described the synthesis of a naphthalene diimide-based COF (**NDI-COF**) which served as an efficient electrocatalysts towards oxygen reduction in alkaline media (Fig. 26).[212] It should be highlighted that this material is not only metal-free but also no additional pyrolysis process was applied prior to the electrochemical studies. Therefore, it should be considered that the electrochemical properties of the building block can effectively influence the final electrochemical features of the resulting COF, which opens a new research field on how to design electroactive COFs.

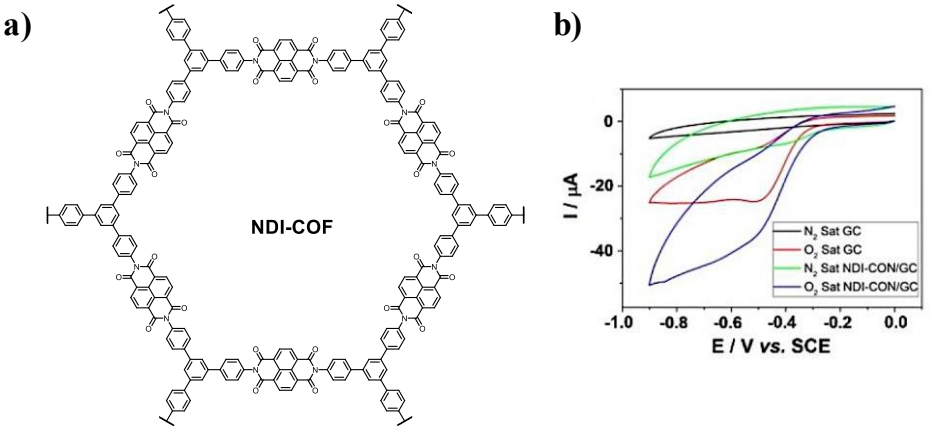

Figure 26. (a) Graphic representation of **NDI-COF** and (b) CV of GC electrode in 0.1M NaOH N_2 (black) or O_2 (red) saturated solution and of NDI-CON/GC electrode in 0.1 M NaOH N_2 (green) or O_2 (blue) saturated solution. Adapted from reference 212.

The development of efficient COF-based electrocatalyst towards the oxygen evolution reaction is still challenging. However, a few examples (**Co-TpBpy COF**, or **IISERP-COF2**)[213,214] have been reported for the oxidation of water molecules.

In a different subject, hydrogen has been pointed out as a new promising alternative to conventional fossil fuels. The electrolysis of water is an interesting and efficient approach to generate H_2 *via* hydrogen evolution reaction. Up to date, Pt-based materials are considered the best electrocatalysts towards HER. However, as it has been previously mentioned, novel metal-free electrocatalysts are highly demanded. Among them, COFs have shown promising results. For example, a porphyrin-based COF (**SB-PORPy-COF**) has been successfully synthesized and applied for HER.[215]

In a similar approach, a series of azine-based COFs were designed for photocatalytic hydrogen evolution.[216] The electron deficient triazine knots facilitated an enhanced electrocatalytic activity of the materials towards HER.

Finally, the efficient reduction of CO_2 into other valuable carbon products has attracted increasing attention among the scientific community. Electrolysis has emerged as an interesting approach to reduce CO_2. Therefore, great efforts have been devoted to the development of novel COF-based electrocatalysts for CO_2RR.

Yaghi and co-workers incorporated cobalt porphyrin monomers into COFs, and the resultant frameworks displayed efficient catalytic activity and selectivity towards CO_2 reduction.[217] Besides porphyrins and their analogues, tricarbonyl rhenium(I) complexes have also shown promising catalytic activity.[218]

The preparation of orientated COF thin films onto electrode surfaces has significantly improved the electrocatalytic performance of these materials toward CO_2 reduction.[219] In addition, metal-free COF-based materials have also been explored. In 2018, Deng and co-workers reported the reduction of an imine-linked COF and the electrochemical study of the resulting framework.[71] They stated that the inherent porosity of the COF together with the functionalization of the framework with amine groups effectively promoted the conversion of CO_2 into carbamate moieties.

1.7.2 Luminescence and sensors

Over the past decades there has been a growing interest in the development of novel luminescent materials, since they can be applied in several fields including chemical sensing, solid-state light emitters, photovoltaics and optoelectronics.[220,221] Due to their extended π conjugation and unique properties, COFs constitute an excellent platform to develop luminescent polymeric systems.

The boronate-ester-based COF **TP-COF** and the boroxine-based COF **PPy-COF** constitute the first two COF-examples in which the photoluminescence properties were investigated.[222,223] Upon excitation of the pyrene moieties, they both exhibited strong blue luminescence at 474 and 484 nm, respectively.

In 2015, Jiang and co-workers reported the design and synthesis of a novel 2D COF in which they successfully incorporated anthracene units.[123] Due to the extended conjugation within the 2D layers, the resulting **Ph-An-COF** displayed strong fluorescence. However, upon irradiation at 360 nm, the anthracene moieties underwent a photo-induced dimerization leading to a loss of planarity and conjugation in the resulting **Ph-An$_{CD}$-COF**. Thus, a quenching of the COF´s fluorescence was observed (Fig. 27). This work highlights the great impact that extended conjugation has in the photophysical properties of COFs, which has been investigated by several researchers.[224,225]

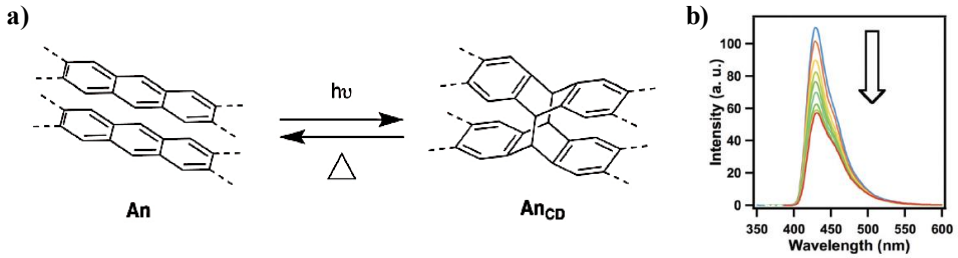

Figure 27. (a) Reversible photo-induced and thermal dimerization of anthracene moieties; (b) **Ph-An-COF** upon irradiation at 360 nm. Adapted from reference 123.

Despite this extended conjugation through the COF backbone, 2D COFs form layered structures that stacked by effective π-π interactions. This usually lead to a loss of the luminescence properties due to aggregation-caused quenching (ACQ) phenomena.[226] Therefore, a different synthetic strategy has been developed in order to achieve light-emitting COFs. It mainly consists in incorporating aggregation-induced emission (AIE) mechanism, in which luminophores are non or less emissive in solution while they display strong fluorescence in the solid state. By integrating AIE-active units in the COF skeleton, light-emitting COFs can be prepared.[227] In this regard, AIE-active tetraphenylethylene (TPE) units have been incorporated to several reported COFs.[228,229] In fact, the boronate-ester-COF **TPE-Ph COF** has become the benchmark for luminescent COFs, with an absolute fluorescence quantum yield of 32% (Fig. 28).[226]

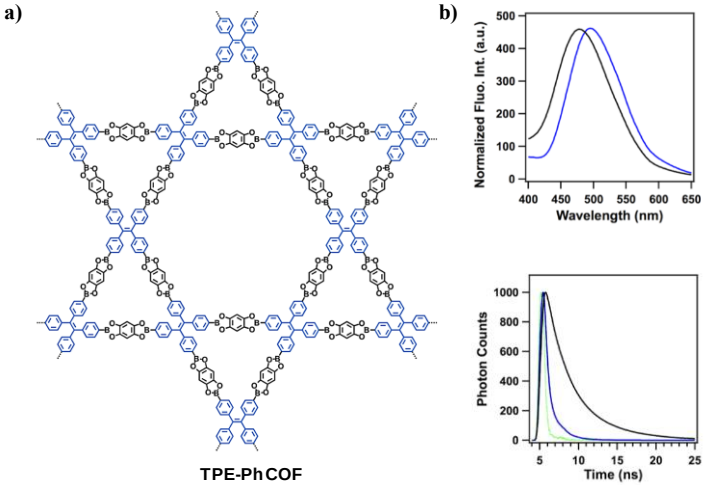

Figure 28. (a) Schematic representation of **TPE-Ph COF**; (b) Fluorescence spectra and lifetime profile of the TPE model compound (black) and the **TPE-Ph COF**.

Introducing pendant bulky groups within the framework or non-planar bonds in the COF skeleton can effectively originate light-emitting COFs. For instance, hydrazine-linked **COF-LZU8** displays strong blue emission at 460 nm due to the selected contorted linkages.[102]

A different alternative is based on the incorporation of fluorophores within the pore surface through post-synthetic modifications. This allowed the synthesis of fluorescent **T-COF-OFITC**, which was covalently modified with fluorescein-isothiocyanate (FITC).[230]

The photophysical properties of COFs have been exploited for different applications, including chemical sensing and the development of biosensors. Due to their inherent porosity and their modular nature, COFs have been widely used for the molecular recognition of different analytes such as explosives, volatile chemicals, anions, toxic metals and biomolecules.[141,231–234] Generally, this chemo- and biosensing is based on the photoinduced electron transfer mechanism. Therefore, an effective fluorescence quenching can be achieved by promoting electron transfer by certain molecules. In contrast to this switch-off sensing, by hindering electron transfer from these targets, the COF luminescence ability can be readily enhanced, leading to a switch-on sensing.

Exfoliated COFs have also been directly applied for the detection of different analytes. Upon exfoliation of 2D **TpBDH-COF** and **TfpBDH-COF**, the resulting CONs were explored for sensing explosives;[235] and the exfoliated amide-linked **PI-COF** was dispersed in ethanol and investigated for the selective and sensitive detection of TNP.[236] Moreover, different pollutants in water (organic dyes and nitroaromatic compounds) could be notably detected by an imine-linked COF (**IMDEA-COF-1**) upon exfoliation into CONs.[237]

1.7.3 Reinforcement in polymer nanocomposites films

Recently, composite materials containing COFs have attracted increasing popularity since they constitute a predesignable platform that can be successfully applied in a plethora of fields ranging from analytical to more sophisticated environmentally related applications. The increased number of publications in this field evidence the growing impact of COF composites films, which have been prepared in combination with a great variety of materials taking advantage of different synthetic strategies.[238]

A different approach that has been less explored is based on the application of COFs as polymer or biopolymer nanofillers. It is known that, in order to improve the structure-property relationship of different polymers, 2D nanoparticles can be embedded in the polymeric matrix as reinforcement nanosheets, which constitute an effective way to improve the final performance of the nanocomposite films.[239] However, only a few examples have been reported on the use of COFs as 2D-nanofillers for biopolymer matrices such as poly(vinyl alcohol) (PVA) and chitosan.[144,240]

In the first reported example, Hu and co-workers described the synthesis and exfoliation of an imine-based COF into nanosheets and the further dispersion of the resulting CONs into chitosan polymeric matrix (Fig. 29). The as-obtained nanocomposite films displayed enhanced thermal, mechanical and flame retardant performance, indicating great interface compatibility between chitosan and the 2D COF nanosheets.[240] In a subsequent study, PVA/COFs nanocomposites films with different weight loading of CONs were prepared (Fig. 29). Due to their inherent crystalline structure, COFs became excellent nucleation agents displaying great dispersibility in the polymeric matrix. Moreover, thermal, mechanical, hydrophobic and flame retardant performances of the PVA/COFs films were successfully improved.[144]

These results indicate the great potential of exfoliated COFs as polymeric nanoreinforcements, since they have shown good interface compatibility, great dispersibility and a significant enhancement of the overall performance of the resulting nanocomposites, especially compared with other inorganic nanofillers. Therefore, it is of big interest the development of novel multifunctional nanocomposites reinforced with COF-based materials that present not only

enhanced mechanical and thermal performances but also additional advanced functional properties.

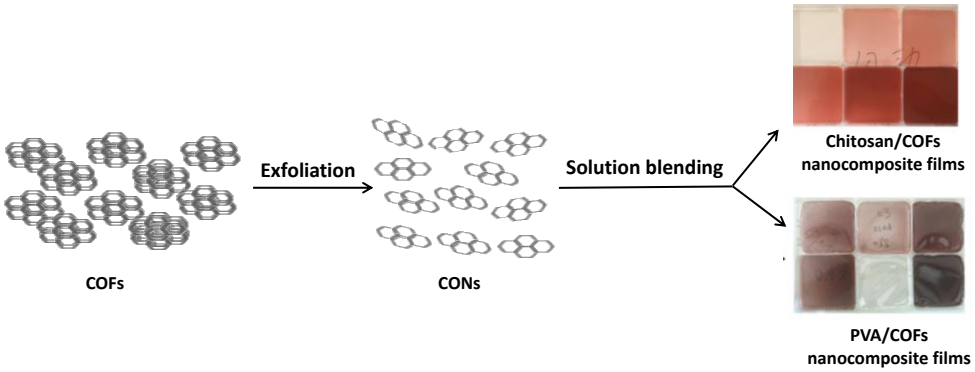

Figure 29. COF nanosheets as polymer nano-enhancer. Adapted from references 144, 240.

1.8 Closing remarks

As it has been exemplified in the previous sections, COFs constitute an emerging multidisciplinary investigation field that has attracted increasing interest in relation to their chemistry, physics and material science key aspects. Their unique predesign structures have enabled the development of different properties and features, allowing the design and synthesis of novel COFs for tailored applications.

However, several aspects must be further explored in order to achieve the great potential of COFs molecular architectures. These issues include the exploration of novel functionalized building blocks, the development of new reactions and synthetic protocols or the progress towards enhanced processability of these materials.

Besides these limitations, great efforts have been devoted in this thesis to the development of novel polymeric COF frameworks for energy, sensing and sustainability- related applications.

Chapter 2:

Aim and scope of the thesis

The relevance of Covalent Organic Frameworks, as shown in chapter 1, makes specially interesting further investigation into the design, synthesis and potential application of these materials in different fields. Thus, the main aim of the present doctoral thesis consists in the development of novel COF-based materials for tailored applications. The general strategy involves, firstly, the synthesis of the molecular building blocks, as well as the organic molecules needed for the post-synthetic modification approach that has been addressed in this work. Since different COF-linkages have been explored in this thesis, a wide range of monomers have been designed and synthesized endowing different functional groups, including aldehydes and amines for the imine-based COFs, and aromatic nitriles and amides for the preparation of triazine-based COFs. The molecular products have been obtained through standard procedures in an advanced organic chemistry laboratory and they have been fully characterized by the usual techniques such as infrared spectroscopy, ^{1}H and ^{13}C nuclear magnetic resonance or mass spectrometry. On the contrary, COFs have been obtained either by solvothermal or ionothermal synthesis conditions. The formation of a polymeric network has been analyzed by infrared spectroscopy and solid-state ^{13}C nuclear magnetic resonance, while the crystallinity and porosity of the materials has been determined by X-ray diffraction and gas sorption isotherms, respectively. Thermogravimetric analysis, scanning electron microscopy, transmission electron microscopy, X-ray photoelectron spectroscopy and dynamic light scattering have also been performed for the characterization of the 2D materials in the solid state. Additionally, the obtained materials have been tested for the desired application.

Thus, in Chapter 3 the design and synthesis of a novel electroactive enamine-linked COF will be addressed, and the as-obtained material will be tested as electrocatalyst for the oxygen reduction reaction (ORR). The effect of porosity and crystallinity on the materials´ performance will be investigated by preparing and evaluating an analogous polymeric amorphous material with the same chemical composition. Furthermore, a comprehensive electrochemical study of this polymeric framework will be performed to evaluate its potential application as a new organic electrode material for energy storage applications.

In Chapter 4, two different COF-based materials based on triazine units (CTFs) will be synthesized and further processed by a straightforward thermal treatment. The resulting microporous carbon structures will be characterized and further tested

for advanced electrochemical applications, including the development of novel organic electrode materials for supercapacitors.

In Chapter 5, a robust quinoline-linked COF will be synthesized by a post-synthetic modification of a readily available imine-linked COF, and bulky pendant units will be grafted onto the pore surface of the material. The so-formed framework will be characterized and studied for the selective recognition of Zn metal ions via "turn-on" fluorescence emission.

In Chapter 6 the post-synthetic modification of an imine-linked COF with catechol moieties will be carried out through a click chemistry reaction, and the as-prepared material will be processed and incorporated into a plasticized biopolymer matrix. Furthermore, the resulting bionanocomposites will be characterized and evaluated as potential non-migrating antioxidant agents for sustainable food packaging applications.

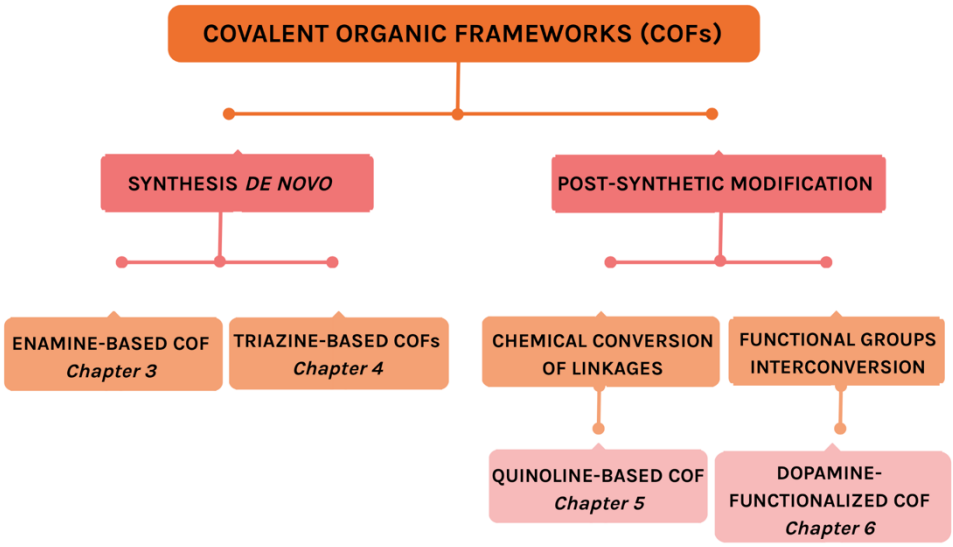

Concept mapping of the general objectives of the present thesis.

Chapter 3:

Pyrenetetraone-based Covalent Organic Framework for electrochemical energy storage and conversion

3.1 Introduction

To date, the increasing energy demand together with the depletion of traditional fossil energy sources has become a big challenge for our rising global population. In addition, growing environmental concerns have motivated an extensive scientific research in the field of sustainable and clean energy technologies, including metal-air batteries and fuel cells, which have been envisioned as promising alternatives for the development of a future low-carbon based society.[241–244] Despite the fact that emerging technologies like fuel cells display high efficiency and sustainability advantages, such as zero pollution or CO_2 gas emissions, efficient electrocatalysts are required in order to promote the key but sluggish chemical cathode reaction involved: oxygen reduction reaction (ORR).[245] Traditionally, noble and rare metals (e.g., Pt) have stand out as the best catalyst for the ORR in fuel cells since they allow the direct 4-electron reduction pathway from O_2 to H_2O, preventing the formation of hydrogen peroxide (H_2O_2).[206] However, the scarcity and high cost seriously hamper the commercial application of this noble-metal catalyst.[207]

Derived from this concern, several organic 2D polymers have been explored as electrocatalysts for ORR, demonstrating satisfactory features for the development of metal-free fuel cells.[246–248] Among those, polymers containing redox-active electron-accepting units based on carbonyl groups, like quinones and its derivatives (anthraquinones, phenanthrenequinones and napthoquinones) have come forth as one of the best organic electrocatalysts for ORR due to their low-cost and suitable chemical functionality.[249–251]

Even though most of the reported quinone electrocatalysts are based on anthraquinone (AQ) moieties, it has been demonstrated that AQ molecules undergo the two-electron pathway in the ORR with the formation of hydrogen peroxide (1):[252,253]

$$O_2 + (2H^+ + 2e^-) \rightarrow H_2O_2 \quad (1)$$

Since the catalytic performance derives directly from the specific electroactive units, it is of big interest the design of novel quinone-based materials which can follow the desired and more efficient four-electron process with the formation of water as a byproduct (2):

$$O_2 + (4H^+ + 4e^-) \rightarrow 2H_2O \quad (2)$$

In this regard, big efforts have been focused in the design of new electroactive organic 2D polymeric networks that can provide catalytic performances similar to Pt-based electrocatalysts.[254] Due to their well-defined molecular and structural features, COFs have become a promising alternative for electrocatalysis.[212,255]

One of the advantages of COFs is that they can be integrated with transition metal (e.g., Fe, Co, Mn, etc) macrocyclic clusters, enhancing significantly the catalytic activity of the material.[208] However, despite the fact that these 2D COFs with nonprecious-metal incorporated macrocycles display high stability and catalytic activity, they usually require an additional pyrolysis treatment in order to enhance their electric conductivity and catalytic stability at higher temperatures.[211,256]

As a result of further investigations, metal-free COF catalysts have been obtained, but they either require additional pyrolysis and/or combination with other conductive supporting nanomaterials to form hybridized systems to improve the critical electron transfer process.[257]

Thus, in this chapter the synthesis and characterization of a novel 2D COF (**DAPT-TFP-COF**) based on quinone moieties connected through robust enamine functional groups will be adressed, and the material´s performance as electrocatalysts towards ORR will be evaluated. In addition, a comparison between the electrocatalytic activity of the COF and an analogous polymeric amorphous material with the same chemical composition (**DAPT-TFP polymer**) ought to provide an insight into the relevance of pore accessibility and crystallinity of the structure for the final application.

Moreover, 2D polymeric networks endowed with redox-active electron-accepting moieties based on carbonyl groups have been envisioned as potential electrode materials for energy storage,[258–260] since the extended π-conjugation in their molecular structure promotes reversible and fast charge storage properties, while the robust polymeric framework prevents the dissolution of small molecular organic compounds in organic electrolytes.[160,261] Consequently, a detailed electrochemical study of the amorphous quinone-based polymer **DAPT-TFP**

polymer in different electrolytes will be discussed to elucidate the potential of the material as an organic electrode for energy storage applications.

3.2 Results and discussion

Two different electrochemically active polymeric materials have been successfully prepared based on *ortho*-quinone units: 2D-**DAPT-TFP polymer** and **DAPT-TFP-COF** (Fig. 30). Despite the fact that both frameworks possess the same chemical composition, they differ in the long-range order of their structure: **DAPT-TFP polymer** displays an amorphous structure while **DAPT-TFP-COF** exhibits a more crystalline pattern. The synthesis and characterization of both materials is further addressed in the following section, including the evaluation of their electrochemical performance.

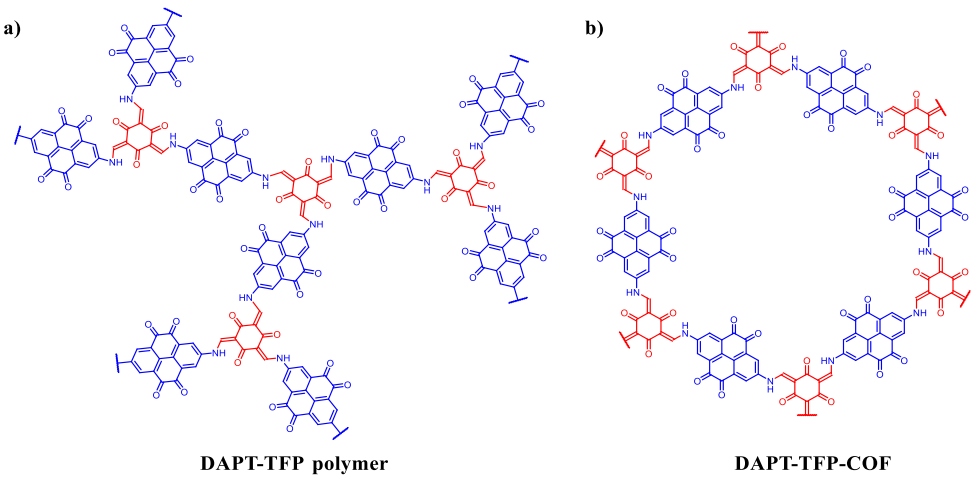

Figure 30. Structures of amorphous (a) **DAPT-TFP polymer** and crystalline (b) **DAPT-TFP-COF**.

3.2.1. Synthesis and characterization

Prior to the synthesis of the polymeric materials, their constituting monomers 2,7-diaminopyrene-4,5,9,10-tetraone (**DAPT**)[262] and 1,3,5-triformylphloroglucinol (**TFP**)[263] were successfully prepared. The synthetic route

to obtain **DAPT** is summarized in Scheme 4. Commercially available pyrene is oxidized at the 4-, 5-, 9- and 10- positions affording compound **1**,[262] which in turn is nitrated at the 2- and 7- positions by treatment with sulfonitric mixture (**2**).[262] Finally, following a reported procedure with slightly modifications, the nitro groups are selectively reduced with $SnCl_2$ in acidic media to afford the amino-functionalized **DAPT** monomer.

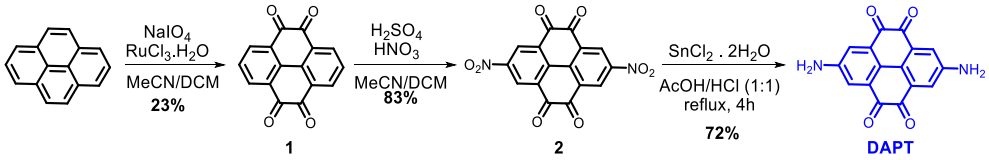

Scheme 4. DAPT synthetic route.[262]

The aldehyde-monomer, **TFP**, is obtained from commercially available phloroglucinol through an effective multiple formylation reaction using formamidine acetate and acetic anhydride (Scheme 5).[263]

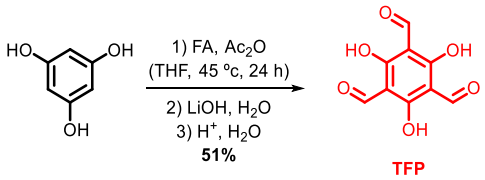

Scheme 5. TFP synthetic route.[263]

The synthesis of both 2D frameworks is based on the formation of robust enamine functional groups *via* co-condensation reaction between the redox-active **DAPT**[262] and **TFP**[263] monomers. The 2D **DAPT-TFP polymer** was obtained at 120 °C under solvothermal conditions in a mixture of solvents *N*,*N*-dimethylacetamide/*o*-dichlorobenzene 1:1 and a catalytic amount of aqueous acetic acid 6M (0.05 eq.) after five days. In an analogous synthetic protocol, crystallization of the sample was induced using supercritical carbon dioxide ($scCO_2$). This enabled an efficient way to develop a more crystalline and open porous framework, namely **DAPT-TFP-COF** (Fig. 31).

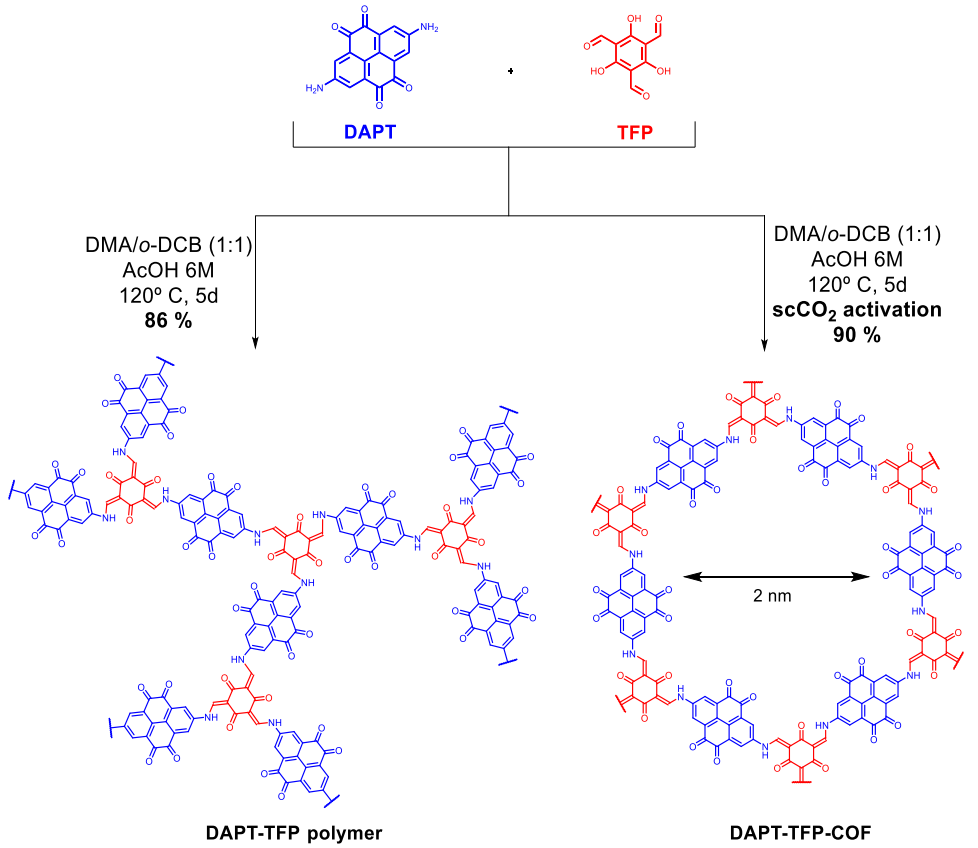

Figure 31. Schematic representation of the synthesis of **DAPT-TFP polymer** and **DAPT-TFP-COF**.

The formation of the β-ketoenamine linkage in both networks was confirmed by Fourier-transform infrared spectroscopy (FTIR). The comparative FTIR spectra of the powders (Fig. 32) show the disappearance of the N−H stretches of the starting diamine material **DAPT** as well as the emergence of a new C−N vibration band in the **DAPT-TFP polymer** and **DAPT-TFP-COF** spectra at 1278 cm^{-1} and 1251 cm^{-1}, respectively. This vibration band is characteristic of the C−N bond in the β-ketoenamine linkage. Moreover, C=O moieties are shifted to a lower energy (1580 cm^{-1} and 1565 cm^{-1}, broad bands) with respect to the C=O bands of the building blocks (1640 and 1665 cm^{-1}), which it is characteristic of a β-ketoenamine C=O stretch band.

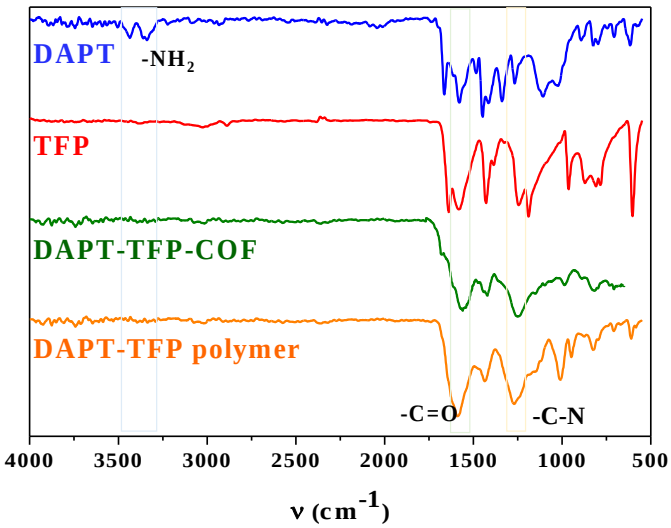

Figure 32. FTIR spectra of **DAPT** monomer (blue), **TFP** monomer (red), **DAPT-TFP-COF** (green) and **DAPT-TFP polymer** (orange).

The formation of a crystalline material after treatment with supercritical carbon dioxide ($scCO_2$) was confirmed by powder X-ray diffraction (PXRD) and further simulation studies performed using Materials Studio (version 5.5) software packages. **DAPT-TFP-COF** exhibits diffraction peaks at 3.08º, 7.29º, 11.30º and a broad peak at 26.36º corresponding to the 100, 110, 210, and 001 reflections, respectively (Fig. 33a) which are typical of 2D layered hexagonal networks. In order to elucidate the structure of **DAPT-TFP-COF**, two structural models, the eclipsed stacking (AA) and the staggered stacking (AB) were simulated and the experimental data of **DAPT-TFP-COF** was in best agreement with the eclipsed stacking (AA) pattern. Full profile Pawley refinement produced a hexagonal unit cell with a = b = 30.4 Å, c = 3.4 Å, α = β = 90° and γ = 120°, with good agreement factors (Rp = 4.97 % and Rwp = 6.44 %). On the contrary, the PXRD pattern of **DAPT-TFP** (Fig. 33b) lacks clear diffraction peaks, as expected from an amorphous polymer.

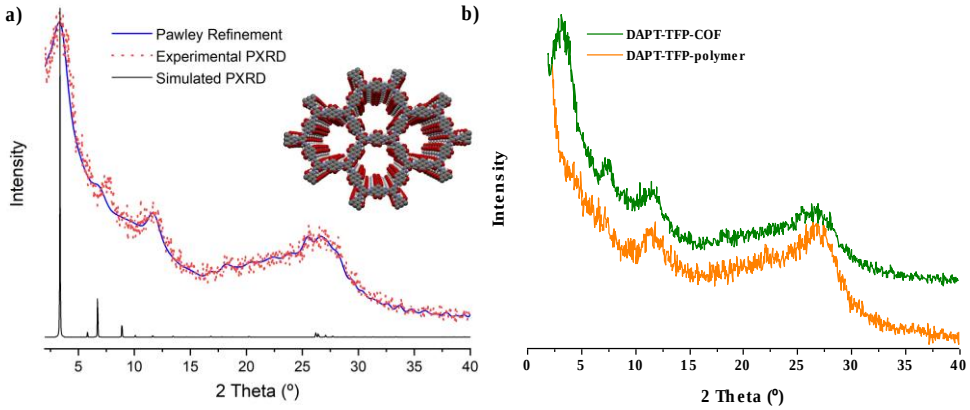

Figure 33. (a) Experimental (black) and predicted (blue) PXRD patterns of **DAPT-TFP-COF**. Inset: extended structure of **DAPT-TFP-**COF. (b) Comparative PXRD patterns of **DAPT-TFP-COF** (green) **and DAPT-TFP polymer** (orange).

^{13}C cross-polarization magic angle spinning NMR (^{13}C-CP/MAS-NMR) spectra of **DAPT-TFP polymer** and **DAPT-TFP-COF** also confirmed the formation of β-ketoenamine bonds (Fig. 34) displaying a signal at 180 ppm corresponding to the carbonyl carbon of the structures. Additional signals centered at 103.6, 109.3, 130.9, 137.3 and 156.3 ppm were assigned to the aromatic carbons of the framework.

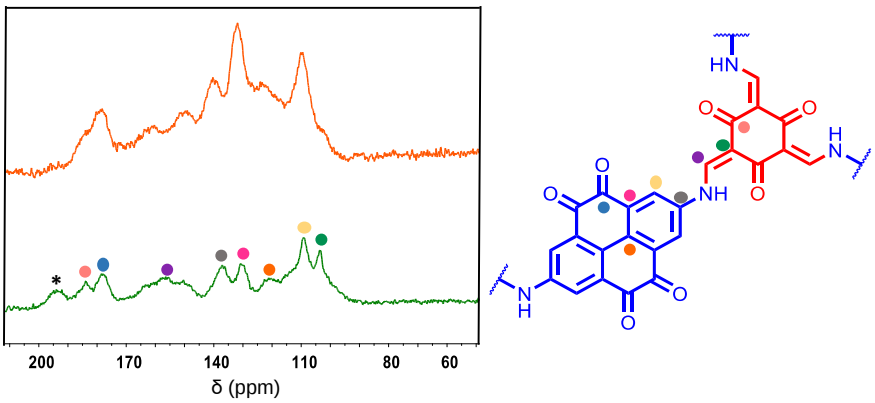

Figure 34. Comparative ^{13}C-CP/MAS-NMR spectra of **DAPT-TFP polymer** (orange) and **DAPT-TFP-COF** (green). Asterisks indicate spinning side bands.

The porosity of the materials was investigated by N_2 sorption isotherms at 77 K (Fig. 35a). **DAPT-TFP-COF** exhibits a type IV isotherm behaviour, typical for

mesoporous materials. A Brunauer-Emmett-Teller (BET) surface area of 200 m^2 g^{-1} and a total pore volume of 0.21 cm^3 g^{-1} were acquired, with a pore diameter of 2 nm (Fig. 35b) calculated by non-local density functional theory (NLDFT). On the contrary, N_2 sorption isotherms at 77 K show that **DAPT-TFP polymer** is a non-porous material with a BET surface area of only 43 m^2 g^{-1} and a pore volume of 0.05 cm^3 g^{-1} (Fig. 35a). The almost negligible porosity of the amorphous material suggests a lateral offset or collapse of the stacked layers, typically described for other 2D networks.[264]

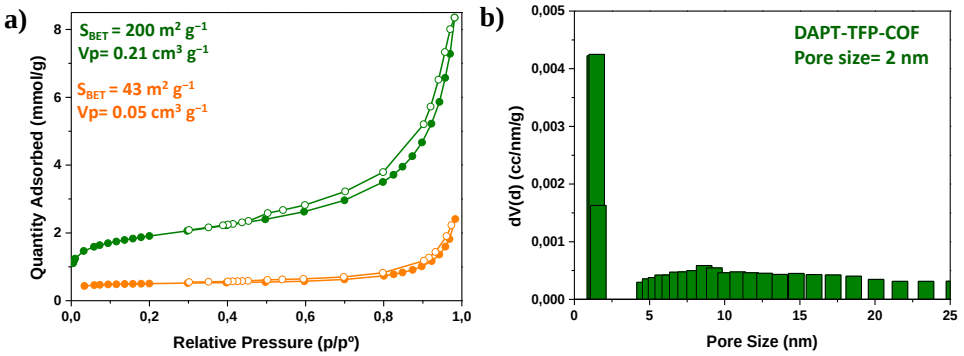

Figure 35. (a) Comparative N_2 sorption isotherms for **DAPT-TFP** (orange) and **DAPT-TFP-COF** (green); (b) Pore size distribution of **DAPT-TFP-COF**.

The thermal stability of **DAPT-TFP polymer** and **DAPT-TFP-COF** was investigated by thermogravimetric analysis (TGA). Although both materials exhibit high thermal stability (thermal degradation starts at 300 °C, Fig. 36), **DAPT-TFP-COF** displays a significant improved thermal stability.

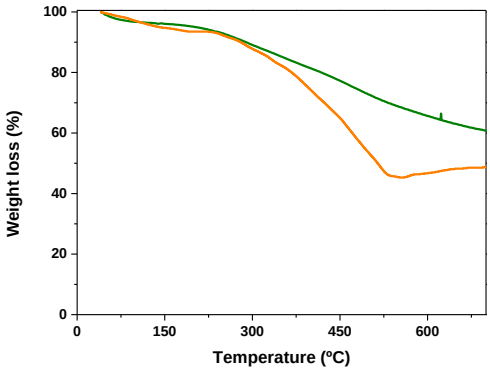

Figure 36. Comparative TGA trace of **DAPT-TFP-COF** (green) and **DAPT-TFP polymer** (orange) using a linear 10 ºC min^{-1} ramp method.

Finally, scanning electron microscopy (SEM) was used to study the morphology and shape of both polymeric frameworks. As shown in SEM micrographs (Fig. 37a-d), despite the fact that both materials have the same chemical composition, they present different morphologies. **DAPT-TFP-COF** sample exhibits a flower-like micrometric structure, while **DAPT-TFP-Polymer** sample consists mostly of micrometric spherical particles.

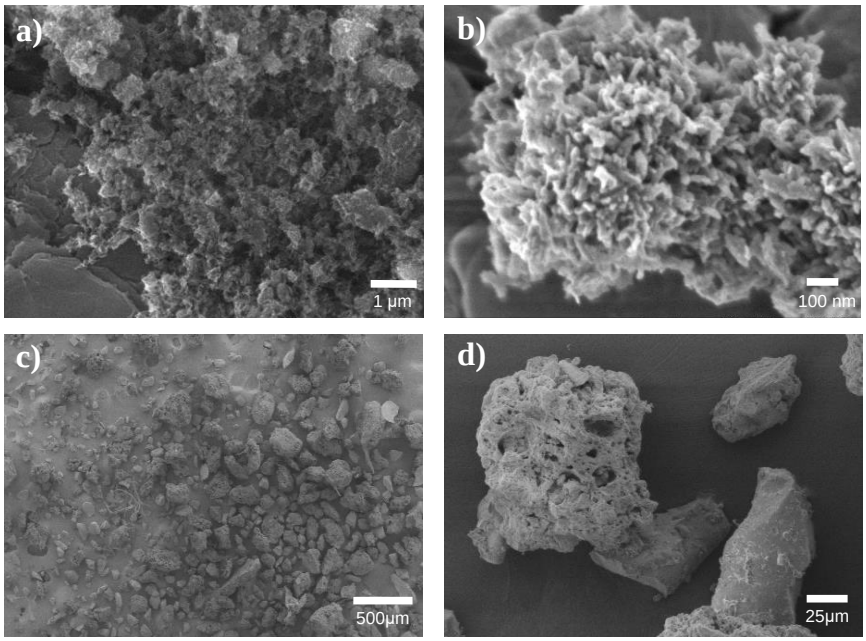

Figure 37. SEM images of (a,b) **DAPT-TFP-COF** and (c,d) **DAPT-TFP polymer**.

On the other hand, in order to efficiently process **DAPT-TFP polymer** it was necessary to exfoliate it into **DAPT-TFPe** following a procedure previously reported by Segura and co-workers.[265] Thus, **DAPT-TFP polymer** was suspended in $CHCl_3$ (0.25 mg mL^{-1}) and sonicated for 90 min (in cycles of 15 min). The resulting colloidal suspension was centrifuged at 1000 rpm for 2 min to remove non-exfoliated polymer. The colloidal character of the suspension was corroborated by the Tyndall effect upon irradiation with a laser beam (Fig. 38a inset). The hydrodynamic sizes of **DAPT-TFPe** nanosheets were analyzed by dynamic light scattering (DLS) showing a monomodal size distribution of *ca.* 630 nm (Fig. 38a). The sheetlike structural aspect of **DAPT-TFPe** was further observed by transmission electron microscopy (TEM, Fig. 38b), confirming its lamellar nature.

Due to its higher crystalline nature and considering that the previous computational modelling already proved the extended layered structure in a fully eclipsed AA stacking mode for **DAPT-TFP-COF**, it can be used straightforward in the following electrochemical studies without further additional treatments.

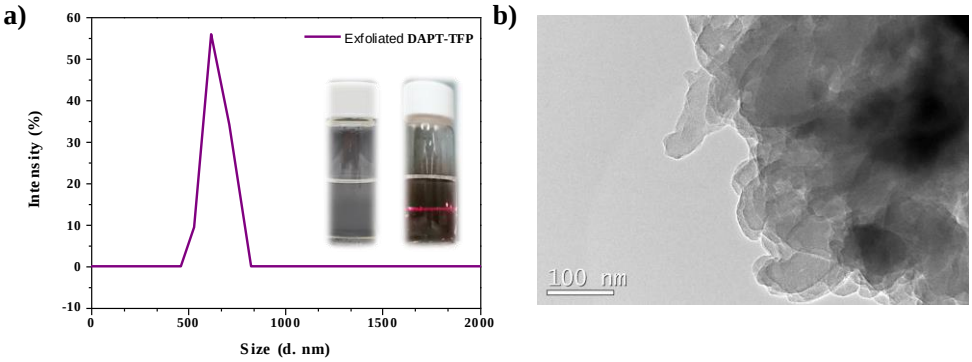

Figure 38. Characterization of **DAPT-TFPe**: (a) DLS measurement and Tyndall effect (inset). (b) TEM micrograph showing a sheetlike structure.

3.2.2 Electrochemical oxygen reduction

In order to study the electrochemical activity of **DAPT-TFP-COF**, cyclic voltammetry (CV) measurements were performed in a glass and Teflon homemade cell using a glassy carbon (GC) as working electrode, where the materials were deposited as thin films; platinum wire coil was used as counter electrode with a homemade saturated calomel electrode (SCE) as reference. A suspension of **DAPT-TFP-COF** in Milli-Q water (1 mg mL^{-1}) was submitted to an ultrasonic treatment for 15 min. Afterwards, 10 μL of the **DAPT-TFP-COF** suspension was deposited by drop-casting over the GC electrode (**DAPT-TFP-COF**/GC) and dried at room temperature. As reference material to study ORR electrocatalysis, 1 mg of platinum on carbon (10 wt%) was suspended in 1 mL of 20% EtOH and 0.02% Nafion; then, 5 μL of this ink was deposited by drop-casting over the GC electrode.

The electrochemical behaviour of **DAPT-TFP-COF** in 0.1 M NaOH was initially evaluated in the absence of oxygen (Fig. 39a, red curve). During the cathodic scan, a reduction peak at -0.43 V *vs.* SCE is observed, while in the reverse scan an oxidation process emerges at -0.28 V *vs.* SCE. This redox couple has a formal potential of -0.35 V *vs.* SCE and can be ascribed to the reduction/oxidation

activity of the electroactive pyrenetetroane (**PTO**) moiety, in which four electrons are exchanged.

To evaluate the potential influence of the porous and crystalline structure of **DAPT-TFP-COF** in the electrochemical performance, the amorphous analogous material was also studied. Thus, a suspension of **DAPT-TFP polymer** in Milli-Q water (1 mg mL^{-1}) was sonicated for 30 min (for shorter exfoliation times the material did not show any electrochemical activity). The as-obtained suspension was drop-casted (10 μL) over GC electrode. As shown in Fig. 39a (blue curve), even though the same redox couple are observed, the intensity of the cathodic and anodic processes is lower compared with **DAPT-TFP COF** behaviour, which evidences that the electrochemically active centres of **DAPT-TFP polymer** are less accessible. In addition, the capacitive current is also smaller, which clearly proves that the amorphous material is less conductive than the COF. Due to its low porosity, the electrolyte diffusion through the material network is seriously hindered.

After the successful evaluation of the electrochemical behaviour of **DAPT-TFP-COF**, its electrocatalytic ability for oxygen reduction reaction (ORR) was studied. Therefore, the cyclic voltammograms were acquired in the presence of oxygen (Fig. 39b). The **DAPT-TFP-COF**/GC electrode (red curve) shows a high increase of the current intensity besides a shift of around 160 mV towards less negative potential values compared with the unmodified GC electrode (black curve). Both effects reflect the great electrocatalytic activity of **DAPT-TFP-COF** towards ORR.

Additionally, **DAPT-TFP polymer** was also subjected to an electrocatalytic study in the presence of oxygen (Fig. 39b, blue curve). Because of the less porous and ordered structure, the amorphous material display neither improvement in the reduction potential and lower reduction current. These results point out the important role of the porous COF structure, which helps the electrolyte to reach the electrochemically active centres.

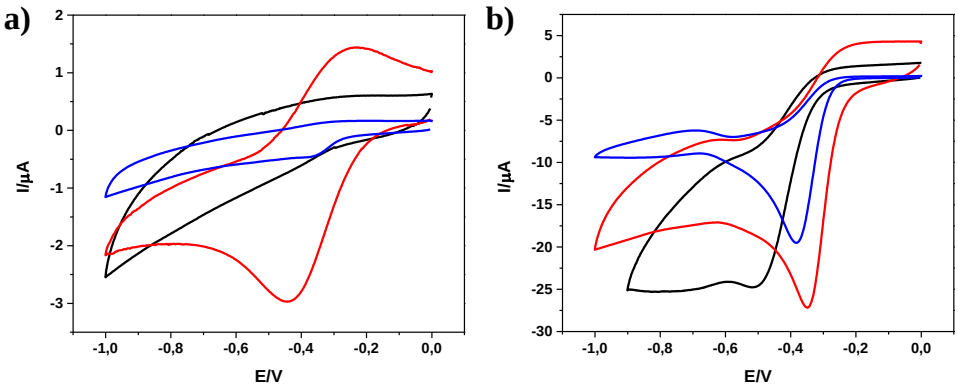

Figure 39. Cyclic voltammograms of GC (black), **DAPT-TFP-COF**/GC (red) and **DAPT-TFP polymer**/GC (blue) in (a) N_2 saturated 0.1 M NaOH solution and (b) O_2 saturated 0.1 M NaOH solution at 10 mV s^{-1}.

Hydrodynamic lineal sweep voltammetry using a rotating Pt/CG ring-disc electrode was used to study the electrocatalytic behaviour of the polymeric materials towards ORR. In the hydrodynamic measurements, the same counter and reference electrode as in the previously described static experiments were employed. For this purpose, a GC disc electrode was modified by drop casting of a **DAPT-TFP-COF** suspension in order to optimize the amount of material deposited on the electrode surface.

As shown in figure 40, increasing amounts of COF material deposited on the electrode up to 0.80 mg cm^{-2} has a positive effect in the ORR activity. However, an excess of **DAPT-TFP-COF** has a negative impact on the ORR, as can be inferred from the current decrease displayed by the electrodes modified with higher amounts of material. This negative effect can be explained by the impediment of the O_2 diffusion.

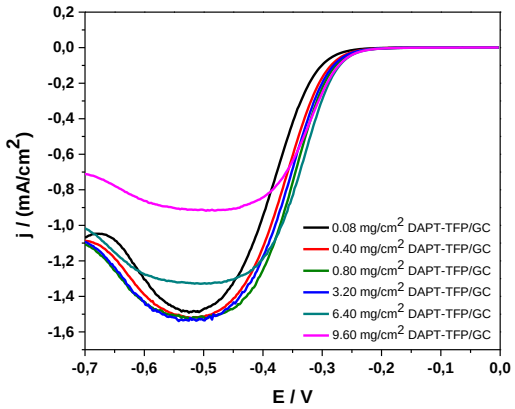

Figure 40. Hydrodynamic lineal sweep voltammetry of different amounts **DAPT-TFP-COF** modified GC rotating electrodes at 1000 RPM at 10 mV s^{-1} in an O_2 saturated 0.1 M NaOH solution.

Thus, a GC electrode modified with 0.80 mg cm^{-2} of **DAPT-TFP-COF** was selected for the following experiments. Then, the electrochemical ORR activity of GC electrode modified with 0.80 mg cm^{-2} of **DAPT-TFP-COF** was compared with bare GC, 10% Pt-C/GC and **DAPT-TFP polymer**/GC electrodes (Fig. 41a). From this comparison, it can be inferred that the onset potential of ORR at **DAPT-TFP-COF**/GC is positively shifted around 60 mV and the diffusion current density enhances around 50 percent respect to the bare GC current. Although this value is still a bit far from that of the 10% Pt-C/GC electrode (green curve) the current density is quite close, what makes **DAPT-TFP-COF**/GC electrode a promising candidate as electrocatalyst in ORR.

It is worth mentioning that **DAPT-TFP-COF** does not content any metals in its structure and, notably, no pyrolysis step is needed. The electrocatalytic activity towards ORR of this electrocatalyst is based on the selection of the appropriate electroactive monomer in the synthesis of the COF. In addition, the ordered and porous structure also play a key role in the material´s electrochemical features. As depicted in figure 41a, the ORR activity is quite remarkable with the COF material while it is not so evident when the amorphous polymer (Fig. 41a, blue curve) is used instead. Furthermore, the onset potential of the polymer is not lowered as much as it is with the COF material.

For the determination of the number of electrons involved in the electrochemical process the hydrodynamic voltammograms at **DAPT-TFP-COF**/GC disc electrode

were recorded at different rotation rates from 100 rpm to 1800 rpm (Fig. 41b) while the Pt ring currents at 0 V *vs.* SCE were registered. The number of electrons involved in the ORR was calculated from equation (3):

$$n = 4\frac{i_D}{i_D + \frac{i_R}{N}} \quad (3)$$

Where *n* is the number of electrons, N is the collection efficiency of the ring (0.37 for the present geometrical arrangement) and i_D and i_R are the measured currents for the disk and ring electrodes, respectively. The number of electrons exchanged during ORR have been plotted versus the potential applied (Fig. 41c). From this plot, the number of electrons exchanged with **DAPT-TFP-COF** is close to 4, suggesting that oxygen is completely transformed into H_2O. A similar result is obtained for the amorphous polymer, which indicates that the nanostructure of the material does not affect the oxygen reduction mechanism. It should be highlighted that at the bare GC electrode the number of electrons involved in the ORR is close to 2. Thus, the modification of GC electrodes with **DAPT-TFP-COF** results on a clear improvement of the ORR.

In order to stablish the **DAPT-TFP-COF** electrocatalyst stability, a constant potential of -0.4 V was applied during 10000 seconds to the **DAPT-TFP-COF**/GC electrode immersed in O_2 saturated 0.1 M NaOH solution with a constant rotation of 1000 RPM. As shown in figure 41d, the reduction current decreases around 20% of its initial value during the first 500 seconds, and then remains almost constant for approximately 10000 seconds. Besides the initial decrease of the current, this result suggests a great stability of the ORR activity.

The morphology of the electrode surface before and after the ORR electrocatalysis for 10000 seconds was studied by SEM (Fig. 42), both displaying similar images, proving the morphology stability despite the long-time operating.

It is also worth mentioning that the material has a strong tolerance to methanol crossover (Fig. 43) overcoming platinum-based ORR electrocatalyst drawback. For decades, this crossover of methanol from the anode to the cathode has led to a significant reduction of the Pt-based electrocatalysts efficiency since they are not selective towards the ORR and therefore they also display catalytic activity towards the methanol oxidation reaction (MOR).[266] In this regard, the design and synthesis

of highly selective electrocatalysts for ORR as **DAPT-TFP-COF** represents an excellent approach for solving the methanol crossover issue in fuel cells.

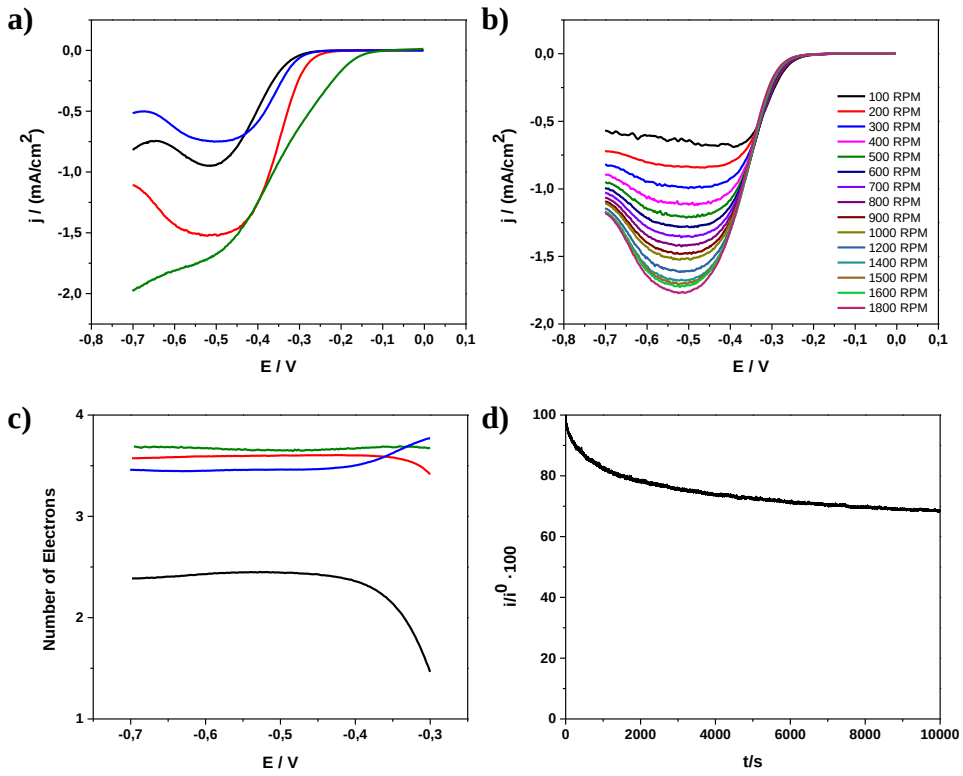

Figure 41. (a) Hydrodynamic linear sweep voltammetry of GC (black), **DAPT-TFP-COF**/GC (red), **DAPT-TFP polymer**/GC (blue) and 10% Pt C/GC (green) electrodes in O_2 saturated 0.1 M NaOH solution at 1000 rpm and 10 mV s^{-1}. (b) Hydrodynamic linear sweep voltammetry of **DAPT-TFP-COF**/GC in O_2 saturated 0.1 M NaOH solution at different rotation rates and 10 mV s^{-1}. (c) Number of electrons calculated for ORR using RRDE at different potentials at 10% Pt C/GC disc electrode (green), bare GC disc electrode (black), **DAPT-TFP-COF**/GC disc electrode (red) and **DAPT-TFP polymer**/GC disc electrode (blue). (d) Current intensity stability of **DAPT-TFP-COF**/GC electrode operating in O_2 saturated 0.1 M NaOH solution at a constant potential (-0.4 V *vs.* SCE).

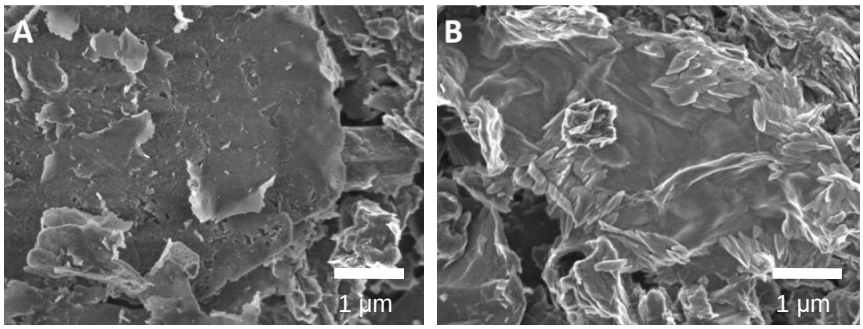

Figure 42. SEM images of **DAPT-TFP-COF**/GC electrode before (a) and after (b) operating for 10000 s in a 0.1 M NaOH O_2 saturated solution at a constant potential of - 0.4 V *vs.* SCE.

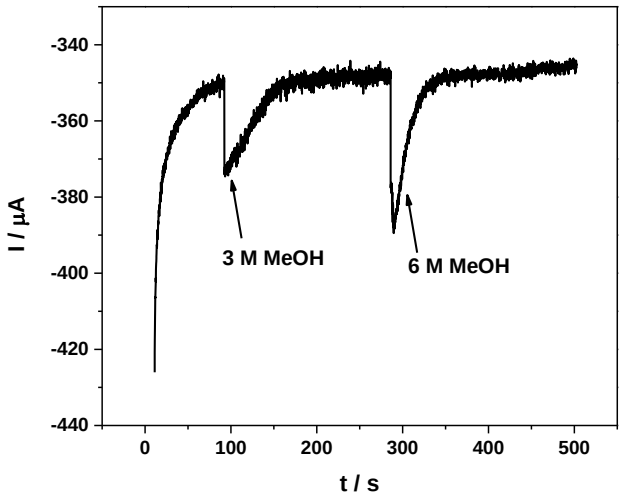

Figure 43. MeOH interference study of **DAPT-TFP-COF**/GC electrode operating at a constant potential (- 0.4 V *vs.* SCE) in an O_2 saturated 0.1 M NaOH solution.

3.2.2 Electrochemical energy storage

Besides the electrocatalytic performance of both materials, **DAPT-TFP polymer** was also evaluated as a potential organic electrode material for battery applications due to its more simple and straightforward synthetic procedure. Therefore, an electrochemical characterization of the polymeric network was performed.

Prior to the electrochemical studies, the chemical stability of **DAPT-TFP polymer** was investigated. Thus, the material was dispersed in 1 M H_2SO_4 for 30 minutes; then, the remaining protons from the acid were neutralized with a basic solution of 1M NaOH. Finally, the solid polymer was separated by filtration and then vacuum-dried at 90 ºC for 12 h. The same procedure was performed for longer times (24 h). As illustrated in figure 44, the PXRD pattern of the material remained unchanged upon treatment in these harsh conditions, indicating high chemical stability in strong acid media. Presumably, this might be due to a synergistic effect of the highly stable enamine linkers together with the high hydrophobicity of the pyrene units.

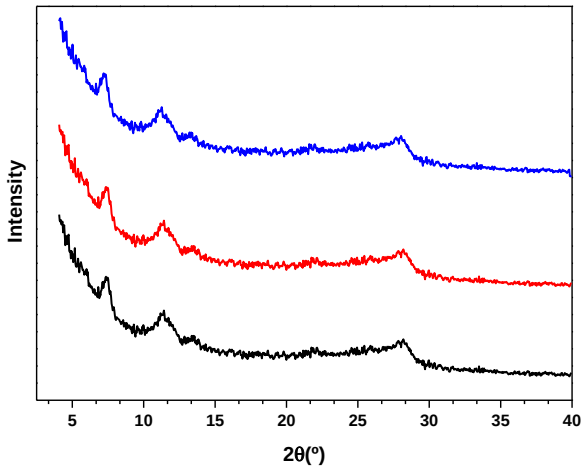

Figure 44. Normalized experimental powder X-ray diffractograms of **DAPT-TFP polymer** as-synthesized (black), after treatment in 1 M H_2SO_4 for 30 minutes (red), after treatment in 1 M H_2SO_4 for 24 h (blue).

To examine the structural and morphological changes of the materials, SEM observation was conducted before and after acid treatment of **DAPT-TFP polymer** (Fig. 45), which did not display any morphological change. Both micrographs exhibit spherical particles of diameter ranging from 90 to 1250 µm.

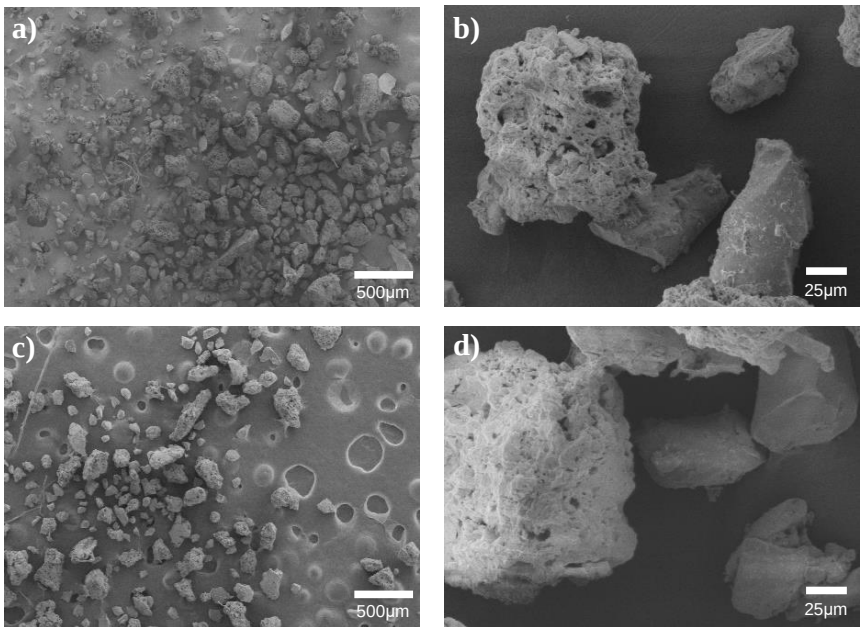

Figure 45. HR-SEM images of **DAPT-TFP polymer** (a,b) as-synthesized and (c,d) after treatment in 1 M H_2SO_4 for 30 minutes.

To gain an insight into the protonation of **DAPT-TFP,** X-ray photoelectron spectroscopy (XPS) of C 1s, N 1s and O 1s was conducted before and after treatment with sulphuric acid (Fig. 46). B. As expected, the C, N and O species are observed, including the Auger lines and probable losses, together with minor peaks due to the sample porter. Comparison of the XPS N1s of both the pristine and the acid treated network (Figure 46a,b) shows a clear emergence of a new component in the treated one with a binding energy of 402.0 eV, matching with a NH^+ group, together with a clearly intensive peak of 400.2 eV assignable to the non-protonated N of the enamine moiety. This value can be assigned to β-ketoenamine linked polymers. Thus, partial protonation of the enamine linkage is observed. On the contrary, XPS O1s peak of both materials remained unaltered, indicating that the carbonyl groups are not protonated. (Fig. 47).

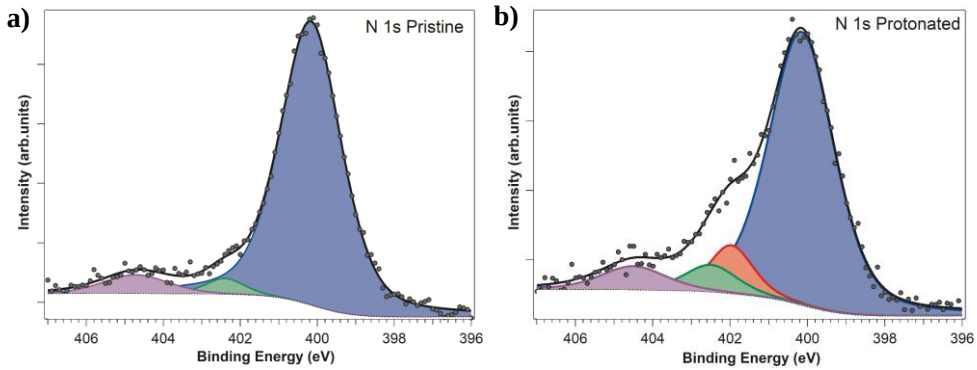

Figure 46. XPS line of the N 1s region before (a) and after (b) acid treatment. Dots are experimental results and the continuous line is a fit. Main components are (C-N) attributable to enamine moieties (blue) and (C-NH^+) from protonated enamine moieties (orange). Minor components are (N-O) (green) and the π-π* loss (violet).

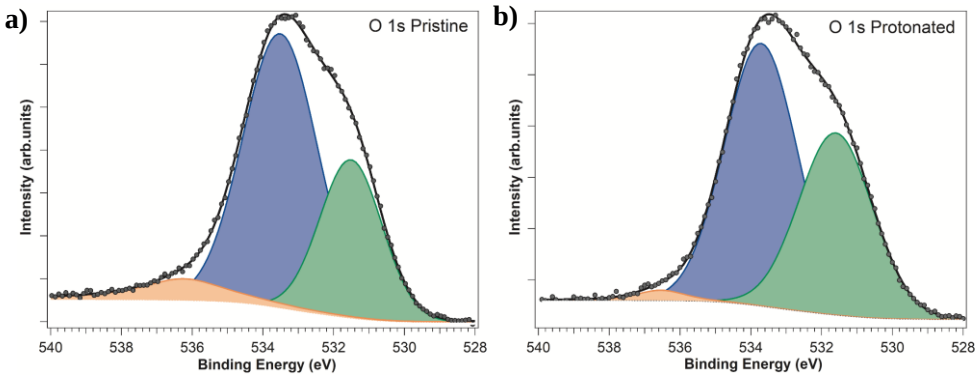

Figure 47. XPS line of the O 1s region before (a) and after (b) acid treatment. Both peaks present the same line shape and components without any significant difference. Dots are experimental results, and the continuous line is a fit. The different components correspond to green (C=O), blue (C-O or OH from adsorbed water), orange (O_2, H_2O chemisorbed).

This protonation of the enamine linkage was also confirmed by FTIR (Fig. 48). Comparison between the FTIR spectra of the pristine and the protonated framework clearly unveils the disappearance of the enamine band at 945 cm^{-1}.

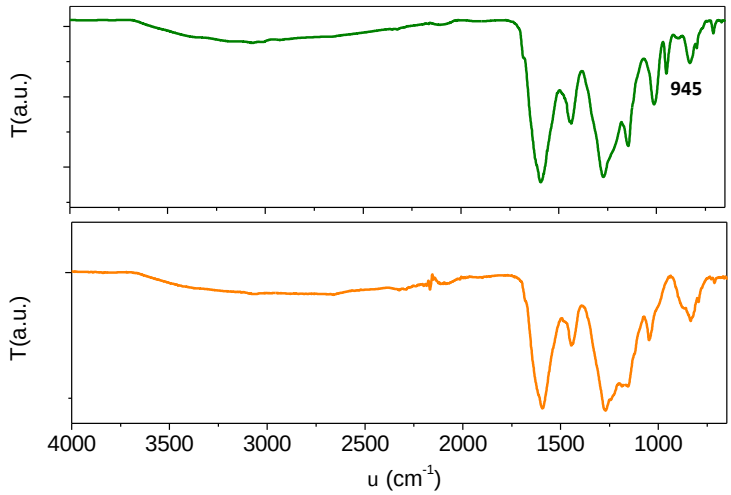

Figure 48. FTIR spectra of pristine **DAPT-TFP polymer** (green) and **DAPT-TFP polymer** after acid treatment (orange).

Encouraged by these results, the electrochemical characterization of **DAPT-TFP polymer** was performed in protic media. Remarkably, once subjected to an acidic treatment, a reversible redox process appeared (Fig. 49a, orange trace) at -0.45 V (vs Ag/AgCl) in neutral aqueous media (0.1 M NaCl). This reversible electrochemical activity (high symmetry and low peak separation, 120 mV) can be attributed to the redox reaction of the quinone groups present in the structure, which exhibit reversible redox reactions and fast kinetics.[267–269] The reversible redox activity of **DAPT-TFP polymer** in neutral aqueous media makes its applicability safer, inexpensive and more environmentally friendly unlike other corrosive or flammable media usually employed for electroactive 2D polymer networks.[188,198,270] It should be also mentioned that the electrochemical characterization of **DAPT-TFP polymer** electrode was performed without using any conductive additive.

The effect of the nature of the supporting salt was further explored. Thus, the effect of the cation on the redox behavior was assessed using different chlorine salts (Fig. 49c). According to the CVs, a clear reduction peak was obtained in a similar potential range (from -0.65 V to -0.5 V vs Ag/AgCl) for all the supporting electrolytes tested. However, the oxidation peak was hardly noticeable in the systems with NH_4Cl and LiCl indicating a poor reversible efficiency. In the case of KCl, a wide and low intense peak was observed. Among the different electrolytes under study, the NaCl-based system showed the highest reversibility with similar

anodic and cathodic current intensity peaks and lowest peak separation (Table 1). This behavior can be explained considering the radius of the different cations and their ability to stabilize the charge. The cations size can be ordered as follows: $NH_4^+ > K^+ > Na^+ > Li^+$.[271]

Table 1. Potential values and parameters extracted from CV characterization.

Supporting salt	Ea (V)	Ec (V)	ΔE(V)	$Ep_{½}$ (V)
LiCl	-0.611	-0.191	0.420	-0.401
NaCl	-0.501	-0.274	0.227	-0.387
KCl	-0.567	-0.130	0.437	-0.348
NH_4Cl	-0.656	-0.119	0.537	-0.387
NaF	-0.750	-0.216	0.534	-0.483
Na_2SO_4	-0.577	-0.431	0.146	-0.503

The ammonium cation is the one with largest size and, therefore, its mobility could be hampered, which can cause an increase in the polarization (large peak separation) of the electrochemical response. In contrast, lithium cation is the smallest one in the selected salts, so a high diffusion ability for charge stabilization could be expected. Nevertheless, the Li^+ is a hard cation so it will be strongly solvated by water molecules. Thus, it behaves as an ion with an effectively larger radius. In addition to the size effect, cations in the protic electrolyte can also stabilize quinone anions *via* coulombic ion pairing, which may further affect the driving force for metal-ion complexation. In this sense, lithium cation has demonstrated a high coordination with quinone groups forming stable adducts, which affects the oxidation reaction.[272] Thus, the electrochemical reversibility was not favored by lithium behavior. The binding energy of sodium cation and quinone anions is lower (≈15%) than for Li^+ which can contribute to the charge stabilization without compromising subsequent redox activity.[273] Regarding these considerations, Na^+ displayed the highest adaptability to the hollow space in the polymer network in terms of size and charge stabilization.

The influence of the anion of the supporting salt on the redox activity of **DAPT-TFP** was also evaluated. The following sodium-based salts were selected: NaF, NaCl and Na_2SO_4. The anion effect on the electrochemical behavior of **DAPT-TFP**

is represented in Figure 49d. The most remarkable difference between the three different systems was the presence of a high intense current peaks in the CV of NaCl in comparison with the other two. The CV based on NaF electrolyte exhibited large peak separation and low reversibility. This fact might be due to the low electrochemical stability of fluorine ions and to its polar kosmotropic character, which results in high interaction with water molecules. Thus, immobilized water molecules are attached to the ion, decreasing the mobility of nearby water molecules and increasing the polarization in that media. Regarding the behavior of the Na_2SO_4 system, it should be pointed out that it was the one with the lowest separation peaks; however, the significantly lower current compared to NaCl system made it uninteresting. These results point out the importance of the supporting salt in the electrochemical properties of **DAPT-TFP polymer**.

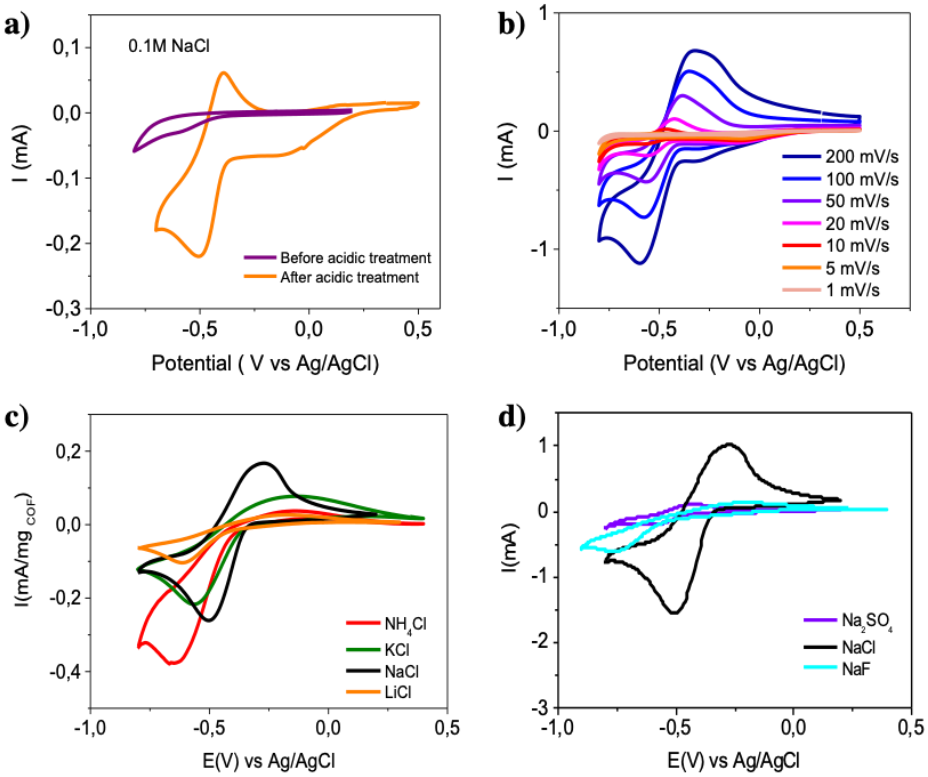

Figure 49. (a) Cyclic Voltammetry (CV) of **DAPT-TFP polymer** electrode in 0.1M NaCl aqueous electrolyte solution at 10 mV s^{-1} before and after acidic treatment (purple and orange lines). (b) CV at different scan rates illustrates the fast charge kinetics of the redox process. (c,d) Effect of cation and anion from supporting electrolytes on the electrochemistry of the 2D polymer.

Finally, the electrochemical characterization of the monomers was carried out by cyclic voltammetry in a three-electrode cell configuration. Thus, it was further confirmed that the redox activity of **DAPT-TFP polymer** could not be attributed to the independent reversible electrochemical activity of the synthesized 2,7-diaminopyrene-4,5,9,10-tetraone (**DAPT**) and pyrene-4,5,9,10-tetraone (**PTO**) monomers (Fig. 50).

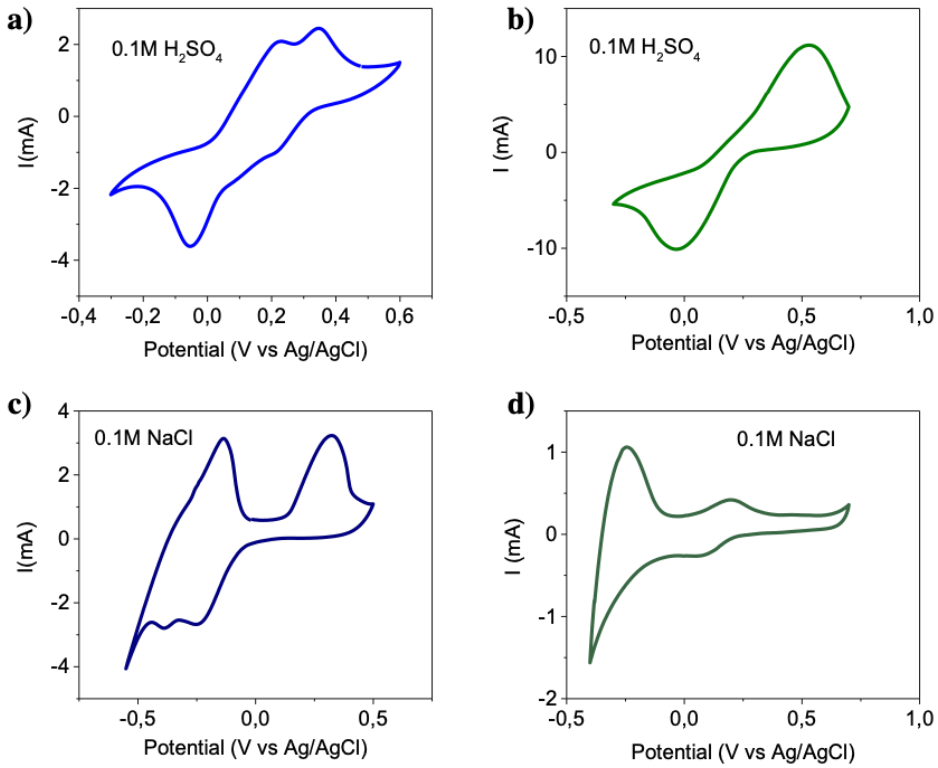

Figure 50. Electrochemical characterization of the monomers utilized in the preparation of the **DAPT-TFP polymer**. (a) CV of pyrene-4,5,9,10-tetraone in 0.1 M H_2SO_4; (b) CV of 2,7-diaminopyrene-4,5,9,10-tetraone in 0.1 M H_2SO_4; (c) CV of pyrene-4,5,9,10-tetraone in 0.1M NaCl; d) CV of 2,7-diaminopyrene-4,5,9,10-tetraone in 0.1 M NaCl.

3.3 Conclusions

In this chapter, a novel 2D COF (**DAPT-TFP-COF**) has been successfully designed and synthesized, incorporating highly electroactive pyrene-4,5,9,10-tetraone (**PTO**) units within the framework. The as-obtained material has been

tested as electrocatalyst towards ORR, and the influence of porosity and crystallinity on the material´s performance has been demonstrated by comparison with an analogous amorphous material with the same chemical composition (**DAPT-TFP polymer**).

Besides the successful electrocatalytic application of **DAPT-TFP-COF** towards oxygen reduction, it is worth mentioning that the polymeric network was directly used without adding any metal or conductive supporting material, and also avoiding any additional carbonization step. The promising results herein described suggest that the electrochemical features of COFs can be significantly improved by the optimal design of its electroactive monomers, which will favor the progress and development of novel low-cost and highly active COFs for the next generation organic electrocatalyst in energy conversion.

In addition, an electrochemical study of the as-prepared **DAPT-TFP polymer** has been performed, evidencing a reversible electrochemical activity of the material at neutral pH without conducting additives after a simple activation treatment. This allows the potential application of **DAPT-TFP polymer** as a low-cost organic electrode material in safer and environmentally friendly electrochemical energy storage devices. This study unrolls stimulating possibilities of developing new electrode materials for energy storage devices by applying low-cost methods to a large family of low-dimensional porous polymers exhibiting poor or non-electroactive properties. Therefore, with these polymeric materials in hand, further studies on the application of **DAPT-TFP-COF** in the battery field are currently in progress.

Chapter 4:

Novel Covalent Triazine Frameworks (CTFs) as effective electrode materials for supercapacitors

4.1 Introduction

In the last years, two-dimensional Covalent Triazine Frameworks (CTFs) have received increasing attention because of the unique structure of the triazine units, which endows CTFs with high thermal and chemical stability, high intrinsic nitrogen content and permanent porosity.[274] Based on these unique features, CTFs have shown great potential in energy storage and conversion due to their intrinsically strong conjugated structure, delocalized electron structure and rich active sites content. Therefore, CTFs have been selected as potential candidates for the development of new organic electrodes in supercapacitors. The design of enlarged π-conjugated skeletons can readily improve the conductivity and electrochemical performance of the framework.[159] The combination of this feature with the readily conversion of CTFs into N-doped microporous carbon materials with large specific surface area (SSA) can pave the way for the development of brilliant electrode materials.[275]

Different synthetic methods have been reported for the preparation of CTFs, all synthesized from a wide range of monomers endowing specific functional groups. The most extended approach involves the trimerization of aromatic nitriles under suitable reaction conditions to obtain triazine units, as firstly reported by Thomas and co-workers.[49] Molten $ZnCl_2$, which is a Lewis acid in nature, has been commonly used as the catalyst of the reaction, since at high temperatures can act as ionic liquids dissolving the aromatic monomers.[276] Varying the amount of catalyst employed as well as increasing the reaction temperature can lead to an increase in the specific surface area and porosity of the framework, but it also results in the formation of extended amorphous structures. A wide variety of protocols have been developed in order to overcome this issue, including the addition of a salt template during the polymerization reaction,[277] the development of milder MW-assisted ionothermal synthesis[278,279] or the use of different catalysts including CF_3SO_3H in $CHCl_3$.[280,281] A recently reported procedure, described by Baek and co-workers, also allows the trimerization either of aromatic nitriles or aromatic amides into *s*-triazine rings catalysed by P_2O_5.[282]

However, most reported CTFs are amorphous or slightly crystalline due to the relatively low reversibility of the trimerization reaction of nitrile groups into triazine units, making it difficult to form ordered structures. Therefore, new synthetic procedures to improve the crystallinity of these type of materials are

required. In fact, crystallinity can improve charge transport in the framework and is beneficial to the photoelectric properties of the material, as it has been demonstrated in their analogues COF polymers.[283]

Therefore, in this chapter the preparation of two crystalline microporous CTFs (**Py-CTF** and **TPE-CTF**) is described. Firstly, the synthesis of two different aromatic scaffolds based on pyrene and tetraphenylethene moieties functionalized with aromatic nitriles and amides, respectively, and their further trimerization into *s*-triazine rings in a condensation reaction catalysed by P_2O_5 will be addressed. Additionally, the electrochemical performance of these carbon-based materials will be evaluated for tailored energy-related applications. To that end, the thermal conversion of the CTFs by carbonization will be detailed, and the electrodes with the synthesized materials will be evaluated by means of cyclic voltammetry in three electrode cell configuration. To gain insight into the specific capacitance of the materials, different aqueous electrolytes will be explored, in order to select the best active material/ electrolyte match.

4.2 Results and discussion

In order to ascertain different possible aromatic cores to the development of the π-conjugated backbone of the framework, two CTFs have been designed: **Py-CTF** (Fig. 51a), a CTF endowed with pyrene moieties within its skeleton; and **TPE-CTF** (Fig. 51b), a CTF based on tetraphenylethene moieties and grafted with pendant nitrile units in its pores.

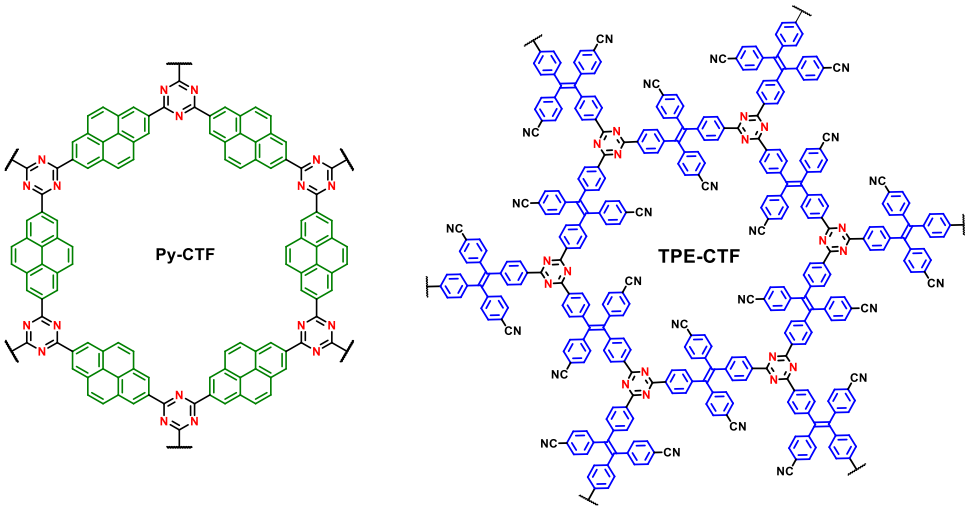

Figure 51. Structures of (a) **Py-CTF** and (b) **TPE-CTF**.

4.2.1 Synthesis and characterization of Py-CTF

For the design of the first CTF, pyrene moieties were selected since several pyrene-based polymers/composites have been widely studied and applied for efficient energy storage applications.[284–289]

To date, some amorphous pyrene-containing CTFs have been described in the literature.[287] However, they display poor crystallinity and low surface areas, which limit their practical application. Therefore, great efforts have been devoted to designing novel synthetic procedures. In this chapter, a modified synthetic protocol has been explored for the preparation of the reported CTFs. It is worth mentioning that the synthetic work described below has led to the formation of a crystalline pyrene-based microporous network, which increases the potential for further applications of this material as supercapacitor electrode in a real device.

Prior to the synthesis of the polymeric scaffold, the 2,7-functionalized pyrene monomer (**7**) was obtained. Synthesis of 2,7-pyrenesubstituted derivatives is usually challenging due to the presence of nodal planes in both the HOMO and the LUMO lying perpendicular to the molecule and through the 2- and 7- positions (Fig. 52).[290] For this reason, direct electrophilic aromatic substitution reactions take only place at the 1-, 3-, 6- and 8-carbon positions, while reactions at the 2- and

7- positions only occur when using $AlCl_3$ and *t*BuCl due to the big steric hindrance at the normal 1-, 3-, 6- and 8-carbon positions.[290]

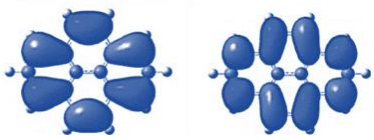

Figure 52. HOMO and LUMO of pyrene. Adapted from reference 290.

Thus, in this work 4-, 5-, 9- and 10- substituted pyrene monomer was firstly synthesized to orientate the subsequent reactions at the desired 2- and 7- positions, since it has been widely described in the literature the homolytic C-O bond cleavage that takes place at the reaction conditions of the ionothermal synthesis.[291,292] Moreover, aromatic methoxy groups become highly reactive in the temperature range of 400–450°C, so the C-O bond become prone to be cleaved easily in this protocol,[293] allowing the preparation of the targeted CTF endowed with bare pyrene units.

For the preparation of monomer **7**, the synthetic route shown in scheme 6 was followed.

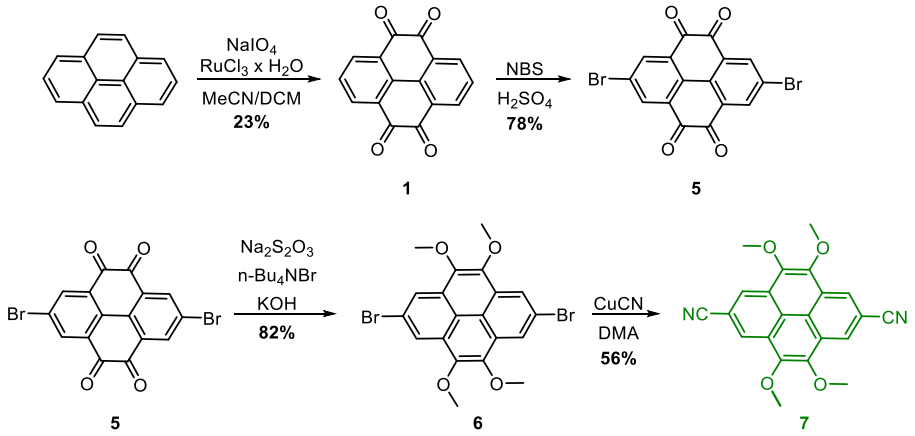

Scheme 6. Pyrene-derivative **7** synthetic route.

Starting from commercially available pyrene, an oxidation reaction using $NaIO_4$ and $RuCl_3 \cdot H_2O$ yielded pyrene-4,5,9,10-tetraone (**1**). A subsequent bromination in the 2, 7-positions using *N*-bromosuccinimide in sulfuric acid afforded compound **5 (**2,7-dibromopyrene-4,5,9,10-tetraone) in a 78% yield. Afterwards, cyanation reaction was performed from the soluble and reactive tetramethyl derivative **6**. Carbonyl groups of compound **5** were protected into methyl ether groups by a reductive alkylation using $Na_2S_2O_4$ and dimethyl sulfate affording compound **6** (82%). In a subsequent step, a Rosenmund-von Braun reaction was carried out with CuCN in DMA, yielding the desired monomer 2,7-dicyano-4,5,9,10-tetramethoxypyrene (**7**) in 56% yield. Compound **7** was readily used for the ionothermal synthesis of **Py-CTF**.

Scheme 7 illustrates the synthesis of **Py-CTF** from the trimerization into *s*-triazine rings of monomer **7** under ionothermal conditions using P_2O_5. According to the literature, P_2O_5 has shown excellent results in the dehydration reaction of amides into nitriles,[294] and it has also been reported the subsequent trimerization of nitriles to *s*-triazine rings in a condensation reaction.[282] Remarkably, it has been proved that both aromatic amide and nitrile functionalized monomers are readily available to synthesize CTFs when P_2O_5 is used as the catalyst of the reaction, and a few examples habe been reported in the literature.[282] The introduction of slight modifications in the synthetic protocol allowed the synthesis of **Py-CTF** as a crystalline microporous network. Therefore, the reaction time was around 12 hours at 400 ℃. The temperature was slowly increased to 400 ℃ at a ramping rate of 2 ℃ min^{-1}, holding 2 hours every 80 ℃ increase. After the reaction time, the temperature was slowly decreased to room temperature at a ramping rate of 5 ℃ min^{-1}.

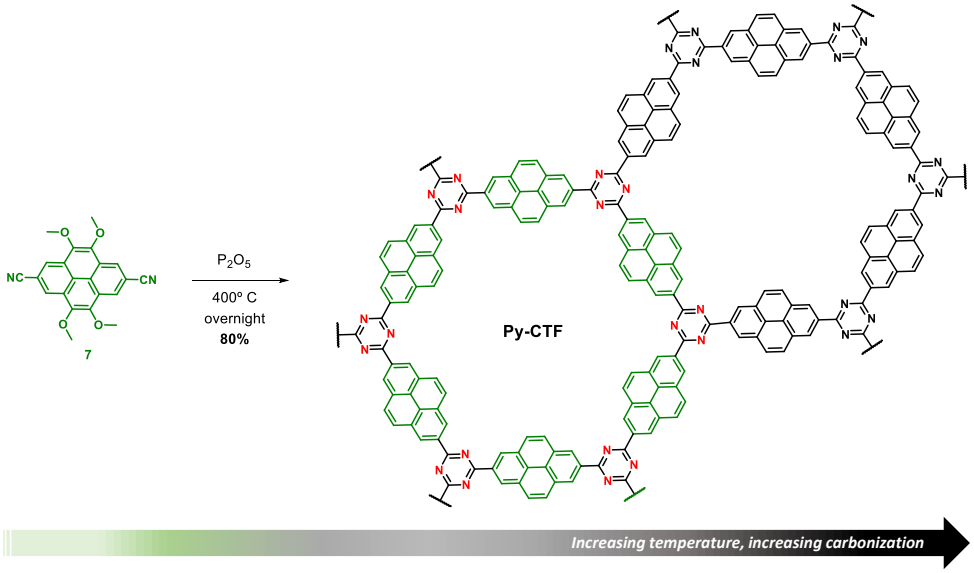

Scheme 7. Schematic representation of the synthesis of **Py-CTF** at 400 ºC, which leads to partial carbonization and partial decomposition of the idealized network structure.

After the cyclotrimerization reaction, the reaction cap was carefully opened and the resulting precipitate was filtered off and washed exhaustively with water to remove unreacted P_2O_5. The product was then washed with dimethyl sulfoxide and methanol, and further subjected to Soxhlet extraction with THF and dried under vacuum at 120 ºC affording **Py-CTF** as a bright dark solid (80%).

The obtained **Py-CTF** powder was analysed by FTIR spectroscopy (Fig. 53a). The characteristic *s*-triazine stretching vibrations can be observed at 1554, 1135 and 1042 cm^{-1}, indicating the successful of the triazine rings formation in the macromolecular network structure. Remarkably, the diagnostic stretching vibration of the methoxy groups of monomer **7** at 2949, 2920 and 2851 cm^{-1} are not present in the FTIR spectrum, confirming the homolytic C-O bond cleavage as a result of the ionothermal protocol used for the synthesis of the material.[291,292]

The successful formation of the triazine rings was further investigated by solid state ^{13}C-CP/MAS-NMR spectroscopy. However, only a broad signal centred at ~130 ppm could be observed, corresponding to the carbon aromatic framework (Fig. 53b). Such a broad signal without high resolution has been previously described for other similar materials such as porous organic polymers,[295] graphite oxide,[296] graphene nanosheets[297] or MWCNTs[298].

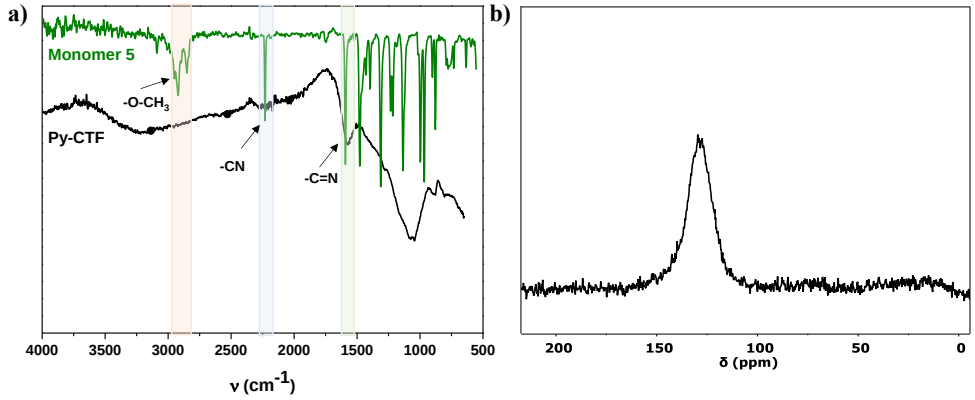

Figure 53. (a) Comparative FTIR spectra of **Py-CTF** (black) and monomer **5** (green); (b) ^{13}C-CP/MAS-NMR spectrum of **Py-CTF**.

Moreover, the formation of a crystalline network was confirmed by PXRD and in silico experiments carried out using the Gaussian09[299] and CASTEP[300] software packages. Extended structure based on a hexagonal lattice network was simulated and two structural models, the eclipsed stacking (AA) and the staggered stacking (AB) were modelled. The experimental PXRD pattern of **Py-CTF** shows an intense reflection at 3.85º, corresponding to the (100) Bragg peak, which is in good agreement with the PXRD pattern of the AA-stacking model, which depicts an intense peak at 3.70 º (Fig. 54). Computational modelling also reveals an interlayer distance of 3.66 Å for the AA eclipsed stacking.

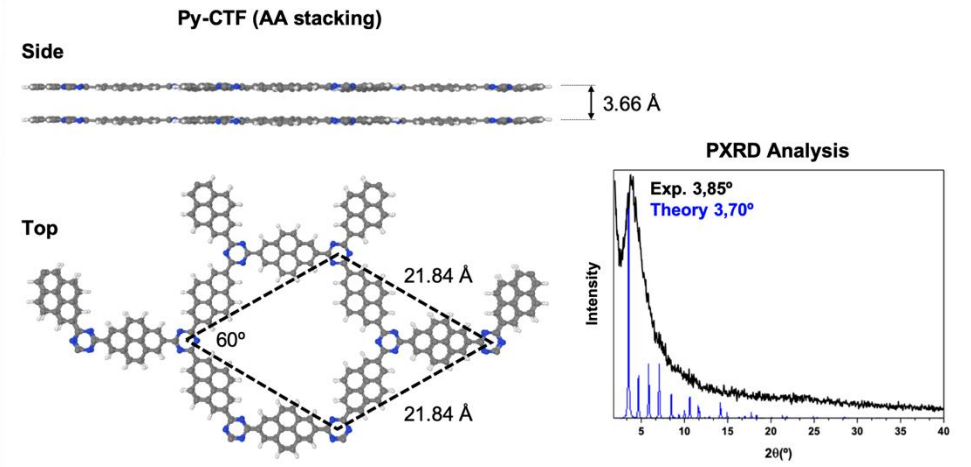

Figure 54. Space filling modelled structure of **Py-CTF** in the eclipsed AA stacking mode (side and top view) and PXRD analysis of **Py-CTF**: experimental (black) and simulated using AA stacking mode (blue).

To study the porosity of the sample, N_2 sorption isotherms at 77 K were analysed (Fig. 55a). **Py-CTF** exhibits a type I isotherm behaviour, typical for microporous materials, with a pore size distribution centred at 1.6 nm (Fig. 55a inset) calculated by non-local density functional theory (NLDFT). A BET surface area of 1385 $m^2 g^{-1}$ and a total pore volume of 0.64 $cm^3 g^{-1}$ were obtained.

Finally, TGA analysis of **Py-CTF** shows a negligible weight loss at temperatures below 900º C (the weight loss remains within 80%, Fig. 55b). The strikingly high thermal stability of the material could be probably due to the high degree of crystallinity of the framework, displaying a rigid 2D extended framework.

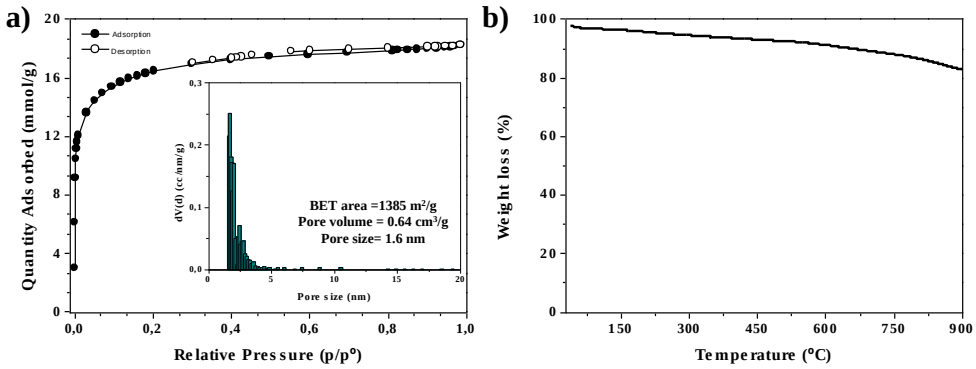

Figure 55. (a) N_2 sorption isotherms for **Py-CTF** (Inset: pore size distribution); (b) TGA of **Py-CTF**.

4.2.2 Synthesis and characterization of TPE-CTF

The successful of the previously described synthesis paved the way to extend this ionothermal protocol for preparing new crystalline tetraphenylethylene-based CTFs, since few examples of TPE-based polymers have been recently explored for direct supercapacitor applications.[301,302] Despite the fact that several TPE-based CTFs have been previously reported in the literature, they are commonly described as amorphous networks which lack any degree of long-range order.[280,303–307]

In this chapter, tetraphenylethylene units were successfully incorporated into a crystalline CTF by using tetrakiscarboxamide-tetraphenylethene (**TA-TPE**) as the building block. In this case, aromatic amide groups were selected as reactive groups since, as stated above, both aromatic amide and nitrile compounds can be used for

the preparation of CTFs using P_2O_5. In this way, the slight modification of the ionothermal method described before could be also extended to a different starting monomer, proving the success of the revised protocol. The synthetic route pursued for the synthesis of **TA-TPE** monomer is illustrated in scheme 8.

TA-TPE was isolated by bromination of commercially available TPE, subsequent halide for cyanide exchange in a Rosenmund-von Braum reaction followed by basic hydrolysis of the resulting tetrakisbenzonitrile and final tetrakiscarboxamide formation by condensation of the carboxylic acids with ammonium hydroxide.

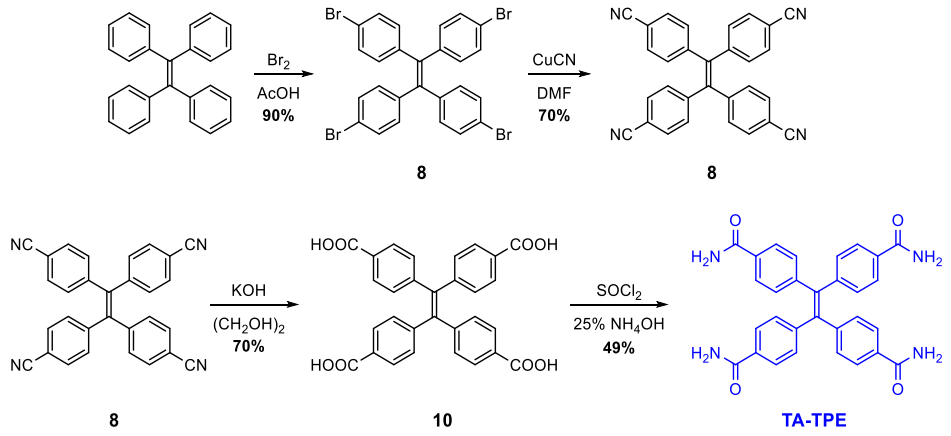

Scheme 8. Monomer **TA-TPE** synthetic route.

Polymeric **TPE-CTF** was synthetized by the direct condensation of the aromatic primary amide groups of the monomer **TA-TPE** into triazine rings (Scheme 9), using P_2O_5 as the catalyst. Remarkably, only the amide groups located in *trans* were involved in the reaction, affording the successful formation of a crystalline polymeric network bearing unreacted pendant nitrile groups in the pore of the framework. Allegedly, since two reactions are involved in this protocol (dehydration of amide groups into nitrile units and consequent trimerization of nitriles to *s*-triazine rings), the crystalline thermodynamic product **TPE-CTF** is prone to be formed in time over other amorphous networks in which the four amide groups undergo the condensation reaction. This supports previous findings in the literature, including the solvent-influenced crystallization chemistry described by Loh and co-workers, who demonstrated that unexpected COF frameworks with

unreacted linker groups within the pores can be obtained by tuning the reaction conditions.[308]

After the cyclotrimerization reaction, the sealed vessel was opened and the obtained precipitate was filtered and thoroughly washed with water to remove unreacted P_2O_5. The product was subsequently washed with dimethyl sulfoxide and methanol, followed by a final Soxhlet extraction with THF for 2 days. Finally, the product was dried under vacuum at 120 °C overnight affording **TPE-CTF** (85%) as a bright dark solid.

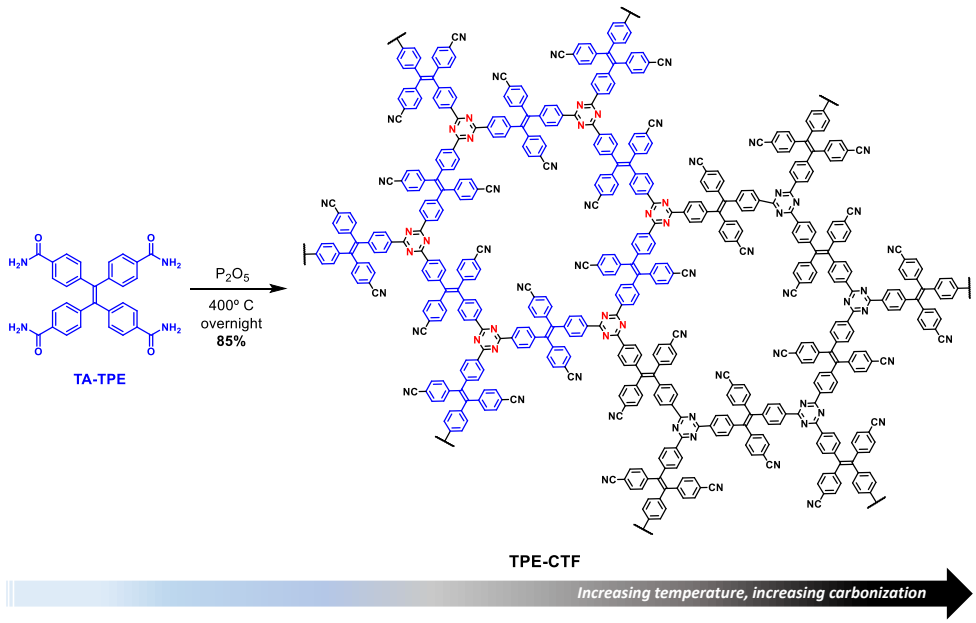

Scheme 9. Schematic representation of the synthesis of **TPE-CTF** at 400 ºC, which leads to partial carbonization and partial decomposition of the idealized network structure.

FTIR spectroscopy analysis unveils the emergence of the characteristic *s*-triazine stretching vibration at 1593, 1398 and 988 cm^{-1}. In addition, the disappearance of the amide-related signals from the monomer **TA-TPE** at 1652, 1603 and 1552 cm^{-1} confirms the successful trimerization of the amide groups into *s*-triazine rings. Furthermore, the emergence peak at 2221 cm^{-1}, characteristic of the -CN bond, indicates the presence of the pendant nitrile groups in the pores of the CTF (Fig. 56a).

As for **Py-CTF** sample, solid state ^{13}C-CP/MAS-NMR spectrum of **TPE-CTF** shows a broad signal centred at ~130 ppm corresponding to the carbon aromatic framework (Fig. 56b). An additional signal at 113.2 ppm was assigned to the carbon from the nitrile groups.

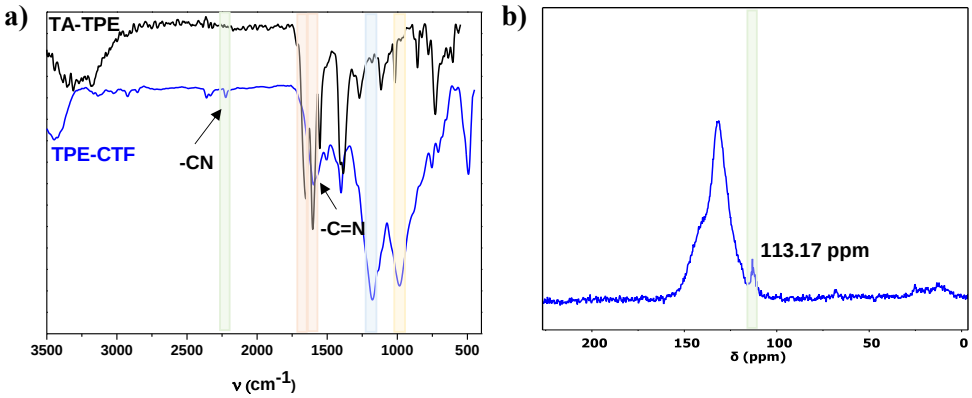

Figure 56. (a) FTIR spectra of **TA-TPE** monomer (black) and **TPE-CTF** (blue); (b) ^{13}C-CP/MAS-NMR spectrum of **TPE-CTF**.

The polymerization into a crystalline network was confirmed by PXRD and further simulation studies performed using the Gaussian09[299] and CASTEP[300] software packages. The PXRD pattern displays broad but intense diffraction peaks (Fig. 57) at 3.82º and 24.03º, suggesting the formation of a network with hexagonal packing pores. The peak at 3.82º could be assigned to the (100) facet, while the broad peak at 24.03º can be ascribed to the interlayer distance between stacked layers, (001) facet. Extended structure based on the hexagonal lattice was simulated and two structural models, the eclipsed stacking (AA) and the staggered stacking (AB) were modelled. The experimental powder profile is in best agreement with the AA-stacking model (Fig. 57), with an interlayer distance of 3.64 Å. DFT calculations also indicate a non-planar disposition of the CTF layers with the benzene units within the pores of the framework twisted against each other to minimize the steric repulsions.

The porosity of **TPE-CTF** was studied by N_2 sorption isotherms at 77 K (Fig. 58a), from which a BET surface area of 500 $m^2 g^{-1}$ and a total pore volume of 0.24 $cm^3 g^{-1}$ were acquired. **TPE-CTF** exhibits a type I isotherm as expected for a microporous material, with a pore size distribution centred at 1.8 nm, calculated by NLDFT (Fig. 58a inset).

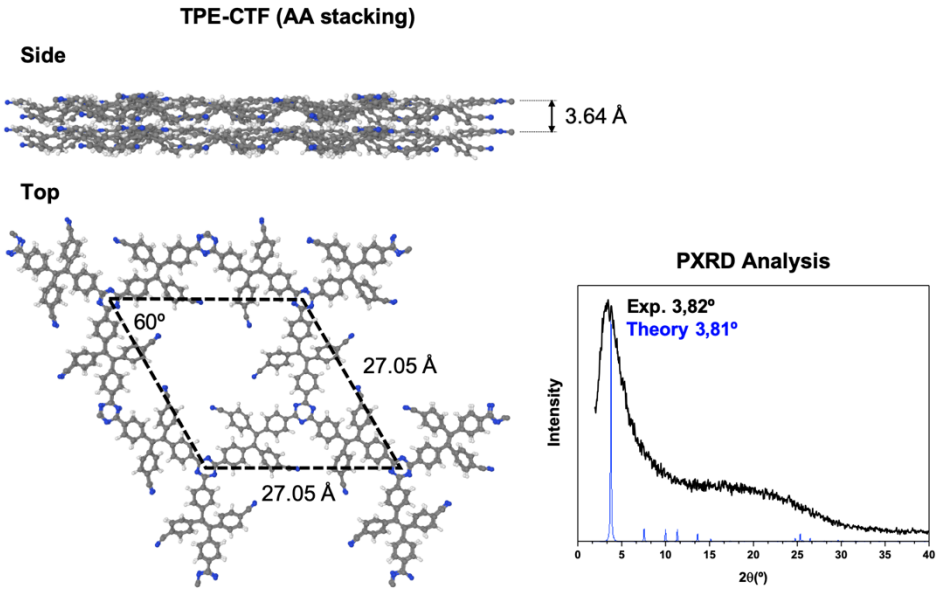

Figure 57. Space filling modelled structure of **TPE-CTF** in the eclipsed AA stacking mode (side and top view) and PXRD analysis of **TPE-CTF**: experimental (black) and simulated using AA stacking mode (blue).

Finally, the thermal stability of **TPE-CTF** was investigated by thermogravimetric analysis (TGA) revealing that the material is highly stable (the weight loss remains within 70% up to 900 °C, Fig. 58b).

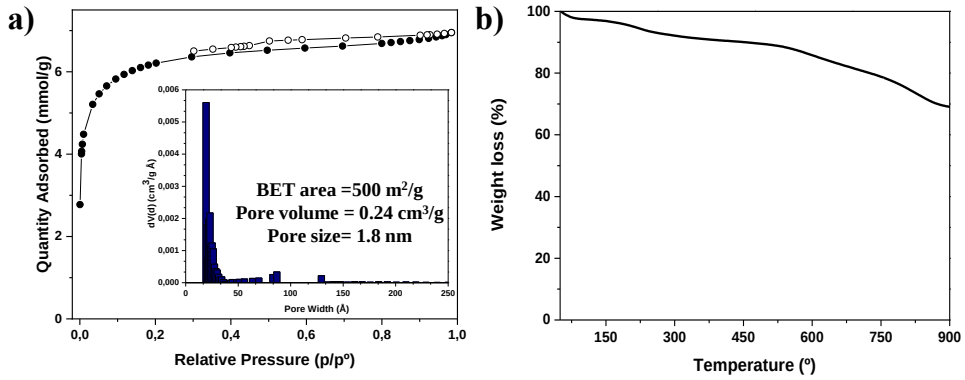

Figure 58. (a) N_2 sorption isotherms of **TPE-CTF** (Inset: pore size distribution); (b) TGA of **TPE-CTF**.

4.2.3 Preparation and characterization of the carbonized CTFs

The as-synthesized CTFs were further subjected to high-temperature treatment at 900º C for 1 h (heating rate of 10º C min^{-1}) under an inert atmosphere of argon. The resulting porous CTF-based carbon nanostructures were denoted as **Py-CTF$_{900}$** and **TPE-CTF$_{900}$**, respectively. On increasing the temperature, the PXRD pattern of the carbonized materials show a significant decrease of the full-width at half-maximum (fwhm) and the peaks become sharper (Fig. 59a, 60a). Notably, the comparative PXRD patterns of the pristine and the thermally treated **TPE-CTF$_{900}$** shows a considerable shift of the peak at 3.8º to a higher angle value (Fig. 60a). These findings indicate an increased graphite crystallite size,[309] supporting that the thermal treatment does not destroy the crystallinity of the framework but contributes to reduce any possible defect on the extended network.

In the comparative FTIR spectra of the **Py-CTF$_{900}$** and **TPE-CTF$_{900}$** powders any characteristic IR band could be identified, suggesting the formation of carbonaceous materials (Fig. 59b and 60b). Therefore, these CTF precursors could serve as promising carbon templates for the preparation of carbon-based materials with intrinsic hierarchical porosity predetermined by the pore size of the pristine COF.

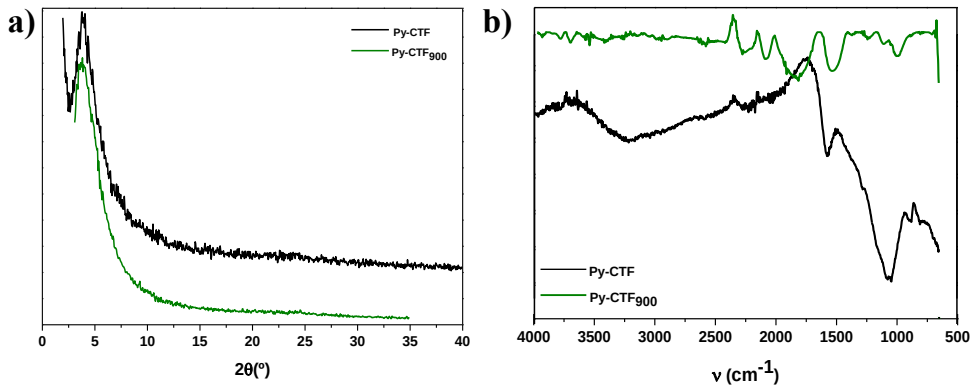

Figure 59. (a) PXRD pattern of **Py-CTF** (black) and **Py-CTF$_{900}$** (green); (b) FTIR spectra of **Py-CTF** (black) and **Py-CTF$_{900}$** (green).

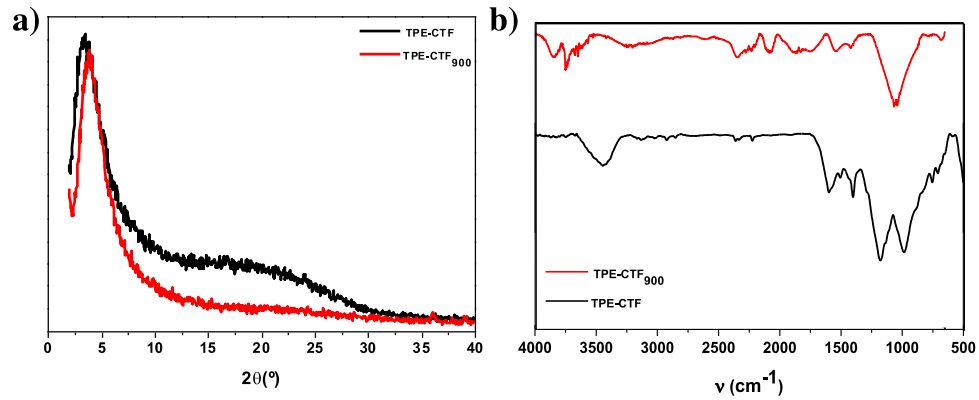

Figure 60. (a) PXRD pattern of **TPE-CTF** (black) and **TPE-CTF$_{900}$** (red); **(**b) FTIR spectra of **TPE-CTF** (black) and **TPE-CTF$_{900}$** (red).

To examine the morphological changes of the materials after the carbonization process, SEM observations were conducted before and after the carbonization of **Py-CTF** and **TPE-CTF (**Fig. 61 and Fig. 62, respectively). While **TPE-CTF** sample consists mostly of spherical particles of diameter ranging from 90 to 150 nm, laminar micrometric structures have been found in major proportion for **Py-CTF** sample. Remarkably, no morphological changes were observed after the carbonization, suggesting a great structural robustness of the COF frameworks in agreement with the results obtained by X ray powder diffraction.

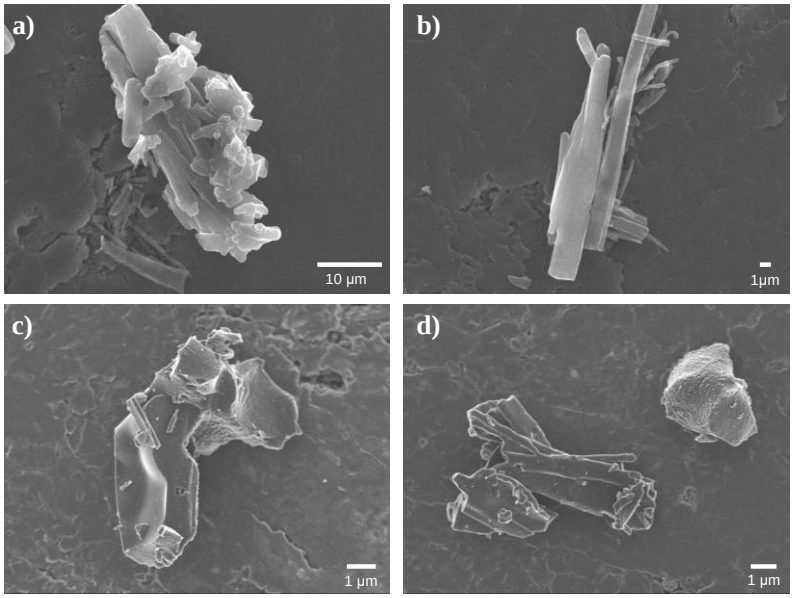

Figure 61. SEM photographs of (a,b) **Py-CTF** and (c,d) **Py-CTF$_{900}$**.

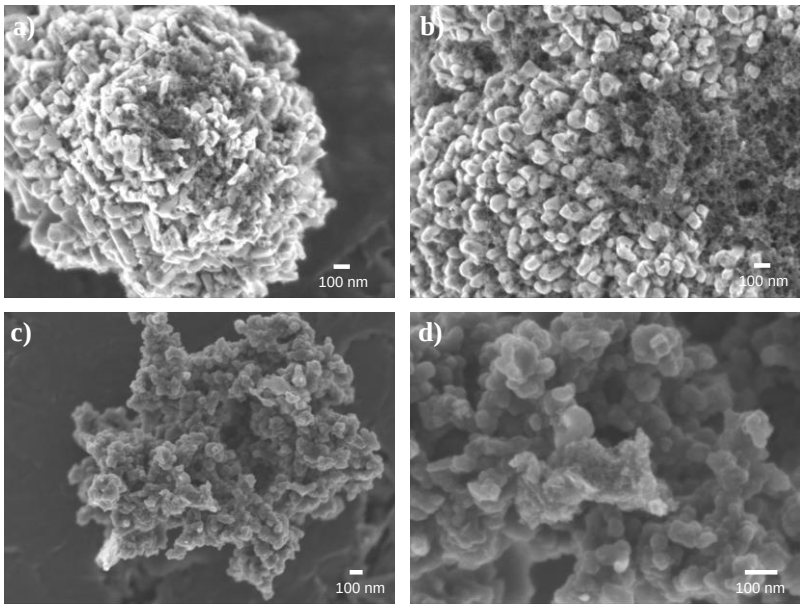

Figure 62. SEM images of (a,b) **TPE-CTF** and (c,d) **TPE-CTF$_{900}$**.

4.2.4 Electrochemical performance for supercapacitor applications

The electrochemical performance of **Py-CTF** and **TPE-CTF** before and after carbonization at 900 ºC was further investigated in order to elucidate the effect of the thermal treatment on the capacitive properties of the materials. Thus, cyclic voltammetry (CV) measurements were performed in a conventional three-electrode cell using a glassy carbon rod as working electrode, where the materials were deposited as thin films; platinum wire was used as counter electrode with an Ag/AgCl electrode as reference.

a) Electrochemical characterization of Py-CTF

Firstly, different electrolytes were explored in order to select the best active material/ electrolyte match in terms of the specific capacitance values. Therefore, H_2SO_4 1 M and LiCl 1 M solutions were tested as acid and neutral electrolyte, respectively. Figure 63 displays the CV curves of the potential window between -2 and 1.25 V for LiCl 1 M and -1.35 and 0.95 V for H_2SO_4 1 M. The sweep rates

of 5 mV s^{-1}, 20 mV s^{-1} and 100 mV s^{-1} were used to evaluate the working electrode. Due to the presence of the triazine moieties, two redox peaks can be observed at approximately -1-0 V in LiCl and at -0.5-0.5 V in H_2SO_4 electrolyte, both acquired during the anodic and cathodic scan. This can be ascribed to the reversible oxidation-reduction process of the electrochemically active polymeric framework, which is further evidenced by the good symmetry of the CV curves even at higher scan rates. This behaviour could possibly indicate pseudocapacitive characteristics.

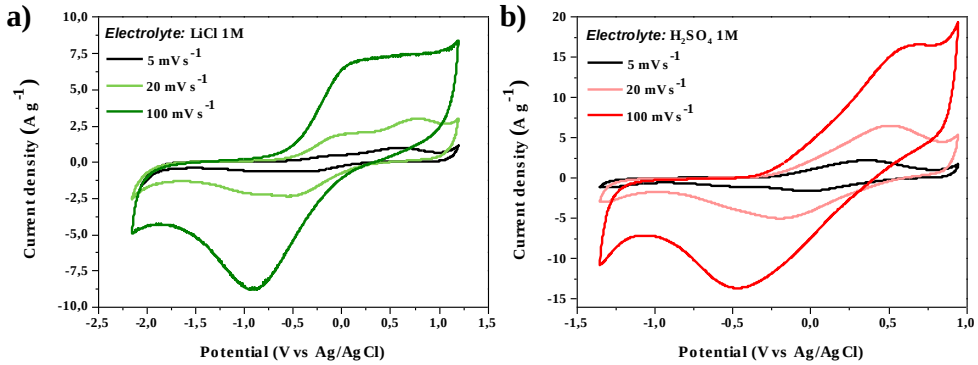

Figure 63. Cyclic voltammetry curves at sweep rates from 5 to 100 mV s^{-1} on three-electrode configuration for **Py-CTF** using (a) LiCl 1 M and and (b) H_2SO_4 1 M solutions as electrolytes.

Remarkably, upon increasing sweep rates a positively shift of the oxidation peak is observed while the reduction peak shifts negatively, mainly caused by the polarization of the electrode and its internal resistance.[310] The specific capacitance (C_{sp}) of the active electrode was calculated from Equation (4):

$$C_{sp} = \frac{\int_{V_1}^{V_2} i(V)\cdot dV}{2\cdot \nu m \cdot \Delta V} \qquad (4)$$

Being i (A) the response current in a whole cycle (positive and negative charge in absolute value along the entire voltage window), ν (V s^{-1}) the sweep rate, m (g) the mass of the CTF active material and V the potential window. As expected, as the sweep rate increases the capacitance decreases significantly in both electrolytes, since ions have less time to diffuse within the framework surface area when the charge is applied faster. Thus, the charge-storage means is mainly a diffusion-controlled process.

It should be highlighted that the shape of the CV curves remains almost unchanged even at high sweep rate of 100 mV s^{-1}, indicating great charge transfer kinetics at the **Py-CTF** electrode surface.[311] The specific capacitance values obtained for the LiCl 1M electrolyte are 63, 53 and 31 F g^{-1} at scan rates of 5, 20 and 100 mV s^{-1}, respectively; for the H_2SO_4 1 M electrolyte the specific capacitance calculated from the CV curves are 146, 108 and 54 F g^{-1} at scan rates of 5, 20 and 100 mV s^{-1}, respectively. Thus, higher capacitance values were obtained in acid electrolyte compared to the neutral one.

To gain insight into the electrolyte concentration effect on the electrochemical performance of **Py-CTF** as a supercapacitor electrode, the material was also studied in LiCl 0.5 M, LiCl 2M, H_2SO_4 0.5 M and H_2SO_4 2 M aqueous solutions (Fig. 64). The CV curves maintain a good symmetry at high sweep rates, which indicates a great electrochemical activity of the CTF. The C_{sp} of the active electrode was calculated from equation (4), and the data is summarized in Tables 2 and 3. These results indicate that the highest C_{sp} values are obtained when using H_2SO_4 2 M as electrolyte.

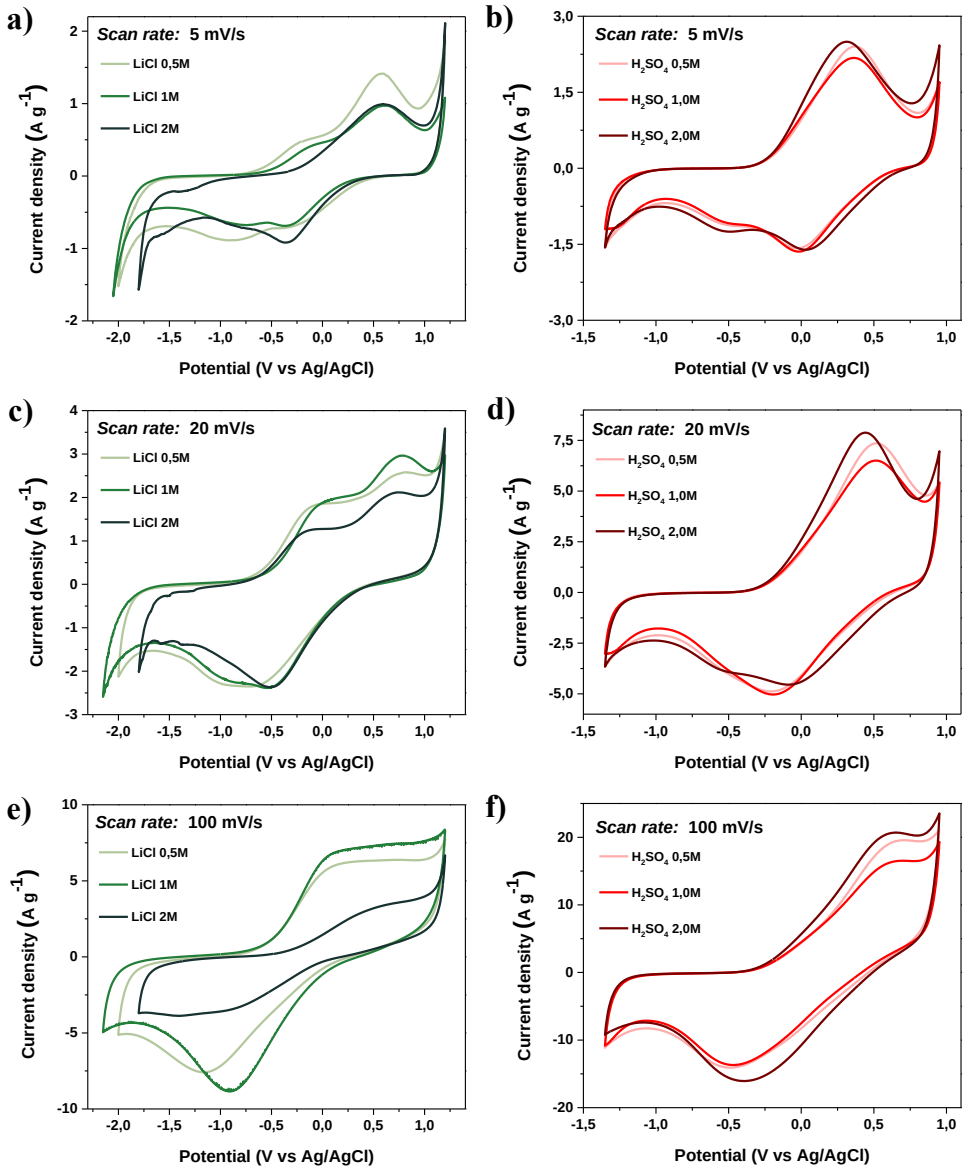

Figure 64. CV curves at sweep rates from 5 to 100 mV s^{-1} on three-electrode configuration for **Py-CTF** using (a) LiCl 0.5 M, (b) H_2SO_4 0.5 M, (c) LiCl 2 M and (d) H_2SO_4 2 M solutions as electrolytes.

Table 2. Specific capacitance values of **Py-CTF** in neutral LiCl electrolyte at different concentrations.

	LiCl 0.5 M			LiCl 1 M			LiCl 2 M		
Scan rate (mV s^{-1})	5	20	100	5	20	100	5	20	100
Capacitance (F g^{-1})	**91**	**53**	**28**	**63**	**53**	**31**	**70**	**45**	**13**

Table 3. Specific capacitance values of **Py-CTF** in acid H_2SO_4 electrolyte at different concentrations.

	H_2SO_4 0.5 M			H_2SO_4 1 M			H_2SO_4 2 M		
Scan rate (mV s^{-1})	5	20	100	5	20	100	5	20	100
Capacitance (F g^{-1})	**151**	**115**	**61**	**146**	**108**	**54**	**165**	**124**	**69**

After the electrochemical characterization of the pristine framework, the electrochemical performance of **Py-CTF$_{900}$** was also evaluated using H_2SO_4 1 M and LiCl 1 M solutions as acid and neutral electrolyte, respectively (Fig.65). The CV curves at different scanning rates show a nearly rectangular shape, indicating a capacitive nature of the tested electrode material. Notably, **Py-CTF$_{900}$** exhibits a higher specific capacitance in LiCl 1M than in the acid electrolyte (H_2SO_4 1 M). The C_{sp} values obtained for the LiCl 1M electrolyte are 177, 178 and 148 F g^{-1} at scan rates of 5, 20 and 100 mV s^{-1}, respectively; for the H_2SO_4 1 M electrolyte the C_{sp} values are 107, 150 and 162 F g^{-1} at scan rates of 5, 20 and 100 mV s^{-1}, respectively.

Nevertheless, **Py-CTF$_{900}$** display an enhanced capacitive behaviour in both electrolytes compared to the pristine CTF material, proving the successful effect of the thermal treatment on the CTF enhanced electrochemical performance. Additionally, no pseudocapacitance contribution from residual redox-active functional groups could be observed.

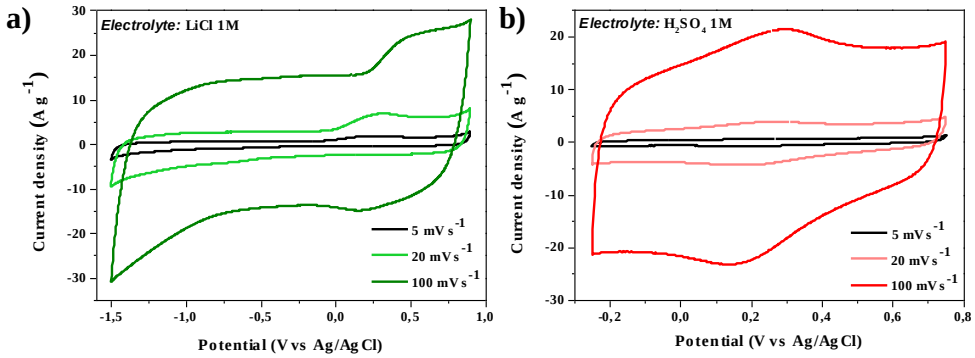

Figure 65. CV curves at sweep rates from 5 to 100 mV s^{-1} on three-electrode configuration for **Py-CTF$_{900}$** using (a) LiCl 1 M and and (b) H_2SO_4 1 M solutions as electrolytes.

The electrochemical performance of **Py-CTF$_{900}$** was also explored at different concentrations of the electrolytes (LiCl 0.5 M, LiCl 2M, H_2SO_4 0.5 M and H_2SO_4 2 M aqueous solutions). The CV curves at sweep rates from 5 to 100 mV s^{-1} in the potential window between -1.5 and 1 V for LiCl and -0.25 and 0.8 V for H_2SO_4 are shown in Figure 66. The obtained C_{sp} values are presented in Tables 4 and 5, being LiCl 1M the electrolyte configuration in which **Py-CTF$_{900}$** displays the highest capacitive behaviour.

Table 4. C_{sp} values of **Py-CTF$_{900}$** in neutral LiCl electrolyte at different concentrations.

	LiCl 0.5 M			**LiCl 1 M**			**LiCl 2 M**		
Scan rate (mV s^{-1})	5	20	100	5	20	100	5	20	100
Capacitance (F g^{-1})	**141**	**148**	**125**	**177**	**178**	**148**	**125**	**148**	**142**

Table 5. C_{sp} values of **Py-CTF$_{900}$** in acid H_2SO_4 electrolyte at different concentrations.

	H_2SO_4 0.5 M			**H_2SO_4 1 M**			**H_2SO_4 2 M**		
Scan rate (mV s^{-1})	5	20	100	5	20	100	5	20	100
Capacitance (F g^{-1})	**100**	**149**	**158**	**107**	**150**	**162**	**90**	**126**	**149**

The optimization of the electrolyte concentration is usually performed to improve the cycling stability of the electrode materials. However, there is not a significant improvement in the electrochemical properties of **Py-CTF$_{900}$** upon increasing concentrations of the electrolyte.

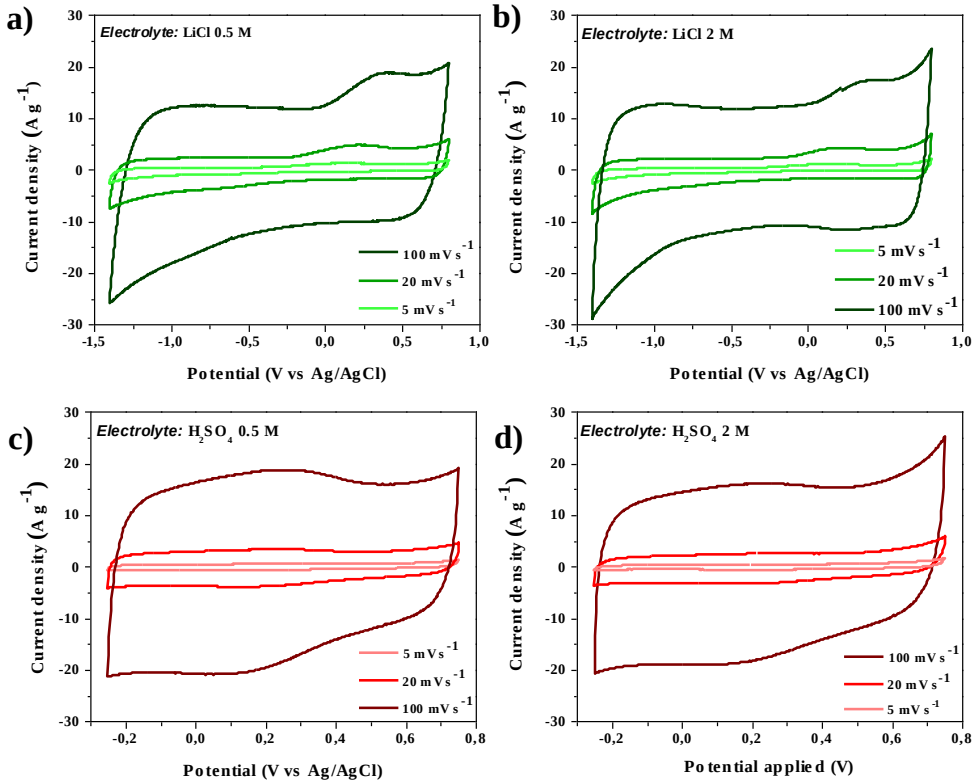

Figure 66. CV curves at sweep rates from 5 to 100 mV s^{-1} on three-electrode configuration for **Py-CTF$_{900}$** using (a) LiCl 0.5 M, (b) H_2SO_4 0.5 M, (c) LiCl 2 M and (d) H_2SO_4 2 M solutions as electrolytes.

Additionally, the CV curves of **Py-CTF$_{900}$** in H_2SO_4 2 M and LiCl 2 M solutions recorded at different scan rates (from 5 to 1000 mV s^{-1}) are presented in Figure 67. The specific capacitance values obtained for the LiCl 2M electrolyte are 141, 162, 152, 140, 116 and 94 F g^{-1} at scan rates of 5, 20, 100, 200, 500 and 1000 mV s^{-1}, respectively. For the H_2SO_4 2 M electrolyte the specific capacitance calculated from the CV curves are 90, 126, 149, 156, 123 and 113 F g^{-1} at scan rates of 5, 20, 100, 200, 500 and 1000 mV s^{-1}, respectively. As expected, the C_{sp} decreases upon increasing potential scan rates, since the ions cannot reach the inner surface of the

porous electrode material (Fig. 68). It should be highlighted that the capacitance retention in both media is quite high (72% in H_2SO_4 2 M and 68% in LiCl 2M), indicating great stability of the CTF as electrode material.

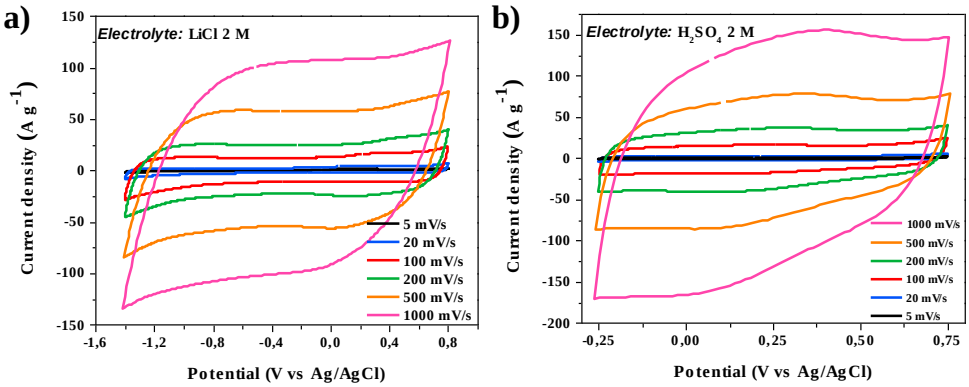

Figure 67. CV curves at sweep rates from 5 to 1000 mV s^{-1} on three-electrode configuration for **Py-CTF$_{900}$** using (a) LiCl 2 M and and (b) H_2SO_4 2 M solutions as electrolytes.

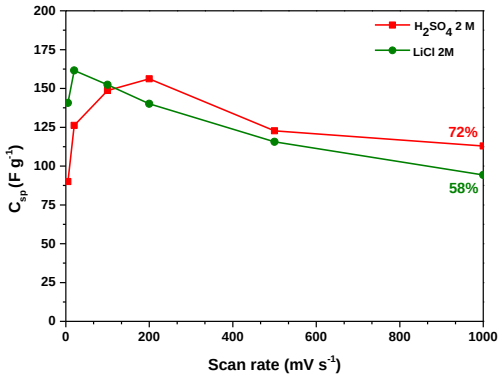

Figure 68. Specific capacitances at various sweep rates from 5 to 1000 mV s^{-1}.

The maximum C_{sp} of 178 F g^{-1} obtained for **Py-CTF$_{900}$** in LiCl 1M at a scan rate of 20 mV s^{-1} is superior to those of many previously reported materials (Table 6). These results forecast the great potential of this crystalline network, which we expect to show more sophisticated performance for supercapacitors applications after further investigations. In particular, it is especially interesting the integration of these materials into an aqueous and organic symmetric supercapacitor cell, which enable to significantly broad the potential window and therefore its possible application as supercapacitor electrodes in a lab-scale full prototype.

Table 6. Comparison of specific capacitance data of previously reported COF-based electrode materials.

Electrode materials	Electrolytes	Current density/ Scan rate	C_{sp} (F g^{-1})	Reference
DqTp-COF	1 M H_2SO_4	1.56 mA cm^{-2}	154	[312]
DAAQ-TFP-COF	1 M H_2SO_4	0.1 A g^{-1}	49	[188]
DAB-TFP-COF	1 M H_2SO_4	0.1 A g^{-1}	21	[188]
TpOMe-DAQ	3 M H_2SO_4	3.3 mA cm^{-2}	169	[313]
Car-TPT COF	0.5 M H_2SO_4	0.2 A g^{-2}	17.4	[314]
NWNU-COF-1	6 M KOH	0.25 A g^{-1}	155.38	[200]
BIBDZ	1 M H_3PO_4	0.5 A g^{-1}	88.4	[199]
TpBD-$(OH)_2$	1 M Phosphate buffer	2 mV s^{-1}	86	[315]
NH2-f-MWCNT @ COFTTA–DHTA	1 M Na_2SO_4	0.4 A g^{-1}	127.5	[97]
DAB-TFP-COF	1 M H_2SO_4	0.1 A g^{-1}	21	[188]
SWCNTs-TpPa-COFs	1 M H_2SO_4	0.5 A g^{-1}	153	[195]
Radical COF (i) [TEMPO]100%-NiP-COF	0.1 M $(C_4H_9)_4NClO_4$ in CH_3CN	0.1 A g^{-1}	(i) 167	[316]
(ii) [TEMPO]50%-NiP-COF			(ii) 124	
Py-CTF_{900}	**1 M LiCl**	**2 mV s^{-1}**	**178**	**This work**

b) Electrochemical characterization of TPE-CTF

Similarly, different electrolytes were explored for the electrochemical characterization of **TPE-CTF**. Thus, H_2SO_4 1 M and LiCl 1 M solutions were tested as acid and neutral electrolyte, respectively. Figure 69 displays the CV curves of the potential window between -0.25 and 0.6 V for LiCl 1 M and -0.2 and 0.65 V for H_2SO_4 1 M. The sweep rates of 5, 20 and 100 mV s^{-1} were used again to evaluate the working electrode. In comparison to the previously described **Py-CTF**, no redox peaks could be observed for this sample, indicating that there is only capacitative contribution. The specific capacitance (C_{sp}) of the active electrode was calculated from equation (4). The C_{sp} values obtained for the LiCl 1M electrolyte are 2.35, 1.20 and 0.48 F g^{-1} at scan rates of 5, 20 and 100 mV s^{-1}, respectively; while for the H_2SO_4 1 M electrolyte the C_{sp} values are 3.45, 1.83 and 0.84 F g^{-1} at scan rates of 5, 20 and 100 mV s^{-1}, respectively. Therefore, even though the material is electrochemically active, its capacitive nature is inconspicuous. It should be noticed that, as expected, a remarkable decrease in the specific capacitance is observed as the scan rate increases.

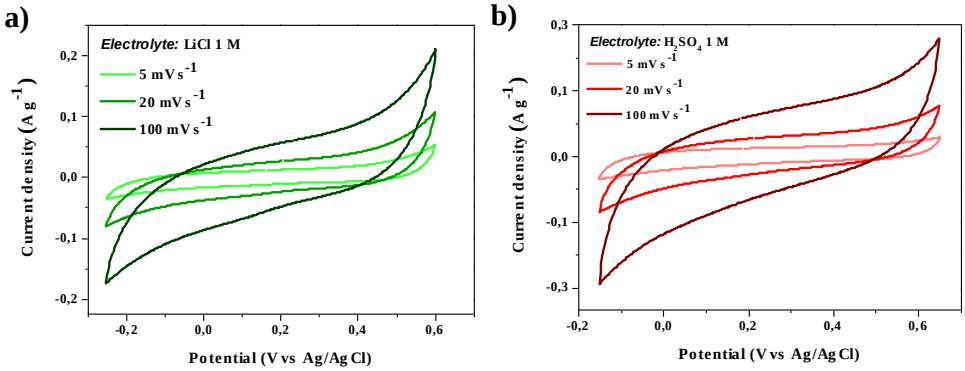

Figure 69. CV curves at sweep rates from 5 to 100 mV s^{-1} on three-electrode configuration for **TPE-CTF** using (a) LiCl 1 M and and (b) H_2SO_4 1 M solutions as electrolytes.

The electrochemical performance of **TPE-CTF$_{900}$** was also explored in H_2SO_4 1 M and LiCl 1 M solutions as electrolytes. The CV curves disclose again a nearly rectangular shape (Fig. 70) proving the capacitive features of the material. The C_{sp} values obtained for the LiCl 1M electrolyte are 10, 9 and 7 F g^{-1} at scan rates of 5, 20 and 100 mV s^{-1}, respectively; while for the H_2SO_4 1 M electrolyte the C_{sp} values are 4, 3 and 3 F g^{-1} at scan rates of 5, 20 and 100 mV s^{-1}, respectively. Thus, **TPE-CTF$_{900}$** exhibits higher specific capacitance values in LiCl 1M than in H_2SO_4 1 M. Despite the fact that these results are quite modest, an enhancement of the

electrochemical properties of the CTF is observed after the thermal carbonization at 900 ºC, indicating the potential of the pyrolysis treatment.

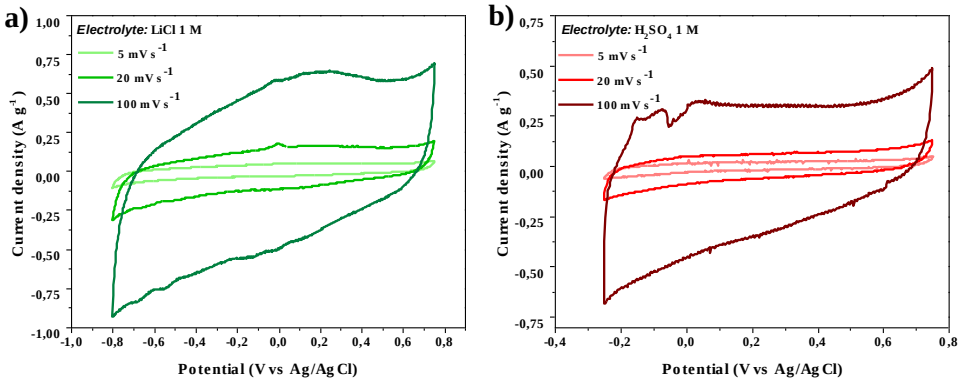

Figure 70. CV curves at sweep rates from 5 to 100 mV s^{-1} on three-electrode configuration for **TPE-CTF$_{900}$** using (a) LiCl 1 M and and (b) H_2SO_4 1 M solutions as electrolytes.

4.3 Conclusions

In summary, a conventional ionothermal protocol has been optimized for the synthesis of two novel crystalline triazine-linked COFs, namely **Py-CTF** and **TPE-CTF**, one incorporating pyrene moieties and other based on tetraphenylethylene units in which only the primary amide groups in *trans* react selectively to cyclotrimerize and form *s*-triazine rings. This protocol has enabled the preparation of crystalline networks designed from strikingly stable linkages, which display a very low degree of reversibility. The as-obtained materials display not only an ordered and porous structure but also an excellent thermal and chemical stability.

Additionally, these crystalline microporous frameworks have been successfully processed by thermal treatment at 900 ºC and converted into conducting porous carbon structures (**Py-CTF$_{900}$** and **TPE-CTF$_{900}$**). Despite the fact that both carbonized polymeric frameworks have demonstrated great energy-storage capacity, **Py-CTF$_{900}$** displays a superior capacitive nature compared to **TPE-CTF$_{900}$**, with a maximum specific capacitance of 162 F g^{-1} at scan rates of 20 mV s^{-1} in LiCl 2M.

These preliminary results suggest the potential of molecularly designed CTFs for the development of novel well-structured microporous carbon architectures for advanced electrochemical applications, since they display good microporosity, large π-conjugated skeleton and high chemical and thermal stability. Future studies on the current topic are therefore suggested in order to develop the next generation of electrochemical energy storage systems based on CTFs in the foreseeable future.

Chapter 5:

Quinoline-based Covalent Organic Framework for fluorescent determination of Zinc ion

5.1 Introduction

Selective and sensitive recognition of metal ions (e.g. Hg, Cd, Fe, Al, Cu, etc.) is a field of increasing scientific interest. In particular, fluorescent sensing has attracted growing significance due to its simplicity, high sensitivity and outstanding selectivity, and it has been applied for a wide range of applications.[317–319] Thus, different metal ions can be detected by spectroscopic changes of fluorescence-based sensory materials, which also allow low-cost and real-time assays.[11,320]

Among different ions, Zinc is the second most abundant transition metal ion in the human body. It is also involved in several essential biological processes of all living organisms such as cell growth and apoptosis, DNA binding and synthesis, gene transcription, immune function, etc.[321,322] However, the excess or lack of the proper amount of zinc ion in the body can cause acute health problems.[323,324] In case of Zn deficiency, severe chronic liver and renal diseases, digestion problems or mental retardation can be generated.[325,326] In contrast, neurotoxicity and the development of serious brain diseases (like Parkinson or Alzheimer) are related to an excess Zn ion concentration in some cells.[325,327] Besides its diverse biological roles, Zinc is also an important transition metal in the environment and industry; several agricultural and industrial products use Zinc, since it protects steel from oxidation and corrosion.[328]

Due to its unique properties, it is of big current interest the selective and sensitive detection of Zn metal ions. In this regard, a great number of analytical and electrochemical techniques (e.g. FAAS, ICP-AES, GFASS, etc.)[329–331] have been applied for the recognition of metal ions, specifically Zn^{2+}. However, most of those methods need sample pre-treatment and/or have high-cost and low selectivity. In addition, Zn detection is specially challenge due to its electron configuration ($3d^{10}$ $4s^{0}$), which limit any spectroscopic or magnetic response.[332,333] For these reasons, in recent years there has been growing attention in the development of novel fluorescence chemosensors, since their simple and precise method of detection has outcome as a promising alternative to conventional analytical methods. Moreover, fluorescence chemosensors can be further applied to bioimaging.[334,335]

Up to now, several Zn^{2+} sensors based on quinoline, anthracene, fluorescein, coumarin, BODIPY or Shiff bases have been reported.[336–341] Among those, quinoline moieties and its derivatives have outstand due to their specific selectivity

towards Zn^{2+} with a "turn-on" fluorescent enhancement that potentially improve the sensitivity of the material.[341–343] Thus, utilization of quinoline as an efficient fluorescence sensor towards metal ions has shown great promise and potential.

In the past few years, COFs have outcome as novel potential fluorescent probes for the detection of biologically and environmentally valuable analytes, specially metal ions, since their high specific surface area and the π-stacked layered structure enable the formation of defined paths within the framework, favoring the interaction with the suitable analytes and also enhancing the sensitivity through signal amplification.[228,344,345] In addition, engineering the pore surface, as it has been discussed in the introduction, can further optimize the diffusion of complementary analytes. In this regard, COFs have been successfully applied for the sensing of different metal ions, including Cu^{2+}, Hg^{2+}, Au^{+}, Fe^{3+} and Pb^{2+}.[102,232,346–348] However, no previous applications of COFs as fluorescent chemosensors towards Zn^{2+} have been reported.

In this chapter, a sensory material with quinoline-based receptors has been designed for the recognition of Zn^{2+} metal ions. Starting from an imine-based COF, the successful linkage transformation through post-synthetic functionalization into a more robust and fully conjugated 2D aromatic network (**QBR-COF**) is described. While the crystallinity and porosity are preserved, the chemical and thermal stability plus the π-electron delocalization in the resultant quinoline-linked COF are significantly enhanced. The as-obtained quinoline-COF has been further studied as a potential "turn-on" selective fluorescent sensor towards Zn metal ions.

5.2 Results and discussion

The first step consists in the preparation of a previously reported imine-based COF (**TPB-DMTP-COF**).[35] Then, in a post-synthetic modification, a quinoline-based COF (**QBR-COF**) decorated with 2,6-diisopropylphenyl pendant groups is synthesized. Both COFs, as well as the starting building blocks, have been fully characterized. In addition, the fluorescence sensing features of the final **QBR-COF** have been studied.

5.2.1. Synthesis and characterization

The synthesis of the imine-linked COF is initiated with the preparation of the building blocks: 2,5-dimethoxyterephthaldehyde (**DMTA**) and 1,3,5-tris(4-aminophenyl)benzene (**TAPB**). The synthetic route to obtain both monomers is summarized in Scheme 10.

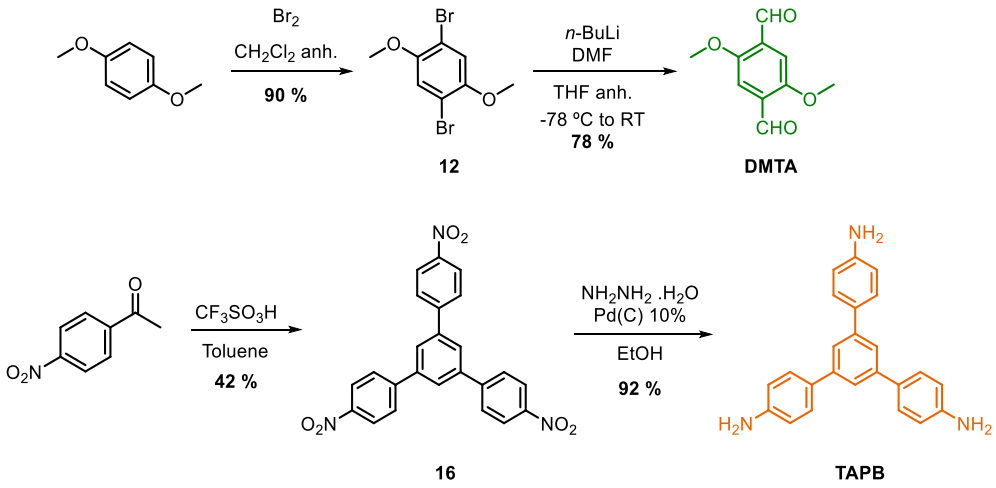

Scheme 10. Synthesis of constituting monomers **DMTA** and **TAPB**.

Starting from the commercially available 1,4-dimethoxybenzene, bromination at the 2- and 5- positions afforded compound **12**,[349] which is then formylated by treatment with *n*-butyllithium and DMF in anhydrous THF yielding **DMTA**[350] in a 78% yield.

The second amine monomer **TAPB** is prepared starting from 4'-nitroacetophenone, which undergoes a cyclotrimerization into nitro-compound **16** catalyzed by trifluoromethanesulfonic acid.[351] The nitro groups are then reduced with hydrazine hydrate in the presence of palladium on carbon, yielding **TAPB** with a 32 % overall yield.[352]

The synthesis of **TPB-DMTP-COF** is based on the condensation of the selected monomers through solvothermal reaction in *o*-dichlorobenzene/*n*-butanol (1:1) at 120 ºC for three days (Scheme 11).[35] Aqueous acetic acid 6 M was used as the catalyst of the reaction.

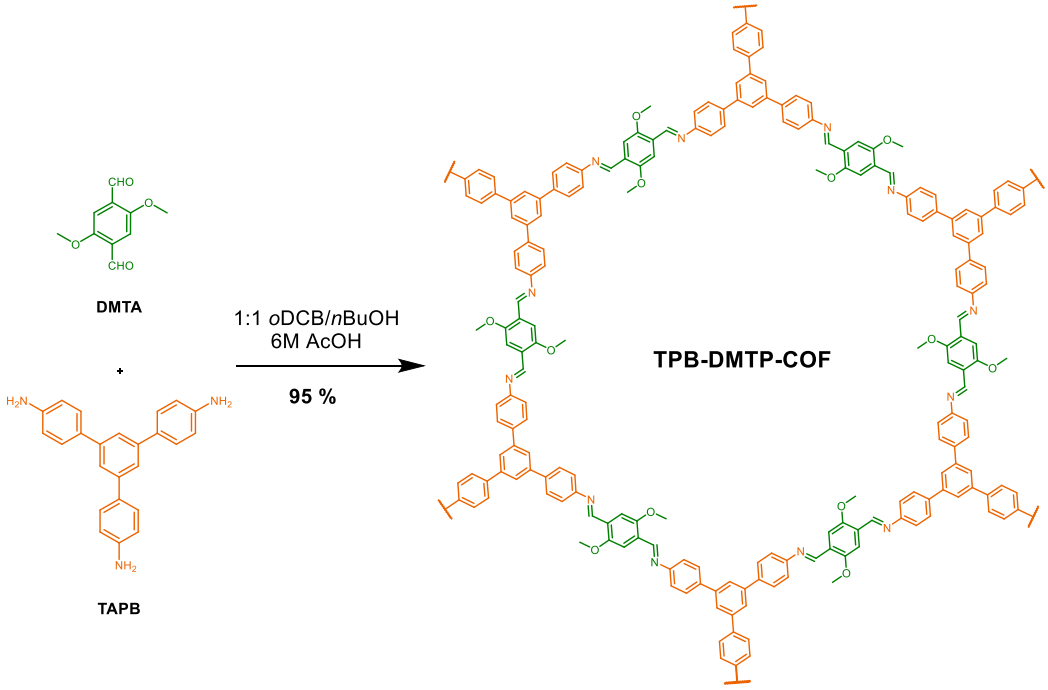

Scheme 11. Synthesis of **TPB-DMTP-COF**.

The success of the polymerization reaction was confirmed by FTIR spectroscopy and solid-state ^{13}C-CP/MAS-NMR. FTIR spectrum shows the clear disappearance of the C=O and N-H stretching bands from the aldehyde and amine building blocks, respectively (Fig. 71a). In addition, an emergence band at 1620 cm^{-1} can be successfully assigned to the C=N imine vibration. Furthermore, in the ^{13}C-CP/MAS NMR spectrum the aromatic signals of the COF skeleton can be observed between 160 and 105 ppm. The O-CH_3 signal is clearly displayed at 55.0 ppm, while the absence of the characteristic aldehyde carbon around 190 ppm further confirms the success of the reaction (Fig. 71b).

PXRD was used to confirm the formation of a crystalline network. Clear diffraction peaks could be observed at 2.94, 4.98, 5.76, 7.56, 9.82 and 25.5 ° (Fig. 71c). These peaks were assigned to the (100), (110), (200), (210), (220) and (001) facets, respectively.

Nitrogen sorption isotherms measured at 77 K present a type IV isotherm, typical from mesoporous materials, confirming the formation of a porous framework (Fig. 71d). The BET surface area and pore volume values are estimated

to be 2166 m^2 g^{-1} and 1.22 cm^3 g^{-1}, respectively. The pore size distribution calculated by NLDFT is centered at 2.6 nm (Fig. 71d inset), showing a great agreement with the previously reported data.[35]

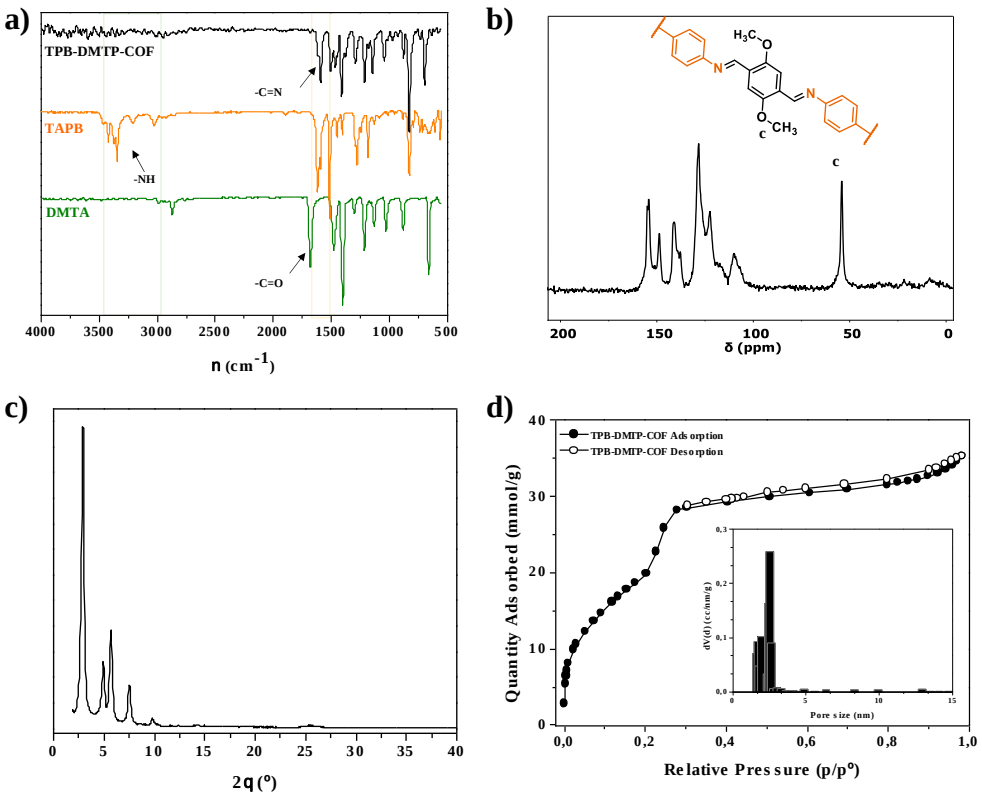

Figure 71. (a) Comparative FTIR spectra of **DMTA** (green) and **TAPB** (orange) monomers and **TPB-DMTP-COF** (black). (b) ^{13}C-CP/MAS-NMR spectra of **TPB-DMTP-COF**. (c) PXRD pattern of **TPB-DMTP-COF**. (d) Nitrogen adsorption/desorption isotherms at 77 K of **TPB-DMTP-COF** (S_{BET} = 2166 m^2 g^{-1}, Vp= 1.22 cm^3 g^{-1}). Inset: pore size distribution calculated by NLDFT (3.4 nm).

Prior to the post-synthetic modification reaction of the imine-based COF, the selected pendant moiety 2,6-diisopropylphenyl is synthesized in two steps (Scheme 12).

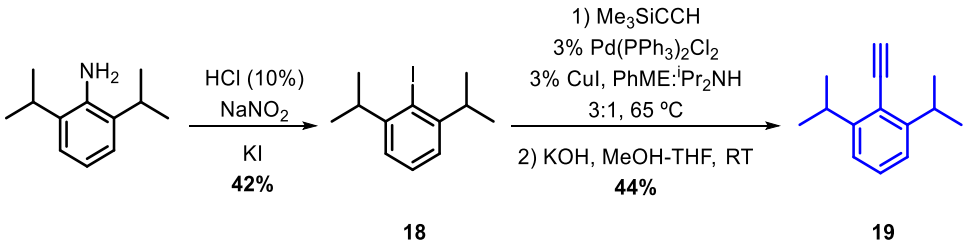

Scheme 12. Synthesis of 2,6-diisopropylphenyl (**12**).

Starting from commercially available 2,6-diisopropylaniline, in a typical Sandmeyer reaction the corresponding aryl halide **18** was obtained from aryl diazonium salt using $NaNO_2$ and KI.[353] Then compound **18** was subjected to a Sonogashira cross-coupling reaction, allowing the formation of the carbon-carbon bond between the trimethylsilylacetylene and the aryl halide. The crude TMS-protected alkyne was directly carried to the following deprotection step, affording **19** in 44% yield over the two steps.[354]

The quinoline-based receptor COF (**QBR-COF**) was prepared from previously described **TPB-DMTP-COF**. The efficient aza-Diels-Alder (aza-DA) reaction between the aryl imines of the **TPB-DMTP-COF** and the alkyne group of the arylalkyne derivative affords the conversion of the dynamic imine linkage into more stable quinoline units (Scheme 13). Due to the potential chemical tunability of the substrates in the cycloaddition reaction, different functionalities can also be introduced within the pores of the COF framework in a post-synthetic approach.[355] In this chapter, 2,6-diisopropylphenyl moieties were integrated onto the pores. While the 2D COF displays strong covalent bonds along the plane, weak van der Waals forces direct the interactions along the out-of plane direction. For this reason, the introduction of this bulky pendant groups within the layered framework will hinder the π-π interaction between layers, enhancing surface/functional group accessibility for further facile diffusion of analytes in sensing applications.[356,357]

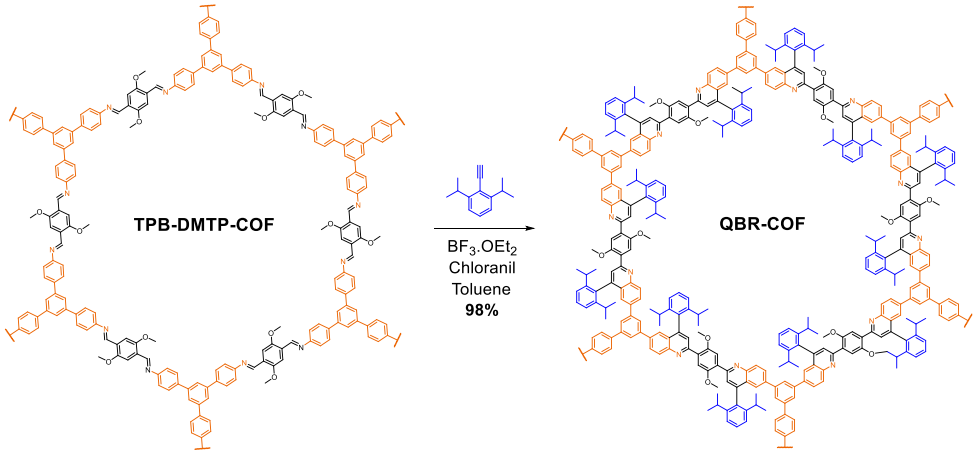

Scheme 13. Synthesis of **QBR-COF** *via* aza-Diels-Alder cycloaddition reaction.

The fruitful incorporation of the bulky 2,6-diisopropylphenylacetylene onto the pristine COF was confirmed by FTIR. The comparative spectra of the powders (Fig. 72a) revealed the characteristic peaks at 1545 and 1582 cm^{-1}, demonstrating the formation of quinolyl species. Furthermore, the spectrum shows the presence of the characteristic C(sp^3)-H stretching band from the 2,6-diisopropylphenyl moieties at 2975 cm^{-1}. C−O−C symmetric and asymmetric stretches associated with methoxy groups are observed at approximately 1038 cm^{-1}. On the other hand, the solid state ^{13}C-CP/MAS NMR spectrum of **QBR-COF** shows two signals at 32.5 and 25.1 ppm, successfully assigned to the sp^3 C of the 2,6-diisopropylphenyl units (Fig. 72b). Moreover, a slightly down-field shift of the aromatic -O-CH_3 substituents is observed in the spectrum of **QBR-COF** in comparison with the corresponding of **TPB-DMTP-COF** (from 56.39 ppm to 55 ppm, respectively). Besides the aromatic (116−149 ppm) and -OCH_3 carbon (55 ppm) peaks, an emergence peak at 154 ppm assignable to the 2-quinolyl carbon was also observed, providing solid evidence for the formation of a quinolyl moiety.

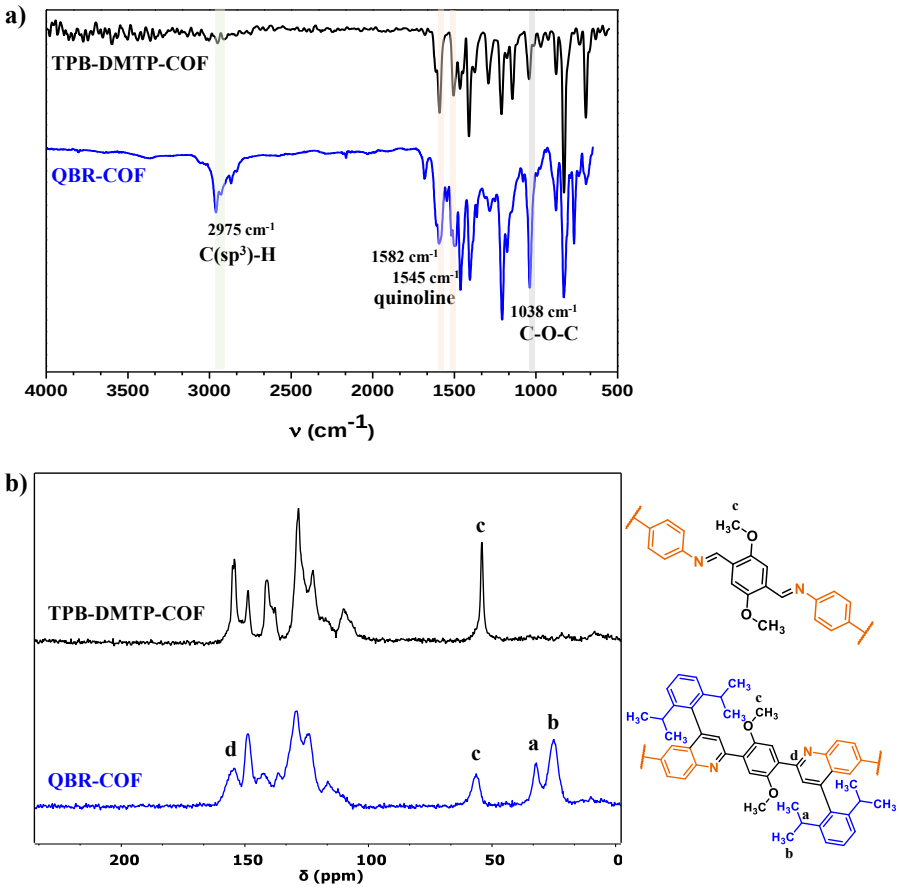

Figure 72. (a) Comparative ATR-FTIR spectra and (b) ^{13}C-CP/MAS-NMR spectra of **TPB-DMTP-COF** (black) and **QBR-COF** (blue).

PXRD pattern of **QBR-COF** (Fig. 73a) displayed a clear diffraction peak at 3.35º, similarly to previously reported quinoline modified-COFs,[44] confirming that the crystallinity of the material remained almost unchanged after the aza-DA reaction. The most intense peak in both diffractograms (**QBR** and **TPB-DMTP-COF**), which correspond to the (100) facet, have a small full-width at half-maximum (FWHM) values of 0.28º and 0.19º, respectively, indicating that crystallinity is preserved. Moreover, just a small shift of this (100) peak is observed.

The effect of the pendant groups on the material´s porosity was evaluated by N_2 sorption isotherms at 77 K (Fig. 73b). Thus, BET surface area of 2166 and 144 m^2 g^{-1} for **TPB-DMTP-COF** and **QBR-COF** were revealed, respectively. A total pore volume of 1.22 and 0.13 cm^3 g^{-1} was derived in each case. The reduction of surface

area and pore volume is in good agreement with the increased framework mass and the introduction of the aromatic phenyl pendant rings. Both materials exhibited a type IV isotherm, suggesting their mesoporous characters, with a uniform pore size distribution centered at 3.4 and 2.5 nm for **TPB-DMTP-COF** and **QBR-COF** (Fig.74), respectively, calculated by NLDFT.

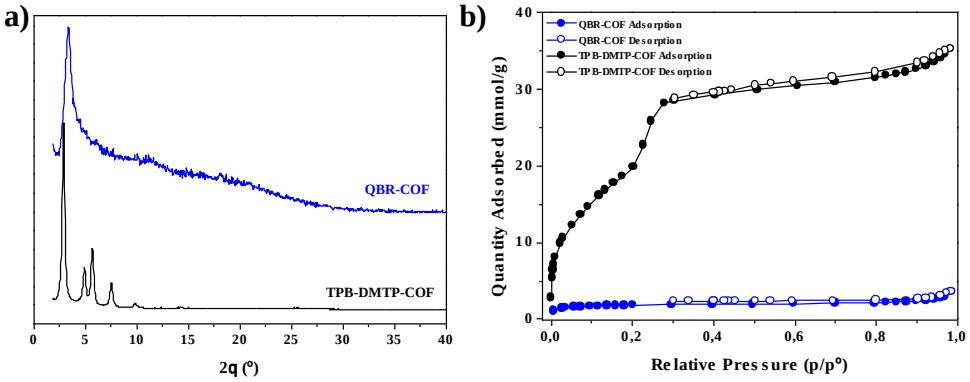

Figure 73. (a) Comparative PXRD patterns and (b) N_2 adsorption/desorption isotherms at 77 K of **TPB-DMTP-COF** (black) and **QBR-COF** (blue).

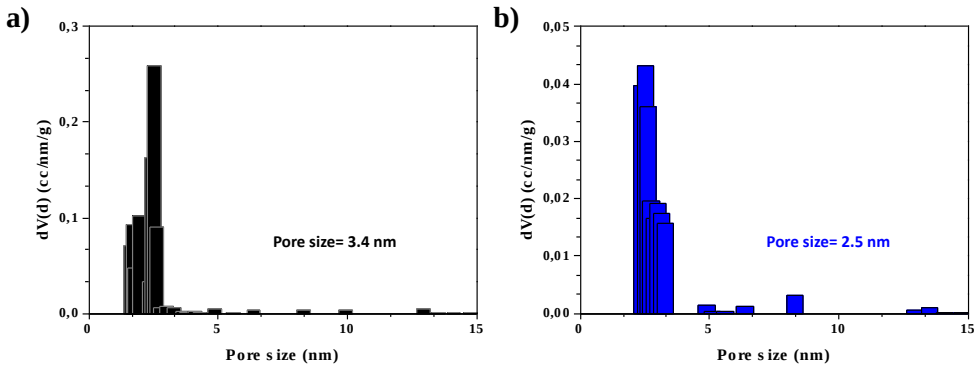

Figure 74. Pore size distribution of **TPB-DMTP-COF** (black) and **QBR-COF** (blue).

As it can be found in Table 7, compared with the **TPB-DMTP-COF** the specific surface area, pore size and pore volume of the **QBR-COF** decrease. This is mainly because of the introduction of 2,6-diisopropylphenyl which occupy the pore channel.

Table 7. The porosity data of COFs.

	S_{BET}[a] ($m^2\ g^{-1}$)	S_L[b] ($m^2\ g^{-1}$)	V_{total}[c] ($cm^3\ g^{-1}$)	D_{pore}[d] (nm)
TPB-DMTP-COF	2166	3530	1.22	3.4
QBR-COF	144	265	0.13	2.5

[a] Specific surface area calculated with the BET method. [b] Langmuir surface area. [c] Total pore volume at $P/P_0 = 0.99$. [d] Data calculated with the NLDFT method.

Finally, the thermal stability of **QBR-COF** was studied by thermogravimetric analysis, revealing that the material has a higher decomposition onset temperature (425 ºC) compared to **TPB-DMTP-COF** (300 ºC), confirming a higher thermal stability due to the more robust quinoline linkages (Fig. 75b).

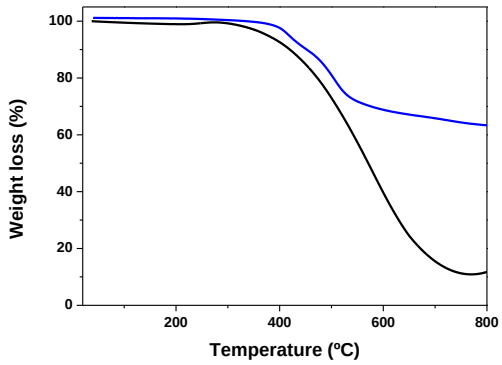

Figure 75. TGA profile of **TPB-DMTP-COF** (black) and **QBR-COF** (blue) using a linear 10 ºC min^{-1} ramp method.

Additionally, both COFs were characterized by SEM, suggesting that not significant changes in the morphology occurred after the chemical transformation (Fig. 76a and 76b). The materials exhibit a loose block morphology with uniformly distributed random-shaped aggregates composed of multiple tiny balls. Furthermore, the layered structure of the 2D **QBR-COF** could be observed by transmission electron microscopy (TEM, Fig. 76c and 76d).

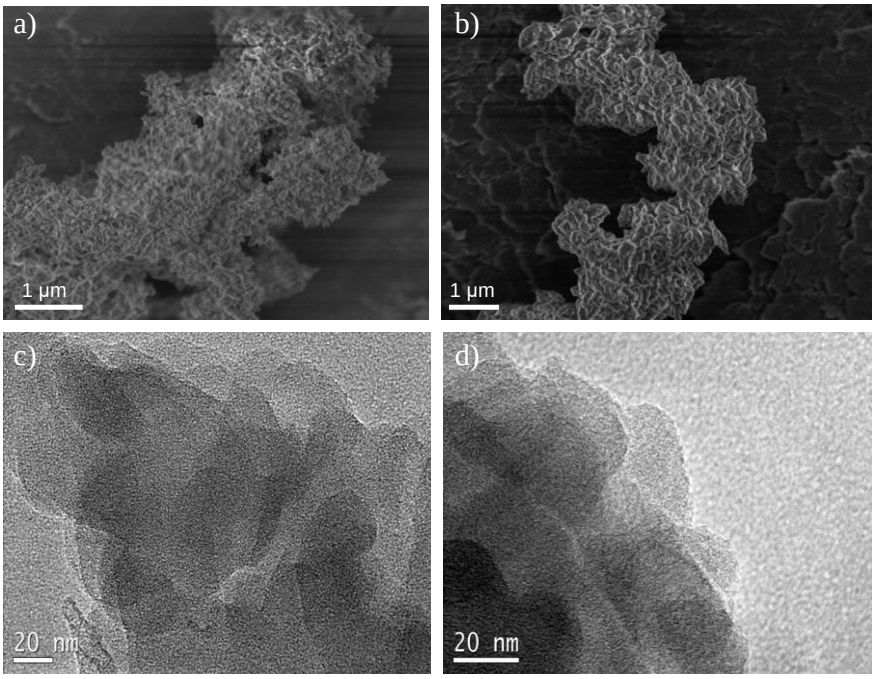

Figure7 6. SEM images of (a) **TPB-DMTP-COF** and (b) **QBR-COF**; (c,d) TEM images of **QBR-COF**.

5.2.2. Fluorescence studies

Due to its structural features and great stability and the presence in the skeleton of the quinoline moieties, **QBR-COF** was considered a promising platform to develop an efficient chemosensor for Zn ions. Thereby, fluorescence spectra for both COFs (**QBR-COF** and **TPB-DMTP-COF**) were acquired. Upon excitation at λ_{ex}= 450 nm, inconspicuous fluorescence was observed for both materials (Fig. 77). The maximum emission band appeared at 520 nm for **TPB-DMTP-COF**, while the corresponding one for **QBR-COF** was centered at 500 nm.

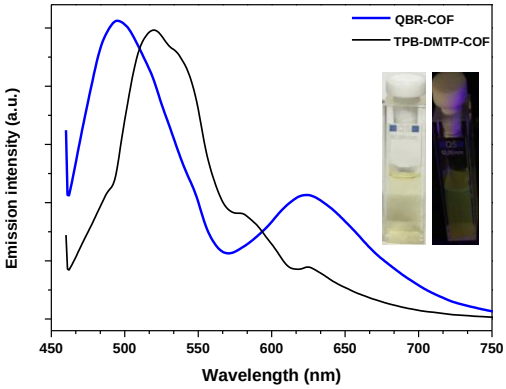

Figure 77. Solid-state fluorescence spectra of **TPB-DMTP-COF** (black) and **QBR-COF** (blue) dispersed in a mixture of THF:H_2O (1:1) (λ_{ex}= 450 nm). Inset: corresponding photographs of **TPB-DMTP-COF** under UV irradiation at 365 nm.

QBR-COF sensing ability towards Zn ions was studied at room temperature, monitoring real-time fluorescence changes upon increasing concentrations of Zn^{2+}. Thus, **QBR-COF** was dispersed in a mixture of THF:H_2O (1:1) at a concentration of 0.08 mg mL^{-1} and further sonicated for 5 min. The fluorescence titrations were performed by systematically increasing the concentration of Zn^{2+} in the cuvette (from $1x10^{-5}$ M until $2x10^{-4}$ M) and subsequent record of the fluorescence intensity of **QBR-COF**. For all the measurements, the excitation wavelength was λ_{ex} = 450 nm and the corresponding emission wavelength was recorded from λ_{em}= 460-750 nm. As shown in figure 78a, the fluorescence intensity of **QBR-COF** is boosted upon increasing concentrations of Zn^{2+}, indicating a real-time "turning on" mechanism and reaching its maximum at [Zn^{2+}] = $1.2x10^{-4}$ M. Interestingly, it can be observed that the fluorescence intensity of the COF sample decreased with further additions of Zn^{2+} (Fig. 78b), which may be due to the enhanced tendency of collision and self-aggregation of the COF material.[358]

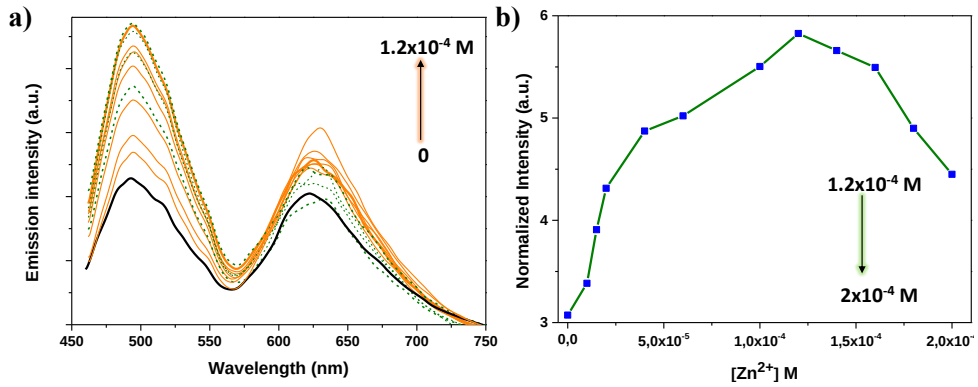

Figure 78. (a) Fluorescence spectra of **QBR-COF** (0.08 mg mL^{-1}) dispersed in THF:H_2O (1:1) containing different concentrations of Zn^{2+} (λ_{ex}=450 nm). (b) The normalized fluorescence intensity of **QBR-COF** dispersion (0.08 mg mL^{-1}) upon increasing concentrations of Zn^{2+} (λ_{ex}=450 nm). Inset: corresponding photographs of **Zn@QBR-COF** under UV irradiation at 365 nm.

To investigate this fluorescence "turning on" process, a confirmatory experiment was designed. Thus, 2.5 mL of a mixture of THF:H_2O (1:1) containing Zn^{2+} ($1.2x10^{-4}$ M) was added to the cuvette, and 200 µL of THF dispersion of **QBR-COF** (0.08 mg mL^{-1}) was added to the cuvette in batches of 20 µL per-time. As before, the excitation wavelength was λ_{ex} = 450 nm and the corresponding emission wavelength was recorded from λ_{em}= 460-750 nm, and the fluorescence emission spectra was continuously monitored. As depicted in figure 79, the fluorescence intensity is significantly enhanced upon addition of **QBR-COF** to the Zn ion solution (represented in blue). This enhancement of the fluorescence intensity can be attributed to the binding of Zn metal ions to the quinoline moieties which result in a weakening of π-π stacking interactions, inhibiting the aggregation caused quenching (ACQ) effect, normally present in bulk COF materials.

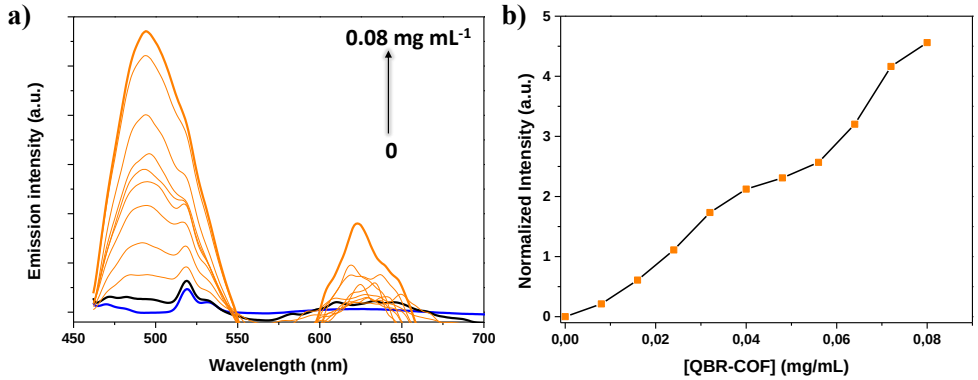

Figure 79. (a) Fluorescence emission spectra of THF:H_2O (1:1) solution containing Zn^{2+} (1.2×10^{-4} M) upon increasing the concentration of **QBR-COF** (λ_{ex}=450 nm). (b) The normalized fluorescence intensity of Zn^{2+} solution (1.2×10^{-4} M) upon addition of increasing concentrations of THF dispersion of **QBR-COF** (0.08 mg mL^{-1}, 20 µL each time, 200 µL in total).

Due to the great number of active sites on the COF skeleton, Zn^{2+} could effectively bound to the quinoline moieties, which lead to the fluorescence on/off phenomenon. This metal ion-COF interaction was further confirmed by dispersing **QBR-COF** in THF solution of Zn ions. The resulting **Zn@QBR-COF** was analyzed by scanning electron microscopy (SEM) and energy-dispersive X-ray spectroscopy (EDX) (Fig. 80a, b), confirming the successful incorporation of the Zn ions to the COF precursor.

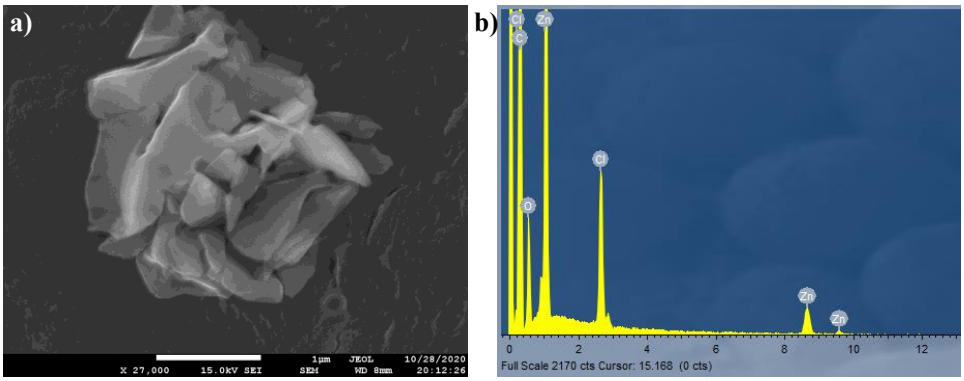

Figure 80. (a) SEM micrograph of **Zn@QBR-COF** and (b) EDX spectra of **Zn@QBR-COF** sample revealing the presence of atomic Zn in the complexed structures.

The selectivity of **QBR-COF** towards Zn^{2+} was then studied by examining the fluorescence changes for COF dispersed in THF:H_2O solutions containing competitive metal ions at equal concentrations ($1.2x10^{-4}$ M). In particular Al^{3+}, Fe^{3+}, Ca^{2+}, Ag^{+}, Mg^{2+}, K^{+}, Na^{+}, Cu^{2+} and Zn^{2+} were added to dispersed solutions of **QBR-COF** (0.08 mg mL^{-1}). As summarized in Figure 81a, the influence of the above mentioned metal ions on the fluorescence spectra of **QBR-COF** was thoroughly evaluated *via* monitoring the change of the fluorescence intensity at 495 nm. Remarkably, it was found that only a dramatic increase (8-fold) of fluorescence intensity was observed for Zn^{2+} compared with the blank control (Fig. 81b). Moreover, in the competitive experiment strong emission could only be observed for Zn^{2+}, while the other dispersions had a negligible emission, further supporting the excellent selectivity of **QBR-COF** and its potential as chemosensor for the detection of Zn^{2+}.

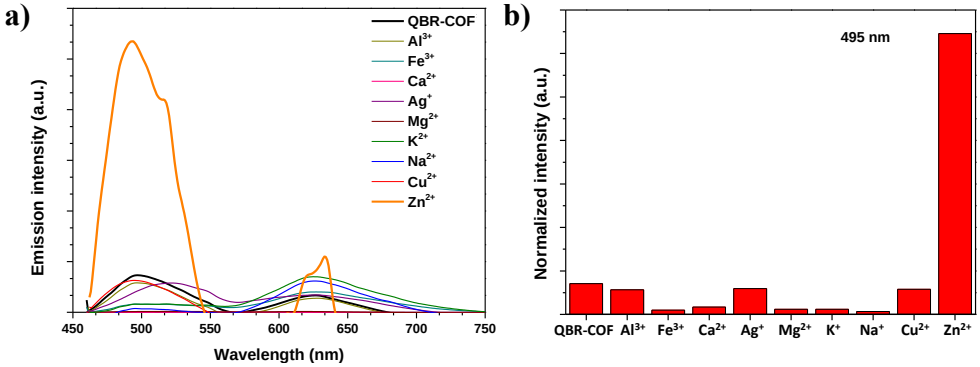

Figure 81. (a) Selective binding of **QBR-COF** to Zn^{2+} ion. The fluorescence spectra of **QBR-COF** dispersed in THF:H_2O (1:1) upon addition of $1.2x10^{-4}$ M of different metal ions (λ_{ex}=450 nm); (b) Normalized fluorescence intensity of **QBR-COF** in THF:H_2O (1:1) dispersion at 495 nm in the presence of different metal ions (λ_{ex}=450 nm); [**QBR-COF**] = 0.08 mg mL^{-1}; [metal ion] = $1.2x10^{-4}$ M.

In a similar study, the anion effect on the fluorescence sensing of Zn^{2+} was also investigated. Thus, Zn^{2+} ions with different contra-ions (Cl^{-}, Br^{-}, CN^{-}) were added to the **QBR-COF** dispersion at the same concentration ($1.2x10^{-4}$ M). Interestingly, Br^{-} and CN^{-} anions did not change the fluorescence emission intensity, while Cl^{-} anion led to a remarkable enhancement (Fig. 82). This could be attributed to an effective interaction of the anion with the highly conjugated aromatic framework (anion-π-interaction),[359] that can be explained considering the radius of the different anions (see Table 8). The anions size can be ordered as follows: Br^{-} > CN^{-} > Cl^{-}. Regarding these results and considerations, Cl^{-} anions demonstrated

higher adaptability to the hollow space in the COF framework in terms of size and charge stabilization, which is not allowed for larger anions.

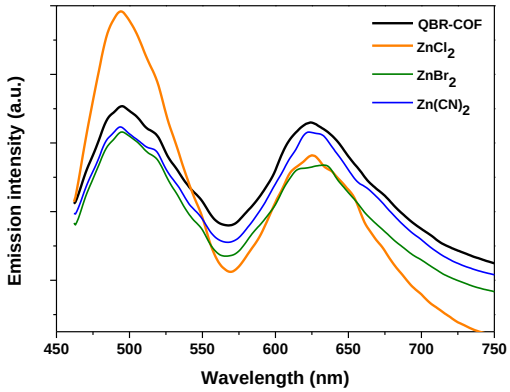

Figure 82. The fluorescence spectra of **QBR-COF** (0.08 mg mL^{-1}) dispersed in THF:H_2O (1:1) upon addition of $1.2x10^{-4}$ M of Zn^{2+} with different anions (λ_{ex}= 450 nm).

Table 8. Radius of different ions[271,360]

Ion	**Zn^{2+}**	**Cl^-**	**CN^-**	**Br^-**
Radii (Å)	0.75	1.81	1.92	1.96

In addition to the above mentioned experiments, **QBR-COF** could be used as an effective dual-mode fluorescent and colorimetric-based pH sensor. On one hand, the emission intensity of **QBR-COF** is enhanced as the pH decreased, displaying a good linear relationship against pH for values between 1 and 7 (Fig. 83a). The inherent porous structure of **QBR-COF** allow the diffusion of protons, which in turn might induce the protonation of quinoline units within the framework (Scheme 14).[361] Furthermore, **QBR-COF** can be recycled and used multiple times due to its great stability (Fig. 83b). To investigate this recyclability, fluorescence emission spectra of **QBR-COF** was recorded within a pH range from 1-7 for five subsequent cycles. As shown in Figure 83b, enhanced fluorescence emission was achieved under acidic conditions (the pH was increased upon addition of HCl 1M). However, after adjusting the pH to 7 using NaOH 1M, the fluorescence emission was quenched. By decreasing the pH again, the emission could be recovered, supporting the great reproducibility of these results.

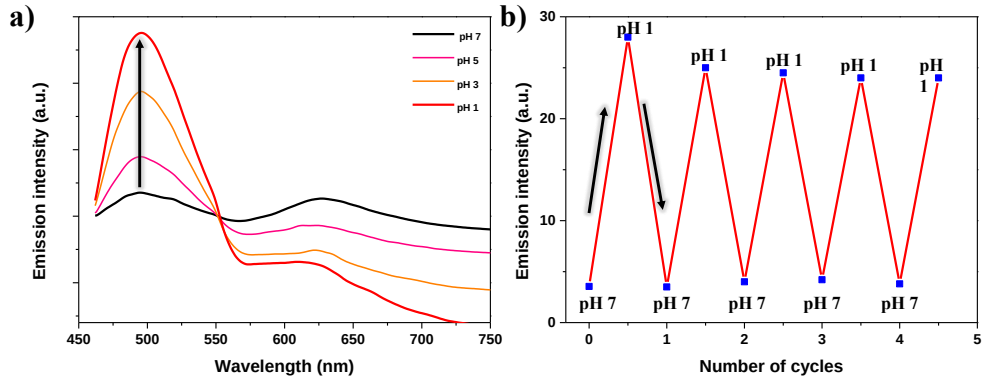

Figure 83. (a) Fluorescence spectra of **QBR-COF** under several acidic conditions (λ_{ex}= 450 nm). (b) Recyclability of **QBR-COF** for five detections runs.

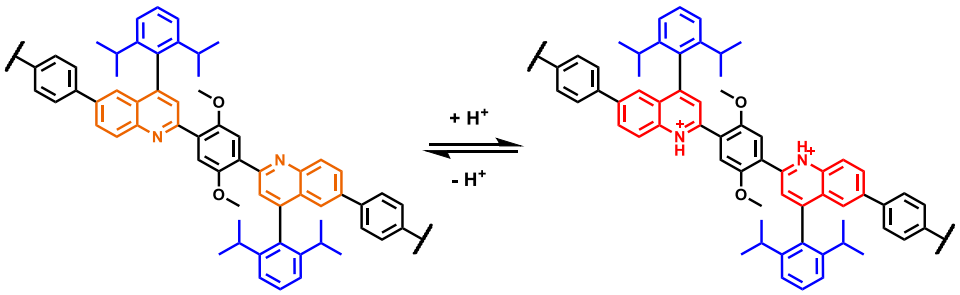

Scheme 14. Protonation and deprotonation of **QBR-COF** in acidic and basic conditions.

On the other hand, as shown in Figure 84, **QBR-COF** displays a discernable color change from yellow to red that can be easily detected by the naked-eye as the pH decreased. This strong correlation of the color with the pH value of the dispersion has been previously reported for a COF functionalized with pendant 8-hydroxyquinoline units.[106] This gradual color change with increasing acidity indicates the great potential of **QBR-COF** for practical applications as a responsive pH sensory material.

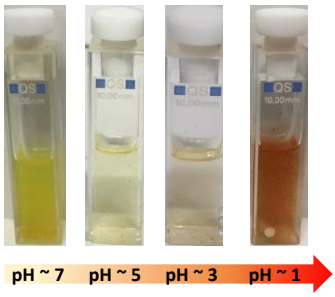

Figure 84. Color changes of **QBR-COF** in acidic media.

5.3 Conclusions

In conclusion, a robust quinoline-linked covalent organic framework (**QBR-COF**) has been successfully synthesized by simple transformation of the dynamic imine linkages of readily available **TPB-DMTP-COF** *via* aza-Diels-Alder reaction, which enabled the integration of 2,6-diisopropylphenyl pendant rings onto the pore surface. The resulting COF displayed not only improved chemical and thermal stability but also an enhanced π-electron delocalization, which provides an effective strategy to develop dual responsive sensory materials.

The incorporation of quinoline moieties and bulky pendant groups within the pores of the polymer facilitated the ion diffusion along the layered framework, enhancing the active sites accessibility. Therefore, further sensing experiments towards metal ions have been performed. Remarkably, great sensitivity and an excellent selective "turn-on" fluorescence emission was observed towards Zn^{2+} ions. These extraordinary results make **QBR-COF** a great potential platform for the detection of Zn metal ions, encouraging further exploitation towards its practical application. In addition, **QBR-COF** could be potentially applied as an effective colorimetric-based pH sensor, broadening the scope of these emerging materials.

Chapter 6:

Covalent Organic Frameworks as novel nanofillers designed for active packaging applications

6.1 Introduction

In the last few years an increasing trend to substitute the use of non-renewable and non-degradable polymers with bio-based and biodegradable ones has been observed, especially in the food packaging sector.[362,363] Among biopolymers, poly(lactic acid) (PLA) has become specially popular for food packaging,[363] since it displays several potential properties including high transparency, high availability in the market, competitive cost and easy processability.[362,364] Furthermore, PLA is not only obtained from renewable resources but it is also compostable.[365]

Additionally, after processing PLA develops stiff and brittle films and therefore other additives, such us plasticizers, are usually added. In this regard, the incorporation of biopolyesters additives such us citrate based esters has become an extended method for the preparation of PLA films for packaging materials, where flexibility is an essential issue.[366–368] In addition, they are widely accepted for direct contact with foodstuff.[369]

However, PLA still shows some disadvantages such us its susceptibility to thermal degradation, high barrier permeability (i.e: to CO_2, O_2 and water vapor) and poor mechanical performance, which hamper its industrial application.[370,371] For intended food packaging applications, an enhanced crystallinity of PLA is also highly necessary in order to overcome its inherent shortcomings. Thus, the incorporation of two-dimensional nanoparticles to biopolymer blends has become a simple and potential approach to increase PLA crystallization rate with the further enhancement of the thermo-mechanical performance of the bionanocomposites.[265,372,373] For instance, it has been reported that nanoparticles considerably enhance the compatibility between PLA and PHAs polymeric matrices, which results in a significant reduction of the permeability in nanocomposites, which is particularly intended for packaging applications.[374] In this context, two-dimensional covalent organic frameworks (COFs) have been envisioned as excellent candidates as novel reinforcements to improve thermal, mechanical and physical properties of biopolymers.[144,240,265] Due to their inherent features such us low mass density, permanent porosity and high thermal and chemical stability, COFs have gained increasing attention for the packaging industry. Moreover, COFs can be specifically designed and therefore predictable porous crystalline frameworks with tunable composition, topology and

functionalities can be achieved.[205,375] In addition, 2D layered COFs can be successfully exfoliated into COF nanosheets under sonication in a simple and scalable process.[212,240]

Besides the improvement in the mechanical behavior of films bionanocomposites, great efforts have been devoted to developing smart packaging materials which can effectively prevent the lipid oxidation of food. Traditionally, antioxidant additives were directly added into the foodstuff. This approach was replaced by the development of active packaging formulations based on the positive migration ability of active agents from the packaging material to the foodstuff.[376,377] However, there is a growing consumer concern about this migration phenomena, and therefore great efforts have been focused in the development of nonmigratory active packaging formulations (Fig. 85).[378,379]

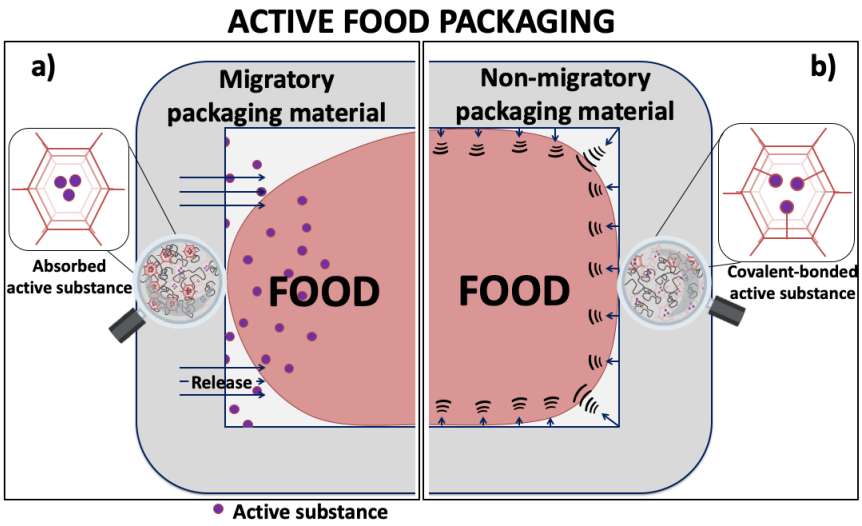

Figure 85. Schematic representation of: (a) migratory and (b) non-migratory active food packaging. Adapted from reference 13.

Among natural free radical scavenging compounds, catechols display high antioxidant activity, mostly related to the ortho dihydroxyl groups in the benzene structure, and therefore several food packaging materials have been designed incorporating catechols groups for further migrating or nonmigrating antioxidant purposes.[265,380–382]

In this chapter, the post-synthetic modification strategy is proposed as an effective tool for the preparation of a novel COF-based material (**COF-DOPA**) endowed with three dopamine moieties in its pores. Successfully, "click-chemistry" and in particular the Copper-catalyzed azide–alkyne cycloaddition (CuAAC) reaction has been selected for the post-synthetic modification. Therefore, the design and synthesis of the dopamine-functionalized COF *via* post-synthetic modification of a previously reported imine-based COF will be addressed. Additionally, this functionalized material has been processed and further used for the development of novel PLA bionanocomposite films with active properties. The structural, thermal and mechanical performance of these biodegradable films have been assesed and will be described in this chapter. Moreover, their nonmigrating antioxidant properties have also been investigated.

6.2 Results and discussion

6.2.1 Synthesis and characterization

In this chapter a novel COF endowed with active catechol pendant units has been synthesized, **COF-DOPA**,[265] which can be obtained post-synthetically from the alkyne-bearing COF **[HC≡C]$_{0.5}$-TPB-DMTP-COF** (Fig. 86).[35]

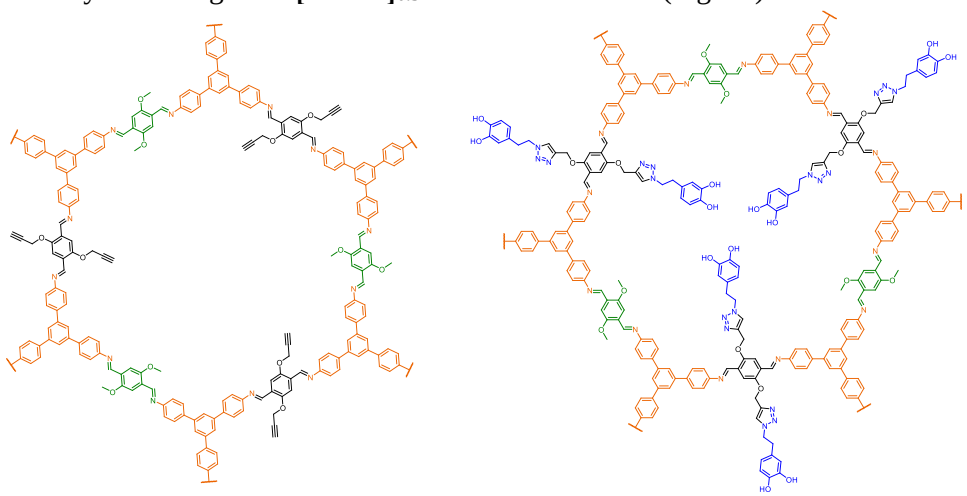

[HC≡C]$_{0.5}$-TPB-DMTP-COF **COF-DOPA**

Fig. 86. Structures of **[HC≡C]$_{0.5}$-TPB-DMTP-COF** and **COF-DOPA**.

Hence, the synthesis of the imine-based COF starts with the preparation of the constituting monomers, namely 2,5-dimethoxyterephthaldehyde (**DMTA**), 2,5-bis(propargyloxy)terephthaldehyde (**BPTA**) and 1,3,5-tris(4-aminophenyl)benzene (**TAPB**); as well as the dopamine azide needed for the post-synthetic modification.

The synthetic routes to obtain **DMTA** and **TAPB** are summarized in Scheme 15, and both have been previously described in Chapter 5.

The second aldehyde monomer, **BPTA**, is obtained from **DMTA** monomer in a two-step synthetic route (Scheme 16). Firstly, both methoxy groups are cleaved by treatment with BBr_3 affording **10** with good yield.[383] Then, a subsequent double Williamson etherification with propargyl bromide yields **BPTA** with 93% yield.

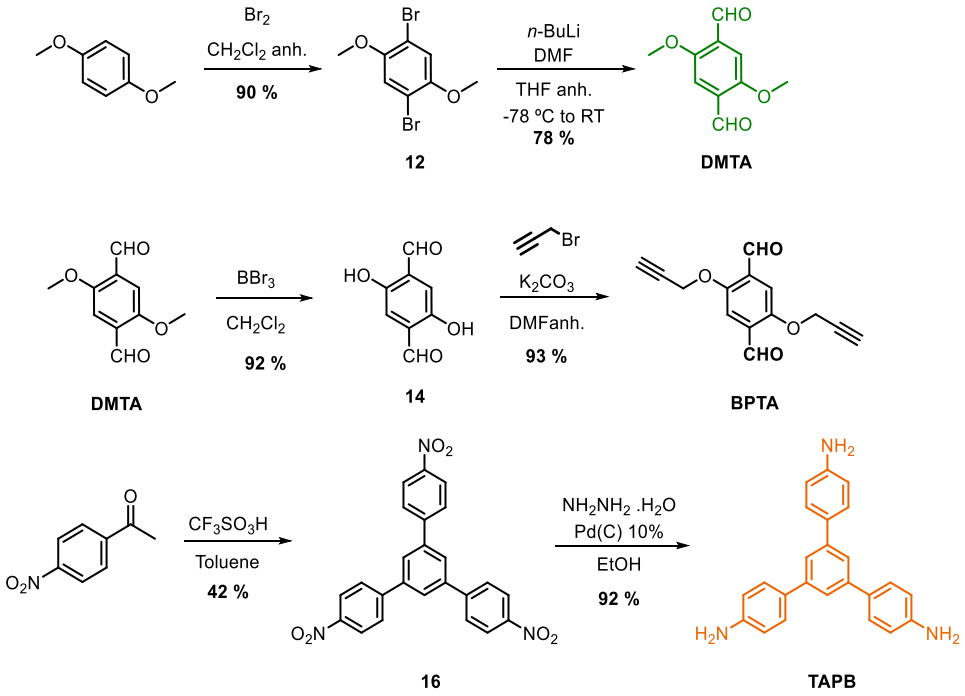

Scheme 15. Synthesis of constituting monomers **DMTA**, **BPTA** and **TAPB**.

The synthesis of the dopamine derivative **20** is summarized in Scheme 16, and it was accomplished in one step by reaction of commercially available dopamine hydrochloride salt with sodium azide.[384]

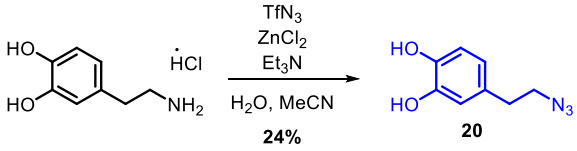

Scheme 16. Synthesis of dopamine azide **20**.

The syntheses of the alkyne-bearing COF is based on the condensation of the three selected monomers under solvothermal conditions in a mixture of *o*-dichlorobenzene/*n*-butanol (1:1) at 120 ºC for three days (Scheme 17), and aqueous acetic acid 6 M was used as the catalyst of the reaction.[35] By controlling the feed ratio of **DMTA** to **BPTA**, a precise control of the amount of propargyl moieties present in the COF pores can be achieved. In this work, the material with three alkynyl moieties and three methoxy moieties in each pore, **[HC≡C]$_{0.5}$-TPB-DMTP-COF**, has been selected. This ratio maximizes the number of active units while still preserving enough porosity after the post-synthetic modification.

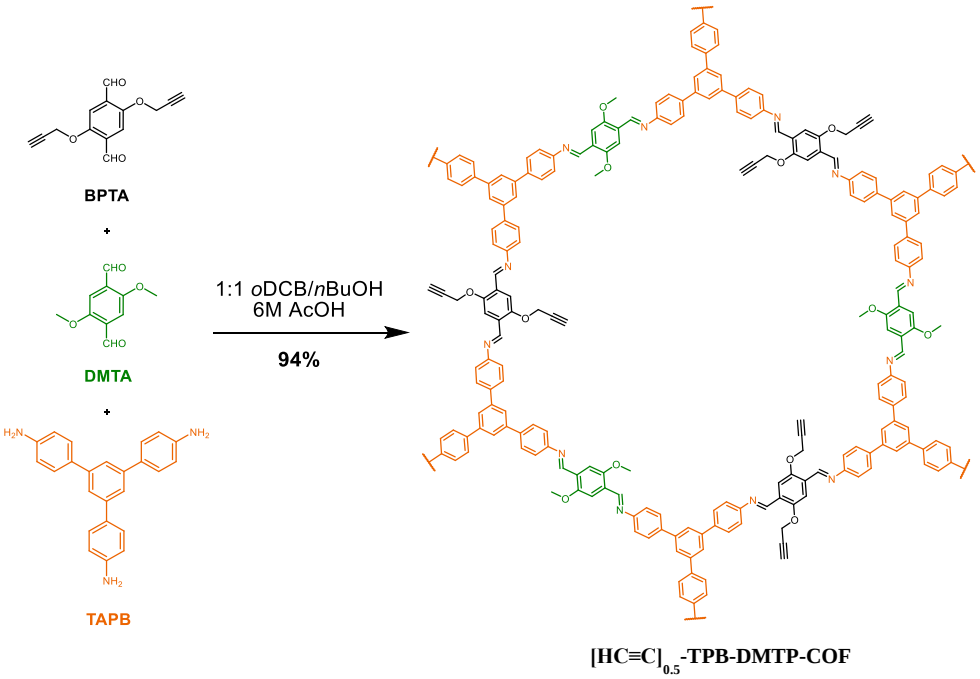

Scheme 17. Synthesis of **[HC≡C]$_{0.5}$-TPB-DMTP-COF**.

The success of the condensation reaction was confirmed by FTIR spectroscopy and solid-state ^{13}C-CP/MAS-NMR. FTIR analysis of the material (Fig. 87a)

displays the disappearance of the C=O and N-H bands from the aldehyde and amine monomers, respectively. In addition, the emergence of a new band at 1590 cm^{-1} can be successfully attributed to the C=N vibration from the imine linkages. On the other hand, in the ^{13}C-CP/MAS NMR spectra the aromatic signals of the alkyne-COF skeleton can be observed between 160 and 105 ppm. The O-CH_3 signal is clearly displayed at 55.0 ppm, while the O-CH_2 signal is centered at 56.7 ppm. In addition, the spectra display both triple bond carbons at 80.3 and 73.0 ppm, while the absence of the CO stretching of the aldehyde functionality at 190 ppm in both spectra further confirms the success of the reactions (Fig. 87b).

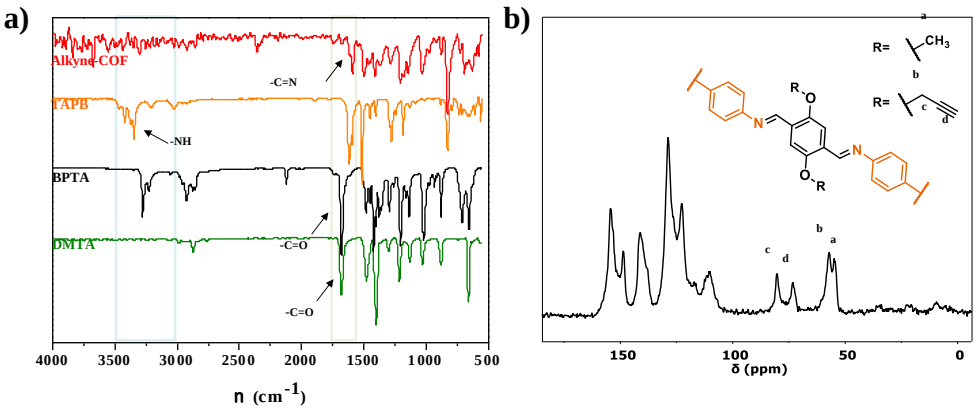

Figure 87. (a) Comparative FTIR spectra of **DMTA** (green), **BPTA** (black) and **TAPB** (orange) monomers and **[HC≡C]$_{0.5}$-TPB-DMTP-COF** (red). (b) ^{13}C-CP/MAS-NMR spectra of **[HC≡C]$_{0.5}$-TPB-DMTP-COF**.

PXRD and nitrogen sorption isotherms were used to confirm the formation of a crystalline and porous network. The PXRD patterns display clear diffraction peaks at 2.91, 4.95, 5.76, 9.82 and 25.50 º (Fig. 88a), which can be assigned to the (100), (110), (200), (210), (220) and (001) planes, respectively, of a hexagonal unit cell with eclipsed AA stacking.

Nitrogen sorption isotherms measured at 77 K present a type IV isotherm, typical of mesoporous materials (Fig. 88b). The BET surface area and pore volume values are estimated to be 1285 $m^2 g^{-1}$ and 0.95 $cm^3 g^{-1}$, respectively. The pore size distribution calculated from NLDFT is centered at 2.3 nm (Fig. 88b inset), showing a great agreement with the previously reported data.[35]

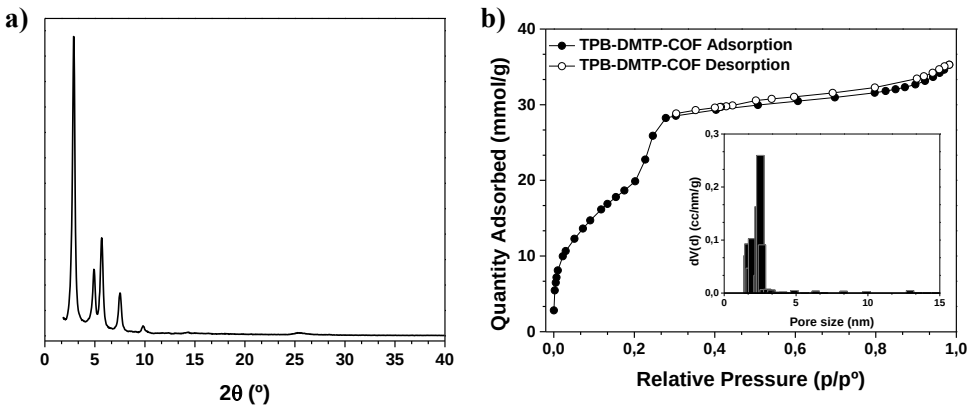

Figure 88. (a) PXRD pattern of **[HC≡C]$_{0.5}$-TPB-DMTP-COF**. (b) Nitrogen adsorption/desorption isotherms at 77 K of **[HC≡C]$_{0.5}$-TPB-DMTP-COF** (S_{BET} = 1285 m^2 g^{-1}, Vp= 0.95 cm^3 g^{-1}). Inset: pore size distribution calculated by NLDFT (2.3 nm).

These characterization data confirm the successful formation of the desired framework. Additionally, by comparison with the unmodified imine-based COF described in Chapter 5, namely **TPB-DMTP-COF**, it can be observed how the microstructure of the COF material is not significantly affected by the introduction of the small propargyl groups within the pores of the framework. While the crystallinity remains unchanged, only a small decrease in the porosity can be remarked.

COF-DOPA is obtained through post-synthetic functionalization of the alkyne-COF using the copper-catalyzed azide-alkyne cycloaddition reaction. Therefore, treatment of **[HC≡C]$_{0.5}$-TPB-DMTP-COF** with azide **20** in the presence of CuI and *N*,*N*-diisopropylethylamine (DIPEA) affords the desired dopamine-functionalized **COF-DOPA** (Scheme 18). The as-obtained material was thoroughly washed with DMF, H_2O, AcOH 50% (v/v) and THF to remove the remaining catalyst and unreacted molecules. Specifically, the efficient removal of copper from the COFs is confirmed by X-ray fluorescence (XRF) analysis.

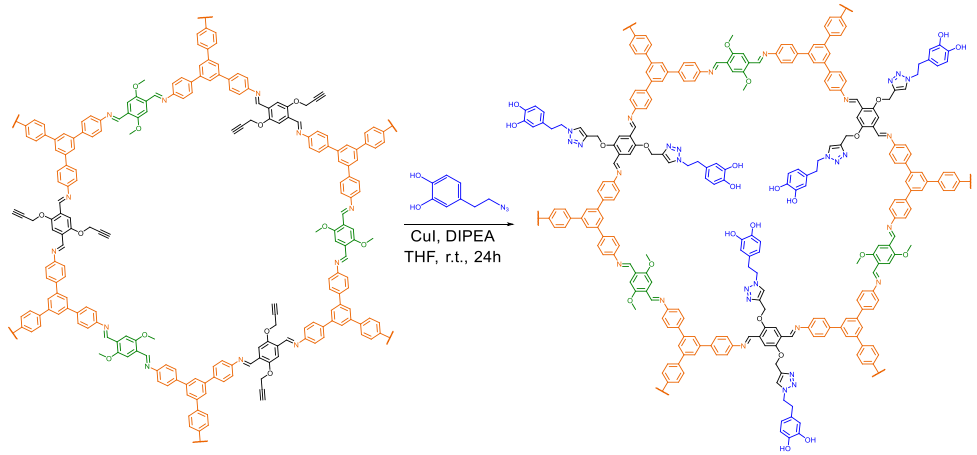

Scheme 18. Synthesis of **COF-DOPA**.

The successful grafting of dopamine into the COF structure was further confirmed by FTIR and ^{13}C-CP/MAS-NMR. The FTIR spectrum of **COF-DOPA**, presented in Fig. 89, displays the broad -OH stretching vibration associated to the catechol units at 3350 cm^{-1}. Furthermore, the absence of the azide band at 2098 cm^{-1} corroborates the success of the post-synthetic reaction and the incorporation of the dopamine moiety into the COF material.

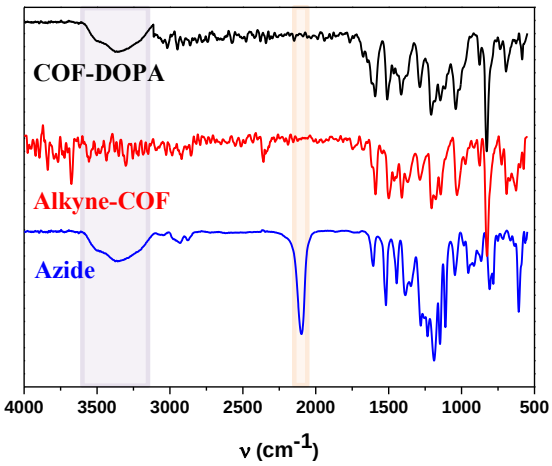

Figure 89. FTIR spectra of dopamine azide (blue), **[HC≡C]$_{0.5}$-TPB-DMTP-COF** (red), and **COF-DOPA** (black).

As shown in Fig. 90, the ^{13}C-CP/MAS NMR spectra clearly disclose the disappearance of the C(sp) signals from the alkyne moieties at 80 and 73 ppm. Additionally, several new signals originated from the click reaction can be observed, including the methylene carbon between the COF backbone and the triazole ring at 57.2 ppm and the triazole carbons at 148.7 ppm.

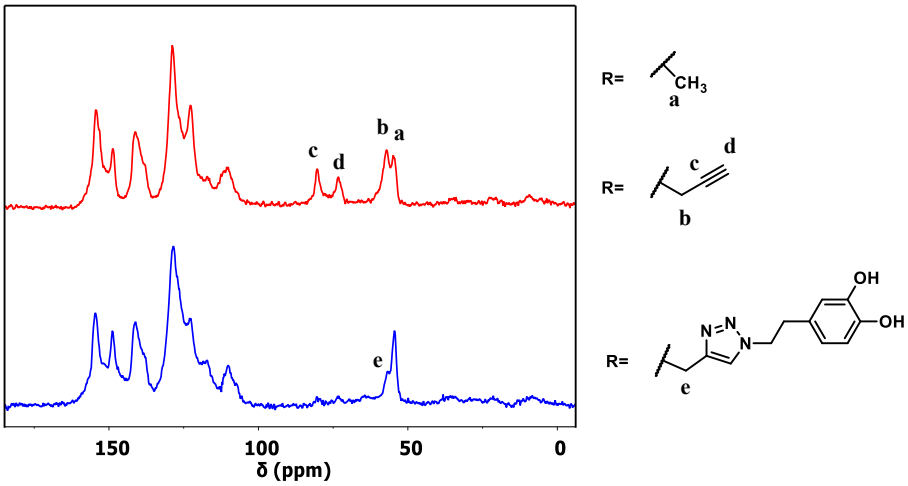

Figure 90. Comparative ^{13}C-CP/MAS-NMR spectra of **[HC≡C]$_{0.5}$-TPB-DMTP-COF** (red) and **COF-DOPA** (blue).

The PXRD pattern of the dopamine-functionalized COF is analogous to the profile of its precursor (Fig. 91a), thus confirming that the crystalline structure remains unchanged upon the post-synthetic modification. Therefore, **COF-DOPA** adopts the AA stacking mode of a *P*6 space group, presenting diffraction peaks at 2.89, 4.95, 5.69, 7.52, 9.82 and 25.69º. These can be assigned to the (100), (110), (200), (210), (220) and (001) planes respectively.

The porosity of **COF-DOPA** was evaluated by nitrogen sorption isotherms at 77 K, revealing type IV isotherms (Fig. 91b) characteristic of mesoporous materials. The BET surface areas and pore volumes values are estimated to be 450 $m^2\ g^{-1}$ and 0.23 $cm^3\ g^{-1}$, respectively. The pore size distribution calculated from NLDFT is centered at 1.4 nm (Fig. 91c, d). The low porosity of the functionalized COF can be ascribed to the big size of the grafted catechol moieties.

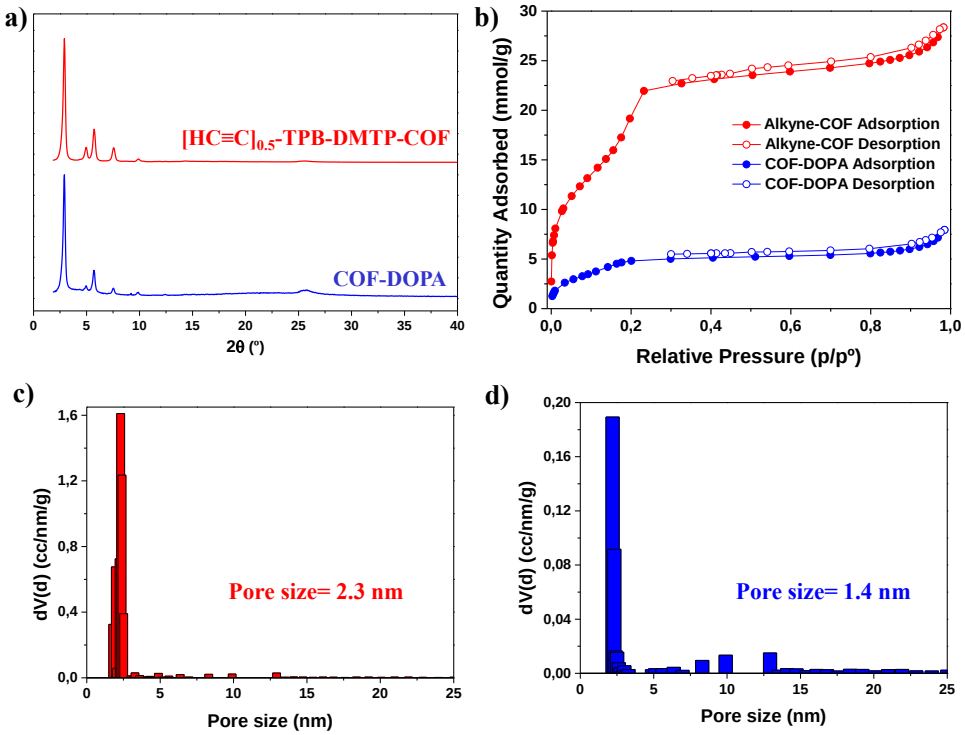

Figure 91. (a) Comparative PXRD patterns of **[HC≡C]$_{0.5}$-TPB-DMTP-COF** (red) and **COF-DOPA** (blue); (b) N_2 adsorption/desorption isotherms at 77 K of **[HC≡C]$_{0.5}$-TPB-DMTP-COF** (red) and **COF-DOPA** (blue); (c) Pore size distribution of **[HC≡C]$_{0.5}$-TPB-DMTP-COF** (red) and (d) pore size distribution of **COF-DOPA** (blue).

The thermal stability of the COF materials was studied by TGA analysis, revealing that they are all stable up to 300 ºC (Fig. 92a). Additionally, both COFs were characterized by UV-Vis spectroscopy (Fig. 92b), displaying a broad absorption band centred at 390 and 430 nm for **[HC≡C]$_{0.5}$-TPB-DMTP-COF** and **COF-DOPA**, respectively.

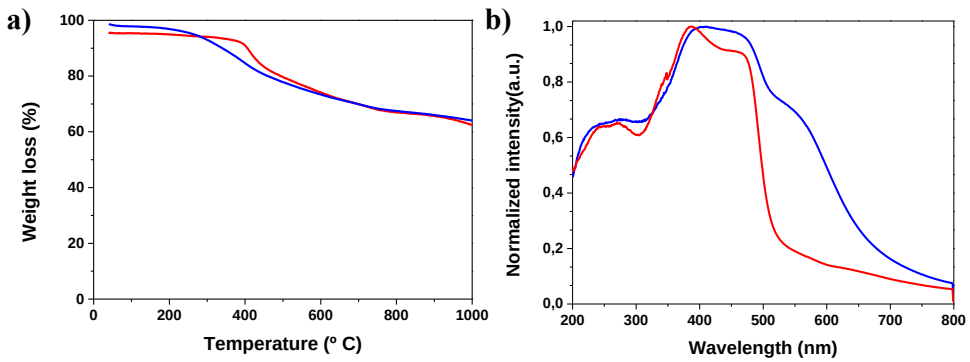

Figure 92. (a) Comparative TGA profile and (b) Normalized solid state UV-Vis absorption spectra of **[HC≡C]$_{0.5}$-TPB-DMTP-COF** (red) and **COF-DOPA** (blue).

Finally, the materials were characterized by SEM, suggesting that not significant changes in the morphology can be observed upon the reaction of the alkyne-COF and the dopamine azide unit (Fig. 93). The SEM micrographs with a 1 μm scale plate display random-shaped aggregation composed of many macroscopic tiny particles.

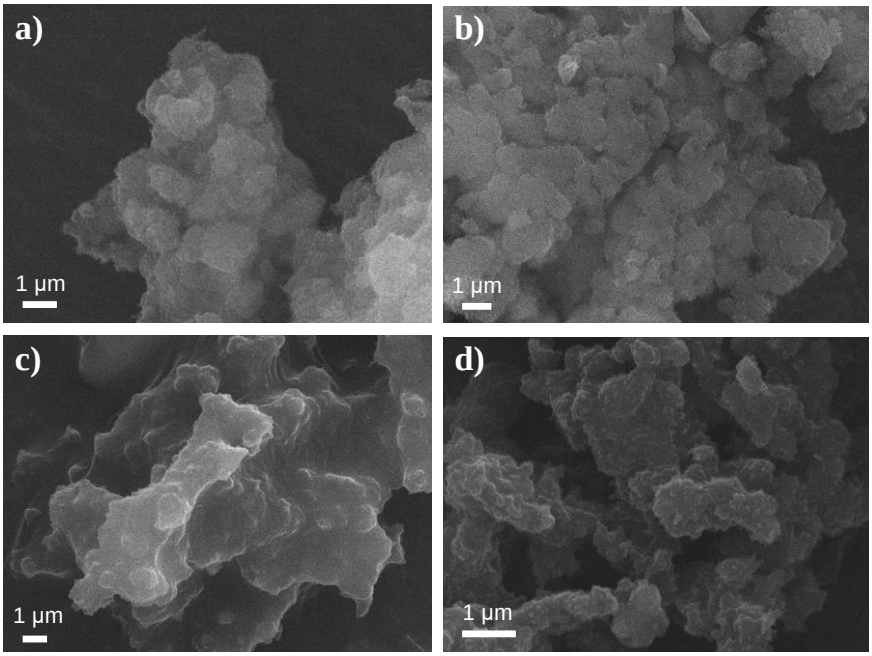

Figure 93. SEM images of (a,b) **[HC≡C]$_{0.5}$-TPB-DMTP-COF** and (c,d) **COF-DOPA.**

From these results it can be concluded that the post-synthetic reaction has taken place with excellent yield, besides the heterogeneous reaction media. In addition, the crystallinity and porosity of the pristine structure is maintained in the as-obtained dopamine-COF, despite the expected decrease in porosity due to the introduction of the catechol moieties in the pore walls (Table 9).

Table 9. The porosity data of COFs.

	S_{BET}[a] ($m^2\ g^{-1}$)	V_{total}[b] ($cm^3\ g^{-1}$)	D_{pore}[c] (nm)
[HC≡C]$_{0.5}$-TPB-DMTP-COF	1285	0.95	2.3
COF-DOPA	450	0.23	1.4

[a] Specific surface area calculated with the BET method. [b] Total pore volume at $P/P_0 = 0.99$. [c] Data calculated with the NLDFT method.

Once all the materials had been fully characterized, **COF-DOPA** was exfoliated into nanosheets to assure a homogeneous dispersion of the nanoparticles into the polymeric matrix. Thus, liquid-phase exfoliation (LPE) was performed since it has been widely described as a simple and scalable top-down approach that can be applied to all type of COFs.[135]

A suspension of **COF-DOPA** in $CHCl_3$ (0.4 mg mL^{-1}) was submitted to an ultrasonic treatment for 90 min in an ice bath (Fig. 94a). The sonication process was performed in cycles of 10 min, in order to avoid the inherent shortcomings of sonication treatment for the exfoliation of 2D materials like the generation of high local temperature due to sonication-induced cavitation.[385] The resulting suspension was centrifuged at 1000 rpm for 5 min to eliminate non exfoliated COF.

The colloidal character of the resulting suspension was corroborated by the Tyndall effect upon irradiation with a laser beam (Fig 94b inset), and the hydrodynamic size of exfoliated COF nanosheets was measured by DLS (Fig 94b). The exfoliated **COF-DOPAe** measurements show mainly a monomodal size distribution of ca. 255 nm, ranging from 190 to 300 nm. The structural aspect of **COF-DOPAe** nanosheets was observed by Transmission Electron Microscopy

(TEM), evidencing the formation of thin transparent nanosheets with lateral dimensions around 100 nm (Fig. 94c).

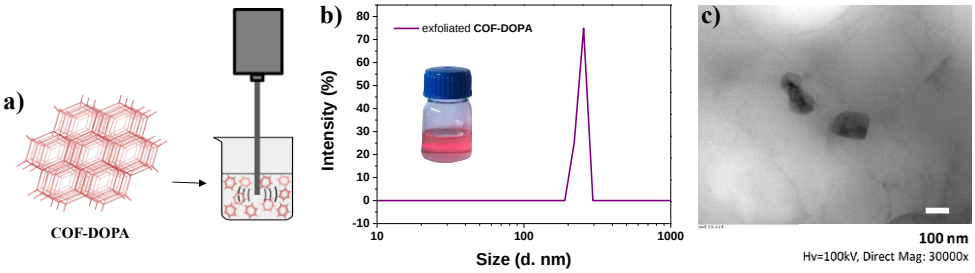

Figure 94. (a) Schematic representation of the exfoliation of **COF-DOPA**; (b) DLS measurements; Inset: Tyndall effect of the exfoliated suspension of **COF-DOPAe**; (c) TEM micrographs.

6.2.2. Bionanocomposites preparation and characterization

All bionanocomposite films were prepared by solving casting method. PLA pellets (0.8 g) were dissolved in 20 mL of $CHCl_3$ and stirred at room temperature. Then, Acetyl Tributyl Citrate (ATBC) was added and the **PLA-ATBC** proportion was set at 85:15.[386,387] These films were subsequently loaded with different predetermined amounts of as-synthesized **COF-DOPA** or exfoliated **COF-DOPAe**, affording bionanocomposites reinforced with 0.5, 1 and 3 wt% of dopamine functionalized COF with respect to PLA matrix. All the developed film formulations and their concentrations are summarized in Table 10. Notably, neat virgin PLA and plasticized **PLA-ATBC** films were also prepared for comparison.

COF-DOPA and **COF-DOPAe** nanosheets were firstly suspended in $CHCl_3$, and afterwards they were added in the required proportion and uniformly dispersed into the polymeric matrix by means of ultrasonication, since it has been reported that sonication helps to disperse hydrophilic particles into PLA based polymeric solutions.[368] The resulting suspensions were cast onto a glass plate and then $CHCl_3$ was evaporated at 60 ºC for 1 h. The films were subsequently dried at 40 ºC for 24 h, and finally they were vacuum-dried to remove traces of solvent.

Table 10. Bionanocomposite film formulations.

Materials	PLA (wt%)	ATBC (wt%)	COF-DOPA (wt%)	COF-DOPAe (wt%)
PLA	100			
PLA/ATBC	85	15		
PLA/ATBC-COF-$DOPA_{0.5}$	84.58	14.93	0.5	
PLA/ATBC-COF-$DOPAe_{0.5}$	84.15	14.85	1	
PLA/ATBC-COF-$DOPA_1$	82.45	14.55	3	
PLA/ATBC-COF-$DOPAe_1$	84.58	14.93		0.5
PLA/ATBC-COF-$DOPA_3$	84.15	14.85		1
PLA/ATBC-COF-$DOPAe_3$	82.45	14.55		3

Transparency is one of the most important aspects to consider when designing new food packaging materials. As shown in Fig. 95a, the reinforced bionanocomposite films proved to be transparent, displaying a reddening effect upon increasing COF content. This amber tonality has been previously observed for other PLA blends formulations containing catechol moieties.[377,388] The transparency was also corroborated by UV-visible absorption measurements (Fig. 95b).

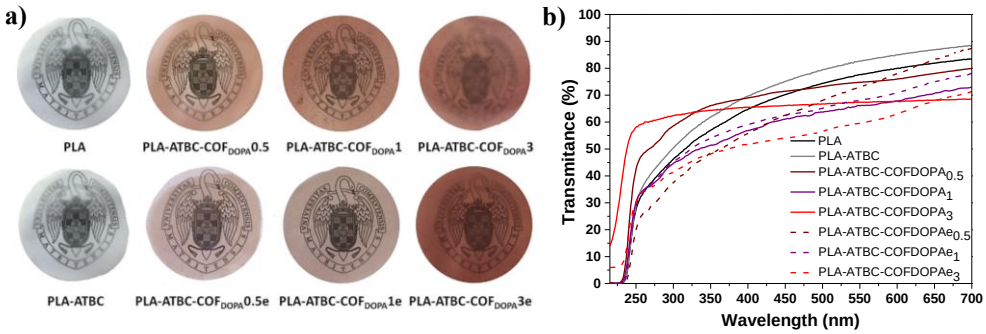

Figure 95. (a) Visual appearance of films and (b) UV-vis spectra measurements.

The microstructural characterization of the cross cryo-fractured sections of PLA, plasticized PLA (**PLA-ATBC**) as well as the **COF-DOPA** and **COF-DOPAe** reinforced bionanocomposite films was observed by FESEM (Fig. 96). As expected, neat PLA film shows a smooth and regular surface typical of amorphous polymers (Fig 96a). **PLA-ATBC** blend (Fig. 96b) shows a rougher surface with no apparent phase separation as a result of the homogeneous dispersion of the plasticizer into the PLA matrix. In the case of bionanocomposites, a rigid and rougher fracture surface is observed for the ones reinforced with non-exfoliated **COF-DOPA** at 0.5 and 1 wt% (Fig. 96c and e), with the presence of small voids, suggesting a poor interfacial adhesion probably due to aggregates formation. On the contrary, these voids tend to disappear in the case of exfoliated **COF-DOPAe** at 0.5 and 1 wt% (Fig. 96d and f). These results suggest that COF nanosheets are able to enhance the interfacial adhesion of the polymeric matrices. Moreover, different regions are clearly observed in the bionanocomposites loaded with higher amounts of COF (3 wt%), displaying ductile and brittle behavior as well as holes, indicating a poor interfacial adhesion due to the irregular dispersion of the COF materials in these formulations (Fig. 96g and h).

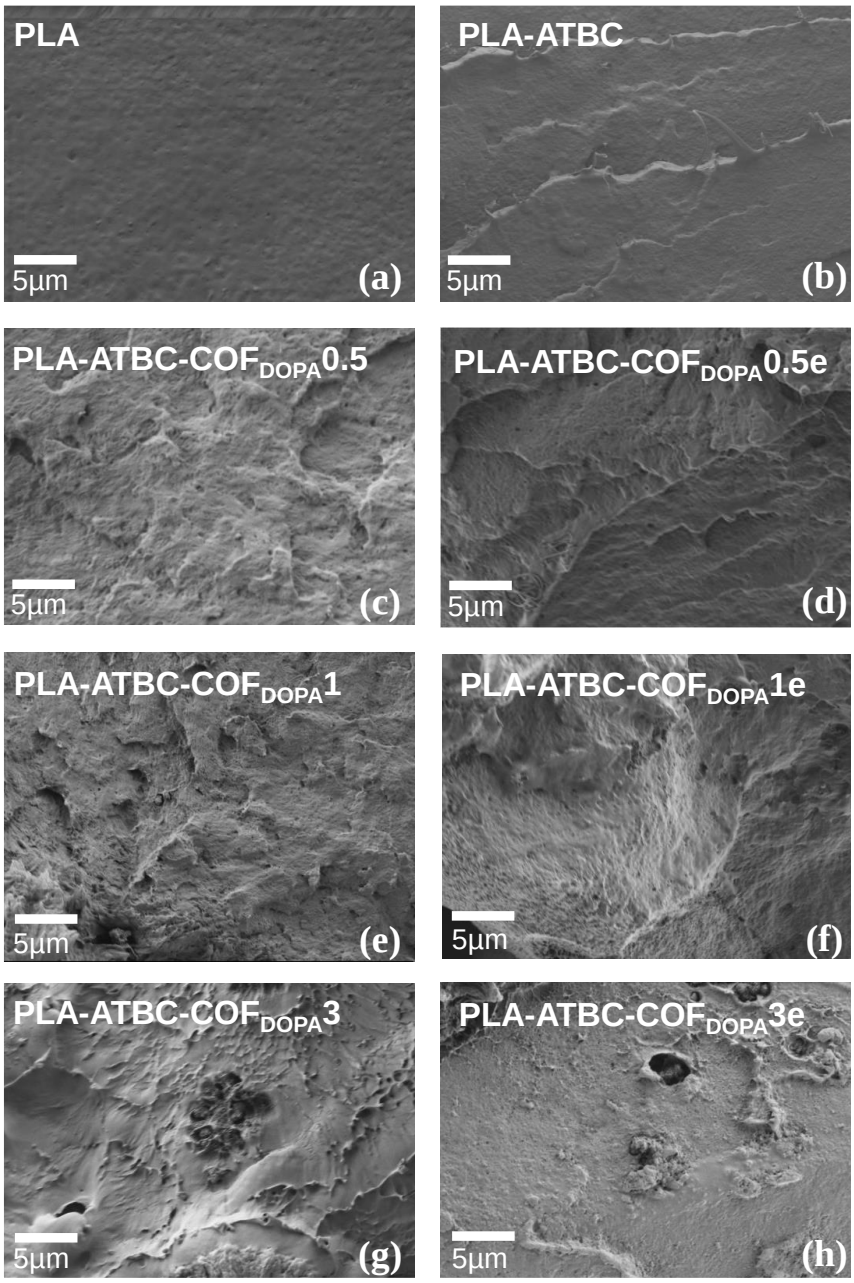

Figure 96. FESEM image of the cryofracture of bionanocomposite films.

Since these materials are intended for food packaging applications, the thermal stability of each formulation was analyzed by isothermal TGA at 180 ºC for 20

minutes (Fig. 97a), which is the typical temperature at which PLA polymer is processed by extrusion. Thus, under isothermal conditions an increased thermal stability is observed for all functionalized bionanocomposite films compared to neat PLA and plasticized **PLA-ATBC**. These results, notably enhanced for the exfoliated COFs, corroborate the thermal stability of the developed formulations for industrial melt-processing in the plastic field. The effect of **COF-DOPA** and **COF-DOPAe** on the thermal properties of the polymeric matrix was also evaluated by dynamic TGA measurements (Fig. 97b). In accordance with previous reports, plasticized PLA displays lower thermal stability than neat PLA.[367] However, the incorporation of **COF-DOPA** and **COF-DOPAe** increased the onset degradation temperature (T_o) of PLA-ATB blend between 9 and 22 ºC, while the maximum degradation temperature (353-356 ºC) is not significantly affected. These results corroborate a successful improvement of the thermal stability of the bionanocomposites due to the incorporation of the 2D nanoparticles.

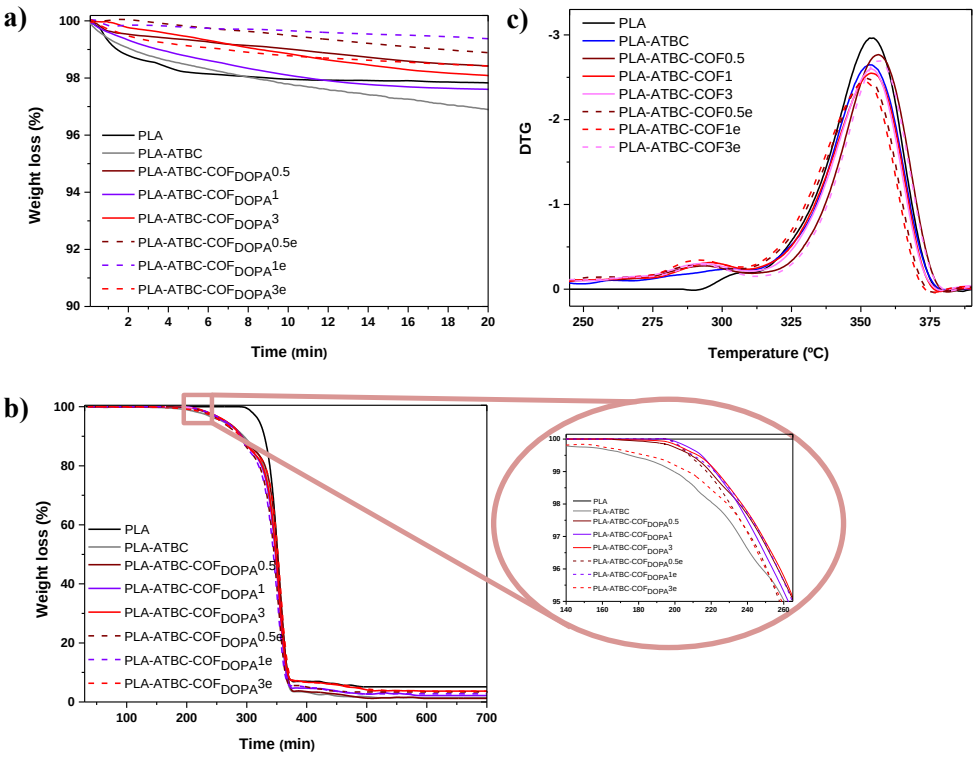

Figure 97. (a) Isothermal TGA and (b) dynamic TGA and (c) DTG of bionanocomposite films.

The mechanical properties of the bionanocomposite films were performed by means of a nanoindenter test. The elastic modulus (E) and hardness (H) for each sample was calculated in the range from 500 to 1000 nm (Fig. 98). As expected, PLA-ATBC displays lower E and H values, indicating the effectiveness of ATBC as a plasticizer. On the contrary, functionalized films show increased E and H values, especially those reinforced with **COF-DOPAe** at 0.5 wt% and 1 wt%, which were able to increase the elastic modulus of PLA matrix in 55.9 and 68.6%, respectively, implying their successful reinforcing effect.

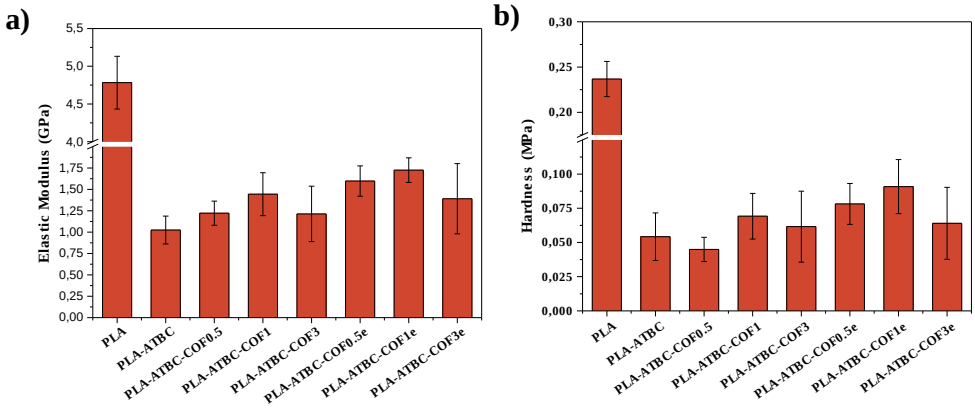

Figure 98. Nanomechanical results: (a) elastic modulus (E) and (b) nanohardness (H).

Since the developed films are intended for non-migratory food packaging applications, overall migration studies were performed in a fatty food simulant D1 (ethanol 50 % v/v). Thus, the bionanocomposites were totally immersed in screw cap vials containing the food simulant (area-to-volume ratio= 6 dm^2 kg^{-1} food simulant) at 40 ºC for 10 days.[389] Then, the films were removed and the solvent evaporated. The vials were further dried in an oven at 110 ºC for 30 min, and the remaining residue was weighted. Overall migration results are shown in Fig. 99a. As it can be inferred, bionanocomposites loaded with high amounts of non-exfoliated **COF-DOPA** (1 wt% and 3 wt%) or exfoliated **COF-DOPAe** at 3 wt% exceed the legal overall migration limit (60 mg kg^{-1} of food simulant): **PLA-ATBC-COF$_{DOPA}$1**= 0.14 mg dm^{-2}, **PLA-ATBC-COF$_{DOPA}$3**= 0.16 mg dm^{-2} and **PLA-ATBC-COF$_{DOPA}$3e**= 0.15 mg dm^{-2}.[390] On the contrary, those bionanocomposite films loaded with low amounts of **COF-DOPA** (0.5 wt%) and **COF-DOPAe** (at 0.5 wt% and 1 wt%) did not exceed the legal regulatory limit, demonstrating its viability for the development of food packaging materials. To gain insight into the migrated compounds, the obtained residue after the migration studies was redissolved in the food simulant D1 and the antioxidant activity was

measured using the DPPH method, determining the reduction of the absorbance at 517 nm by UV-Vis spectroscopy. The radical scavenging activity (RSA) was calculated from Equation (5):

$$RSA\ (\%) = \frac{A_{Control} - A_{Sample}}{A_{Control}} x\ 100\% \qquad (5)$$

where $A_{Control}$ is the absorbance of 2,2-difenil-1-picrylhydrazyl (DPPH) in ethanolic solution and A_{Sample} the absorbance of DPPH after 15 min in contact with each film. As expected, the films that were below the legal overall migration limit (PLA, **PLA-ATBC**, **PLA-ATBC-COF$_{DOPA}$0.5**, **PLA-ATBC-COF$_{DOPA}$0.5e** and **PLA-ATBC-COF$_{DOPA}$1e**) did not show any change in the DPPH absorbance, proving the non-migratory behaviour. On the contrary, the residue from the bionanocomposites that were above the regulatory limits presented antioxidant activity (a slight decrease in the DPPH absorbance could be observed at 517 nm), suggesting that the functionalized COF nanosheets were migrating from the film to the foodstuff.

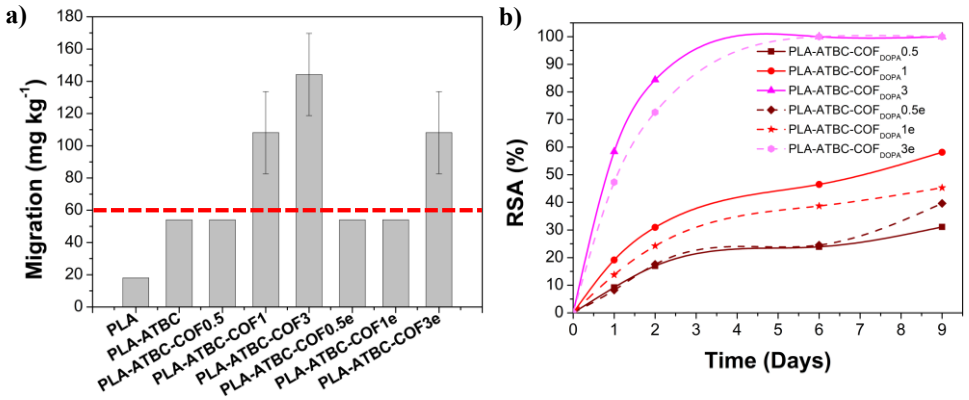

Figure 99. (a) Overall migration and (b) RSA of bionanocomposite films.

To evaluate the antioxidant capacity of the bionanocomposites the DPPH-method was also used. Thus, all films were totally immersed in glass vials containing a DPPH solution in methanol (area-to-volume ratio= 6 dm^2 L^{-1} DPPH). To assure full contact between the bionanocomposites and the DPPH solution, the films were stored at room temperature in the dark for 10 days, and UV-Vis measurements were then performed. Plasticized **PLA-ATBC** film was considered as control sample (not shown). As expected, non-functionalized PLA and **PLA-ATBC** films did not display any antioxidant activity, while the COF functionalized films show efficient DPPH radical scavenging activity (Fig 99b). The RSA results are expressed as the equivalent of gallic acid (GA) concentration (mg kg^{-1}) by using

a calibrated curve of gallic acid concentration versus RSA (%). As shown in Fig. 99b, the antioxidant activity is boosted upon increasing concentrations of the **COF-DOPA** or **COF-DOPAe**. It is worth mentioning that the bionanocomposites that complied the legislation displaying non-migratory behavior still present an efficient antioxidant activity despite the lower concentrations of dopamine-COF.

6.3 Conclusions

In this chapter, the copper-catalyzed azide-alkyne cycloaddition reaction has been explored as an efficient approach for the post-synthetic functionalization of COFs, allowing the incorporation of active catechol moieties into the pore walls. All the COFs have been characterized by solid-state characterization techniques, supporting the successful preparation of the materials. In addition, it has been proved that the crystalline and porous structure is preserved after the post-synthetic modification.

Due to its layered structure, **COF-DOPA** has been successfully processed and exfoliated into COF nanosheets, which have been further incorporated and dispersed into plasticized PLA matrix in 0.5, 1 and 3 wt%. Even though high transparent bionanocomposites were obtained, a slightly reddish hue could be observed in the developed films. Notably, the incorporation of exfoliated and non-exfoliated **COF-DOPA** to the polymeric blend (**PLA-ATBC**) resulted in a significant enhancement of the thermal stability and mechanical performance of the resulting films. In addition, the non-migratory behavior of the functionalized bionanocomposites was evaluated. According to the results, the films reinforced with higher amounts of **COF-DOPA** (1 wt% and 3 wt%) and **COF-DOPAe** (3 wt%) exceed the legal overall migration limits, while lower concentrations of the **COF-DOPA** (0.5 wt%) and **COF-DOPAe** (0.5 wt% and 1 wt%) prevent the release of the active compound into the foodstuff. These results are in good agreement with FESEM micrographs, in which a better interfacial adhesion is observed for smaller concentrations of **COF-DOPA** and **COF-DOPAe** in the polymeric matrix. Finally, the inherent antioxidant activity of the bionanocomposites was investigated using the DPPH method, revealing that the functionalized material could successfully scavenge the DPPH radical. Even though there is still a long way ahead, this work can motivate further research for the synthesis of new covalently functionalized active COFs for the development of novel smart packaging materials with non-migrating antioxidant features.

Chapter 7:

Experimental Section

7.1 General techniques

All air and moisture sensitive reactions were carried out under argon atmosphere using standard Schlenk techniques. All chemicals and solvents, unless stated otherwise, were purchased from commercial suppliers and used as received. Purification by column chromatography was carried out on silica gel (flash column, SiO_2= 40-63 μm). Thin-layer chromatography (TLC) was carried out using pre-coated silica gel 60 F254 and developed in the corresponding solvent system. Compounds were visualized under UV light (λ = 365 or 254 nm).

- *FTIR Spectroscopy*: infrared spectra were recorded in a Bruker Tensor 27 spectrophotometer equipped with an ATR dispositive. The signals are expressed in wavenumber units (cm^{-1}).
- *Nuclear Magnetic Resonance Spectroscopy (NMR)*: ^{1}H and ^{13}C NMR spectra were recorded in a Bruker Avance-300 spectrometer at 298 K using partly deuterated solvents as internal reference. Chemical shifts are reported in ppm and referenced to the residual non-deuterated solvent frequencies ($CDCl_3$: δ 7.26 ppm for ^{1}H, 77.0 ppm for ^{13}C; DMSO-d_6: 2.50 ppm for ^{1}H, 39.52 for ^{13}C). Coupling constants (*J*) are expressed in Hertzs (Hz) and depending on their multiplicity the signals are reported as follows: s = singlet, d = doublet, t = triplet, q = quartet, quint = quintet, dt = doublet of triplets, ddt = double doublet of triplets, m = multiplet, bs = broad singlet.
- *^{13}C-CP/MAS-NMR spectroscopy*: solid-state NMR spectra were recorded on a Bruker AVANCE III HD-WB 400 MHz spectrometer using a 4mm MAS WB DVT probe and 2.5 mm ZrO_2 rotors. Cross-polarization with magic angle spinning (CP-MAS) was used to acquire the ^{13}C data at a spinning rate of 12 kHz.
- *Mass Spectrometry (MS)*: mass spectra were obtained by electrospray ionization (ESI) in a Bruker HCT-Ultra ion trap mass spectrometer or by fast atom bombardment (FAB) ionization in a Finnigan MAT95XP system from Thermo Fisher. High-resolution mass spectra were measured by the matrix-assisted laser desorption/ionization time-of-flight (MALDI-TOF/TOF) technique in a Bruker ULTRAFLEX mass spectrometer using DCTB as matrix.
- *Powder X-ray diffraction (PXRD)*: PXRD diffraction patterns were collected with a Bruker X'PERT MPD X-ray diffractometer using conventional Bragg-Brentano geometry and Cu Kα radiation (λ = 1.5406 Å). Patterns were measured in the 2θ = 2° - 40° range with a step size of 0.04° and an exposure time of 2 s/step.

- *Nitrogen adsorption/desorption isotherms*: measurements were carried out at 77 K on a Micromeritics Tristar 3000 instrument. Samples were previously activated under high vacuum (<10-7 bar) at 120 °C.
- *Thermogravimetric analysis (TGA)*: thermograms were recorded with a TGA-Q50 instrument on a platinum plate, heating the samples under nitrogen atmosphere at a heating rate of 10 °C min^{-1}.
- *Scanning electron microscopy (SEM)*: SEM images were obtained using a JOEL JSM 6335F scanning electron microscope. Samples were dispersed over a slice of conductive graphite adhesive, which was placed on a flat copper sample holder, and then gold-coated with a sputter coater.
- *High resolution scanning electron microscopy (HRSEM)*: HRSEM images were acquired using a Hitachi S-8000 model with field emission filament and a voltage of 1.0 kV.
- *Transmission electron microscopy (TEM)*: TEM micrographs were obtained using a JEOL JEM 2100 transmission electron microscope operating at 200 kV.

7.2 Chapter-specific techniques

Chapter 3 - Theoretical methods and structure modelling

Molecular modeling, powder diffraction simulation and Pawley refinement were carried out using The Accelrys Materials Studio software package (version 5.5). All structures were optimized including energy minimization and cell parameters optimization employing the parameters from the Universal Force Field.[391] The experimental data was subjected to a Pawley refinement where the peak positions and line shape parameters were refined using the Pseudo-Voigt peak shape position.

Chapter 3 - X-ray photoelectron spectroscopy (XPS)

XPS experiments were performed in ultrahigh vacuum (UHV) chamber. MgKα radiation excites core level photoelectrons, which are detected using a Specs Phoibos-150 electron analyzer with a constant pass energy of 20 eV. The electron analyzer axis was fixed and coincided with the surface normal. The core level binding energies were calibrated using as references the binding energies of C 1s and Au 4f in contact with the sample. The line shape of core levels was fitted using

a Shirley background and asymmetric singlet pseudo-Voigt functions. The fit was optimized using a Levenberg–Marquardt algorithm with a routine running in IGOR Pro (WaveMatrix Inc.).[392] The quality of the fit was judged from a reliability factor, the normalized χ^2.

Chapter 3 - Electrochemical measurements for energy conversion

Electrochemical experiments were carried out with a Bipotentiostat PGSTAT302N MBA (Metrohm Autolab) using the software package NOVA 1.11 (Metrohm Autolab).

For the static electrochemical measurements, a glass and Teflon cell were used. Glassy Carbon (GC) electrodes (0.07 cm^2 Ø of an electrochemical area of 0.1 cm^2) from CH Instruments were used as working electrodes, Pt wire as counter electrode and a saturated calomel electrode (SCE) as reference electrode.

Rotating disk-ring electrode (RRDE) measurements were carried out using a glassy carbon disk/platinum ring RRDE electrode from PINE and the same counter and reference electrode as in static measurements. A modulated speed rotator from PINE Instruments and a commercial electrochemical cell adapted to rotating disc electrodes were used. **DAPT-TFP-COF** was suspended in doubled distilled Milli-Q water (1 mg mL^{-1}) and sonicated for 15 min. The generated black suspension was drop-casted over glassy carbon electrodes (**DAPT-TFP-COF**/GC) in different volumes to get insight into the effects of the deposited amount of COF material. The optimal GC electrodes modification was carried out by drop-casting 10 µL of the **DAPT-TFP-COF** suspension (1mg mL^{-1}) and letting it dry at room temperature. 5 µL of 1 mg/mL platinum on carbon (10 wt%) in 20% EtOH, 0.02% Nafion ink were drop-casted over the GC electrodes and allowed to dry at room temperature. Suspensions of 1 mg of **DAPT-TFP polymer** in 1 mL of Milli Q water were prepared and sonicated for 30 min. 10 µL of the suspension were then drop-casted over GC disc electrodes of at the disc of a GC disc/ Pt ring RRDE.

3 mm thick carbon discs of 15 mm Ø for mounting specimens were used to take the SEM micrographs of **DAPT-TFP-COF** before and after electrocatalysis. The **DAPT-TFP-COF** modified Carbon disc (10 µL of **DAPT-TFP-COF** suspension in an area around 0.1 cm^2) was used as working electrode, and a potential of -0.4 V

vs. SCE was applied with the electrode surface immersed in an O_2 saturated 0.1 M NaOH solution for 10000 seconds.

Chapter 3 – Electrochemical measurements for energy storage

All the salts (NH_4Cl, KCl, NaCl, LiCl, NaF and Na_2SO_4) used in the preparation of the aqueous electrolytes used in the study were purchased from Sigma Aldrich. The preparation of the **DAPT-TFP polymer** solid-electrode was carried out by mixing the 2D material with a solid (powder) polytratefluoroethylene (PTFE) binder (90:10 wt%). Then, the paste was rolled into a platinum mesh with coin/circular shape. For the pyrene-4,5,9,10-tetraone (**PTO**) and 2,7-diaminopyrene-4,5,9,10-tetraone (**DAPT**) electrode preparation a conductive carbon additive (carbon C-Nergy Timcal Super C65, from Imerys) was incorporated into the mixture to obtain the paste with the following weight percentage proportion: active material 80%, carbon additive 10%, and PTFE 10%.

The electrochemical characterization was performed by cyclic voltammetry using a three-electrode configuration where an Ag/AgCl electrode was used as reference electrode and a platinum wire as counter electrode. The system was controlled by a Biologic VMP multichannel potentiostat.

Chapter 4 – Theoretical methods and structure modelling

Density Functional Theory (DFT) calculations were carried out in order to optimize ground state geometries of the 2D CTFs, as well as their 3D crystal structure in different stacking fashions.

The periodic models of the 2D structures were optimized with CASTEP plane-wave DFT code.[300] The calculations account for an empirical efficient vdW R^{-6} correction (DFT+TS method).[393] Additionally, infinite crystal-bulk structures in both the eclipsed stacking (AA) and the staggered stacking (AB) fashions have been computed for each CTF material. The theoretical crystal-powder diffractograms have been simulated from the DFT-optimized structures by using the MERCURY package.[394] A direct comparison between the experimental and simulated PXRD reveals that in both materials the best agreement is obtained for the simulated eclipsed pattern.

Chapter 5 – Fluorescence studies

The fluorescence spectra of **QBR-COF** were recorded on a Jasco FP-6300 spectrofluorometer. **QBR-COF** was dispersed in a mixture of THF:H_2O (1:1) at a concentration of 0.08 mg mL^{-1} and further sonicated for 5 min. UV–vis spectra were obtained with a UV–vis spectrometer for solid samples. The base line was register using Teflon.

The fluorescence titrations were performed by systematically increasing the concentration of Zn^{2+} in the cuvette and subsequent record of the fluorescence intensity of **QBR-COF** from an initial concentration of $1x10^{-5}$ M until a concentration of $2x10^{-4}$ M. For all the measurements, the excitation wavelength was λ_{ex} = 450 nm and the corresponding emission wavelength was recorded from λ_{em} = 460-750 nm.

To explore the sensing properties towards different metal ions, the fluorescence spectra of **QBR-COF** in a mixture of THF:H_2O (1:1) was recorded before and after adding different metal ions to a concentration of $1.2x10^{-4}$ M.

Fluorescence emission spectra of **QBR-COF** was also recorded within a pH range from 1-7 for five subsequent cycles.

Chapter 5 – Energy-dispersive X-ray spectroscopy (EDX)

The morphology of **QBR-COF** was visualized using a JEOL 6400 JSM microscope in transmission mode operated at 25 kV. EDX of the sample was performed with a resolution of 133 eV.

Chapter 6 – Characterization of exfoliated COF-DOPA

The particle size of **COF-DOPAe** dispersed in $CHCl_3$ was determined by dynamic light scattering analyser (DLS, Zetasizer Nano series ZS, Malvern Instrument Ltd., U.K.) at 20 ºC.

Micrographs of **COF-DOPAe** nanosheets were observed by Transmission Electron Microscopy (TEM, JEOL JEM-1010) operating at 100 kV. One droplet of

the material suspension was deposited on carbon-coated copper grids and dried at room temperature during 20 min before observation.

Chapter 6 – Characterization of bionanocomposites

The absorption spectra of nanocomposites, obtained in the 700-250 nm region, were measured using a Perkin-Elmer (Lambda 35, USA) UV-VIS spectrophotometer.

FESEM micrographs of the cryo-fractured cross-sections of the films were acquired with a field emission scanning electron microscope (FESEM) ZEISS model ULTRA 55 (Eindhoven, The Netherlands). Image acquisitions were conducted at an accelerating voltage of 5 kV. Prior to be observed fractured surfaces of samples were coated with a thin layer of platinum in a high vacuum sputter coater EM MED20 from Leica Microsystem (Milton Keynes, United Kingdom).

Thermogravimetric analysis (TGA) was conducted in Linseis TGA PT1000 (Selb, Germany) under isothermal mode at 180 ºC for 20 min and under dynamic mode with a heating rate of 10 ºC/min, from 30 to 700 ºC, in a N_2 atmosphere (flow 20 cm^3/min).

The nanomechanical properties of films were measured by a nanoindenter machine G-200 (Agilent Technologies, Santa Clara, CA, USA). All samples were indented in the same experiment. Indentations were performed at maximum 1000 nm constant depth using a Berkovich diamond tip. An array of 8 indentations was performed for each sample. The function area used to estimate the contact area at low depths was previously calibrated in fused silica. The stiffness required to calculate the contact area beyond indenter and elastic modulus was obtained by means of the continuous stiffness measurement (CSM) technique.[377,395] The CSM technique provides in-depth profiles of the hardness (H) and elastic modulus (E).

Overall migration studies were conducted in a faty food simulant (Simulant D1= ethanol 50% v/v), by the total immersion of the bionanocomposite films in food simulant D1 (area-to-volume ratio= 6 dm^2 kg^{-1} food simulant) at 40 ºC for 10 days. After 10 days films were removed, and the food simulant was evaporated on a heating plate and then dried in an oven at 110 ºC for 30 min. The residue was

weighed in an analytical balance Sartorius BP211D (Goettingen, Germany) to ± 0.1 mg to determine the overall migration expressed as mg/ kg of food simulant.

The obtained residue after the overall migration tests was dissolved in 2.25 mL of 50% v/v ethanol and the antioxidant activity was determined according to the DPPH-method, determining the reduction of the absorbance at 517 nm by UV–Vis using a Varian Cary spectrophotometer. The radical scavenging activity (RSA) was determined according to Equation (5).

$$RSA\ (\%) = \frac{A_{Control} - A_{Sample}}{A_{Control}}\ x\ 100\% \quad (5)$$

where $A_{Control}$ is the absorbance of 2,2-difenil-1-picrylhydrazyl (DPPH) in ethanolic solution and A_{Sample} the absorbance of DPPH after 15 min in contact with each film. The results were expressed as radical scavenging activity (RSA), denoted as the equivalent of gallic acid (GA) concentration (mg kg^{-1}) by using a calibrated curve of gallic acid concentration versus RSA (%).

7.3 Synthetic details and characterization

Pyrene-4,5,9,10-tetraone (1)[262]

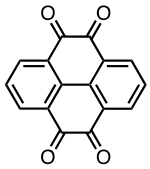

To a solution of pyrene (5.0 g, 24.7 mmol) in CH_2Cl_2 (100 mL) and MeCN (100 mL) was added $NaIO_4$ (42.8 g, 0.2 mol), H_2O (125 mL), and $RuCl_3xH_2O$ (0.67 g, 3.0 mmol). The dark brown suspension was heated at 40 °C overnight. The organic solvents were removed under reduced pressure. Subsequently the dark green residue was filtrated and rinsed with 500 mL of H_2O. Purification by flash column chromatography (SiO_2, CH_2Cl_2) afforded **1** as golden needles (1.49 g, 23%). ^1H NMR (300 MHz, $CDCl_3$) δ (ppm): 8.52 (d, *J* = 8 Hz, 4H), 7.73 (t, *J* = 8 Hz, 2H). ^{13}C NMR (75 MHz, DMSO-d_6) δ (ppm): 131.3, 131.5, 134.8, 136.8, 178.2. FTIR (ATR), ῡ (cm^{-1}): 1704, 1690, 1683, 1673, 1560, 1451, 1422, 1337, 1282, 1273, 1175, 1104, 1055, 1002, 961, 909, 807, 710, 643, 547. HRMS (MALDI-TOF) calcd. for $C_{16}H_6O_4$ $[M]^+$: 262.0264; found: 262.0264. Mp >350 ºC (literature mp > 350 ºC).

2,7-Dinitropyrene-4,5,9,10-tetraone (2)[262]

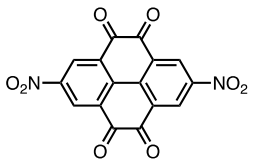

A mixture of fuming nitric acid (5 mL) and 98% sulfuric acid (5 mL) was added dropwise to **1** (2.0 g, 7.5 mmol), and the resulted orange solution was heated at 85 ºC for an hour. The same amount of the sulfonitric mixture was added to the flask for two more times at a 1 hour interval. After 1 h, the suspension was allowed to cool down to room temperature and it was poured into 40 mL of H_2O. The suspension was filtrated and rinsed with H_2O, and then dried in vacuum to afford **2** as a bright yellow powder (2.2 g, 83%). ^{1}H NMR (300 MHz, DMSO-d_6) δ (ppm): 8.89 (s, 4H). ^{13}C NMR (75 MHz, DMSO-d_6) δ (ppm): 174.3, 148.8, 135.9, 134.2, 126.0. FTIR (ATR), ϑ (cm^{-1}): 3089, 1720, 1693, 1687, 1651, 1588, 1529, 1519, 1421, 1342, 1282, 1242, 1092, 1013, 986, 949, 932, 746, 712, 583. HRMS (MALDI-TOF) calcd. for $C_{16}H_4N_2O_8$ $[M]^+$: 351.9968; found: 351.9976. Mp >350 ºC.

2,7-Diaminopyrene-4,5,9,10-tetraone (3, DAPT)[262]

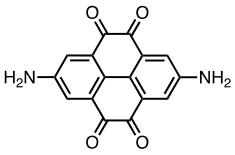

Acetic acid (2.0 mL) and concentrated hydrochloric acid (2.0 mL) were added to **2** (200 mg, 0.57 mmol) to form a yellow suspension which was heated at 50 °C for 15 min. Then $SnCl_2 \cdot 2H_2O$ (1.02 g, 4.50 mmol) was slowly added and the reaction mixture was stirred at 50 °C for 4 h. After that, the mixture was cooled in an ice bath and the resulting brown precipitate was filtrated and repeatedly washed with Et_2O. A solution of NaOH 2M was added dropwise to the brown solid whereupon it turned into a deep purple colour. This precipitate was filtered, washed with H_2O and dried under vacuum to afford **DAPT** (119.5 mg, 72%) which was used without further purification. ^{1}H NMR (300 MHz, DMSO-d_6) δ (ppm): 7.36 (s, 4H), 5.97 (bs, 4H, -NH_2). ^{13}C NMR (75 MHz, DMSO-d_6) δ (ppm): 178.34, 148.42, 130.79, 124.40, 118.91. FTIR (ATR) ϑ (cm^{-1}): 3469, 3437, 3343, 3211, 3078, 1663, 1614, 1590, 1447, 1339, 1270, 1074, 1032, 896, 828, 709. Mp >350 ºC.

1,3,5-triformylphloroglucinol (4, TFP)[263]

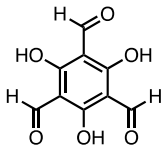

To a solution of 2,7-formamidine acetate (8.20 g, 79.3 mmol) and phloroglucinol (2.00 g, 15.9 mmol) in THF (200 mL) at 45 °C acetic anhydride (14.7 mL, 159 mmol) was added, and the reaction was stirred for 24 h. After the reaction time THF solvent was removed under reduced pressure, followed by stirring in water (200 mL) at 40 °C for 2 h. Aqueous LiOH (2 M, 600.0 mL, 1.2 mol) was slowly added. After 18 h aqueous HCl (2 M, 300 mL, 600 mmol) was added, whereupon a very pale salmon-coloured powder precipitated. The product was extracted into CH_2Cl_2 (4 × 60 mL), dried over $MgSO_4$ and evaporated to give pure **TFP** as a white powder (1.71 g, 51%). ^{1}H NMR (300 MHz, $CDCl_3$) δ (ppm): 14.12 (s, 3H), 10.15 (s, 3H). ^{13}C NMR (75 MHz, $CDCl_3$) δ (ppm): 192.15, 173.59, 108.83. FTIR ($CHCl_3$) $\tilde{\upsilon}$ (cm^{-1}): 3832, 2886, 1631, 1591, 1434, 1384, 1247, 1187, 964, 872, 786, 609. HRMS (MALDI-TOF) calcd. for $C_9H_6O_6$ $[M]^+$: 210.0168; found: 210.0159. Mp 197-199 ºC (literature mp 198-200 ºC).

DAPT-TFP polymer[260]

A suspension of **DAPT** (20.86 mg, 0.071 mmol) and **TFP** (10.00 mg, 0.048 mmol) in DMA/*o*-DCB (0.5 mL/0.5 mL) and AcOH (6M, 50 μL) in a Pyrex vessel (ϕ = 18 mm, h = 10 cm) was briefly sonicated to get a homogenous dispersion. The ampoule was degassed *via* three freeze-pump-thaw cycles, flame sealed and heated at 120 °C for 5 days. The resulting polymer was collected by filtration and repeatedly washed with DMA and H_2O. After Soxhlet extraction with THF, the dark brown recovered solid was dried under vacuum for 12 h at 90 ºC affording **DAPT-TFP** (24 mg, 86% yield). ^{13}C NMR (100 MHz, ss-CP/MAS) δ (ppm): 180, 150, 142, 135, 110. FTIR (ATR) $\tilde{\upsilon}$ (cm^{-1}): 1558, 1424, 1256, 1089, 803, 602.

DAPT-TFP-COF

In a pyrex tube (ϕ = 18 mm, h = 10 cm) **DAPT** (100 mg, 0.34 mmol) and **TFP** (86 mg, 0.41 mmol) were suspended in a mixture of DMA/*o*-DCB (2.5 mL/2.5 mL) and AcOH (6M, 0.25 mL). The mixture was sonicated for 3 min to get a

homogenous dispersion and the tube was further degassed via three freeze-pump-thaw cycles, flame sealed and heated at 120 °C for 5 days. The resulting precipitate was isolated by filtration and further extracted with CO_2 under supercritical conditions for 6 h yielding 121.28 mg (90%) of **DAPT-TFP-COF** as a brown powder. ^{13}C NMR (100 MHz, ss-CP/MAS) δ (ppm): 193.3, 183.9, 177.9, 156.47, 137.1, 130.1, 109.3, 103.7. FTIR (ATR) ῡ (cm^{-1}): 1683, 1565, 1442, 1422, 1251, 1149, 1092, 989, 890, 822, 730, 668. PXRD 2θ (°): 3.54, 6.97. 11.54, 28.31.

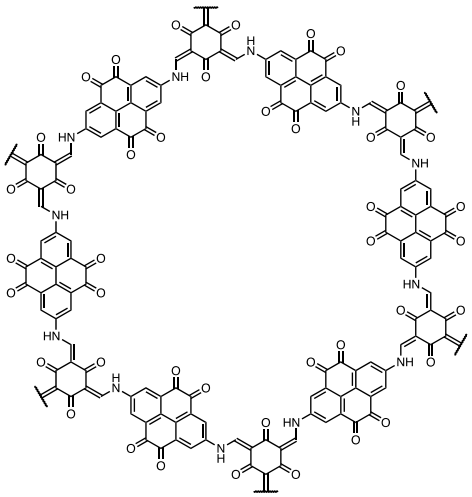

2,7-Dibromopyrene-4,5,9,10-tetraone (5)[396]

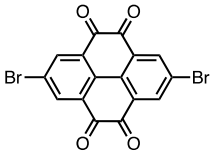

In a 25 mL round bottom flask **1** (100 mg, 0.38 mmol) was added into 2 ml of H_2SO_4 and then NBS (223 mg, 1.14 mmol) was added into the mixture. The resulting reaction mixture was stirred at 40 ºC for 2 h. The reaction was quenched with water (200 mL) and the precipitate was collected by filtration and repeatedly washed with water. Recrystallization from CH_2Cl_2 afforded **3** (128.2 mg, 80%) as an orangish powder. ^1H NMR (300 MHz, $CDCl_3$), δ (ppm): 8.59 (s, 4H). FTIR (ATR), ῡ (cm^{-1}): 3069, 2853, 1717, 1689, 1576, 1547, 1461, 1418, 1374, 1255, 1089, 1048, 902, 755, 723. HRMS (MALDI-TOF) calcd. for $C_{16}H_4Br_2O_4$ $[M]^+$: 417.8460; found: 417.8476. Mp >350 ºC.

2,7-Dibromo-4,5,9,10-tetraomethoxypyrene (6)[396]

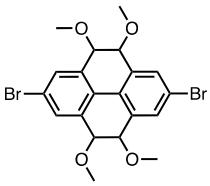

To a solution of **5** (450 mg, 1.07 mmol) and n-Bu_4NBr (241.8 mg, 0.75 mmol) in THF (10 mL) and water (6 mL), $Na_2S_2O_4$ (1.14 g, 6.54 mmol) was added and the resulting mixture was stirred at 25 ºC for 5 min. Dimethyl sulfate (1.41 g, 11.1 mmol) and aqueous NaOH (1.09 g, 27.2 mmol) were added to the solution and the mixture was stirred at 40 ºC for 4 h. Then, toluene and water were added and the organic phase was washed with brine, dried over $MgSO_4$, filtered, and concentrated *in vaccuo.* The residue was purified by recrystallization from CH_2Cl_2 to afford **4** (411.5 mg, 80%) as a white solid. ^{1}H NMR (300 MHz, $CDCl_3$) δ (ppm): 8.55 (s, 4H), 4.18 (s, 12H). ^{13}C NMR (75 MHz, $CDCl_3$) δ (ppm): 111.8, 119.3, 120.8, 121.5, 123.5, 162.2. FTIR ($CHCl_3$) ϋ (cm^{-1}): 2996, 2968, 2955, 1602, 1496, 1475, 1449, 1312, 1265, 1206, 1154, 1092, 997, 988, 910, 881, 808, 786, 730. HRMS (MALDI-TOF) calcd. for $C_{20}H_{20}Br_2O_4$ $[M]^+$: 481.9728; found: 481.9710. Mp > 350 ºC.

2,7-Dicyano-4,5,9,10-tetraomethoxypyrene (7)[396]

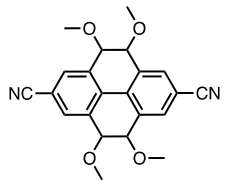

Compound **6** (290 mg, 0.6 mmol) and CuCN (161 mg, 1.8 mmol) were suspended in 5 mL of N,N-dimethylacetamide under argon and the resulting mixture was refluxed at 180 ºC for 10 h. After cooling to room temperature, aqueous solution of $FeCl_3$ (1 M, 200 mL) and CH_2Cl_2 (10 mL) were added to the mixture. Then the organic phase was washed with brine and dried over $MgSO_4$, filtered, and concentrated *in vaccuo.* The residue was purified by flash column chromatography (SiO_2, CH_2Cl_2) to afford **5** as a yellow solid (126.3 mg, 56 %). ^{1}H NMR (300 MHz, $CDCl_3$) δ (ppm): 8.73 (s, 4H), 4.22 (s, 12H). ^{13}C NMR (75 MHz, $CDCl_3$) δ (ppm): 142.5, 123.4, 121.5, 113.4, 32.7, 30.6. FTIR ($CHCl_3$) ϋ (cm^{-1}): 2949, 2920, 2851, 2230, 1592, 1478, 1429, 1396, 1312, 1233, 1216, 1135, 997, 966, 901, 878, 791, 776, 732, 634. HRMS (MALDI-TOF) calcd. for $C_{22}H_{20}N_2O_4$ $[M]^+$: 376.1423; found: 376.1413. Mp >350 ºC (literature mp > 350 ºC).

Py-CTF

Compound **7** (60 mg, 0.16 mmol, 1 eq.) and P_2O_5 (68.6 mg, 0.48 mmol, 3 eq.) were loaded into a Pyrex tube, which was further degassed *via* three freeze-pump-thaw cycles and flame sealed. The reaction time for the synthesis of P_2O_5-catalyzed covalent triazine framework was around 12 hours at 400 ℃. The temperature was slowly increased to 400 ℃ at a ramping rate of 2 ℃/min, and holding 2 hours every 80 ℃ increase. After the reaction time (12 hours at 400 ℃), the temperature was slowly decreased to room temperature at a ramping rate of 5 ℃/min. The resulting precipitate was filtered off, washed exhaustively with water, dimethyl sulfoxide, and methanol. The solid was subjected to Soxhlet extraction with THF for 2 days and dried under vacuum at 120 ℃ overnight, yielding 50 mg of **Py-CTF** as a bright dark solid. ^{13}C NMR (100 MHz, ss-CP/MAS) δ (ppm): 145-115 ppm. FTIR (ATR) ῡ (cm^{-1}): 1554, 1135, 1042. PXRD 2θ (°): 3.85, 22.61.

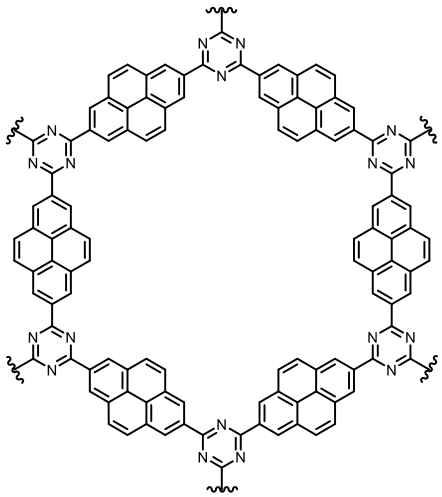

Tetrakis(4-bromophenyl)ethylene (8)[397]

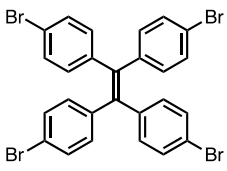

To a solution of tetraphenylethylene (3.05 g, 10.54 mmol) in 20 mL of glacial acetic acid and 20 mL of dichloromethane, Br_2 (4.31 mL, 84.32 mmol) was added dropwise at 0 ºC. The reaction mixture was stirred at room temperature for 3 h, and then it was poured into 150 mL ice

water. The organic phase was extracted with CH_2Cl_2, dried over $MgSO_4$, filtered and concentrated *in vacuo*. Recrystallization from methanol afforded **8** as a white solid (5.65 g, 95%). ^{1}H NMR (300 MHz, $CDCl_3$) δ (ppm): 7.26 (d, *J* = 8 Hz, 8H), 6.85 (d, *J* = 8 Hz, 8H). ^{13}C NMR (75 MHz, $CDCl_3$) δ (ppm): 142.1, 139.6, 132.9, 131.4, 122.2. FTIR (ATR, CH_2Cl_2) ῡ (cm^{-1}): 3087, 3054, 3025, 2925, 2851, 1903, 1712, 1655, 1583, 1485, 1392, 1349, 1267, 1225, 1176, 1103, 1071, 1008, 862, 793, 739. HRMS (MALDI-TOF) calcd. for $C_{26}H_{16}Br_4$ $[M]^+$: 643.7986; found: 643.7798. Mp 250-252 ºC (literature mp 251-252 ºC).

Tetrakis(4-cyanophenyl)ethylene (9)[398]

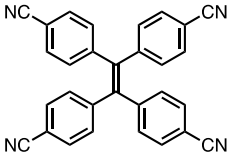

To a solution of **8** (2.0 g, 3.1 mmol) in 20 mL of anhydrous DMF, CuCN (2.2 g, 30.8 mmol) was added. The reaction flask was vacuumed/flashed with argon three times, and the reaction mixture was refluxed under argon atmosphere for 48 h. Then the reaction mixture was poured into 150 mL of water, and *N*,*N'*-dimethylethylenediamine (5 mL, 75 mmol) was added. The reaction was stirred for additional 1 h at100 ºC. After cooling to room temperature, the resulting precipitate was filtered and thoroughly washed with water, affording **9** as a yellow solid (0.93 g, 70%). The product was used without further purification. ^{1}H NMR (300 MHz, $CDCl_3$) δ (ppm): 7.49 (d, *J* = 8 Hz, 8H), 7.08 (d, *J* = 8 Hz, 8H). ^{13}C NMR (75 MHz, $CDCl_3$) δ (ppm): 112.21, 118.17, 131.74, 132.45, 141.63, 145.63. FTIR ($CHCl_3$) ῡ (cm^{-1}): 3449, 3360, 3193, 3062, 2921, 2798, 2224, 2117, 1708, 1670, 1601, 1552, 1500, 1401, 1266, 1111, 977, 950, 874, 838, 733, 699. HRMS (MALDI-TOF) calcd. for $C_{30}H_{16}N_4$ $[M]^+$: 432.1375; found: 432.1382. Mp 166-167 ºC.

Tetrakis(4-carboxyphenyl)ethylene (10)[398]

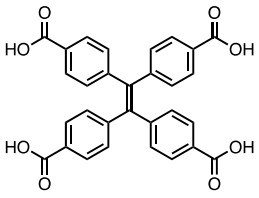

To a solution of **9** (4.5 g, 10.4 mmol) in ethylene glycol (250 mL), KOH (6 g, 107.2 mmol) was added and the reaction mixture was refluxed for 3 days. After cooling to room temperature, distilled water (30 mL) was added to the mixture, which was subsequently washed with CH_2Cl_2. The aqueous/ethylene glycol fraction was then acidified using HCl (1 M) and the

yellow precipitate was washed with water and CH_2Cl_2. Recrystallization from a CH_2Cl_2/EtOH mixture afforded **10** as a pale yellow solid (3.7 g, 70%). ^{1}H NMR (300 MHz, DMSO-d_6) δ (ppm): 12.84 (s, 4H), 7.73 (d, *J* = 8 Hz, 8H), 7.11 (d, *J* = 8 Hz, 8H). ^{13}C NMR (75 MHz, DMSO-d_6) δ (ppm): 129.16, 129.42, 130.87, 141.20, 146.46, 166.94. FTIR (ATR), ῡ (cm^{-1}): 1684, 1603, 1563, 1505, 1411, 1243, 1176, 1106, 1016, 586, 772, 747, 722, 630. HRMS (MALDI-TOF) calcd. for $C_{30}H_{20}O_8$ $[M]^+$: 508.1158; found: 508.1158. Mp 210-211 ºC.

Tetrakis(4-amidophenyl)ethylene (11, TA-TPE)

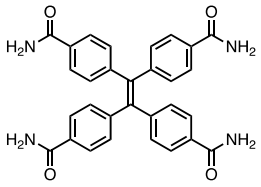

Compound **10** (200 mg, 0.46 mmol) and $SOCl_2$ (5 mL) were added to a 25 mL flask, and the mixture was refluxed for 1 h. After the reaction time, the excess of $SOCl_2$ was distilled, and NH_4OH was added dropwise to the resulting precipitate, whereupon it turned pale brown. The solid was filtered, washed with water and dried under vacuum affording **TA-TPE** (116.7 mg, 50%). ^{1}H NMR (300 MHz, DMSO-d_6) δ (ppm): 7.89 (s, 4H), 7.66 (d, *J* = 8 Hz, 8H), 7.31 (s, 4H), 7.06 (d, *J* = 8 Hz, 8H). ^{13}C NMR (125 MHz, DMSO-d_6) δ (ppm): FTIR (ATR), ῡ (cm^{-1}): 3383, 3355, 3311, 3270, 3216, 1652, 1603, 1552, 1385, 1270, 1181, 1115, 1016, 855, 778, 728, 636. HRMS (MALDI-TOF) calcd. for $C_{30}H_{24}N_4O_4$ $[M+Na]^+$: 527.1801; found: 527.1698.

TPE-CTF

TA-TPE (120 mg, 0.24 mmol) and P_2O_5 (101 mg, 0.71 mmol) were loaded into a Pyrex tube, which was further degassed *via* three freeze-pump-thaw cycles, flame sealed and heated at 400 ºC for 8 h. The temperature was slowly increased at a ramping rate of 2 ºC/min, and holding 2 h every 80 ºC. The resulting precipitate was filtered off, washed exhaustively with water, dimethyl sulfoxide, and methanol. The solid was subjected to Soxhlet extraction with THF for 2 days and dried under vacuum at 120 °C overnight, yielding **TPE-CTF** (88 mg, 85%) as a bright dark solid. ^{13}C NMR (100 MHz, ss-CP/MAS) δ (ppm): 145-120, 113.17. FTIR (ATR) ῡ (cm^{-1}): 3130, 2915, 2355, 2333, 2221, 1593, 1501, 1398, 1170, 988, 752, 704. PXRD 2θ (°): 3.82, 5.26, 24.03.

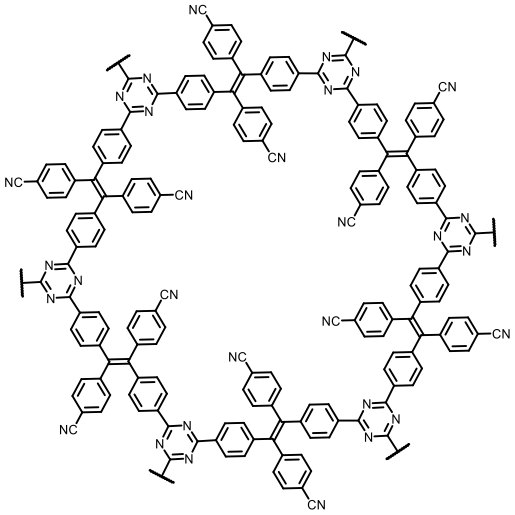

1,4-Dibromo-2,5-dimethoxybenzene (12)[399]

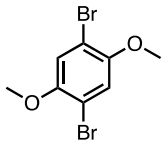

To a solution of *p*-dimethoxybenzene (5.0 g, 36.2 mmol) in anhydrous CH_2Cl_2 (25 mL) Br_2 (9.2 mL, 178 mmol) was added dropwise at room temperature in the absence of light. The reaction mixture was stirred for 1 h and poured into an excess amount of 1 M KOH. The solution was extracted with CH_2Cl_2, washed with water, dried over $MgSO_4$, filtered and concentrated *in vacuo*. Recrystallization from ethanol afforded **12** as a white solid (9.65 g, 90%). ^{1}H NMR (300 MHz, $CDCl_3$) δ (ppm): 7.10 (s, 2H), 3.85 (s, 6H). ^{13}C NMR (75 MHz, $CDCl_3$) δ (ppm): 150.5, 117.1, 110.5, 57.0. FTIR (ATR, CH_2Cl_2) ϑ (cm^{-1}): 1488, 1431, 1353, 1272, 1207, 1182, 1060, 1015, 855, 754. Mp 143-145 ºC (literature mp 144-145 ºC).

2,5-Dimethoxyterephthalaldehyde (13, DMTA)[350]

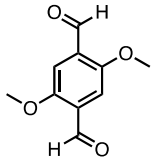

A solution of **12** (500 mg, 1.67 mmol) in anhydrous THF (8.5 mL) was cooled to -78 °C and *n*-BuLi (1.6 M in hexane, 2.3 mL, 3.68 mmol) was added dropwise. After 3 h, DMF (0.6 mL) was added and the resulting mixture was stirred for 1 h at -78 °C. The pale-yellow solution was allowed to reach room temperature and stirred for an additional h. The reaction mixture was quenched with saturated ammonium chloride, THF was

eliminated under reduced pressure and the resulting solution extracted with CH_2Cl_2. The organic phase was dried over $MgSO_4$ and the solvent removed *in vacuo*. Purification by flash column chromatography (SiO_2, 9:1 Hex/EtOAc) afforded **DMTA** as a yellow solid (258 mg, 78 %). ^{1}H NMR (300 MHz, $CDCl_3$) δ (ppm): 10.49 (s, 2H), 7.45 (s, 2H), 3.94 (s, 6H). ^{13}C NMR (75 MHz, $CDCl_3$) δ(ppm): 189.3, 155.7, 129.1, 110.9, 56.2. FTIR (ATR, CH_2Cl_2) ῡ (cm^{-1}): 2872, 1680, 1478, 1401, 1301, 1214, 1130, 1028, 880, 659. HRMS (MALDI-TOF) calcd. for $C_{10}H_{10}O_4$ $[M]^+$: 194.0579; found: 194.0583. Mp 205-207 ºC (literature mp 206-207 ºC).

2,5-Dihydroxyterephthalaldehyde (14, DHTA)[383]

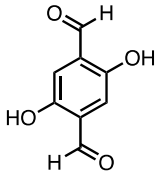

To a solution of **13** (900 mg, 4.64 mmol) in CH_2Cl_2 (20 mL) under Ar atmosphere BBr_3 (1M in CH_2Cl_2, 20 mL, 20 mmol) was added dropwise at -78 °C. The solution was allowed to warm to room temperature and stirred overnight. The reaction was quenched with water (40 mL) and the resulting mixture was extracted repeatedly with CH_2Cl_2. The organic phase was dried over $MgSO_4$, filtered, and concentrated *in vaccuo*. The resulting yellow solid was recrystallized from EtOAc to afford the title compound **14** (696 mg, 90 %).^{1}H NMR (300 MHz, $CDCl_3$) δ (ppm): 10.23 (s, 2H), 9.96 (s, 2H), 7.24 (s, 2H). ^{13}C NMR (75 MHz, DMSO-d_6) δ (ppm): 190.2, 152.8, 127.7, 115.17. FTIR (ATR, CH_2Cl_2) ῡ (cm^{-1}): 3280, 2888, 1668, 1477, 1281, 1127, 888, 832, 796, 679. Mp 242-245 ºC (literature mp 244-245 ºC).

2,5-Bis(propargyloxy)terephthalaldehyde (15, BPTA)

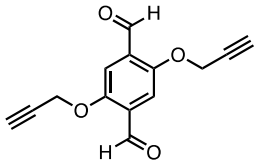

A mixture of **14** (300 mg, 1.8 mmol) and anhydrous K_2CO_3 (750 mg, 5.44 mmol) in anhydrous DMF (7 mL) was heated to 60 °C for 30 minutes, cooled to room temperature and propargyl bromide (80 % wt in toluene, 0.43 mL, 4.0 mmol) was added. The reaction mixture was stirred overnight and afterwards water was added to precipitate the product, which was collected by centrifugation (5 minutes, 6000 rpm). The supernatant was removed, water (10 mL) was added and the mixture centrifuged. This process was repeated 3 times affording a yellow solid which was filtered, dissolved in CH_2Cl_2,

dried over $MgSO_4$, filtered and the solvent removed under reduced pressure. **BPTA** was obtained as a yellow solid (406 mg, 93 %). ^{1}H NMR (300 MHz, $CDCl_3$) δ (ppm): 10.50 (s, 2H), 7.60 (s, 2H), 4.86 (d, ^4J = 3 Hz, 4H), 2.57 (t, ^4J = 3 Hz, 2H). ^{13}C NMR (75 MHz, $CDCl_3$) δ (ppm): 188.8, 153.8, 130.1, 113.3, 77.2, 76.9, 57.1. FTIR (ATR, CH_2Cl_2) ῡ (cm^{-1}): 3278, 3228, 2923, 2874, 2854, 2121, 1679, 1481, 1450, 1421, 1377, 1294, 1205, 1017, 878, 708, 654. Mp 144-146 ºC.

1,3,5-Tris-(4-nitrophenyl)benzene (16)[400]

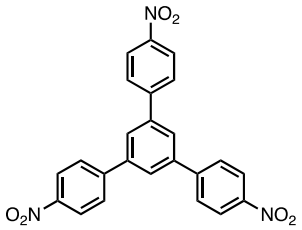

To a solution of 4'-nitroacetophenone (23 g, 140 mmol) in toluene (100 mL) trifluoromethanesulfonic acid (0.5 mL) was added. The mixture was then refluxed for 48 h and water was removed from the reaction mixture employing a Dean-Stark apparatus. After cooling to room temperature, the slurry was filtered giving a black solid which was thoroughly washed with boiling DMF to yield a pale green solid (6.89 g, 42 %). The product was insoluble in any common deuterated solvent. FTIR (KBr) ῡ (cm^{-1}): 1593, 1508, 1342, 1317, 1251, 1105, 861, 841, 814, 748, 689. Mp 151-153 ºC (literature mp 152-153 ºC).

1,3,5-Tris-(4-aminophenyl)benzene (17, TAPB)[401]

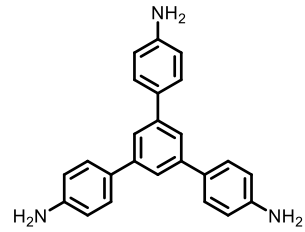

Compound **16** (5.0 g, 11.3 mmol) and Pd/C (10 % wt, 0.87 g) were refluxed in 200 mL of ethanol, and hydrazine hydrate (50- 60 %, 43 mL) was added dropwise through an addition funnel. The reaction mixture was then refluxed overnight, hot filtered through a 1 cm Celite pad and allowed to cool to room temperature. The resulting precipitate was further recrystallized from ethanol affording **TAPB** as a white solid (3.30 g, 92 %). ^{1}H NMR (300 MHz, $CDCl_3$) δ (ppm): 7.60 (s, 3H), 7.51 (d, ^3J = 9 Hz, 6H), 6.78 (d, ^3J = 9 Hz, 6H), 3.74 (bs, 6H). ^{13}C NMR (75 MHz, $CDCl_3$) δ (ppm): 145.8, 142.0, 131.9, 128.2, 122.9, 115.4. FTIR (KBr) ῡ (cm^{-1}): 3433, 3352, 3211, 3027, 1618, 1512, 1448, 1405, 1282, 1178, 827, 706, 560. HRMS (MALDI-TOF) calcd. for $C_{24}H_{21}N_3$ $[M]^+$: 351.1735; found: 351.1724. Mp 163-164 ºC (literature mp 164-165 ºC).

TPB-DMTP-COF [35]

A suspension of **DMTA** (84 mg, 0.43 mmol) and **TAPB** (100 mg, 0.29 mmol) in *o*-DCB/*n*-butanol (2 mL/2 mL) and acetic acid (6 M, 0.4 mL) was briefly sonicated for 2 minutes to get a homogenous dispersion. The tube was degassed *via* three freeze-pump-thaw cycles, flame sealed and heated at 120 °C for 3 days. The precipitate was filtered, Soxhlet extracted with THF and finally dried at 120 °C under vacuum overnight affording **TPB-DMTP-COF** (162 mg, 95 %) as a yellow powder. ^{13}C NMR (100 MHz, ss-CP/MAS) δ (ppm): 154.5, 149.1, 140.5, 138.3, 128.6, 123.1, 117.9, 110.1, 107.8, 80.2, 72.9, 56.8, 55.0. FTIR (ATR) ῡ (cm^{-1}): 2926, 1592, 1504, 1464, 1410, 1290, 1211, 1144, 1042, 879, 823, 693. PXRD 2θ (º): 2.94, 4.98, 5.76, 7.56, 9.82, 25.5.

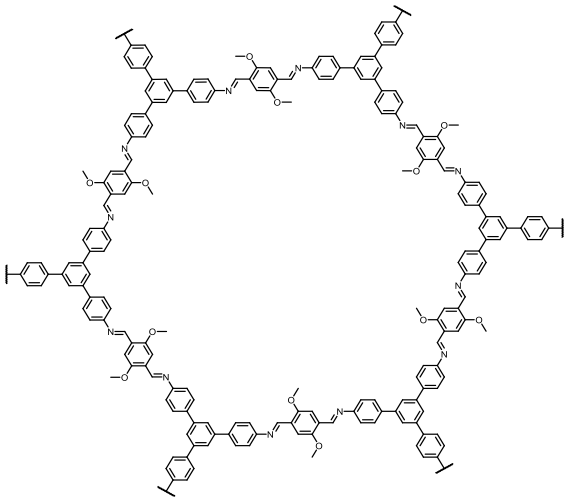

2-Iodo-1,3- diisopropylbenzene (18)[402]

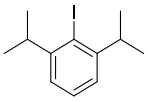

To a solution of 2,6-diisopropylaniline (400 mg, 2.26 mmol) in water (20 mL), 2.5 mL of HCl were added and the reaction mixture was stirred at room temperature overnight. The resulting solution was cooled to 0 °C, and a solution of $NaNO_2$ (202.4 mg, 2.93 mmol) in H_2O (3 mL) was added dropwise. The reaction mixture was stirred at 0 °C for 20 min, then a solution of KI (486.9 g, 2.93 mmol) in H_2O (3 mL) was added. After 4 h, the solution was extracted with Et_2O and the combined ether layers were washed with water, brine, dried over $MgSO_4$, filtered and the solvent removed under reduced

pressure. Purification by flash column chromatography (SiO_2, hexane) afforded **18** (273 mg, 42 %). ^{1}H NMR (300 MHz, $CDCl_3$) δ (ppm): 7.22 (m, 1H), 7.04 (m, 2H), 3.37 (septet, ^3J= 6.9 Hz, 2H), 1.20 (d, ^3J= 6.9 Hz, 12H). ^{13}C NMR (75 MHz, $CDCl_3$) δ (ppm): 151.1, 128.3, 123.8, 109.1, 39.4, 23.4. FTIR (CH_2Cl_2) ῡ (cm^{-1}): 2950, 2915, 2850, 2230, 1907, 1665, 1490, 1463, 1365, 1105, 1020, 910, 872, 835, 790, 728. Bp 95-97 ºC (literature bp 92-97 ºC).

2,6-Diisopropylphenylacetylene (19)[403]

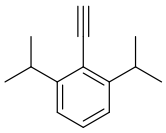

Compound **18** (158 mg, 0.55 mmol) was dissolved in 6 mL of piperidine, and $PdCl_2(PPh_3)_2$ (7.7 mg, 0.01 mmol) and CuI (1.04 mg, 0.005 mmol) were added. The solution was degassed, and trimethylsilylacetylene (0.12 mL, 0.83 mmol) was added under argon. The resulting mixture was stirred under argon at 65 ºC overnight. After cooling down to room temperature, the reaction mixture was passed through a silica plug (eluent: EtOAc) and the solvent was removed under reduced pressure. The residue was purified by flash column chromatography (SiO_2, hexane) to afford the crude TMS-protected alkyne as a pale-yellow oil which was directly carried to the next step. The oil was dissolved in MeOH (5 mL) and the solution was degassed by bubbling argon gas through for ca. 30 min. K_2CO_3 (156.66 mg, 1.13 mg) was added to the reaction flask, and the mixture was stirred at room temperature for 2 h. The solvent was removed under reduced pressure, and the solution was extracted with Et_2O, washed with water and brine, dried over $MgSO_4$, filtered and concentrated *in vacuo*. Purification by flash column chromatography (SiO_2, hexane) afforded **19** as a colourless oil (45 mg, 44% over 2 steps). ^{1}H NMR (300 MHz, $CDCl_3$) δ (ppm): 7.30 (t, J = 7 Hz, 1H), 7.14 (d, J = 7 Hz, 2H), 3.55 (sept, J = 7 Hz, 2H), 3.38 (s, 1H), 1.20 (d, J = 7 Hz, 12H). ^{13}C NMR (75 MHz, $CDCl_3$) δ (ppm): 151.7, 129.0, 122.3, 120.0, 85.3, 80.7, 31.8, 23.5. FTIR (CH_2Cl_2) ῡ (cm^{-1}): 2960, 2850, 1575, 1443, 1362, 1253, 1118, 1060, 930, 754. HRMS (MALDI-TOF) calcd. for $C_{14}H_{18}$ $[M]^+$: 186.1430; found: 186.1445.

QBR-COF

QBR-COF was synthesized by following a previously reported procedure based on Povarov reaction with slightly modifications.[44] **TPB-DMTP-COF** (100 mg), 2,6-diisopropylphenylacetylene (233 mg, 1.25 mmol), BF3•OEt_2 (100 μL, 0.75 mmol), chloranil (200 mg, 0.75 mmol), and toluene (50 mL) were added to an ace pressure tube. The tube was sealed and heated under argon at 110 °C for 3 days. After the reaction time, the mixture was cooled to room temperature and the precipitate was filtered. The reaction mixture was then washed with THF and quenched with saturated aqueous Na_2CO_3. The resulting precipitate was washed with H_2O, Soxhlet extracted with THF and dried under vacuum at 120 °C, yielding **QBR-COF** as a yellow solid (200 mg, quantitative). ^{13}C NMR (100 MHz, ss-CP/MAS) δ (ppm): 154.31, 148.93, 142.53, 136.72, 129.20, 124.83, 115.99, 56.39, 32.51, 25.10. FTIR (ATR) ῡ (cm^{-1}): 2964, 2857, 1681, 1582, 1545, 1461, 1410, 1402, 1208, 1180, 1038, 876, 835, 774. PXRD 2θ (°): 3.35, 11.36, 18.12, 20.65, 28.43.

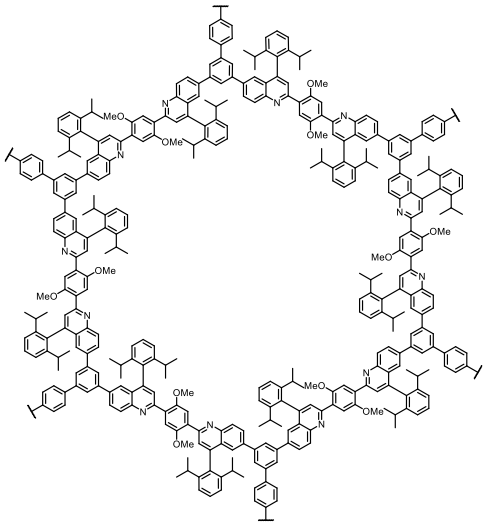

Dopamine azide (20)[384]

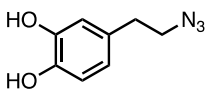

To a solution of dopamine hydrochloride salt (1.0 g, 5.27 mmol, 1.0 equiv) and $ZnCl_2$ (71.8 mg, 0.53 mmol, 0.1 eq.) in 25 mL H_2O:CH_3CN (3:7) Et_3N (2.21 mL, 15.81 mmol, 3.0 equiv.) and freshly prepared TfN_3 were added. The reaction mixture was stirred at

rt overnight, filtered, and the solvent was removed under reduced pressure to remove CH_3CN. The organic phase was extracted with EtOAc, dried over $MgSO_4$, filtered and the solvent removed *in vacuo*. Purification by flash column chromatography (SiO_2, 1:1 Hex/EtOAc) yielded the desired azide (**20**) as a reddish oil (730 mg, 74%). ^{1}H NMR (300 MHz, $CDCl_3$) δ (ppm): 6.80 (d, ^3J = 8 Hz, 1H), 6.74 (d, J = 2 Hz, 1H), 6.65 (dd, ^3J = 8 Hz, 1H), 6.42 (bs, 2H), 3.45 (t, ^3J = 8 Hz, 2H), 2.78 (t, ^3J = 8 Hz, 2H). 2.73 (t, J = 8 Hz, 2H). ^{13}C NMR (75 MHz, $CDCl_3$) δ (ppm): 143.4, 142.1, 131.0, 121.3, 116.0, 115.7, 52.4, 34.3. FTIR ($CHCl_3$) (cm^{-1}): 2929, 2878, 2098, 1606, 1519, 1445, 1686,1348, 1280,1234,1188,1148,1111, 1046, 984, 954, 916, 866, 808, 782, 751, 716, 666, 636, 608, 564. HRMS (ESI) calcd. for $C_8H_9N_3O_2$ $[M]^+$: 179.0695; found: 179.0562.

HC≡CH]$_{0.5}$-TPB-DMTP-COF[35]

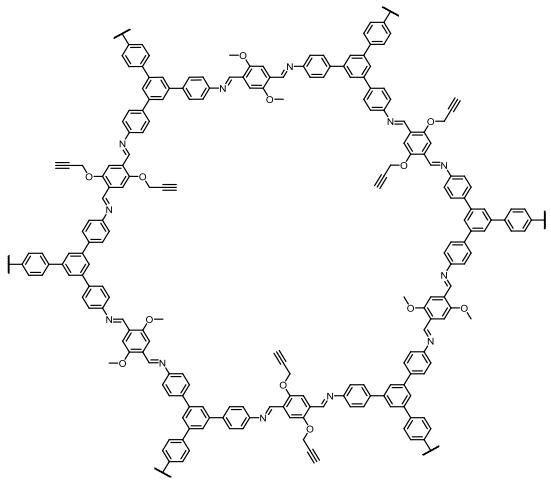

In a pyrex vessel (ϕ = 29 mm, h = 10 cm) **DMTA** (215 mg, 1.1 mmol), **BPTA** (270 mg, 1.1 mmol) and **TAPB** (515 mg, 1.48 mmol) were suspended in a mixture of *o*-DCB/ n-butanol (10 mL/10 mL) and acetic acid (6 M, 2.1 mL) was added. The mixture was briefly sonicated, and the tube was degassed via three freeze-pump-thaw cycles, flame sealed and heated at 120 °C for 3 days. The precipitate was collected by filtration, Soxhlet extracted with THF and dried at 120 °C under vacuum overnight to afford 870.0 mg (94 %) of **HC≡CH]$_{0.5}$-TPB-DMTP-COF** as a yellow powder. ^{13}C NMR (100 MHz, ss-CP/MAS) δ (ppm): 154.1, 148.7, 141.2, 137.8, 128.7, 122.7, 116.9, 110.7, 80.3, 73.3, 57.2, 54.6. FTIR (ATR) ῡ (cm^{-1}):

2357, 1590, 1500, 1462, 1410, 1369, 1286, 1206, 1177, 1144, 1031, 974, 876, 826, 725, 691, 671, 627, 598, 574. PXRD 2θ (°): 2.94, 4.98, 5.76, 7.56, 9.82, 25.5.

COF-DOPA[265]

To 100 mg of **[HC≡CH]$_{0.5}$-TPB-DMTP-COF** suspended in a mixture of THF/H2O (13 mL; 3/1), CuI (27.69 mg, 0.146 mmol) and DIPEA (87 μL, 0.50 mmol) were added. The suspension was purged with argon for 5 minutes, and 0.28 mL (0.28 mmol, 1 M THF) of **20** were added. The mixture was stirred overnight at room temperature under argon. After the reaction time, the solid was filtered and then washed with H_2O, MeCN and THF, and further dried under vacuum at 120 °C, yielding **COF-DOPA** as a reddish solid (170 mg, quantitative). ^{13}C NMR (100 MHz, ss-CP/MAS) δ (ppm): 154.33, 147.40, 140.99, 128.63, 123.06, 54.57. FTIR (ATR) ῡ (cm^{-1}): 1586, 1491, 1461, 1410, 1287, 1208, 1176, 1144, 1031, 878, 825, 787, 691, 663. PXRD 2θ (°): 2.89, 4.95, 5.69, 7.52, 9.82, 25.69

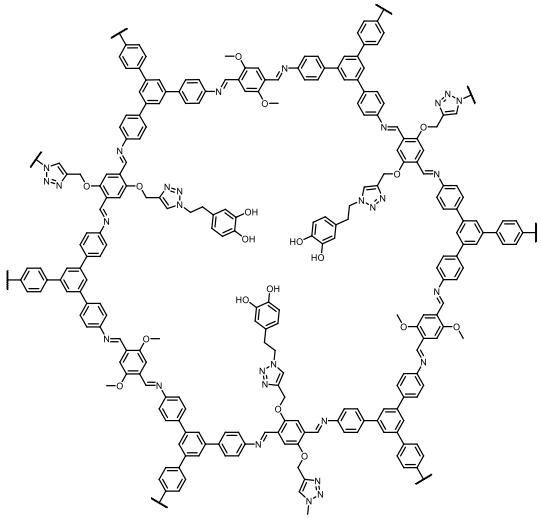

Summary

Covalent organic frameworks constitute an emerging class of organic polymeric materials which are formed through the atomically precise assembly of organic building units. One of the most important features of COFs is that they are fully designable, meaning that the selection of the appropriate building units allows the preparation of predefined extended hierarchical architectures with great control over chemical composition, topology and geometry. COFs also display several enhanced features compared to other traditional materials including lower densities, larger surface area and fine-tunable properties. In this regard, functionalization of COFs has enabled the design and preparation of novel materials with tuned properties towards tailored applications.

The introduction of specific functional groups within the COF structure has been tackled from two different perspectives: pre- and post-synthetically functionalization of the organic backbone. In the pre-synthetic modification approach, specific functional groups are introduced in the constituting building units prior to the formation of the COF. Remarkably, the additional functional group must not interfere with the experimental reaction conditions of the COF synthesis, which can hamper the preparation of the functionalized material in one step. Consequently, post-synthetic modifications are carried out to overcome this issue. To assure the successful modification, porosity of the framework is essential. Moreover, defects can arise from this strategy since it is highly difficult for the reagents to reach every active site of the framework. Therefore, unreacted sites might be randomly distributed along the network.

The main aim of the present doctoral thesis consists in the design and synthesis of novel COF-based materials for tailored applications. To achieve this goal, both functionalization strategies described above have been explored as powerful tools for preparing COFs with specific function and predesigned physical and chemical properties. The general approach involves the use of synthetic organic chemistry to prepare building units bearing specific functional groups which will impart readily functionality to the framework or in turn will serve as potential platforms for post-synthetic modification. The targeted COFs are constructed from these monomers, and subsequent post-synthetic reactions are carried out if needed. Due to the close relationship between the nanostructure of the COFs and their physicochemical properties, a fully characterization of their structural and textural properties has been performed by different means of solid-state characterization techniques. Finally, the COFs´ performance for the tailored application fields are investigated.

Thus, in Chapter 3 the design and synthesis of a robust polymeric enamine-based COF (**DAPT-TFP-COF**) through solvothermal synthetic conditions is described, including the preparation of the constituting monomers (namely **DAPT** and **TFP**) employing standard organic chemistry synthetic toolbox. Likewise, an analogous material has been prepared, **DAPT-TFP polymer**, which presents the same chemical composition but lacks the well stablished long-range order and porosity of **DAPT-TFP-COF**. The capability of these materials for efficient electrochemical reduction of oxygen is evaluated, showing that **DAPT-TFP-COF** is able to successfully electrocatalyze the oxygen reduction reaction through the efficient four-electron process readily leading to the formation of water instead of hydrogen peroxide. On the contrary, amorphous **DAPT-TFP polymer** electrocatalytic features are significantly lower. These remarkable results point towards the key role that crystallinity and porosity display in the final electrochemical properties of the framework. Additionally, and due to its outstanding chemical stability, an electrochemical study of **DAPT-TFP polymer** in different electrolytes is performed to gain insight into the potential of these materials as effective organic electrodes in energy storage applications.

Chapter 4 comprises the design and synthesis of novel covalent triazine frameworks (CTFs) under ionothermal conditions, affording the preparation of triazine-based COFs based on pyrene and tetraphenyl units (**Py-CTF** and **TPE-CTF**, respectively). The described protocol enables the cyclotrimerization reaction of the corresponding aromatic nitrile and amide groups catalyzed by P_2O_5. Remarkably, by selecting the proper synthetic conditions, a functionalized COF with unreacted nitrile groups within the pore surface can be obtained (**TPE-CTF**), since only the amide groups located in *trans* are involved in the reaction. Both frameworks display an enhanced crystalline structure compared to previously described CTFs, as revealed by their X-ray diffraction patterns. They also present high porosity and excellent thermal stability, unveiled by their nitrogen sorption isotherms and their thermogravimetric analysis. Therefore, both materials are successfully subjected to a thermal carbonization at 900 ºC, yielding porous carbon structures (**Py-CTF$_{900}$** and **TPE-CTF$_{900}$**) with enhanced conducting properties. The carbonized CTFs are tested as supercapacitor electrodes, with the material based on pyrene moieties presenting a higher capacitive nature, and proving the potential of these microporous CTFs for advanced energy-storage applications.

In Chapter 5, the synthesis of a starting imine-based COF (**TPB-DMTP-COF**) and a subsequent post-synthetic modification reaction of **TPB-DMTP-COF** *via* aza-Diels-Alder reaction is described, yielding **QBR-COF** as a novel polymeric material endowed with quinoline moieties and 2,6-diisopropylphenyl groups grafted onto its pores. Remarkably, while the crystallinity and porosity are preserved, the chemical and thermal stability together with the π-electron delocalization are significantly improved in the resultant quinoline-linked COF. Additionally, **QBR-COF** is evaluated as a potential platform for the development of a dual responsive sensory material: on one hand, as a "turn-on" selective fluorescent sensor towards Zn metal ions; and on the other hand, as an effective colorimetric-based pH sensor. These remarkable results promote the development of novel functionalized COFs and their application in this promising field, developing smart sensory materials that can be simultaneously applied in fluorescent and colorimetric sensing.

Finally, Chapter 6 is centered on the preparation of the necessary monomers, **DMTA**, **BPTA** and **TAPB**, under standard synthetic conditions, as well as the formation of the targeted COFs under solvothermal conditions. In this case, an imine-based COF with accessible alkyne groups is prepared, **[HC≡C]$_{0.5}$-TPB-DMTP-COF**, which in turn is post-synthetically modified *via* CuAAC reaction. Thus, a novel COF-based material is obtained, **COF-DOPA**, endowed with three dopamine moieties in its pores. The catechol-functionalized COF is processed and successfully exfoliated in covalent organic nanosheets (CONs) which are used for the preparation of novel PLA-based bionanocomposite films with nonmigrating antioxidant properties. Furthermore, the structural, thermal and mechanical features of these bionanocomposites are evaluated.

Resumen

Las redes orgánicas covalentes (*covalent organic frameworks*, COFs) constituyen una nueva clase de materiales poliméricos formados mediante el ensamblaje de subunidades orgánicas con precisión atómica. Una de las propiedades más relevantes de los COFs es que sus estructuras son fácilmente modulables, lo que implica que variando la elección de los monómeros constituyentes se pueden obtener estructuras previamente diseñadas con un gran control sobre la composición química, topología y geometría de la red. Los COFs presentan además otras ventajas frente a otro tipo de materiales tradicionales como una densidad baja, áreas superficiales elevadas y propiedades muy versátiles. En este sentido, la correcta funcionalización de estos polímeros ha permitido el diseño y obtención de nuevos materiales con propiedades avanzadas para su posterior aplicación en diversos campos.

La incorporación de grupos funcionales específicos en la estructura de los COFs se ha abordado desde dos perspectivas distintas: la funcionalización pre- y post-sintética. En el primer caso, los grupos funcionales específicos son incorporados en los monómeros de forma previa a la síntesis de los COFs. Cabe señalar que el grupo funcional no debe interferir con las condiciones de síntesis del polímero, lo cual limita enormemente la extensión de esta estrategia para la funcionalización de COFs en un solo paso. Con el objeto de solventar este inconveniente, la modificación post-síntesis se ha propuesto como una solución efectiva. Es importante señalar que en este caso la porosidad del material juega un papel clave, ya que en muchos casos los reactivos no pueden llegar a todos los centros activos del COF y por tanto una considerable cantidad de grupos funcionales quedan sin reaccionar dentro de la estructura, originando defectos en la red.

El objetivo principal de la presente tesis doctoral es el diseño y síntesis de nuevos COFs para aplicaciones sostenibles. Para conseguir este objetivo, se han explorado ambas estrategias de funcionalización con el objeto de obtener materiales poliméricos con las propiedades fisicoquímicas diseñadas. La táctica general incluye el empleo de estrategias sintéticas de química orgánica para la obtención de los monómeros orgánicos funcionalizados, a partir de los cuáles se obtendrán los COFs diseñados. En algunos casos, la estrategia de modificación post-sintética es aplicada para la obtención de nuevos materiales basados en COFs. Dada la estrecha relación entre la estructura y las propiedades de la red, los materiales sintetizados serán caracterizados de forma extensa mediante distintas

técnicas de caracterización en estado sólido. De forma adicional, se evaluarán las propiedades de los COFs en los distintos campos de aplicación investigados.

En este sentido, el capítulo 3 se centra en el diseño y síntesis de una nueva red covalente basada en enlaces enamina (**DAPT-TFP-COF**) mediante síntesis solvotermal a partir de los monómeros constituyentes (**DAPT** y **TFP**). De forma análoga, se prepara un material con la misma composición química pero de estructura amorfa y no porosa, y se estudia la aplicación de ambos materiales para catalizar la reducción electroquímica de oxígeno. Cabe señalar que la actividad electrocatalítica del COF es muy superior a la del material amorfo, destacando de este modo el papel clave que juegan la cristalinidad y porosidad en las propiedades electroquímicas de estos polímeros. De forma adicional, se incluye un estudio electroquímico detallado del polímero amorfo **DAPT-TFP polymer** en distintos electrolitos con el objeto de estudiar la potencial aplicación de estos materiales para el desarrollo de electrodos orgánicos en sistemas de almacenamiento de energía.

El capítulo 4 recoge el diseño y síntesis de dos nuevos COFs basados en enlaces de triazina (*covalent triazine frameworks*, CTFs) obtenidos mediante condiciones de síntesis ionotermal (**Py-CTF** and **TPE-CTF**). Las condiciones descritas permiten la obtención de los CTFs a través de la ciclotrimerización de los correspondientes grupos nitrilo o amida aromáticos, catalizada por P_2O_5. Cabe señalar que, a partir de la correcta optimización de las condiciones sintéticas, se ha preparado un COF funcionalizado con grupos nitrilo en los poros, ya que los grupos nitrilo situados en *trans* no reaccionan en estas condiciones y permanecen inmutables. Ambos materiales muestran estructuras altamente porosas y cristalinas en comparación con CTFs previamente descritos en la literatura, además de una estabilidad térmica excepcional. Motivados por estas propiedades, estos polímeros son sometidos a un tratamiento térmico a 900 ºC, permitiendo la obtención de nanoestructuras microporosas de carbono con propiedades conductoras y electroquímicas mejoradas. Una vez realizado el tratamiento, estos materiales pirolizados son estudiados como potenciales electrodos para el desarrollo de condensadores orgánicos, mostrando resultados altamente satisfactorios.

El capítulo 5 incluye la preparación de un COF basado en enlaces imina (**TPB-DMTP-COF**) y su posterior modificación post-sintética mediante una reacción de cicloadición aza-Diels-Alder, permitiendo la obtención de un nuevo material COF, **QBR-COF**, el cual incorpora unidades de quinolina en su esqueleto y grupos 2,6-

diisopropilfenilos en los poros de la red. Cabe señalar que tras la modificación el COF no sólo preserva sus propiedades cristalinas y porosas, sino que además presenta una mayor estabilidad química y térmica y una deslocalización electrónica mayor. De forma adicional, el COF se investiga para su potencial aplicación como sensor con una doble funcionalidad: por un lado, la detección selectiva de iones Zn mediante activación de la fluorescencia, y por otro lado como sensor óptico de pH. Estos prometedores resultados abren la puerta a futuras investigaciones con el objeto de desarrollar nuevos materiales inteligentes basados en COFs que puedan ser empleados de forma simultánea como sensores fluorescentes y colorimétricos.

Finalmente, el capítulo 6 se centra en la preparación de los monómeros necesarios (**DMTA**, **BPTA** y **TAPB**) para la obtención de un COF imina, **[HC≡C]$_{0.5}$-TPB-DMTP-COF**, mediante síntesis solvotermal y funcionalizado con grupos alquino terminales. Una vez obtenido el polímero de partida, mediante modificación post-sintética empleando una reacción de cicloadición catalizada por cobre (o reacción de tipo "click") se obtiene el **COF-DOPA**, el cuál incorpora tres unidades de catecol por poro. Este COF funcionalizado es después procesado y exfoliado en nanoláminas, las cuáles son empleadas posteriormente para el desarrollo de bionanocomposites de PLA con propiedades activas. Las propiedades estructurales, térmicas y mecánicas de estos films así como sus propiedades antioxidantes no-migratorias son evaluadas en esta sección.

References

[1] G. N. Lewis, *J. Am. Chem. Soc.* **1916**, *38*, 762–785.

[2] J.-M. Lehn, *Angew. Chemie Int. Ed. English* **1990**, *29*, 1304–1319.

[3] J. M. Lehn, *Science.* **1993**, *260*, 1762 LP – 1763.

[4] C. S. Diercks, O. M. Yaghi, *Science* **2017**, *355*, 923-931.

[5] O. M. Yaghi, *J. Am. Chem. Soc.* **2016**, *138*, 15507–15509.

[6] J. Jiang, Y. Zhao, O. M. Yaghi, *J. Am. Chem. Soc.* **2016**, *138*, 3255–3265.

[7] K. E. Cordova, O. M. Yaghi, *Mater. Chem. Front.* **2017**, *1*, 1304–1309.

[8] O. M. Yaghi, *ACS Cent. Sci.* **2019**, *5*, 1295–1300.

[9] J.-M. Lehn, *Chem. – A Eur. J.* **1999**, *5*, 2455–2463.

[10] J.-M. Lehn, A. V Eliseev, *Science.* **2001**, *291*, 2331 LP – 2332.

[11] M. Vendrell, D. Zhai, J. C. Er, Y.-T. Chang, *Chem. Rev.* **2012**, *112*, 4391–4420.

[12] J. Hu, S. K. Gupta, J. Ozdemir, M. H. Beyzavi, *ACS Appl. Nano Mater.* **2020**, *3*, 6239–6269.

[13] A. P. Côté, A. I. Benin, N. W. Ockwig, M. O. Keeffe, A. J. Matzger, O. M. Yaghi, *Science* **2005**, *310*, 1166– 1170.

[14] N. Huang, P. Wang, D. Jiang, *Nat. Rev. Mater.* **2016**, *1*, 16068.

[15] M. S. Lohse, T. Bein, *Adv. Funct. Mater.* **2018**, *28*, 1705553.

[16] X. Chen, K. Geng, R. Liu, K. T. Tan, Y. Gong, Z. Li, S. Tao, Q. Jiang, D. Jiang, *Angew. Chemie Int. Ed.* **2020**, *59*, 5050–5091.

[17] S. B. Alahakoon, S. D. Diwakara, C. M. Thompson, R. A. Smaldone, *Chem. Soc. Rev.* **2020**, *49*, 1344–1356.

[18] X. Ding, J. Guo, X. Feng, Y. Honsho, J. Guo, S. Seki, P. Maitarad, A. Saeki, S. Nagase, D. Jiang, *Angew. Chem. Int. Ed. Engl.* **2011**, *50*, 1289–1293.

[19] T.-Y. Zhou, S.-Q. Xu, Q. Wen, Z.-F. Pang, X. Zhao, *J. Am. Chem. Soc.* **2014**, *136*, 15885–15888.

[20] S. Dalapati, M. Addicoat, S. Jin, T. Sakurai, J. Gao, H. Xu, S. Irle, S. Seki, D. Jiang, *Nat. Commun.* **2015**, *6*, 7786.

[21] S.-Q. Xu, R.-R. Liang, T.-G. Zhan, Q.-Y. Qi, X. Zhao, *Chem. Commun.* **2017**, *53*, 2431–2434.

[22] Z.-J. Yin, S.-Q. Xu, T.-G. Zhan, Q.-Y. Qi, Z.-Q. Wu, X. Zhao, *Chem. Commun.* **2017**, *53*, 7266–7269.

[23] C. Qian, Q.-Y. Qi, G.-F. Jiang, F.-Z. Cui, Y. Tian, X. Zhao, *J. Am. Chem. Soc.* **2017**, *139*, 6736–6743.

[24] B. Zhang, H. Mao, R. Matheu, J. A. Reimer, S. A. Alshmimri, S. Alshihri, O. M. Yaghi, *J. Am. Chem. Soc.* **2019**, *141*, 11420–11424.

[25] S.-L. Cai, Z.-H. He, X.-L. Li, K. Zhang, S.-R. Zheng, J. Fan, Y. Liu, W.-G. Zhang, *Chem. Commun.* **2019**, *55*, 13454–13457.

[26] B. P. Biswal, S. Chandra, S. Kandambeth, B. Lukose, T. Heine, R. Banerjee, *J. Am. Chem. Soc.* **2013**, *135*, 5328–5331.

[27] J. Dong, Y. Wang, G. Liu, Y. Cheng, D. Zhao, *CrystEngComm* **2017**, *19*, 4899–4904.

[28] Z. Li, T. He, Y. Gong, D. Jiang, *Acc. Chem. Res.* **2020**, *53*, 1672–1685.

[29] L. M. Lanni, R. W. Tilford, M. Bharathy, J. J. Lavigne, *J. Am. Chem. Soc.* **2011**, *133*, 13975–13983.

[30] H. Ma, B. Liu, B. Li, L. Zhang, Y.-G. Li, H.-Q. Tan, H.-Y. Zang, G. Zhu, *J. Am. Chem. Soc.* **2016**, *138*, 5897–5903.

[31] A. Nagai, Z. Guo, X. Feng, S. Jin, X. Chen, X. Ding, D. Jiang, *Nat. Commun.* **2011**, *2*, 536.

[32] S. J. Rowan, S. J. Cantrill, G. R. L. Cousins, J. K. M. Sanders, J. F. Stoddart, *Angew. Chemie Int. Ed.* **2002**, *41*, 898–952.

[33] X. Chen, M. Addicoat, E. Jin, L. Zhai, H. Xu, N. Huang, Z. Guo, L. Liu, S. Irle, D. Jiang, *J. Am. Chem. Soc.* **2015**, *137*, 3241–3247.

[34] S. Kandambeth, D. B. Shinde, M. K. Panda, B. Lukose, T. Heine, R. Banerjee, *Angew. Chem. Int. Ed. Engl.* **2013**, *52*, 13052–13056.

[35] H. Xu, J. Gao, D. Jiang, *Nat. Chem.* **2015**, *7*, 905–912.

[36] M. Martínez-Abadía, A. Mateo-Alonso, *Adv. Mater.* **2020**, *32*, 2002366.

[37] T. Ma, E. A. Kapustin, S. X. Yin, L. Liang, Z. Zhou, J. Niu, L.-H. Li, Y.

Wang, J. Su, J. Li, X. Wang, W. D. Wang, W. Wang, J. Sun, O. M. Yaghi, *Science* **2018**, *361*, 48–52.

[38] A. M. Evans, L. R. Parent, N. C. Flanders, R. P. Bisbey, E. Vitaku, M. S. Kirschner, R. D. Schaller, L. X. Chen, N. C. Gianneschi, W. R. Dichtel, *Science.* **2018**, *361*, 52–57.

[39] A. M. Evans, I. Castano, A. Brumberg, L. R. Parent, A. R. Corcos, R. L. Li, N. C. Flanders, D. J. Gosztola, N. C. Gianneschi, R. D. Schaller, W. R. Dichtel, *J. Am. Chem. Soc.* **2019**, *141*, 19728–19735.

[40] L. Liang, Y. Qiu, W. D. Wang, J. Han, Y. Luo, W. Yu, G.-L. Yin, Z.-P. Wang, L. Zhang, J. Ni, J. Niu, J. Sun, T. Ma, W. Wang, *Angew. Chemie Int. Ed.* **2020**, *59*, 17991–17995.

[41] X. Feng, X. Ding, D. Jiang, *Chem. Soc. Rev.* **2012**, *41*, 6010–6022.

[42] B. T. Koo, W. R. Dichtel, P. Clancy, *J. Mater. Chem.* **2012**, *22*, 17460–17469.

[43] B. Lukose, A. Kuc, J. Frenzel, T. Heine, *Beilstein J. Nanotechnol.* **2010**, *1*, 60–70.

[44] X. Li, C. Zhang, S. Cai, X. Lei, V. Altoe, F. Hong, J. J. Urban, J. Ciston, E. M. Chan, Y. Liu, *Nat. Commun.* **2018**, *9*, 2998–3005.

[45] A. P. Côté, H. M. El-Kaderi, H. Furukawa, J. R. Hunt, O. M. Yaghi, *J. Am. Chem. Soc.* **2007**, *129*, 12914–12915.

[46] S. Jin, K. Furukawa, M. Addicoat, L. Chen, S. Takahashi, S. Irle, T. Nakamura, D. Jiang, *Chem. Sci.* **2013**, *4*, 4505–4511.

[47] M. Thommes, K. Kaneko, A. V Neimark, J. P. Olivier, F. Rodriguez-Reinoso, J. Rouquerol, K. S. W. Sing, *Pure Appl. Chem.* **2015**, *87*, 1051–1069.

[48] Y. Du, K. Mao, P. Kamakoti, B. Wooler, S. Cundy, Q. Li, P. Ravikovitch, D. Calabro, *J. Mater. Chem. A* **2013**, *1*, 13171–13178.

[49] P. Kuhn, M. Antonietti, A. Thomas, *Angew. Chemie Int. Ed.* **2008**, *47*, 3450–3453.

[50] X. Feng, L. Chen, Y. Honsho, O. Saengsawang, L. Liu, L. Wang, A. Saeki, S. Irle, S. Seki, Y. Dong, D. Jiang, *Adv. Mater.* **2012**, *24*, 3026–3031.

[51] S. Kandambeth, A. Mallick, B. Lukose, M. V Mane, T. Heine, R. Banerjee,

J. Am. Chem. Soc. **2012**, *134*, 19524–19527.

[52] A. Wilson, G. Gasparini, S. Matile, *Chem. Soc. Rev.* **2014**, *43*, 1948–1962.

[53] Y. Jin, C. Yu, R. J. Denman, W. Zhang, *Chem. Soc. Rev.* **2013**, *42*, 6634–6654.

[54] J. Guo, Y. Xu, S. Jin, L. Chen, T. Kaji, Y. Honsho, M. A. Addicoat, J. Kim, A. Saeki, H. Ihee, S. Seki, S. Irle, M. Hiramoto, J. Gao, D. Jiang, *Nat. Commun.* **2013**, *4*, 2736.

[55] B. Zhang, M. Wei, H. Mao, X. Pei, S. A. Alshmimri, J. A. Reimer, O. M. Yaghi, *J. Am. Chem. Soc.* **2018**, *140*, 12715–12719.

[56] X. Zhuang, W. Zhao, F. Zhang, Y. Cao, F. Liu, S. Bi, X. Feng, *Polym. Chem.* **2016**, *7*, 4176–4181.

[57] S. Ren, M. J. Bojdys, R. Dawson, A. Laybourn, Y. Z. Khimyak, D. J. Adams, A. I. Cooper, *Adv. Mater.* **2012**, *24*, 2357–2361.

[58] K. Wang, L.-M. Yang, X. Wang, L. Guo, G. Cheng, C. Zhang, S. Jin, B. Tan, A. Cooper, *Angew. Chem. Int. Ed. Engl.* **2017**, *56*, 14149–14153.

[59] F. J. Uribe-Romo, J. R. Hunt, H. Furukawa, C. Klöck, M. O'Keeffe, O. M. Yaghi, *J. Am. Chem. Soc.* **2009**, *131*, 4570–4571.

[60] G. Das, D. Balaji Shinde, S. Kandambeth, B. P. Biswal, R. Banerjee, *Chem. Commun.* **2014**, *50*, 12615–12618.

[61] F. J. Uribe-Romo, C. J. Doonan, H. Furukawa, K. Oisaki, O. M. Yaghi, *J. Am. Chem. Soc.* **2011**, *133*, 11478–11481.

[62] S. Dalapati, S. Jin, J. Gao, Y. Xu, A. Nagai, D. Jiang, *J. Am. Chem. Soc.* **2013**, *135*, 17310–17313.

[63] A. Nagai, X. Chen, X. Feng, X. Ding, Z. Guo, D. Jiang, *Angew. Chemie Int. Ed.* **2013**, *52*, 3770–3774.

[64] J. Guo, Y. Xu, S. Jin, L. Chen, T. Kaji, Y. Honsho, M. A. Addicoat, J. Kim, A. Saeki, H. Ihee, S. Seki, S. Irle, M. Hiramoto, J. Gao, D. Jiang, *Nat. Commun.* **2013**, *4*, 2736.

[65] Q. Fang, Z. Zhuang, S. Gu, R. B. Kaspar, J. Zheng, J. Wang, S. Qiu, Y. Yan, *Nat. Commun.* **2014**, *5*, 4503.

[66] S. Bi, C. Yang, W. Zhang, J. Xu, L. Liu, D. Wu, X. Wang, Y. Han, Q. Liang,

F. Zhang, *Nat. Commun.* **2019**, *10*, 2467.

[67] H. Lyu, C. S. Diercks, C. Zhu, O. M. Yaghi, *J. Am. Chem. Soc.* **2019**, *141*, 6848–6852.

[68] X. Chen, M. Addicoat, E. Jin, H. Xu, T. Hayashi, F. Xu, N. Huang, S. Irle, D. Jiang, *Sci. Rep.* **2015**, *5*, 14650.

[69] H. Li, Q. Pan, Y. Ma, X. Guan, M. Xue, Q. Fang, Y. Yan, V. Valtchev, S. Qiu, *J. Am. Chem. Soc.* **2016**, *138*, 14783–14788.

[70] P. J. Waller, S. J. Lyle, T. M. Osborn Popp, C. S. Diercks, J. A. Reimer, O. M. Yaghi, *J. Am. Chem. Soc.* **2016**, *138*, 15519–15522.

[71] H. Liu, J. Chu, Z. Yin, X. Cai, L. Zhuang, H. Deng, *Chem* **2018**, *4*, 1696–1709.

[72] B. J. Smith, W. R. Dichtel, *J. Am. Chem. Soc.* **2014**, *136*, 8783–8789.

[73] B. J. Smith, A. C. Overholts, N. Hwang, W. R. Dichtel, *Chem. Commun.* **2016**, *52*, 3690–3693.

[74] D. M. Fischbach, G. Rhoades, C. Espy, F. Goldberg, B. J. Smith, *Chem. Commun.* **2019**, *55*, 3594–3597.

[75] R. L. Li, N. C. Flanders, A. M. Evans, W. Ji, I. Castano, L. X. Chen, N. C. Gianneschi, W. R. Dichtel, *Chem. Sci.* **2019**, *10*, 3796–3801.

[76] C. Feriante, A. M. Evans, S. Jhulki, I. Castano, M. J. Strauss, S. Barlow, W. R. Dichtel, S. R. Marder, *J. Am. Chem. Soc.* **2020**, *142*, 18637–18644.

[77] M. M. Unterlass, *Angew. Chem. Int. Ed. Engl.* **2018**, *57*, 2292–2294.

[78] J. Á. Martín-Illán, D. Rodríguez-San-Miguel, C. Franco, I. Imaz, D. Maspoch, J. Puigmartí-Luis, F. Zamora, *Chem. Commun.* **2020**, *56*, 6704–6707.

[79] E. L. Spitler, M. R. Giovino, S. L. White, W. R. Dichtel, *Chem. Sci.* **2011**, *2*, 1588–1593.

[80] Z. Xie, B. Wang, Z. Yang, X. Yang, X. Yu, G. Xing, Y. Zhang, L. Chen, *Angew. Chem. Int. Ed. Engl.* **2019**, *58*, 15742–15746.

[81] P.-L. Wang, S.-Y. Ding, Z.-C. Zhang, Z.-P. Wang, W. Wang, *J. Am. Chem. Soc.* **2019**, *141*, 18004–18008.

[82] K. Wang, Z. Jia, Y. Bai, X. Wang, S. E. Hodgkiss, L. Chen, S. Y. Chong, X. Wang, H. Yang, Y. Xu, F. Feng, J. W. Ward, A. I. Cooper, *J. Am. Chem. Soc.* **2020**, *142*, 11131–11138.

[83] M. J. Bojdys, J. Jeromenok, A. Thomas, M. Antonietti, *Adv. Mater.* **2010**, *22*, 2202–2205.

[84] X. Guan, Y. Ma, H. Li, Y. Yusran, M. Xue, Q. Fang, Y. Yan, V. Valtchev, S. Qiu, *J. Am. Chem. Soc.* **2018**, *140*, 4494–4498.

[85] N. L. Campbell, R. Clowes, L. K. Ritchie, A. I. Cooper, *Chem. Mater.* **2009**, *21*, 204–206.

[86] H. Wei, S. Chai, N. Hu, Z. Yang, L. Wei, L. Wang, *Chem. Commun.* **2015**, *51*, 12178–12181.

[87] E. Troschke, S. Grätz, T. Lübken, L. Borchardt, *Angew. Chemie Int. Ed.* **2017**, *56*, 6859–6863.

[88] D. Zhou, X. Tan, H. Wu, L. Tian, M. Li, *Angew. Chemie Int. Ed.* **2019**, *58*, 1376–1381.

[89] D. D. Medina, J. M. Rotter, Y. Hu, M. Dogru, V. Werner, F. Auras, J. T. Markiewicz, P. Knochel, T. Bein, *J. Am. Chem. Soc.* **2015**, *137*, 1016–1019.

[90] D. Rodríguez-San-Miguel, A. Abrishamkar, J. A. R. Navarro, R. Rodriguez-Trujillo, D. B. Amabilino, R. Mas-Ballesté, F. Zamora, J. Puigmartí-Luis, *Chem. Commun.* **2016**, *52*, 9212–9215.

[91] Z.-Z. Gao, Z.-K. Wang, L. Wei, G. Yin, J. Tian, C.-Z. Liu, H. Wang, D.-W. Zhang, Y.-B. Zhang, X. Li, Y. Liu, Z.-T. Li, *ACS Appl. Mater. Interfaces* **2020**, *12*, 1404–1411.

[92] M. Zhang, J. Chen, S. Zhang, X. Zhou, L. He, M. V Sheridan, M. Yuan, M. Zhang, L. Chen, X. Dai, F. Ma, J. Wang, J. Hu, G. Wu, X. Kong, R. Zhou, T. E. Albrecht-Schmitt, Z. Chai, S. Wang, *J. Am. Chem. Soc.* **2020**, *142*, 9169–9174.

[93] J. W. Colson, A. R. Woll, A. Mukherjee, M. P. Levendorf, E. L. Spitler, V. B. Shields, M. G. Spencer, J. Park, W. R. Dichtel, *Science* **2011**, *332*, 228–231.

[94] P. Wang, Q. Wu, L. Han, S. Wang, S. Fang, Z. Zhang, S. Sun, *RSC Adv.* **2015**, *5*, 27290–27294.

[95] N. A. A. Zwaneveld, R. Pawlak, M. Abel, D. Catalin, D. Gigmes, D. Bertin,

L. Porte, *J. Am. Chem. Soc.* **2008**, *130*, 6678–6679.

[96] Z. Zha, L. Xu, Z. Wang, X. Li, Q. Pan, P. Hu, S. Lei, *ACS Appl. Mater. Interfaces* **2015**, *7*, 17837–17843.

[97] B. Sun, J. Liu, A. Cao, W. Song, D. Wang, *Chem. Commun.* **2017**, *53*, 6303–6306.

[98] T. Bao, P. Tang, D. Kong, Z. Mao, Z. Chen, *J. Chromatogr. A* **2016**, *1445*, 140–148.

[99] H. Wang, Z. Zeng, P. Xu, L. Li, G. Zeng, R. Xiao, Z. Tang, D. Huang, L. Tang, C. Lai, D. Jiang, Y. Liu, H. Yi, L. Qin, S. Ye, X. Ren, W. Tang, *Chem. Soc. Rev.* **2019**, *48*, 488–516.

[100] X. Wu, X. Han, Y. Liu, Y. Liu, Y. Cui, *J. Am. Chem. Soc.* **2018**, *140*, 16124–16133.

[101] H.-Q. Yin, F. Yin, X.-B. Yin, *Chem. Sci.* **2019**, *10*, 11103–11109.

[102] S.-Y. Ding, M. Dong, Y.-W. Wang, Y.-T. Chen, H.-Z. Wang, C.-Y. Su, W. Wang, *J. Am. Chem. Soc.* **2016**, *138*, 3031–3037.

[103] L.-G. Ding, B.-J. Yao, F. Li, S.-C. Shi, N. Huang, H.-B. Yin, Q. Guan, Y.-B. Dong, *J. Mater. Chem. A* **2019**, *7*, 4689–4698.

[104] W. Cao, W. D. Wang, H.-S. Xu, I. V Sergeyev, J. Struppe, X. Wang, F. Mentink-Vigier, Z. Gan, M.-X. Xiao, L.-Y. Wang, G.-P. Chen, S.-Y. Ding, S. Bai, W. Wang, *J. Am. Chem. Soc.* **2018**, *140*, 6969–6977.

[105] J.-C. Shen, W.-L. Jiang, W.-D. Guo, Q.-Y. Qi, D.-L. Ma, X. Lou, M. Shen, B. Hu, H.-B. Yang, X. Zhao, *Chem. Commun.* **2020**, *56*, 595–598.

[106] L. Chen, L. He, F. Ma, W. Liu, Y. Wang, M. A. Silver, L. Chen, L. Zhu, D. Gui, J. Diwu, Z. Chai, S. Wang, *ACS Appl. Mater. Interfaces* **2018**, *10*, 15364–15368.

[107] H.-L. Qian, C.-X. Yang, X.-P. Yan, *Nat. Commun.* **2016**, *7*, 12104.

[108] L.-K. Wang, J.-J. Zhou, Y.-B. Lan, S.-Y. Ding, W. Yu, W. Wang, *Angew. Chemie Int. Ed.* **2019**, *58*, 9443–9447.

[109] J. L. Segura, S. Royuela, M. Mar Ramos, *Chem. Soc. Rev.* **2019**, *48*, 3903–3945.

[110] W. Seo, D. L. White, A. Star, *Chem. – A Eur. J.* **2017**, *23*, 5652–5657.

[111] Z. Fu, X. Wang, A. M. Gardner, X. Wang, S. Y. Chong, G. Neri, A. J. Cowan, L. Liu, X. Li, A. Vogel, R. Clowes, M. Bilton, L. Chen, R. S. Sprick, A. I. Cooper, *Chem. Sci.* **2020**, *11*, 543–550.

[112] H. Vardhan, G. Verma, S. Ramani, A. Nafady, A. M. Al-Enizi, Y. Pan, Z. Yang, H. Yang, S. Ma, *ACS Appl. Mater. Interfaces* **2019**, *11*, 3070–3079.

[113] L. A. Baldwin, J. W. Crowe, D. A. Pyles, P. L. McGrier, *J. Am. Chem. Soc.* **2016**, *138*, 15134–15137.

[114] J. Dong, X. Han, Y. Liu, H. Li, Y. Cui, *Angew. Chemie Int. Ed.* **2020**, *59*, 13722–13733.

[115] J. Romero, D. Rodriguez-San-Miguel, A. Ribera, R. Mas-Ballesté, T. F. Otero, I. Manet, F. Licio, G. Abellán, F. Zamora, E. Coronado, *J. Mater. Chem. A* **2017**, *5*, 4343–4351.

[116] Q. Sun, B. Aguila, J. Perman, N. Nguyen, S. Ma, *J. Am. Chem. Soc.* **2016**, *138*, 15790–15796.

[117] L.-H. Li, X.-L. Feng, X.-H. Cui, Y.-X. Ma, S.-Y. Ding, W. Wang, *J. Am. Chem. Soc.* **2017**, *139*, 6042–6045.

[118] S.-Y. Ding, J. Gao, Q. Wang, Y. Zhang, W.-G. Song, C.-Y. Su, W. Wang, *J. Am. Chem. Soc.* **2011**, *133*, 19816–19822.

[119] Y. Hou, X. Zhang, J. Sun, S. Lin, D. Qi, R. Hong, D. Li, X. Xiao, J. Jiang, *Microporous Mesoporous Mater.* **2015**, *214*, 108–114.

[120] H. Liu, J. Chu, Z. Yin, X. Cai, L. Zhuang, H. Deng, *Chem* **2018**, *4*, 1696–1709.

[121] F. Haase, E. Troschke, G. Savasci, T. Banerjee, V. Duppel, S. Dörfler, M. M. J. Grundei, A. M. Burow, C. Ochsenfeld, S. Kaskel, B. V. Lotsch, *Nat. Commun.* **2018**, *9*, 2600.

[122] H.-L. Qian, F.-L. Meng, C.-X. Yang, X.-P. Yan, *Angew. Chemie Int. Ed.* **2020**, *59*, 17607–17613.

[123] N. Huang, X. Ding, J. Kim, H. Ihee, D. Jiang, *Angew. Chem. Int. Ed. Engl.* **2015**, *54*, 8704–8707.

[124] M. A. Khayum, S. Kandambeth, S. Mitra, S. B. Nair, A. Das, S. S. Nagane, R. Mukherjee, R. Banerjee, *Angew. Chemie - Int. Ed.* **2016**, *55*, 15604–15608.

[125] A. Acharjya, P. Pachfule, J. Roeser, F.-J. Schmitt, A. Thomas, *Angew. Chemie Int. Ed.* **2019**, *58*, 14865–14870.

[126] A. Nagai, Z. Guo, X. Feng, S. Jin, X. Chen, X. Ding, D. Jiang, *Nat. Commun.* **2011**, *2*, 536.

[127] S.-L. Ji, H.-L. Qian, C.-X. Yang, X. Zhao, X.-P. Yan, *ACS Appl. Mater. Interfaces* **2019**, *11*, 46219–46225.

[128] Y. Deng, Z. Zhang, P. Du, X. Ning, Y. Wang, D. Zhang, J. Liu, S. Zhang, X. Lu, *Angew. Chemie Int. Ed.* **2020**, *59*, 6082–6089.

[129] J. Hao, Q. Zhang, P. Chen, X. Zheng, Y. Wu, D. Ma, D. Wei, H. Liu, G. Liu, W. Lv, *Environ. Sci. Nano* **2019**, *6*, 3374–3387.

[130] B. Dong, L. Wang, S. Zhao, R. Ge, X. Song, Y. Wang, Y. Gao, *Chem. Commun.* **2016**, *52*, 7082–7085.

[131] N. Han, Z. Zhang, H. Gao, Y. Qian, L. Tan, C. Yang, H. Zhang, Z. Cui, W. Li, X. Zhang, *ACS Appl. Mater. Interfaces* **2020**, *12*, 2926–2934.

[132] M. S. Lohse, T. Stassin, G. Naudin, S. Wuttke, R. Ameloot, D. De Vos, D. D. Medina, T. Bein, *Chem. Mater.* **2016**, *28*, 626–631.

[133] Y. Jiang, C. Liu, A. Huang, *ACS Appl. Mater. Interfaces* **2019**, *11*, 32186–32191.

[134] L. Guo, S. Jia, C. S. Diercks, X. Yang, S. A. Alshmimri, O. M. Yaghi, *Angew. Chemie Int. Ed.* **2020**, *59*, 2023–2027.

[135] D. Rodríguez-San-Miguel, F. Zamora, *Chem. Soc. Rev.* **2019**, *48*, 4375–4386.

[136] D. D. Medina, V. Werner, F. Auras, R. Tautz, M. Dogru, J. Schuster, S. Linke, M. Döblinger, J. Feldmann, P. Knochel, T. Bein, *ACS Nano* **2014**, *8*, 4042–4052.

[137] P. Payamyar, K. Kaja, C. Ruiz-Vargas, A. Stemmer, D. J. Murray, C. J. Johnson, B. T. King, F. Schiffmann, J. Vandevondele, A. Renn, S. Götzinger, P. Ceroni, A. Schütz, L.-T. Lee, Z. Zheng, J. Sakamoto, A. D. Schlüter, *Adv. Mater.* **2014**, *26*, 2052–2058.

[138] J. I. Feldblyum, C. H. McCreery, S. C. Andrews, T. Kurosawa, E. J. G. Santos, V. Duong, L. Fang, A. L. Ayzner, Z. Bao, *Chem. Commun.* **2015**, *51*, 13894–13897.

[139] K. Dey, M. Pal, K. C. Rout, S. S. Kunjattu, A. Das, R. Mukherjee, U. K. Kharul, R. Banerjee, *J. Am. Chem. Soc.* **2017**, *139*, 13083–13091.

[140] X. Li, P. Yadav, K. P. Loh, *Chem. Soc. Rev.* **2020**, *49*, 4835–4866.

[141] Y. Peng, Y. Huang, Y. Zhu, B. Chen, L. Wang, Z. Lai, Z. Zhang, M. Zhao, C. Tan, N. Yang, F. Shao, Y. Han, H. Zhang, *J. Am. Chem. Soc.* **2017**, *139*, 8698–8704.

[142] D. N. Bunck, W. R. Dichtel, *J. Am. Chem. Soc.* **2013**, *135*, 14952–14955.

[143] S. Chandra, S. Kandambeth, B. P. Biswal, B. Lukose, S. M. Kunjir, M. Chaudhary, R. Babarao, T. Heine, R. Banerjee, *J. Am. Chem. Soc.* **2013**, *135*, 17853–17861.

[144] X. Mu, J. Zhan, J. Wang, W. Cai, B. Yuan, L. Song, Y. Hu, *J. Colloid Interface Sci.* **2019**, *539*, 609–618.

[145] J. Yao, C. Liu, X. Liu, J. Guo, S. Zhang, J. Zheng, S. Li, *J. Memb. Sci.* **2020**, *601*, 117864.

[146] J. Dong, X. Li, S. B. Peh, Y. Di Yuan, Y. Wang, D. Ji, S. Peng, G. Liu, S. Ying, D. Yuan, J. Jiang, S. Ramakrishna, D. Zhao, *Chem. Mater.* **2019**, *31*, 146–160.

[147] N. Huang, P. Wang, M. A. Addicoat, T. Heine, D. Jiang, *Angew. Chemie Int. Ed.* **2017**, *56*, 4982–4986.

[148] S. Mitra, S. Kandambeth, B. P. Biswal, A. Khayum M., C. K. Choudhury, M. Mehta, G. Kaur, S. Banerjee, A. Prabhune, S. Verma, S. Roy, U. K. Kharul, R. Banerjee, *J. Am. Chem. Soc.* **2016**, *138*, 2823–2828.

[149] H. Singh, M. Devi, N. Jena, M. M. Iqbal, Y. Nailwal, A. De Sarkar, S. K. Pal, *ACS Appl. Mater. Interfaces* **2020**, *12*, 13248–13255.

[150] L. Wang, C. Zeng, H. Xu, P. Yin, D. Chen, J. Deng, M. Li, N. Zheng, C. Gu, Y. Ma, *Chem. Sci.* **2019**, *10*, 1023–1028.

[151] A. Mal, S. Vijayakumar, R. K. Mishra, J. Jacob, R. S. Pillai, B. S. Dileep Kumar, A. Ajayaghosh, *Angew. Chemie Int. Ed.* **2020**, *59*, 8713–8719.

[152] G. Das, S. K. Sharma, T. Prakasam, F. Gándara, R. Mathew, N. Alkhatib, N. Saleh, R. Pasricha, J.-C. Olsen, M. Baias, S. Kirmizialtin, R. Jagannathan, A. Trabolsi, *Commun. Chem.* **2019**, *2*, 106.

[153] D. W. Burke, C. Sun, I. Castano, N. C. Flanders, A. M. Evans, E. Vitaku,

D. C. McLeod, R. H. Lambeth, L. X. Chen, N. C. Gianneschi, W. R. Dichtel, *Angew. Chem. Int. Ed. Engl.* **2020**, *59*, 5165–5171.

[154] S. A. Ahmed, Q.-B. Liao, Q. Shen, M. M. F. A. Baig, J. Zhou, C.-F. Shi, P. Muhammad, S. H. Hanif, K. Xi, X.-H. Xia, K. Wang, *Chem. – A Eur. J.* **2020**, 1–7.

[155] Y. Song, Q. Sun, B. Aguila, S. Ma, *Adv. Sci.* **2019**, *6*, 1801410.

[156] W. Zhao, L. Xia, X. Liu, *CrystEngComm* **2018**, *20*, 1613–1634.

[157] K. Zhang, K. O. Kirlikovali, R. S. Varma, Z. Jin, H. W. Jang, O. K. Farha, M. Shokouhimehr, *ACS Appl. Mater. Interfaces* **2020**, *12*, 27821–27852.

[158] X. Zhan, Z. Chen, Q. Zhang, *J. Mater. Chem. A* **2017**, *5*, 14463–14479.

[159] M. Wang, H. Guo, R. Xue, Q. Li, H. Liu, N. Wu, W. Yao, W. Yang, *ChemElectroChem* **2019**, *6*, 2984–2997.

[160] Z. Zhu, M. Hong, D. Guo, J. Shi, Z. Tao, J. Chen, *J. Am. Chem. Soc.* **2014**, *136*, 16461–16464.

[161] C. Friebe, A. Lex-Balducci, U. S. Schubert, *ChemSusChem* **2019**, *12*, 4093—4115.

[162] M. R. Rao, Y. Fang, S. De Feyter, D. F. Perepichka, *J. Am. Chem. Soc.* **2017**, *139*, 2421–2427.

[163] D.-H. Yang, Z.-Q. Yao, D. Wu, Y.-H. Zhang, Z. Zhou, X.-H. Bu, *J. Mater. Chem. A* **2016**, *4*, 18621–18627.

[164] Z. Luo, L. Liu, J. Ning, K. Lei, Y. Lu, F. Li, J. Chen, *Angew. Chemie Int. Ed.* **2018**, *57*, 9443–9446.

[165] G. Wang, N. Chandrasekhar, B. P. Biswal, D. Becker, S. Paasch, E. Brunner, M. Addicoat, M. Yu, R. Berger, X. Feng, *Adv. Mater.* **2019**, *31*, 1901478.

[166] J. Lv, Y.-X. Tan, J. Xie, R. Yang, M. Yu, S. Sun, M.-D. Li, D. Yuan, Y. Wang, *Angew. Chemie Int. Ed.* **2018**, 1–6.

[167] S. Wang, Q. Wang, P. Shao, Y. Han, X. Gao, L. Ma, S. Yuan, X. Ma, J. Zhou, X. Feng, B. Wang, *J. Am. Chem. Soc.* **2017**, *139*, 4258–4261.

[168] J. Li, X. Jing, Q. Li, S. Li, X. Gao, X. Feng, B. Wang, *Chem. Soc. Rev.* **2020**, *49*, 3565–3604.

[169] D.-G. Wang, N. Li, Y. Hu, S. Wan, M. Song, G. Yu, Y. Jin, W. Wei, K. Han, G.-C. Kuang, W. Zhang, *ACS Appl. Mater. Interfaces* **2018**, *10*, 42233–42240.

[170] D.-G. Wang, Y. Wang, M. Song, G.-C. Kuang, K. Han, *Chem. Commun.* **2019**, *55*, 13247–13250.

[171] S. Gu, S. Wu, L. Cao, M. Li, N. Qin, J. Zhu, Z. Wang, Y. Li, Z. Li, J. Chen, Z. Lu, *J. Am. Chem. Soc.* **2019**, *141*, 9623–9628.

[172] Z. Lei, Q. Yang, Y. Xu, S. Guo, W. Sun, H. Liu, L.-P. Lv, Y. Zhang, Y. Wang, *Nat. Commun.* **2018**, *9*, 576.

[173] Q. Xu, S. Tao, Q. Jiang, D. Jiang, *J. Am. Chem. Soc.* **2018**, *140*, 7429–7432.

[174] G. Zhang, Y. Hong, Y. Nishiyama, S. Bai, S. Kitagawa, S. Horike, *J. Am. Chem. Soc.* **2019**, *141*, 1227–1234.

[175] Z. Guo, Y. Zhang, Y. Dong, J. Li, S. Li, P. Shao, X. Feng, B. Wang, *J. Am. Chem. Soc.* **2019**, *141*, 1923–1927.

[176] H. Xu, S. Tao, D. Jiang, *Nat. Mater.* **2016**, *15*, 722–726.

[177] D. B. Shinde, H. B. Aiyappa, M. Bhadra, B. P. Biswal, P. Wadge, S. Kandambeth, B. Garai, T. Kundu, S. Kurungot, R. Banerjee, *J. Mater. Chem. A* **2016**, *4*, 2682–2690.

[178] S. Chandra, T. Kundu, K. Dey, M. Addicoat, T. Heine, R. Banerjee, *Chem. Mater.* **2016**, *28*, 1489–1494.

[179] Z. Meng, A. Aykanat, K. A. Mirica, *Chem. Mater.* **2019**, *31*, 819–825.

[180] J. Yan, Q. Wang, T. Wei, Z. Fan, *Adv. Energy Mater.* **2014**, *4*, 1300816.

[181] J. Libich, J. Máca, J. Vondrák, O. Čech, M. Sedlaříková, *J. Energy Storage* **2018**, *17*, 224–227.

[182] B. Babakhani, D. G. Ivey, *Electrochim. Acta* **2010**, *55*, 4014–4024.

[183] P. Xu, J. Liu, P. Yan, C. Miao, K. Ye, K. Cheng, J. Yin, D. Cao, K. Li, G. Wang, *J. Mater. Chem. A* **2016**, *4*, 4920–4928.

[184] X. Li, C. Hao, B. Tang, Y. Wang, M. Liu, Y. Wang, Y. Zhu, C. Lu, Z. Tang, *Nanoscale* **2017**, *9*, 2178–2187.

[185] S. Faraji, F. N. Ani, *J. Power Sources* **2014**, *263*, 338–360.

[186] Y. Yao, Y. Zhang, L. Li, S. Wang, S. Dou, X. Liu, *ACS Appl. Mater. Interfaces* **2017**, *9*, 34944–34953.

[187] Y.-T. Weng, N.-L. Wu, *J. Power Sources* **2013**, *238*, 69–73.

[188] C. R. Deblase, K. E. Silberstein, T. T. Truong, H. D. Abruña, W. R. Dichtel, *J. Am. Chem. Soc.* **2013**, *135*, 16821–16824.

[189] C. R. Deblase, K. Hernández-Burgos, K. E. Silberstein, G. G. Rodríguez-Calero, R. P. Bisbey, H. D. Abruña, W. R. Dichtel, *ACS Nano* **2015**, *9*, 3178–3183.

[190] C. R. Mulzer, L. Shen, R. P. Bisbey, J. R. McKone, N. Zhang, H. D. Abruña, W. R. Dichtel, *ACS Cent. Sci.* **2016**, *2*, 667–673.

[191] Y. Wu, D. Yan, Z. Zhang, M. M. Matsushita, K. Awaga, *ACS Appl. Mater. Interfaces* **2019**, *11*, 7661–7665.

[192] M. A. Khayum, V. Vijayakumar, S. Karak, S. Kandambeth, M. Bhadra, K. Suresh, N. Acharambath, S. Kurungot, R. Banerjee, *ACS Appl. Mater. Interfaces* **2018**, *10*, 28139–28146.

[193] H. Yang, S. Zhang, L. Han, Z. Zhang, Z. Xue, J. Gao, Y. Li, C. Huang, Y. Yi, H. Liu, Y. Li, *ACS Appl. Mater. Interfaces* **2016**, *8*, 5366–5375.

[194] A. Khayum M, V. Vijayakumar, S. Karak, S. Kandambeth, M. Bhadra, K. Suresh, N. Acharambath, S. Kurungot, R. Banerjee, *ACS Appl. Mater. Interfaces* **2018**, *10*, 28139–28146.

[195] Y. Han, Q. Zhang, N. Hu, X. Zhang, Y. Mai, J. Liu, X. Hua, H. Wei, *Chinese Chem. Lett.* **2017**, *28*, 2269–2273.

[196] S. Liu, L. Yao, Y. Lu, X. Hua, J. Liu, Z. Yang, H. Wei, Y. Mai, *Mater. Lett.* **2019**, *236*, 354–357.

[197] Y. Han, N. Hu, S. Liu, Z. Hou, J. Liu, X. Hua, Z. Yang, L. Wei, L. Wang, H. Wei, *Nanotechnology* **2017**, *28*, 33LT01.

[198] A. M. Khattak, Z. A. Ghazi, B. Liang, N. A. Khan, A. Iqbal, L. Li, Z. Tang, *J. Mater. Chem. A* **2016**, *4*, 16312–16317.

[199] A. Roy, S. Mondal, A. Halder, A. Banerjee, D. Ghoshal, A. Paul, S. Malik, *Eur. Polym. J.* **2017**, *93*, 448-457.

[200] R. Xue, H. Guo, L. Yue, T. Wang, M. Wang, Q. Li, H. Liu, W. Yang, *New J. Chem.* **2018**, *42*, 13726–13731.

[201] L. Hao, J. Ning, B. Luo, B. Wang, Y. Zhang, Z. Tang, J. Yang, A. Thomas, L. Zhi, *J. Am. Chem. Soc.* **2015**, *137*, 219–225.

[202] H. Wei, J. Ning, X. Cao, X. Li, L. Hao, *J. Am. Chem. Soc.* **2018**, *140*, 11618–11622.

[203] J. Sun, A. Klechikov, C. Moise, M. Prodana, M. Enachescu, A. V Talyzin, *Angew. Chem. Int. Ed. Engl.* **2018**, *57*, 1034–1038.

[204] M. Wang, H. Guo, R. Xue, Q. Li, H. Liu, N. Wu, W. Yao, W. Yang, *ChemElectroChem* **2019**, *6*, 2984–2997.

[205] K. Geng, T. He, R. Liu, S. Dalapati, K. T. Tan, Z. Li, S. Tao, Y. Gong, Q. Jiang, D. Jiang, *Chem. Rev.* **2020**, *120*, 8814–8933.

[206] X. Wang, Z. Li, Y. Qu, T. Yuan, W. Wang, Y. Wu, Y. Li, *Chem* **2019**, *5*, 1486–1511.

[207] C. Sealy, *Mater. Today* **2008**, *11*, 65–68.

[208] W. Ma, P. Yu, T. Ohsaka, L. Mao, *Electrochem. commun.* **2015**, *52*, 53–57.

[209] X. Zhao, P. Pachfule, S. Li, T. Langenhahn, M. Ye, G. Tian, J. Schmidt, A. Thomas, *Chem. Mater.* **2019**, *31*, 3274–3280.

[210] S. Wu, M. Li, H. Phan, D. Wang, T. S. Herng, J. Ding, Z. Lu, J. Wu, *Angew. Chem. Int. Ed. Engl.* **2018**, *57*, 8007–8011.

[211] Q. Xu, Y. Tang, X. Zhang, Y. Oshima, Q. Chen, D. Jiang, *Adv. Mater.* **2018**, *30*, 1–8.

[212] S. Royuela, E. Martínez-Periñán, M. P. Arrieta, J. I. Martínez, M. M. Ramos, F. Zamora, E. Lorenzo, J. L. Segura, *Chem. Commun.* **2020**, *56*, 1267–1270.

[213] H. B. Aiyappa, J. Thote, D. B. Shinde, R. Banerjee, S. Kurungot, *Chem. Mater.* **2016**, *28*, 4375–4379.

[214] D. Mullangi, V. Dhavale, S. Shalini, S. Nandi, S. Collins, T. Woo, S. Kurungot, R. Vaidhyanathan, *Adv. Energy Mater.* **2016**, *6*, 1600110.

[215] S. Bhunia, S. K. Das, R. Jana, S. C. Peter, S. Bhattacharya, M. Addicoat, A. Bhaumik, A. Pradhan, *ACS Appl. Mater. Interfaces* **2017**, *9*, 23843–23851.

[216] V. S. Vyas, F. Haase, L. Stegbauer, G. Savasci, F. Podjaski, C. Ochsenfeld, B. V Lotsch, *Nat. Commun.* **2015**, *6*, 8508.

[217] S. Lin, C. S. Diercks, Y.-B. Zhang, N. Kornienko, E. M. Nichols, Y. Zhao, A. R. Paris, D. Kim, P. Yang, O. M. Yaghi, C. J. Chang, *Science* **2015**, *349*, 1208–1213.

[218] D. A. Popov, J. M. Luna, N. M. Orchanian, R. Haiges, C. A. Downes, S. C. Marinescu, *Dalt. Trans.* **2018**, *47*, 17450–17460.

[219] C. S. Diercks, S. Lin, N. Kornienko, E. A. Kapustin, E. M. Nichols, C. Zhu, Y. Zhao, C. J. Chang, O. M. Yaghi, *J. Am. Chem. Soc.* **2018**, *140*, 1116–1122.

[220] L. Dou, Y. Liu, Z. Hong, G. Li, Y. Yang, *Chem. Rev.* **2015**, *115*, 12633–12665.

[221] S. Dalapati, C. Gu, D. Jiang, *Small* **2016**, *12*, 6513–6527.

[222] S. Wan, J. Guo, J. Kim, H. Ihee, D. Jiang, *Angew. Chemie - Int. Ed.* **2008**, *47*, 8826–8830.

[223] S. Wan, J. Guo, J. Kim, H. Ihee, D. Jiang, *Angew. Chemie - Int. Ed.* **2009**, *48*, 5439–5442.

[224] E. Jin, J. Li, K. Geng, Q. Jiang, H. Xu, Q. Xu, D. Jiang, *Nat. Commun.* **2018**, *9*, 4143.

[225] Y. Zhao, H. Liu, C. Wu, Z. Zhang, Q. Pan, F. Hu, R. Wang, P. Li, X. Huang, Z. Li, *Angew. Chem. Int. Ed. Engl.* **2019**, *58*, 5376–5381.

[226] S. Dalapati, E. Jin, M. Addicoat, T. Heine, D. Jiang, *J. Am. Chem. Soc.* **2016**, *138*, 5797–5800.

[227] L. Ma, X. Feng, S. Wang, B. Wang, *Mater. Chem. Front.* **2017**, *1*, 2474–2486.

[228] Q. Gao, X. Li, G.-H. Ning, K. Leng, B. Tian, C. Liu, W. Tang, H.-S. Xu, K. P. Loh, *Chem. Commun.* **2018**, *54*, 2349–2352.

[229] S. Yan, X. Guan, H. Li, D. Li, M. Xue, Y. Yan, V. Valtchev, S. Qiu, Q. Fang, *J. Am. Chem. Soc.* **2019**, *141*, 2920–2924.

[230] S. Rager, M. Dogru, V. Werner, A. Gavryushin, M. Götz, H. Engelke, D. D. Medina, P. Knochel, T. Bein, *CrystEngComm* **2017**, *19*, 4886–4891.

[231] Z. Li, N. Huang, K. H. Lee, Y. Feng, S. Tao, Q. Jiang, Y. Nagao, S. Irle, D. Jiang, *J. Am. Chem. Soc.* **2018**, *140*, 12374–12377.

[232] G. Chen, H.-H. Lan, S.-L. Cai, B. Sun, X.-L. Li, Z.-H. He, S.-R. Zheng, J. Fan, Y. Liu, W.-G. Zhang, *ACS Appl. Mater. Interfaces* **2019**, *11*, 12830–12837.

[233] A. Mal, R. K. Mishra, V. K. Praveen, M. A. Khayum, R. Banerjee, A. Ajayaghosh, *Angew. Chemie Int. Ed.* **2018**, *57*, 8443–8447.

[234] S. Dalapati, S. Jin, J. Gao, Y. Xu, A. Nagai, D. Jiang, *J. Am. Chem. Soc.* **2013**, *135*,17310–17313.

[235] G. Das, B. P. Biswal, S. Kandambeth, V. Venkatesh, G. Kaur, M. Addicoat, T. Heine, S. Verma, R. Banerjee, *Chem. Sci.* **2015**, *6*, 3931–3939.

[236] C. Zhang, S. Zhang, Y. Yan, F. Xia, A. Huang, Y. Xian, *ACS Appl. Mater. Interfaces* **2017**, *9*, 13415–13421.

[237] P. Albacete, A. López-Moreno, S. Mena-Hernando, A. E. Platero-Prats, E. M. Pérez, F. Zamora, *Chem. Commun.* **2019**, *55*, 1382–1385.

[238] J. J. Jarju, A. M. Lavender, B. Espiña, V. Romero, L. M. Salonen, *Molecules* **2020**, *25*, 5404.

[239] M. Šupová, G. S. Martynková, K. Barabaszová, *Sci. Adv. Mater.* **2011**, *3*, 1–25.

[240] X. Mu, J. Zhan, X. Feng, W. Cai, L. Song, Y. Hu, *Compos. Part A Appl. Sci. Manuf.* **2018**, *110*, 162–171.

[241] S. Shafiee, E. Topal, *Energy Policy* **2009**, *37*, 181–189.

[242] E. Serrano, G. Rus, J. García-Martínez, *Renew. Sustain. Energy Rev.* **2009**, *13*, 2373–2384.

[243] I. Capellán-Pérez, M. Mediavilla, C. de Castro, Ó. Carpintero, L. J. Miguel, *Energy* **2014**, *77*, 641–666.

[244] H. B. Gray, *Nat. Chem.* **2009**, *1*, 7.

[245] M. Shao, Q. Chang, J.-P. Dodelet, R. Chenitz, *Chem. Rev.* **2016**, *116*, 3594–3657.

[246] Z. Xiang, Y. Xue, D. Cao, L. Huang, J.-F. Chen, L. Dai, *Angew. Chem. Int. Ed. Engl.* **2014**, *53*, 2433–2437.

[247] Y. Li, P. Peng, Z. Liao, F. Huo, Y. Liu, X. Shao, Z. Xiang, *ACS Sustain. Chem. Eng.* **2020**, *8*, 3728–3733.

[248] L. Huo, B. Liu, G. Zhang, R. Si, J. Liu, J. Zhang, *J. Mater. Chem. A* **2017**, *5*, 4868–4878.

[249] D. Wielend, M. Vera-Hidalgo, H. Seelajaroen, N. S. Sariciftci, E. M. Pérez, D. R. Whang, *ACS Appl. Mater. Interfaces* **2020**, *12*, 32615–32621.

[250] F. Yu, K. Wang, C. Wang, X. He, Y. Liao, S. Zhao, H. Mao, X. Li, J. Ma, *Chem. Res. Chinese Univ.* **2020**, 36, 1332–1338.

[251] F. Mirkhalaf, K. Tammeveski, D. J. Schiffrin, *Phys. Chem. Chem. Phys.* **2004**, *6*, 1321–1327.

[252] K. Tammeveski, K. Kontturi, R. J. Nichols, R. J. Potter, D. J. Schiffrin, *J. Electroanal. Chem.* **2001**, *515*, 101–112.

[253] A. Sarapuu, K. Vaik, D. J. Schiffrin, K. Tammeveski, *J. Electroanal. Chem.* **2003**, *541*, 23–29.

[254] P. Xiao, Y. Xu, *J. Mater. Chem. A* **2018**, *6*, 21676–21695.

[255] X. Cui, S. Lei, A. C. Wang, L. Gao, Q. Zhang, Y. Yang, Z. Lin, *Nano Energy* **2020**, *70*, 104525.

[256] D. Wu, Q. Xu, J. Qian, X. Li, Y. Sun, *Chem. – A Eur. J.* **2019**, *25*, 3105–3111.

[257] J. Guo, C.-Y. Lin, Z. Xia, Z. Xiang, *Angew. Chem. Int. Ed. Engl.* **2018**, *57*, 12567–12572.

[258] H. Wang, C.-J. Yao, H.-J. Nie, K.-Z. Wang, Y.-W. Zhong, P. Chen, S. Mei, Q. Zhang, *J. Mater. Chem. A* **2020**, *8*, 11906–11922.

[259] K. Amin, L. Mao, Z. Wei, *Macromol. Rapid Commun.* **2019**, *40*, 1800565.

[260] P. García-Arroyo, P. Navalpotro, M. J. Mancheño, E. Salagre, J. J. Cabrera-Trujillo, E. G. Michel, J. L. Segura, J. Carretero-González, *Polymer* **2021**, *212*, 123273.

[261] A. Ahmad, Q. Meng, S. Melhi, L. Mao, M. Zhang, B.-H. Han, K. Lu, Z. Wei, *Electrochim. Acta* **2017**, *255*, 145–152.

[262] Y. Liang, Y. Jing, S. Gheytani, K. Y. Lee, P. Liu, A. Facchetti, Y. Yao, *Nat. Mater.* **2017**, *16*, 841–848.

[263] S. H. M. Mehr, H. Depmeier, K. Fukuyama, M. Maghami, M. J. MacLachlan, *Org. Biomol. Chem.* **2017**, *15*, 581–583.

[264] L. Stegbauer, S. Zech, G. Savasci, T. Banerjee, F. Podjaski, K. Schwinghammer, C. Ochsenfeld, B. V. Lotsch, *Adv. Energy Mater.* **2018**, *8*, 1–8.

[265] P. García-Arroyo, M. P. Arrieta, D. Garcia-Garcia, R. Cuervo-Rodríguez, V. Fombuena, M. J. Mancheño, J. L. Segura, *Polymer* **2020**, *196*, 122466.

[266] M. L. Perry, T. F. Fuller, *J. Electrochem. Soc.* **2002**, *149*, S59.

[267] K. Wedege, E. Dražević, D. Konya, A. Bentien, *Sci. Rep.* **2016**, *6*, 39101.

[268] P. S. Guin, S. Das, P. C. Mandal, *Int. J. Electrochem.* **2011**, *2011*, 816202.

[269] M. Quan, D. Sanchez, M. F. Wasylkiw, D. K. Smith, *J. Am. Chem. Soc.* **2007**, *129*, 12847–12856.

[270] P. Bhanja, K. Bhunia, S. K. Das, D. Pradhan, R. Kimura, Y. Hijikata, S. Irle, A. Bhaumik, *ChemSusChem* **2017**, *10*, 921–929.

[271] Y. Marcus, *Chem. Rev.* **1988**, *88*, 1475–1498.

[272] C. Han, H. Li, R. Shi, T. Zhang, J. Tong, J. Li, B. Li, *J. Mater. Chem. A* **2019**, *7*, 23378–23415.

[273] H. Wang, R. Emanuelsson, A. Banerjee, R. Ahuja, M. Strømme, M. Sjödin, *J. Phys. Chem. C* **2020**, *124*, 13609–13617.

[274] M. Liu, L. Guo, S. Jin, B. Tan, *J. Mater. Chem. A* **2019**, *7*, 5153–5172.

[275] Y. Li, S. Zheng, X. Liu, P. Li, L. Sun, R. Yang, S. Wang, Z.-S. Wu, X. Bao, W.-Q. Deng, *Angew. Chemie Int. Ed.* **2018**, *57*, 7992–7996.

[276] N. Tahir, C. Krishnaraj, K. Leus, P. Van Der Voort, *Polymers (Basel).* **2019**, *11*, 1326.

[277] E. Troschke, S. Grätz, L. Borchardt, D. Haubold, I. Senkovska, A. Eychmueller, S. Kaskel, *Microporous Mesoporous Mater.* **2017**, *239*, 190–194.

[278] D. Kong, X. Han, J. Xie, Q. Ruan, C. D. Windle, S. Gadipelli, K. Shen, Z. Bai, Z. Guo, J. Tang, *ACS Catal.* **2019**, *9*, 7697–7707.

[279] L. Lin, Z. Yu, X. Wang, *Angew. Chemie - Int. Ed.* **2019**, *58*, 6164–6175.

[280] X. Wang, C. Zhang, Y. Zhao, S. Ren, J. X. Jiang, *Macromol. Rapid Commun.* **2016**, *37*, 323–329.

[281] T. Geng, G. Chen, C. Zhang, L. Ma, W. Zhang, H. Xia, *J. Macromol. Sci. Part A* **2019**, *56*, 1004–1011.

[282] S. Y. Yu, J. Mahmood, H. J. Noh, J. M. Seo, S. M. Jung, S. H. Shin, Y. K. Im, I. Y. Jeon, J. B. Baek, *Angew. Chemie - Int. Ed.* **2018**, *57*, 8438–8442.

[283] S. Thomas, H. Li, R. R. Dasari, A. M. Evans, I. Castano, T. G. Allen, O. G. Reid, G. Rumbles, W. R. Dichtel, N. C. Gianneschi, S. R. Marder, V. Coropceanu, J.-L. Brédas, *Mater. Horizons* **2019**, *6*, 1868–1876.

[284] H.-C. Jung, R. Vinodh, C. V. V. M. Gopi, M. Yi, H.-J. Kim, *Mater. Lett.* **2019**, *257*, 126732.

[285] S. Bandyopadhyay, C. Singh, P. Jash, M. D. W. Hussain, A. Paul, A. Patra, *Chem. Commun.* **2018**, *54*, 6796–6799.

[286] Y. Zhao, F. Xie, C. Zhang, R. Kong, S. Feng, J.-X. Jiang, *Microporous Mesoporous Mater.* **2017**, *240*, 73–79.

[287] M. G. Mohamed, A. F. M. EL-Mahdy, Y. Takashi, S.-W. Kuo, *New J. Chem.* **2020**, *44*, 8241–8253.

[288] B. Anothumakkool, P.-L. Taberna, B. Daffos, P. Simon, Y. Sayed-Ahmad-Baraza, C. Ewels, T. Brousse, J. Gaubicher, *J. Mater. Chem. A* **2017**, *5*, 1488–1494.

[289] Z. Li, W. Zhang, Y. li, H. Wang, Z. Qin, *Chem. Eng. J.* **2018**, *334*, 845–854.

[290] A. G. Crawford, Z. Liu, I. A. I. Mkhalid, M.-H. Thibault, N. Schwarz, G. Alcaraz, A. Steffen, J. C. Collings, A. S. Batsanov, J. A. K. Howard, T. B. Marder, *Chem. – A Eur. J.* **2012**, *18*, 5022–5035.

[291] K. H. Kim, X. Bai, R. C. Brown, *J. Anal. Appl. Pyrolysis* **2014**, *110*, 254–263.

[292] R. Slamet, D. Wege, *Tetrahedron* **2007**, *63*, 12621–12628.

[293] A. Pandey, C. Larroche, C.-G. Dussap, E. Gnansounou, S. K. Khanal, S. Ricke, in *Biomass, Biofuels, Biochem.* (Eds.: A. Pandey, C. Larroche, C.-G. Dussap, E. Gnansounou, S.K. Khanal, S.B.T.-B.A.F. and C.P. for the P. of L. and G.B. (Second E. Ricke), Academic Press, **2019**, pp. xvii–xviii.

[294] N. K. Bhattacharyya, S. Jha, T. Y. Bhutia, G. Adhikary, *International Journal of Chemistry and Applications*, **2012**, *4*, 295-304.

[295] A. Bhunia, V. Vasylyeva, C. Janiak, *Chem. Commun.* **2013**, *49*, 3961–3963.

[296] L. B. Casabianca, M. A. Shaibat, W. W. Cai, S. Park, R. Piner, R. S. Ruoff, Y. Ishii, *J. Am. Chem. Soc.* **2010**, *132*, 5672–5676.

[297] X. Wang, Y. Hu, L. Song, H. Yang, W. Xing, H. Lu, *J. Mater. Chem.* **2011**, *21*, 4222–4227.

[298] E. Abou-Hamad, M.-R. Babaa, M. Bouhrara, Y. Kim, Y. Saih, S. Dennler, F. Mauri, J.-M. Basset, C. Goze-Bac, T. Wågberg, *Phys. Rev. B* **2011**, *84*, 165417.

[299] R. A. Gaussian09, *Inc., Wallingford CT* **2009**, *121*, 150–166.

[300] S. J. Clark, M. D. Segall, C. J. Pickard, P. J. Hasnip, M. I. J. Probert, K. Refson, M. C. Payne, *Zeitschrift fur Krist.* **2005**, *220*, 567–570.

[301] D. F. Romdhane, Y. Satlaoui, R. Nasraoui, A. Charef, R. Azouzi, *J. Chem.* **2020**, 4376173.

[302] A. F. M. EL-Mahdy, M. G. Mohamed, T. H. Mansoure, H.-H. Yu, T. Chen, S.-W. Kuo, *Chem. Commun.* **2019**, *55*, 14890–14893.

[303] A. Bhunia, D. Esquivel, S. Dey, R. Fernández-Terán, Y. Goto, S. Inagaki, P. Van Der Voort, C. Janiak, *J. Mater. Chem. A* **2016**, *4*, 13450–13457.

[304] A. Bhunia, V. Vasylyeva, C. Janiak, *Chem. Commun.* **2013**, *49*, 3961–3963.

[305] Z. Sun, Y. Li, L. Chen, X. Jing, Z. Xie, *Cryst. Growth Des.* **2015**, *15*, 542–545.

[306] X. Zheng, Q. Ruan, Q. Jiang, K. Wang, Q. Wang, Y. Tang, H. Huang, C. Zhong, *J. Colloid Interface Sci.* **2018**, *532*, 1–11.

[307] S. Dey, A. Bhunia, H. Breitzke, P. B. Groszewicz, G. Buntkowsky, C. Janiak, *J. Mater. Chem. A* **2017**, *5*, 3609–3620.

[308] Q. Gao, X. Li, G. H. Ning, H. Sen Xu, C. Liu, B. Tian, W. Tang, K. P. Loh, *Chem. Mater.* **2018**, *30*, 1762–1768.

[309] X. Wei, X. Jiang, J. Wei, S. Gao, *Chem. Mater.* **2016**, *28*, 445–458.

[310] L. Li, F. Lu, H. Guo, W. Yang, *Microporous Mesoporous Mater.* **2021**, *312*, 110766.

[311] F. Zhao, Y. Wang, X. Xu, Y. Liu, R. Song, G. Lu, Y. Li, *ACS Appl. Mater.*

Interfaces **2014**, *6*, 11007–11012.

[312] T. Li, W.-D. Zhang, Y. Liu, Y. Li, C. Cheng, H. Zhu, X. Yan, Z. Li, Z.-G. Gu, *J. Mater. Chem. A* **2019**, *7*, 19676–19681.

[313] A. Halder, M. Ghosh, A. Khayum M, S. Bera, M. Addicoat, H. S. Sasmal, S. Karak, S. Kurungot, R. Banerjee, *J. Am. Chem. Soc.* **2018**, *140*, 10941–10945.

[314] A. F. M. EL-Mahdy, C. Young, J. Kim, J. You, Y. Yamauchi, S.-W. Kuo, *ACS Appl. Mater. Interfaces* **2019**, *11*, 9343–9354.

[315] S. Chandra, D. Roy Chowdhury, M. Addicoat, T. Heine, A. Paul, R. Banerjee, *Chem. Mater.* **2017**, *29*, 2074–2080.

[316] F. Xu, H. Xu, X. Chen, D. Wu, Y. Wu, H. Liu, C. Gu, R. Fu, D. Jiang, *Angew. Chemie - Int. Ed.* **2015**, *54*, 6814–6818.

[317] K. P. Carter, A. M. Young, A. E. Palmer, *Chem. Rev.* **2014**, *114*, 4564–4601.

[318] J. Zhang, F. Cheng, J. Li, J.-J. Zhu, Y. Lu, *Nano Today* **2016**, *11*, 309–329.

[319] Y. Liu, Q. Ouyang, H. Li, M. Chen, Z. Zhang, Q. Chen, *J. Agric. Food Chem.* **2018**, *66*, 6188–6195.

[320] B. Kaur, N. Kaur, S. Kumar, *Coord. Chem. Rev.* **2018**, *358*, 13–69.

[321] K. Nakashima, X. Zhou, G. Kunkel, Z. Zhang, J. M. Deng, R. R. Behringer, B. de Crombrugghe, *Cell* **2002**, *108*, 17–29.

[322] Q. Niu, K. Gao, W. Wu, *Carbohydr. Polym.* **2014**, *110*, 47–52.

[323] J. L. Domingo, *J. Toxicol. Environ. Health* **1994**, *42*, 123–141.

[324] R. Eisler, *Zinc Hazards to Fish, Wildlife, and Invertebrates: A Synoptic Review*, Laurel, MD, **1993**.

[325] D. Maity, T. Govindaraju, *Chem. Commun.* **2012**, *48*, 1039–1041.

[326] X. Chen, C. S. Lim, D. Lee, S. Lee, S. J. Park, H. M. Kim, J. Yoon, *Biosens. Bioelectron.* **2017**, *91*, 770–779.

[327] Y. W. Choi, G. R. You, J. J. Lee, C. Kim, *Inorg. Chem. Commun.* **2016**, *63*, 35–38.

[328] A. Kalendová, P. Kalenda, D. Veselý, *Prog. Org. Coatings* **2006**, *57*, 1–10.

[329] G. A. Antunes, H. S. dos Santos, Y. P. da Silva, M. M. Silva, C. M. S. Piatnicki, D. Samios, *Energy & Fuels* **2017**, *31*, 2944–2950.

[330] Z. Wang, X. Wang, Q. Wang, X. Xiong, H. Luo, K. Huang, *Microchem. J.* **2019**, *149*, 104052.

[331] Y. Zheng, X. Huang, Y. Ling, W. Huang, J. Wang, Z. Zheng, X. Wang, H. Wang, *Spectrochim. Acta Part B At. Spectrosc.* **2019**, *157*, 27–36.

[332] N. Narayanaswamy, T. Govindaraju, *Sensors Actuators B Chem.* **2012**, *161*, 304–310.

[333] L. Chen, T. Lou, C. Yu, Q. Kang, L. Chen, *Analyst* **2011**, *136*, 4770–4773.

[334] D. Maity, D. Karthigeyan, T. K. Kundu, T. Govindaraju, *Sensors Actuators B Chem.* **2013**, *176*, 831–837.

[335] F. Qian, C. Zhang, Y. Zhang, W. He, X. Gao, P. Hu, Z. Guo, *J. Am. Chem. Soc.* **2009**, *131*, 1460–1468.

[336] H. Lee, K. Kim, G. Park, Y. Na, H. Jo, S. Lee, *Inorg. Chem. Commun.* **2014**, *39*, 61–65.

[337] K. Chantalakana, N. Choengchan, P. Yingyuad, P. Thongyoo, *Tetrahedron Lett.* **2016**, *57*, 1146–1149.

[338] S. Mizukami, S. Okada, S. Kimura, K. Kikuchi, *Inorg. Chem.* **2009**, *48*, 7630–7638.

[339] H. He, D. K. P. Ng, *Chem. – An Asian J.* **2013**, *8*, 1441–1446.

[340] V. Gupta, A. Singh, L. Kumawat, *Sensors Actuators B Chem.* **2014**, *204*, 507–514.

[341] A. Kim, H. Lee, D. Yun, U. Jung, K.-T. Kim, C. Kim, *Spectrochim. Acta Part A Mol. Biomol. Spectrosc.* **2020**, *241*, 118652.

[342] Y. Chen, L. Zhao, J. Jiang, *Spectrochim. Acta Part A Mol. Biomol. Spectrosc.* **2017**, *175*, 269–275.

[343] S. Sinha, B. Chowdhury, N. N. Adarsh, P. Ghosh, *Dalt. Trans.* **2018**, *47*, 6819–6830.

[344] X. Liu, D. Huang, C. Lai, G. Zeng, L. Qin, H. Wang, H. Yi, B. Li, S. Liu, M. Zhang, R. Deng, Y. Fu, L. Li, W. Xue, S. Chen, *Chem. Soc. Rev.* **2019**, *48*, 5266–5302.

[345] X. Zhang, G. Li, D. Wu, B. Zhang, N. Hu, H. Wang, J. Liu, Y. Wu, *Biosens. Bioelectron.* **2019**, *145*, 111699.

[346] Y. Cai, Y. Jiang, L. Feng, Y. Hua, H. Liu, C. Fan, M. Yin, S. Li, X. Lv, H. Wang, *Anal. Chim. Acta* **2019**, *1057*, 88–97.

[347] Z. Zhou, W. Zhong, K. Cui, Z. Zhuang, L. Li, L. Li, J. Bi, Y. Yu, *Chem. Commun.* **2018**, *54*, 9977–9980.

[348] T. Zhang, C. Gao, W. Huang, Y. Chen, Y. Wang, J. Wang, *Talanta* **2018**, *188*, 578–583.

[349] K.-S. Lee, J.-S. Lee, *Chem. Mater.* **2006**, *18*, 4519–4525.

[350] J. Zhen, S. Ding, J. Liu, Z. Huang, W. Wang, Q. Zheng, *CrystEngComm* **2016**, *18*, 1039–1045.

[351] A. de la Peña Ruigómez, D. Rodríguez-San-Miguel, K. C. Stylianou, M. Cavallini, D. Gentili, F. Liscio, S. Milita, O. M. Roscioni, M. L. Ruiz-González, C. Carbonell, D. Maspoch, R. Mas-Ballesté, J. L. Segura, F. Zamora, *Chemistry* **2015**, *21*, 10666–10670.

[352] Y. He, Z. Bian, C. Kang, Y. Cheng, L. Gao, *Tetrahedron* **2010**, *66*, 3553–3563.

[353] J. Huang, J.-T. Hong, S. H. Hong, *European J. Org. Chem.* **2012**, *2012*, 6630–6635.

[354] J. Bouffard, B. K. Keitz, R. Tonner, G. Guisado-Barrios, G. Frenking, R. H. Grubbs, G. Bertrand, *Organometallics* **2011**, *30*, 2617–2627.

[355] X. Li, C. Zhang, S. Cai, X. Lei, V. Altoe, F. Hong, J. J. Urban, J. Ciston, E. M. Chan, Y. Liu, *Nat. Commun.* **2018**, *9*, 1–8.

[356] S. Haldar, K. Roy, R. Kushwaha, S. Ogale, R. Vaidhyanathan, *Adv. Energy Mater.* **2019**, *9*, 1902428.

[357] S. Kim, H. C. Choi, *ACS Omega* **2020**, *5*, 948–958.

[358] Y. Li, M. Chen, Y. Han, Y. Feng, Z. Zhang, B. Zhang, *Chem. Mater.* **2020**, *32*, 2532–2540.

[359] Y. S. Rosokha, S. V Lindeman, S. V Rosokha, J. K. Kochi, *Angew. Chemie Int. Ed.* **2004**, *43*, 4650–4652.

[360] D. F. C. Morris, *Acta Crystallogr.* **1961**, *14*, 547–548.

[361] H.-Y. Li, Y.-L. Wei, X.-Y. Dong, S.-Q. Zang, T. C. W. Mak, *Chem. Mater.* **2015**, *27*, 1327–1331.

[362] R. Auras, B. Harte, S. Selke, *Macromol. Biosci.* **2004**, *4*, 835–864.

[363] M. P. Arrieta, M. D. Samper, M. Aldas, J. López, *Materials (Basel).* **2017**, *10*, 1–26.

[364] E. Fortunati, M. Peltzer, I. Armentano, A. Jiménez, J. M. Kenny, *J. Food Eng.* **2013**, *118*, 117–124.

[365] C. Villegas, M. P. Arrieta, A. Rojas, A. Torres, S. Faba, M. J. Toledo, M. A. Gutierrez, E. Zavalla, J. Romero, M. J. Galotto, X. Valenzuela, *Compos. Part B Eng.* **2019**, *176*, 107336.

[366] I. T. Seoane, L. B. Manfredi, V. P. Cyras, L. Torre, E. Fortunati, D. Puglia, *Polymers (Basel).* **2017**, *9*, 561.

[367] M. P. Arrieta, L. Peponi, D. López, M. Fernández-García, *Ind. Crops Prod.* **2018**, *111*, 317–328.

[368] M. P. Arrieta, C. López de Dicastillo, L. Garrido, K. Roa, M. J. Galotto, *Eur. Polym. J.* **2018**, *103*, 145–157.

[369] E. EFSA Panel on Food Contact Materials Flavourings and Processing Aids (CEF), *EFSA J.* **2012**, *10*, 2563.

[370] S. Mattioli, M. Peltzer, E. Fortunati, I. Armentano, A. Jiménez, J. M. Kenny, *Carbon N. Y.* **2013**, *63*, 274–282.

[371] F.-L. Jin, R.-R. Hu, S.-J. Park, *Compos. Part B Eng.* **2019**, *164*, 287–296.

[372] M. P. Arrieta, E. Fortunati, F. Dominici, E. Rayón, J. López, J. M. Kenny, *Carbohydr. Polym.* **2014**, *107*, 16–24.

[373] J. González-Ausejo, J. Gámez-Pérez, R. Balart, J. M. Lagarón, L. Cabedo, *Polym. Compos.* **2019**, *40*, E156–E168.

[374] M. Farmahini-Farahani, H. Xiao, A. Khan, Y. Pan, Y. Yang, *Ind. Eng. Chem. Res.* **2015**, *54*, 11277–11284.

[375] S. J. Lyle, P. J. Waller, O. M. Yaghi, *Trends Chem.* **2019**, *1*, 172–184.

[376] R. Scaffaro, L. Botta, A. Maio, G. Gallo, *Compos. Part B Eng.* **2017**, *109*, 138–146.

[377] M. P. Arrieta, M. del M. Castro-López, E. Rayón, L. F. Barral-Losada, J. M. López-Vilariño, J. López, M. V. González-Rodríguez, *J. Agric. Food Chem.* **2014**, *62*, 10170–10180.

[378] V. Muriel-Galet, J. N. Talbert, P. Hernandez-Munoz, R. Gavara, J. M. Goddard, *J. Agric. Food Chem.* **2013**, *61*, 6720–6727.

[379] F. Tian, E. A. Decker, J. M. Goddard, *J. Agric. Food Chem.* **2012**, *60*, 7710–7718.

[380] K. Li, S. Jin, J. Li, H. Chen, *Ind. Crops Prod.* **2019**, *132*, 197–212.

[381] M. Puertas-Bartolomé, M. Fernández-Gutiérrez, L. García-Fernández, B. Vázquez-Lasa, J. San Román, *Eur. Polym. J.* **2018**, *98*, 47–55.

[382] M. P. Arrieta, A. Díez García, D. López, S. Fiori, L. Peponi, *Nanomater. (Basel, Switzerland)* **2019**, *9*, 346.

[383] Y. Okada, M. Sugai, K. Chiba, *J. Org. Chem.* **2016**, *81*, 10922–10929.

[384] S. Pagoti, D. Dutta, J. Dash, *Adv. Synth. Catal.* **2013**, *355*, 3532–3538.

[385] M. Yi, Z. Shen, *J. Mater. Chem. A* **2015**, *3*, 11700–11715.

[386] M. P. Arrieta, E. Fortunati, F. Dominici, J. López, J. M. Kenny, *Carbohydr. Polym.* **2015**, *121*, 265–275.

[387] M. P. Arrieta, M. D. Samper, J. López, A. Jiménez, *J. Polym. Environ.* **2014**, *22*, 460–470.

[388] M. P. Arrieta, V. Sessini, L. Peponi, *Eur. Polym. J.* **2017**, *94*, 111–124.

[389] European Commission, *Off. J. Eur. Union* **2011**, 1–89.

[390] K. Grob, S. Pfenninger, W. Pohl, M. Laso, D. Imhof, K. Rieger, *Food Control* **2007**, *18*, 201–210.

[391] N. Metropolis, A. W. Rosenbluth, M. N. Rosenbluth, A. H. Teller, E. Teller, *J. Chem. Phys.* **1953**, *21*, 1087–1092.

[392] M. Schmid, H.-P. Steinrück, J. M. Gottfried, *Surf. Interface Anal.* **2014**, *46*, 505-511.

[393] A. Tkatchenko, M. Scheffler, *Phys. Rev. Lett.* **2009**, *102*, 73005.

[394] C. F. Macrae, P. R. Edgington, P. McCabe, E. Pidcock, G. P. Shields, R. Taylor, M. Towler, J. van de Streek, *J. Appl. Crystallogr.* **2006**, *39*, 453–

457.

[395] E. Rayón, S. Ferrandiz, M. I. Rico, J. López, M. P. Arrieta, *Int. J. Food Prop.* **2015**, *18*, 1211–1222.

[396] S. Kawano, M. Baumgarten, D. Chercka, V. Enkelmann, K. Müllen, *Chem. Commun.* **2013**, *49*, 5058–5060.

[397] X. Wang, X. Zhao, W. Dong, X. Zhang, Y. Xiang, Q. Huang, H. Chen, *J. Mater. Chem. A* **2019**, *7*, 16277–16284.

[398] N. B. Shustova, B. D. McCarthy, M. Dincă, *J. Am. Chem. Soc.* **2011**, *133*, 20126–2019.

[399] K. S. Lee, J. S. Lee, *Chem. Mater.* **2006**, *18*, 4519–4525.

[400] A. de la Peña Ruigómez, D. Rodríguez-San-Miguel, K. C. Stylianou, M. Cavallini, D. Gentili, F. Liscio, S. Milita, O. M. Roscioni, M. L. Ruiz-González, C. Carbonell, D. Maspoch, R. Mas-Ballesté, J. L. Segura, F. Zamora, *Chem. – A Eur. J.* **2015**, *21*, 10666–10670.

[401] Y. He, Z. Bian, C. Kang, Y. Cheng, L. Gao, *Tetrahedron* **2010**, *66*, 3553-3563.

[402] J. Huang, J.-T. Hong, S. H. Hong, *European J. Org. Chem.* **2012**, *2012*, 6630–6635.

[403] J. Bouffard, B. K. Keitz, R. Tonner, G. Guisado-Barrios, G. Frenking, R. H. Grubbs, G. Bertrand, *Organometallics* **2011**, *30*, 2617–2627.